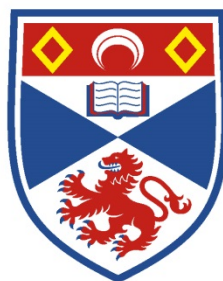


Magnetic Resonance Spectroscopy of Organic Photovoltaic Cells

Stuart A. J. Thomson



University of
St Andrews

This thesis is submitted in partial fulfilment for the degree of PhD

at the University of St Andrews

August 2017

Candidate's declarations

I Stuart Thomson, hereby certify that this thesis, which is approximately 56,000 words in length, has been written by me, and that it is the record of work carried out by me, or principally by myself in collaboration with others as acknowledged, and that it has not been submitted in any previous application for a higher degree.

I was admitted as a research student in August 2013 and as a candidate for the degree of Doctor of Philosophy in August 2013; the higher study for which this is a record was carried out in the University of St Andrews between 2013 and 2017.

Stuart A. J. Thomson

Date

Supervisor's declaration

I hereby certify that the candidate has fulfilled the conditions of the Resolution and Regulations appropriate for the degree of Doctor of Philosophy in the University of St Andrews and that the candidate is qualified to submit this thesis in application for that degree.

Ifor D. W. Samuel

Date

Permission for publication

In submitting this thesis to the University of St Andrews I understand that I am giving permission for it to be made available for use in accordance with the regulations of the University Library for the time being in force, subject to any copyright vested in the work not being affected thereby. I also understand that the title and the abstract will be published, and that a copy of the work may be made and supplied to any bona fide library or research worker, that my thesis will be electronically accessible for personal or research use unless exempt by award of an embargo as requested below, and that the library has the right to migrate my thesis into new electronic forms as required to ensure continued access to the thesis. I have obtained any third-party copyright permissions that may be required in order to allow such access and migration, or have requested the appropriate embargo below.

The following is an agreed request by candidate and supervisor regarding the publication of this thesis:

PRINTED COPY

Embargo on all of the print copy for a period of 1 year on the following ground:

Publication would preclude future publication

ELECTRONIC COPY

Embargo on all of the electronic copy for a period 1 year on the following ground:

Publication would preclude future publication

Stuart A. J. Thomson

Date

Ifor D. W. Samuel

Date

Abstract

Organic photovoltaics (OPV) have the potential advantages of low-cost, flexibility and high throughput production. However, at present their efficiency is lower than other thin film technologies and they are susceptible to degradation which limits cell lifetimes. Magnetic resonance spectroscopy is a powerful technique to study the key processes involved in the operation of OPV cells. In this thesis a range of electron paramagnetic resonance (EPR) methods are used to investigate the processes which influence cell efficiencies.

The understanding of degradation pathways and how they influence cell performance is important if OPV cells are to reach commercialisation. The efficiency of PTB7:PC₇₁BM cells is severely reduced when exposed to ambient atmosphere during processing. Current-voltage analysis was combined with EDMR spectroscopy to investigate the source of this performance loss. This investigation revealed that exposure of PTB7:PC₇₁BM films to the solvent additive DIO and ambient atmosphere leads to electron trap formation on the PC₇₁BM which acts as a recombination centre.

Using time resolved EPR spectroscopy the variation of charge separation across blends of the DTS family of small molecule electron donors with PC₆₁BM is investigated. Charge separation is found to be slowest in the [1,2,5]thiadiazolo[3,4-c]pyridine blend. This slower separation is accompanied by a higher population of triplet excitons formed by back electron transfer. This finding demonstrates that back electron transfer is a loss mechanism in these molecular systems when charge separation is slow.

The EPR signatures of negative polarons on two high efficiency non-fullerene acceptors, ITIC and IDTBR, are identified using multifrequency light induced EPR spectroscopy. The polaron signatures of ITIC and IDTBR were found to overlap with polarons on P3HT at all three microwave frequencies. Using multifrequency simulations the negative polaron signatures and g-tensors of ITIC and IDTBR were determined for the first time.

Acknowledgements

The work presented in this thesis was only made possible through the help of many individuals.

I would like to thank my supervisor Prof. Ifor Samuel, for the opportunity to carry out this project, the many discussions on the interpretation of the results, guidance on what direction to proceed, and insightful feedback on my work.

I am also very grateful to Dr. David Keeble, who much of this work was in collaboration with, and in effect served as my second supervisor. I wish to thank him for taking the time to teach me EDMR and EPR spectroscopy and for the countless hours we spent discussing the interpretation of EDMR and EPR spectra.

I was also like to thank Dr. Oleg Poluektov and Dr. Jens Niklas from Argonne National Laboratory for inviting me to visit and being such gracious hosts during my stay. I am grateful for their patience in teaching a novice about time resolved EPR and for their continued help long after I returned to Scotland.

I am also grateful to many people at St Andrews. Thanks to Dr. Hassane El Mkami for his expertise and help when using the E580 spectrometer and Dr. Rob Hunter for running the HIPER spectrometer and for the many hours spent helping me with the laser. I would also like to thank Callum Smith and the rest of the cleanroom team for keeping everything running and being there to help when it all went wrong.

Many members Organic Optoelectronics Group have influenced this project over the years. In particular I would like to thank to Dr. Bernd Ebenhoch for teaching me how to actually make a solar cell and Dr. Lethy Krishnan Jagadamma for answering my many cell fabrication questions with her seemingly infinite knowledge of OPV cells. I would also like to thank Jon Harwell for making the cleanroom more tolerable with his endless (bad) puns and cleanroom singing. Also thanks to Natalie Mica for her invaluable help with the charge mobility measurements and unparalleled enthusiasm for the ‘wonders’ of Time of Flight spectroscopy.

Lastly, I would like to thank my parents for their love and encouragement throughout the last four years and always being there for me.

Contents

Abstract.....	iii
Acknowledgements	iv
Contents.....	v
1 Introduction	1-1
2 Background.....	2-1
2.1 Organic Semiconductors.....	2-1
2.2 Organic Photovoltaics	2-6
2.2.1 Overview	2-6
2.2.2 Absorption	2-8
2.2.3 Exciton Diffusion & Charge Transfer	2-9
2.2.4 Charge Separation.....	2-10
2.2.5 Charge Transport	2-11
2.2.6 Charge Extraction	2-15
2.2.7 Generating Power	2-17
2.3 References.....	2-18
3 Electron Paramagnetic Resonance.....	3-1
3.1 An Electron in a Magnetic Field.....	3-1
3.2 What is the g-factor?.....	3-3
3.3 Interactions with Magnetic Nuclei.....	3-5
3.3.1 Nuclear Zeeman Interaction	3-5
3.3.2 Nuclear Hyperfine Interaction.....	3-6
3.4 Electron-Electron Interactions	3-8
3.4.1 Exchange Interaction	3-9
3.4.2 Dipolar Interaction.....	3-10
3.4.3 Spin Correlated Radical Pair	3-12
3.5 Application to Organic Photovoltaics.....	3-15
3.5.1 Photoinduced Excited States	3-15
3.5.2 Polaron Pair	3-16
3.5.3 Free Polarons	3-20
3.5.4 Triplet Excitons	3-21

3.6	References.....	3-26
4	Experimental Methods.....	4-1
4.1	OPV Fabrication	4-1
4.1.1	Substrate Cleaning.....	4-1
4.1.2	Film Deposition	4-1
4.1.3	Contact Deposition	4-1
4.2	J-V Characterisation	4-2
4.2.1	Cell Fabrication	4-2
4.2.2	Measuring Solar Cell Performance	4-2
4.2.3	Intensity Dependent J-V	4-4
4.3	Electron Paramagnetic Resonance Spectroscopy	4-7
4.3.1	The EPR Spectrometer	4-7
4.3.2	Continuous Wave EPR.....	4-9
4.3.3	Pulsed EPR	4-10
4.3.4	Light Induced EPR (LEPR).....	4-19
4.3.5	Time-Resolved EPR (TR-EPR).....	4-19
4.3.6	Field Calibration	4-20
4.4	Electrically Detected Magnetic Resonance Spectroscopy	4-21
4.4.1	Introduction	4-21
4.4.2	Intermediate Pair Model	4-23
4.4.3	cwEDMR	4-25
4.4.4	pEDMR.....	4-26
4.4.5	EDMR Substrate Fabrication	4-28
4.4.6	EDMR Cell Fabrication.....	4-29
4.4.7	EDMR Cell Testing	4-30
4.4.8	EDMR Setup	4-31
4.5	Time of Flight	4-34
4.5.1	Principle of ToF.....	4-34
4.5.2	ToF Cell Fabrication.....	4-37
4.5.3	ToF Measurement.....	4-38
4.5.4	Thickness Measurement	4-41
4.6	References.....	4-41

5	Air Exposure Induced Recombination in PTB7:PC ₇₁ BM Solar Cells as Studied by Electrically Detected Magnetic Resonance	5-1
5.1	Introduction.....	5-1
5.2	Background.....	5-1
5.3	Materials	5-3
5.3.1	PTB7.....	5-3
5.3.2	PC ₇₁ BM	5-4
5.3.3	DIO	5-4
5.4	Experimental.....	5-5
5.4.1	Sample Preparation.....	5-5
5.5	Results.....	5-5
5.5.1	J-V Characterisation	5-5
5.5.2	Influence of Processing Environment on EDMR of PTB7:PC ₇₁ BM	5-8
5.5.3	Power Saturation	5-14
5.5.4	Spin Flip Satellites.....	5-15
5.5.5	Breakdown of the Simulation at High Powers	5-19
5.5.6	Pulsed EDMR.....	5-20
5.5.7	Rabi Oscillation	5-22
5.5.8	Selective Injection of Carriers	5-27
5.5.9	An Aside: Lineshape of the Injection Spectra.....	5-30
5.5.10	Single Component Cells	5-32
5.5.11	Location of the Recombination Sites in the blend.....	5-37
5.6	Conclusions.....	5-41
5.7	References.....	5-42
6	Polaron Electronic Structure, Charge Separation and Triplet Exciton Formation Pathways in All Molecular Solar Cells.....	6-1
6.1	Introduction.....	6-1
6.2	Background.....	6-2
6.3	Materials	6-2
6.3.1	DTS Family of Small Molecule Donors.....	6-2
6.3.2	PC ₆₁ BM	6-4
6.4	Experimental.....	6-4
6.5	Results.....	6-5

6.5.1	9.8 GHz LEPR of DTS(FBTTh ₂) ₂ :PC ₆₁ BM Blend	6-5
6.5.2	9.8 GHz LEPR of donor:PC ₆₁ BM Blends	6-9
6.5.3	130 GHz LEPR of donor: PC ₆₁ BM	6-10
6.5.4	ENDOR of DTS(FBTTh ₂) ₂ :PC ₆₁ BM	6-12
6.5.5	ENDOR of donor:PC ₆₁ BM blends	6-14
6.5.6	Comparison of Experimental Results with DFT Calculations	6-15
6.5.7	TR-EPR of Charge Separation	6-21
6.5.8	TR-EPR of Triplet Excitons	6-24
6.6	Conclusion	6-31
6.7	References.....	6-32
7	EPR Spectroscopic Signatures of Negative Polarons on the Non-Fullerene Acceptors ITIC and IDTBR.....	7-1
7.1	Introduction.....	7-1
7.2	Background.....	7-1
7.3	Materials	7-2
7.3.1	ITIC	7-2
7.3.2	IDTBR	7-3
7.3.3	PC ₆₁ BM	7-3
7.3.4	P3HT.....	7-4
7.4	Experimental.....	7-4
7.5	Results.....	7-5
7.5.1	LEPR Spectra of P3HT:Acceptor Blends.....	7-5
7.5.2	Simulation of P3HT:PC ₆₁ BM LEPR Spectra	7-7
7.5.3	Simulation of P3HT:ITIC LEPR Spectra	7-11
7.5.4	Simulation of P3HT:IDTBR LEPR Spectra.....	7-15
7.5.5	ENDOR	7-19
7.5.6	DFT and Future Work	7-25
7.6	Conclusion	7-26
7.7	References.....	7-27
8	Charge Carrier Mobility of Non-Fullerene Acceptors	8-1
8.1	Introduction.....	8-1
8.2	Background.....	8-1

8.3	Materials	8-2
8.3.1	ITIC	8-2
8.3.2	PTB7-Th.....	8-3
8.4	Experimental.....	8-3
8.4.1	Sample Preparation.....	8-3
8.4.2	ToF Measurement.....	8-4
8.5	Results.....	8-4
8.5.1	Electron Mobility of Neat ITIC	8-4
8.5.2	Electron and Hole Mobility of PTB7-Th:ITIC.....	8-7
8.6	Conclusion	8-12
8.7	References.....	8-13
9	Conclusions	9-1

1 Introduction

Global energy demand is increasing. With a rising global population and the rapid economic growth of developing nations, the global average power consumption is expected to increase from its current value of 18 terawatts to 27 terawatts by 2040.^[1] At present over 85 % of this energy demand is met with fossil fuels.^[2] While there are sufficient fossil fuel reserves to meet the global energy requirements for the next two or three centuries,^[3] the level of the atmospheric CO₂ that would result from such a use is expected to cause severe environmental and societal damage.^[2] Atmospheric CO₂ levels are currently 400 ppm, and a continuation of meeting the world energy demand using fossil fuels as the primary energy source is predicted to raise the CO₂ concentration to over 600 ppm by 2100.^[2, 4, 5] At this level of atmospheric CO₂ the global temperature is expected to increase 3-5 °C by the end of the century.^[2, 4] The Intergovernmental Panel on Climate Change (IPCC) identified a 2 °C increase in global temperature to be the “upper limit beyond which the risks of grave damage to ecosystems, and of non-linear responses, are expected to increase”.^[6] There is therefore a dichotomy between supplying the increasing energy demand required for economic and societal growth and preventing the global temperature rise from exceeding 2 °C. To achieve both will require a major shift in energy generation towards low CO₂ emission sources, namely nuclear and renewables.

Of the renewable energy sources, solar has by far the greatest potential in terms of scale. The annual energy potentially obtainable from solar radiation is over two orders of magnitude larger than all the other renewable energy sources combined.^[7] Using currently available solar photovoltaic (PV) technology the electricity demand of the United States could be supplied using PV installations that cover 0.4 % of the land area of the continental United States.^[8] To put this area in perspective, it is approximately half of the area currently in use in the United States to grow corn crops for ethanol fuel production.^[8] At present PV accounts for less than 1% of global electricity generation.^[8] The primary reason for this low contribution is cost, as PV has traditionally been one of the most expensive energy technologies. This is changing; the cost of PV has been rapidly declining over the past several decades and is now beginning to reach economic competitiveness with other grid scale electricity sources in certain regions of the world.^[2]

At present crystalline silicon technology dominates the PV market, with over 90 % of the new installations being either monocrystalline or polycrystalline silicon.^[2] While crystalline PV modules are highly efficient they suffer from poor mechanical flexibility which limits installation options; are heavy which raises installation costs; and they require high temperature processing which results in a large embodied energy and long energy payback times.^[2,9] In response to these shortcomings there are a range of emerging thin film technologies currently under active research such as dye sensitised, perovskite and organic which could provide flexible, light weight and short energy payback PV.^[2,9,10]

The work presented in this thesis focuses on organic photovoltaics (OPV) which use carbon based semiconductors in place of silicon. These carbon based materials are solution processable and can therefore be deposited using low temperature and large area roll-to-roll methods such as spray coating and printing. While a promising technology, the efficiency of OPV cells and their long term stability must be improved if they are to reach commercialisation.^[10] In this thesis the processes limiting cell efficiencies and the degradation mechanisms responsible for the poor stability are investigated using magnetic resonance spectroscopy.

Chapter 2 introduces the chemistry and physics behind what makes certain organic molecules and polymers semiconducting. This is followed by a description of the operational principles behind organic photovoltaic cells with discussions on the potential loss mechanisms.

Chapter 3 starts with a general introduction to the theory behind electron paramagnetic resonance (EPR). The interactions of electrons with a magnetic field, nuclei and each other are described using spin Hamiltonians. The chapter then focuses on the paramagnetic species present in the operation of organic photovoltaic cells and describes their EPR signatures.

Chapter 4 details the fabrication methods and experimental techniques that were used throughout the thesis. This starts with sections on OPV cell fabrication and their testing using steady state and variable light intensity J-V analysis. Conventional EPR spectroscopy is then introduced with information on continuous wave and pulsed EPR

spectroscopy and descriptions of the pulse sequences used within this thesis. This is followed by a section on electrically detected magnetic resonance spectroscopy, highlighting the advantages and difference in detection compared with conventional EPR. The chapter is concluded with an introduction into charge mobility measurements using the time of flight method.

Chapter 5 presents a study into the source of the performance loss when PTB7:PC₇₁BM cells are exposed to ambient atmosphere during processing. J-V analysis is combined with electrically detected magnetic resonance spectroscopy to reveal that the performance loss is due to increased trap assisted recombination as a result of DIO and oxygen mediated trap formation. Comparison of the magnetic resonance spectra of the blend to the neat components demonstrates that the recombination is caused by oxidised fullerenes which serve as electron traps. This study highlights the need to move away from the solvent additive DIO towards less reactive alternatives in order to improve air stability and showcases the power of electrically detected magnetic resonance spectroscopy to probe recombination in OPV cells.

Chapter 6 reports a light induced and time resolved EPR study on the DTS family of small molecule donors. The g-tensors and hyperfine coupling constants of this family of donors are reported for the first time and the positive polaron is shown to be delocalised over two to three units of the donor molecule which may lead to more efficient charge separation in these systems. Using time resolved EPR the charge separation dynamics are shown to vary across the DTS family, with slower separation in blends with the [1,2,5]thiadiazolo[3,4-c]pyridine donor compared with the fluorobenzothiadiazole donors. The slower charge separation in the [1,2,5]thiadiazolo[3,4-c]pyridine blend is accompanied by a higher population of triplet excitons formed by back electron transfer from the triplet CT state. This finding demonstrates that back electron transfer to the triplet of the donor is a loss mechanism in these molecular systems when charge separation is slow.

Chapter 7 investigates the EPR properties of two new non-fullerene acceptors; ITIC and IDTBR. ITIC and IDTBR are blended with P3HT and the light induced EPR spectra recorded at three microwave frequencies. The EPR response of the negative polaron on the acceptor is found to be obscured by the positive polaron at all frequencies. By

simulating the spectra across the three frequencies the EPR signatures and g-tensors of negative polarons of ITIC and IDTBR are identified for the first time. To gain further information on the environment of the negative polarons the hyperfine coupling is measured using double resonance spectroscopy. These results provide information on the electronic excited states of this increasingly important class of molecules and can direct and validate the spin density distributions and conformations predicted by DFT electronic structure calculations.

Chapter 8 presents a time of flight study into the charge carrier mobility of the non-fullerene acceptor ITIC. The electron mobility of neat ITIC and in the blend with PTB7-Th was measured using the time of flight technique. The electron mobility was found to be similar in the neat film and the blend with a value of $8(2) \times 10^{-5} \text{ cm}^2 \text{ V}^{-1} \text{ s}^{-1}$ at $1.5 \times 10^5 \text{ V cm}^{-1}$, which indicates that the microstructure of the blend does not limit the electron mobility. The hole mobility of the blend was also measured and found to be approximately a factor of two to three higher than electron mobility at similar electric fields, which shows that the mobility in PTB7-Th:ITIC is balanced.

1. International Energy Outlook 2016. (U.S. Energy Information Administration, 2016).
2. 2016 Food, Water, Energy & Climate Outlook. (Massachusetts Institute of Technology Joint Program on the Science and Policy of Global Change, 2016).
3. N. S. Lewis and D. G. Nocera, Powering the Planet: Chemical Challenges in Solar Energy Utilization. *Proc. Natl. Acad. Sci. U.S.A.* **103** (43), 15729-15735 (2006).
4. Climate Change 2013: The Physical Science Basis. Contribution of Working Group I to the Fifth Assessment Report of the Intergovernmental Panel on Climate Change. (Cambridge University Press, Cambridge, United Kingdom and New York, NY, USA, 2013).
5. D. P. van Vuuren, J. Edmonds, M. Kainuma, K. Riahi, A. Thomson, K. Hibbard, G. C. Hurtt, T. Kram, V. Krey, J. F. Lamarque, T. Masui, M. Meinshausen, N. Nakicenovic, S. J. Smith and S. K. Rose, The representative concentration pathways: an overview. *Clim. Change* **109** (1-2), 5-31 (2011).
6. Climate Change 2007: Mitigation of Climate Change. Working Group III contribution to the Fourth Assessment Report of the Intergovernmental Panel on Climate Change. (Cambridge University Press, Cambridge, United Kingdom and New York, NY, USA, 2007).

7. Solar Update Vol. 62 November 2015. (International Energy Agency Solar Heating and Cooling Programme, 2015).
8. The Future of Solar Energy. (Energy Initiative Massachusetts Institute of Technology, 2015).
9. N. Espinosa, M. Hoesel, D. Angmo and F. C. Krebs, Solar cells with one-day energy payback for the factories of the future. *Energy Environ. Sci.* **5** (1), 5117-5132 (2012).
10. K. A. Mazzi and C. K. Luscombe, The future of organic photovoltaics. *Chem. Soc. Rev.* **44** (1), 78-90 (2015).

2 Background

2.1 Organic Semiconductors

The ability to use organic molecules and polymers in a host of optoelectronic applications stems from their semiconducting properties, but what gives rise to this semiconducting nature? Our daily experience with organic materials such as polyethylene bags and polyvinyl chloride insulation suggests they should be electrical insulators and this is indeed true for the majority of organic materials. However there exists a small subset of organic materials with a particular electronic structure that exhibit semiconducting properties and shall be introduced here.

Carbon is the building block of organic compounds, it has an atomic number of six and therefore six electrons which have a configuration of $1s^2 2s^2 2p^2$. The leading number is the principal quantum number and corresponds to the shell the electrons are in. The letter refers to the orbital angular momentum quantum number and describes the shape of the atomic orbital and the superscript is the number of electrons in that orbital type. The orbitals are those given by the solution of the Schrödinger equation applied to the hydrogen atom and are shown in Figure 2.1. The 1s and 2s orbitals have a spherical probability density centred on the nucleus and capable of holding two electrons each. There are three 2p orbitals which are degenerate and mutually orthogonal with a figure-of-eight probability density and are able to hold six electrons in total. It is worth stressing that the two lobes (red and blue) belong to a single orbital. The colour indicates the phase of the orbital wave function, Ψ , in that region. Strictly speaking as it is the probability density, $|\Psi|^2$, shown in Figure 2.1 then the phase information should be omitted; however

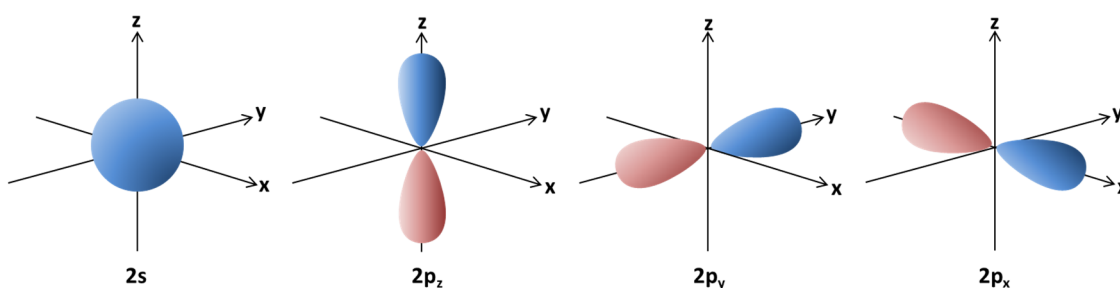


Figure 2.1: The probability density of the valence atomic orbitals of carbon.

it is common practise to retain it as it provides a useful visualisation of constructive and destructive interference during orbital overlap.

In molecular orbital (MO) theory the orbitals of a molecule are constructed from a linear combination of the atomic orbitals of the constituent atoms. The atomic orbitals are lost and replaced with new molecular orbitals that describe the electron density across the molecule as a whole. Molecular orbitals can have two types of symmetry, σ and π . In σ orbitals the electron density is found along the axis between the two nuclei. They are formed from the overlap of s orbitals or the 'end on' overlap of p orbitals as shown in Figure 2.2. In π orbitals the electron density is found above and below the internuclear axis and they are formed from the 'side on' overlap of p orbitals as can be seen in Figure 2.2. As the MOs are formed from a linear combination of atomic orbitals, the orbital wave functions can be combined in or out of phase. Combining the orbitals in phase leads to

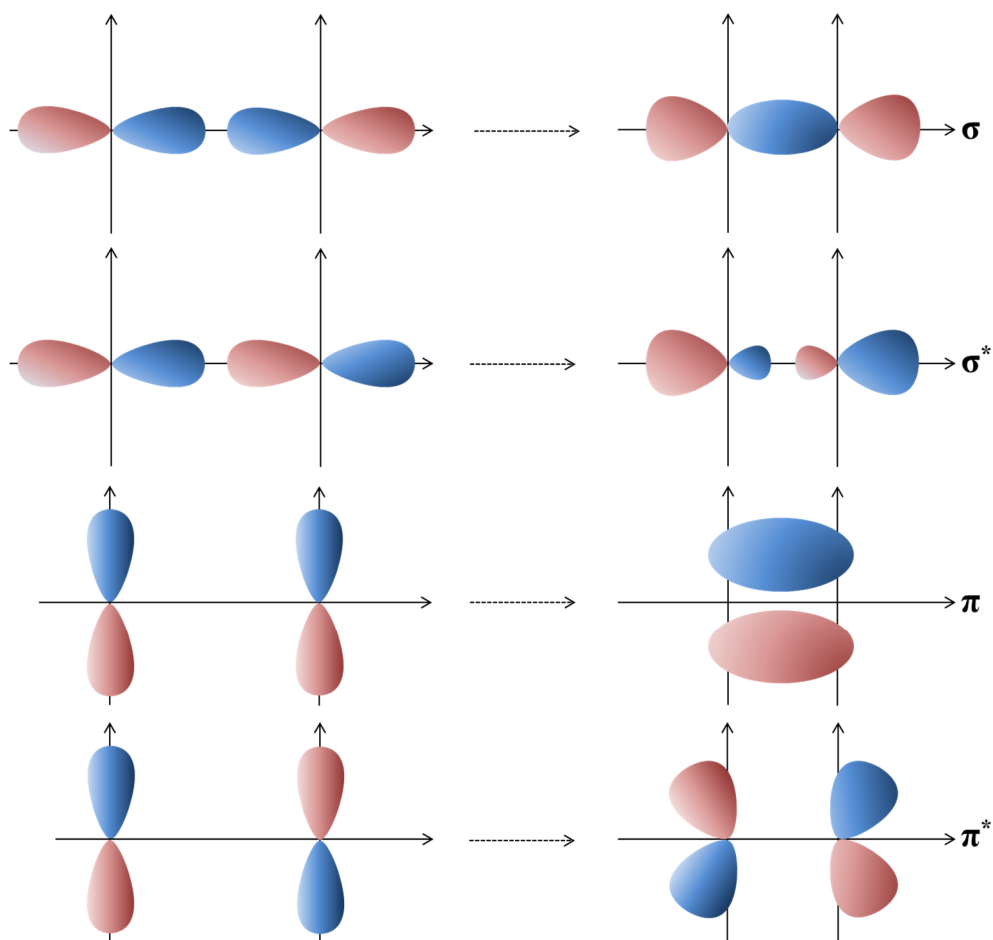


Figure 2.2: σ and π molecular orbitals.

increased electron density between the nuclei and a lowering of the energy and are called bonding orbitals. An out of phase combination results in reduced electron density between the nuclei and a raising of the system energy; these are termed antibonding orbitals and denoted by a * after the orbital name.

Considering the $1s^2 2s^2 2p^2$ electrons of carbon; the 1s orbital can be ignored as it does not influence the bonding which leaves the 2s and three 2p orbitals. Using MO theory the molecular orbitals of any organic compound could now be constructed from these atomic orbitals, however a pedagogical simplification can be made by introducing hybrid atomic orbitals. The concept of hybridisation was historically introduced to mitigate the flaws of the simpler valence bond (VB) theory, where it is a necessity to explain the bonding of carbon. In MO theory hybridisation is not required but it simplifies the description and allows the bonding to be easily visualised. The hybrid orbitals are constructed by a linear combination of the 2s and 2p orbitals, also called mixing. There are three possible types of hybrid orbital as shown in Figure 2.3. Mixing of the 2s and three 2p orbitals yields four equivalent sp^3 orbitals. The mixing of the 2s and two 2p orbitals yields three sp^2 orbitals and leaving one 2p orbital unchanged. Similarly a mixture of the 2s and one 2p orbital yields two sp orbitals leaving two 2p orbitals unchanged. Bonding using hybrid orbitals results in σ bonds.

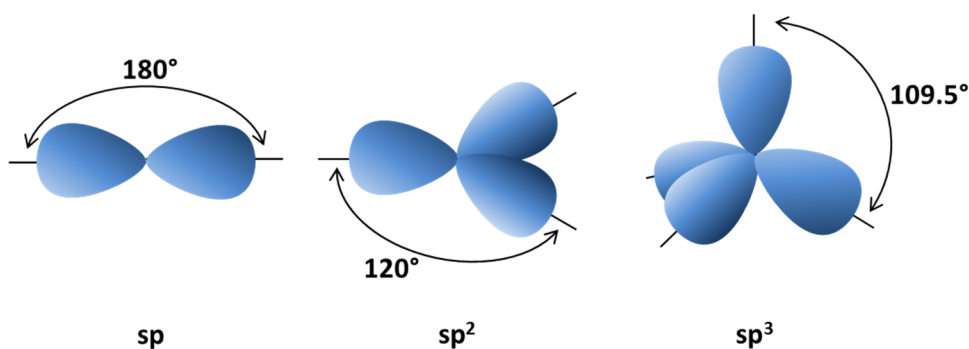


Figure 2.3: The hybrid orbitals of carbon. The leftover p orbitals are not shown. Adapted from Köhler & Bässler.^[1]

The simplest organic molecule that contains both σ and π MOs is ethene and therefore serves as a useful example. The carbons are sp^2 hybridised with four of the sp^2 orbitals overlapping with the 1s orbitals of the hydrogen atoms to form σ bonds while the remaining two overlap to form the carbon to carbon σ bond. The 2p orbital on each carbon overlap to form a carbon to carbon π bond. An energy level diagram of the ethene MOs

is shown in Figure 2.4. The diagram has been simplified by ignoring the carbon hydrogen interactions. The molecular orbitals are filled in order of increasing energy. The orbital with most energy that contains at least one electron is known as the highest occupied molecular orbital (HOMO). The next orbital in energy is termed the lowest unoccupied molecular orbital (LUMO). It can be seen from Figure 2.4 that the energy separation between the valence shell σ and σ^* MOs is substantially greater than the separation between the π and π^* . The reason for this difference is that when σ MOs are formed there is a strong overlap of atomic orbitals giving rise to a large perturbation from original atomic orbital energies. In π MOs the p orbitals weakly overlap resulting in a smaller deviation in energy.

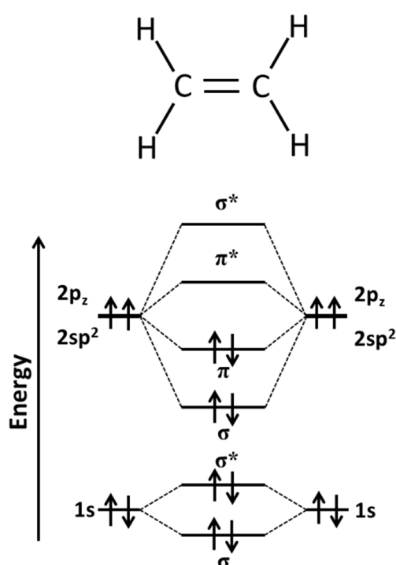


Figure 2.4: Simplified energy level diagram of ethene. Interactions with the hydrogen atoms are omitted. Adapted from Köhler & Bäessler.^[1]

The ability of an organic molecule or polymer to act as a semiconductor crucially depends on the energies of the HOMO and LUMO. The HOMO – LUMO separation is analogous to the bandgap in conventional inorganic semiconductors, and the ability to act as a semiconductor depends on the accessibility of these levels. In OPV cells the HOMO-LUMO separation needs to fall within the visible or near infrared region of the electromagnetic spectrum so that electrons can be photoexcited from the HOMO to LUMO. In addition ohmic contacts to the electrodes must be possible to allow charge extraction in OPVs and charge injection in OLEDs. This requires that the HOMO and LUMO are around -5eV and -2eV respectively which is only possible with π MOs; in

contrast σ only compounds have a HOMO and LUMO closer to -8eV and 0 eV which prevents charge injection and extraction.

The energy gap in ethene is around 7.5 eV which falls within the far ultraviolet region of the spectrum and is therefore still too large to serve as a semiconductor.^[2] The key insight of what makes an organic molecule a semiconductor comes by adding additional sp^2 hybridised carbon atoms. The next molecule in complexity is 1,3 butadiene which contains four sp^2 hybridised carbons. The p orbital on each carbon overlaps with the adjacent p orbitals to create continuous π MOs along the chain which is known as conjugation and results in delocalisation of the π electrons along the length of the conjugation. The four p orbitals can be combined in four different ways to create four π MOs as shown in Figure 2.5.

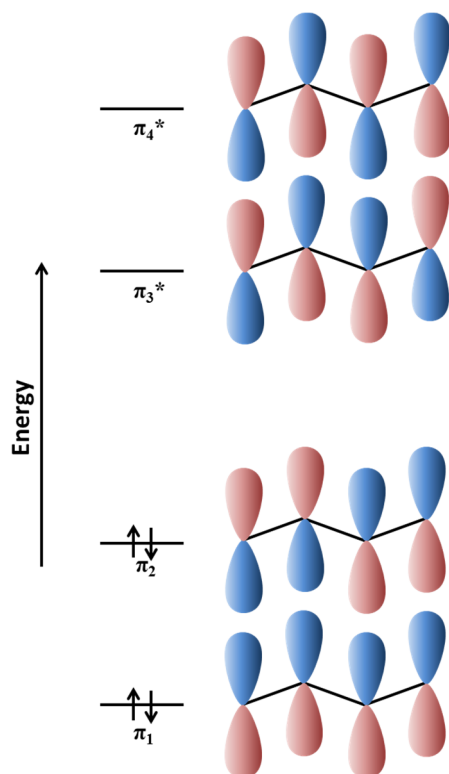


Figure 2.5: Energy levels of the π molecular orbitals in 1,3-Butadiene.

The inclusion of the two additional p orbitals in 1,3 butadiene lowers the HOMO-LUMO separation to around 5.5 eV .^[2] This is a general trend, as length of the π conjugation increases the separation between the HOMO and LUMO decreases. The length of the π conjugation is analogous to box length in the classic particle in a box problem; as the box length is increased the separation between the energy levels decreases. Extensive π

conjugation is the hallmark structural feature of organic semiconductors. In addition, as the conjugation length is increased there is an increasingly dense cluster of electronic states below the HOMO and above the LUMO. In highly conjugated systems these clusters become quasi continuous and are analogous to the valence and conduction band in traditional crystalline semiconductors. By careful molecular and polymeric design the conjugation length can be adjusted to achieve the desired HOMO and LUMO energies for the optoelectronic operation of interest. Indeed one of the key advantages of organic semiconductors is the wealth of control available when tuning these levels.

2.2 Organic Photovoltaics

2.2.1 Overview

In an organic photovoltaic cell (OPV) a thin layer of organic semiconducting material is sandwiched between two electrodes. When light is absorbed by the organic layer tightly bound singlet excitons are formed which are then split apart into free electrons and holes. The electrons and holes are transported through the organic layer and collected at opposite electrodes giving rise to a voltage and current. Organic semiconductors possess a variety of attractive properties that make them well suited for use in photovoltaic devices. They have a high absorption coefficient which enables very thin absorbing layers of 50 – 150 nm to be used, which reduces material costs and enables the creation of flexible and lightweight devices. By functionalising the semiconductors with solubilising groups the semiconductors can be dissolved in a wide range of organic solvents which enables large area and high throughput solution processed deposition methods, such as roll-to-roll printing and spray coating, to be employed; resulting in potentially lower fabrication costs.^[3] Lastly, the optical, electrical and mechanical properties of organic semiconductors can be extensively tuned through molecular design, enabling novel semiconductors to be designed to accommodate the desired application.

In order to take advantage of these properties OPV cells with sufficient efficiency have to be created. Extensive research into the photophysical processes, cell fabrication techniques and materials development has steadily raised the power conversion efficiency (PCE) of OPV over the last 15 years. The PCE of OPV versus time is shown alongside other PV technologies in Figure 2.6, where OPV is shown by the solid red circles. As of

2017, OPV PCEs of greater than 10 % are now being routinely achieved,^[4-7] with a record single junction NREL certified efficiency of 11.5%.^[8] Despite this impressive advancement in efficiency, it can be seen from Figure 2.6 that more work needs to be done. The efficiency of OPV is significantly lower than commercially available crystalline silicon (blue) which boasts cell efficiencies of over 25 %. In addition metal halide perovskite solar cells (red border with yellow centre) have recently exploded onto the PV research scene and have achieved a truly remarkable increase in efficiency from 10 % to 22% in under four years. When first developed the primary appeal of OPV was their potential of offering low cost solar power through solution processability using high throughput and low cost fabrication methods.^[3] However in the intervening years the price of commercial silicon modules has been markedly reduced. Since 2008 the price of silicon modules has dropped from around \$4 per watt to less than \$1 per watt and is now competitive with traditional energy sources.^[9] This cost reduction coupled with the rise of metal halide perovskites and the lower efficiency of OPV makes it doubtful that OPV will ever be able to compete on a price per watt level and is therefore unlikely to play a role in large scale power generation. Instead the commercial applications of OPV will likely be in niche markets where the novel properties of organic semiconductors

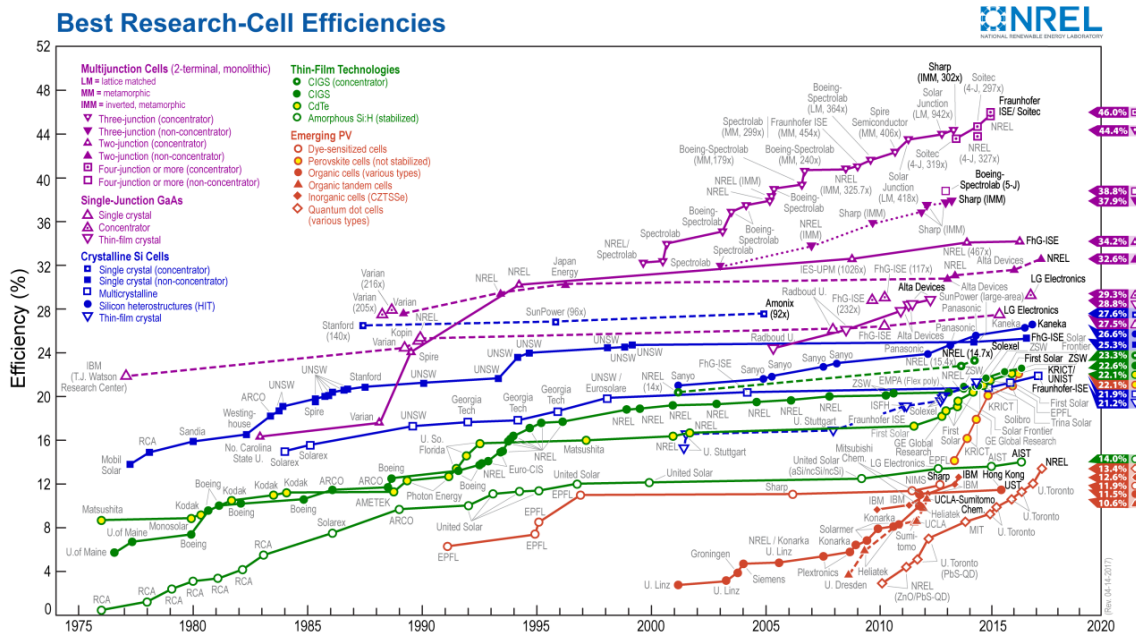


Figure 2.6: NREL certified efficiencies of research cells.^[10]

can be exploited. Their light weight and mechanical flexibility makes them well suited for portable power applications such as wearable electronics, chargers for consumer electronic devices and emerging markets such as powering the sensors required for the Internet of Things. In addition OPV cells possess excellent low light performance and have a more favourable spectral match to the emission spectrum of modern indoor lighting technologies than silicon.^[11, 12] This makes OPV an attractive technology for indoor applications; where ambient room light is used to power household electronic devices rather than disposable batteries. Another potential role for OPV is in building integrated photovoltaics (BIPV).^[13] Here the bandgap tunability and low film thickness of OPV can potentially be exploited to create aesthetic photovoltaic facades and semi-transparent photovoltaic lamination for windows.^[14] In summary, despite lower PCEs than other PV technologies OPV is still commercially promising and this coupled with the wide variety of interesting physics present in OPV makes it a valuable and rewarding area of research.

2.2.2 Absorption

The first stage in the operation of any photovoltaic cell is absorption of light. Organic semiconductors possess high absorption coefficients, typically in the range of 10^5 cm^{-1} ,^[11] which means that a 100 nm layer is capable of absorbing nearly 90 % of the incident light if a reflective back contact is used. For comparison the absorption coefficient of crystalline silicon is over two orders of magnitude lower; with values around 10^3 cm^{-1} at 600 nm,^[15] and therefore requires a layer several hundreds of microns thick. While organic semiconductors have an advantage over silicon in terms of absorption coefficient, they are not so fortunate when it comes to dielectric constant. Silicon has a dielectric constant of ~ 12 ,^[16] which screens the Coulomb interaction between the electron and hole formed after a photon is absorbed. The high dielectric constant and extensive charge delocalisation results in electron-hole binding energies of approximately 15 meV.^[17] Given that the thermal energy at room temperature is 26 meV the electron and hole will quickly dissociate followed by extraction to the electrodes. In contrast the dielectric constant of typical organic semiconductors is significantly lower with values in the range 3 to 4.^[1, 18] When a photon is absorbed in an organic semiconductor the low dielectric constant combined with localisation effects,^[19] leads to creation of strongly bound electron-hole pairs called Frenkel excitons, which have binding energies in the 0.1-0.4

eV range.^[20-22] As the binding energy is over an order of magnitude larger than the thermal energy almost no excitons will thermally dissociate to yield free charge carriers at room temperature. To dissociate the exciton, early OPV cells relied on strong internal electric fields created by using two electrodes with a large difference in work function or doping the organic layer to dissociate the exciton at impurity sites.^[23] However the low number of free charge carriers created in these early cells limited the PCE to fractions of a percent. The major breakthrough came in 1986 when Dr. Ching W. Tang working at Eastman Kodak developed the planar heterojunction architecture.^[24]

2.2.3 Exciton Diffusion & Charge Transfer

The breakthrough demonstrated by Tang was to combine two organic semiconductors with differing energy levels. By combining an electron donating and electron accepting semiconductor, where the HOMO and LUMO energies of the donor are higher than the acceptor, a heterojunction is created at the interface of two semiconductors. The energy offset at the heterojunction can then be used to break apart the photogenerated exciton through electron or hole transfer as shown in Figure 2.7. Typical energy offsets are 0.4 eV which is sufficient to promote charge transfer while limiting energy loss. The simplest OPV design to achieve this is a planar heterojunction where the donor and acceptor are deposited one atop the other as shown in Figure 2.8a. The excitons reach the donor acceptor interface through diffusion which is described by a random walk hopping mechanism. The length that excitons can travel is termed the exciton diffusion length and is determined by the exciton lifetime and mobility. The one dimensional exciton diffusion

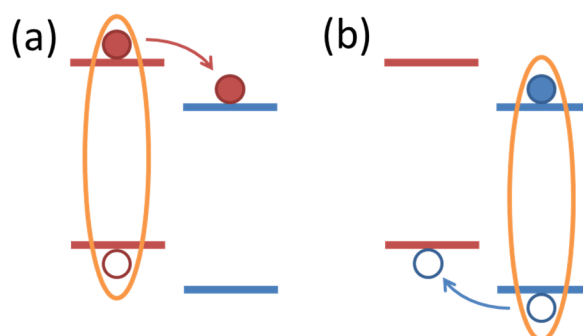


Figure 2.7: Schematic illustration of exciton dissociation through (a) electron transfer and (b) hole transfer at a heterojunction.

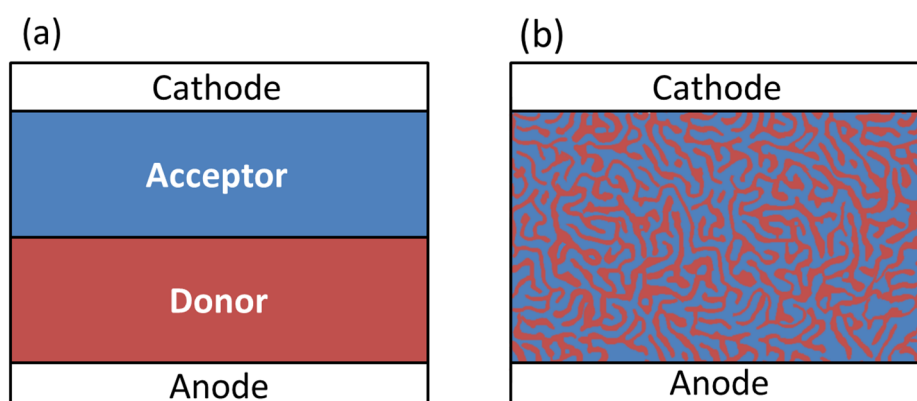


Figure 2.8: Simplified architecture of (a) planar heterojunction and (b) bulk heterojunction.

lengths in organic semiconductors are in the range of 5-20 nm.^[25, 26] This poses a problem for the planar architecture as only excitons photogenerated within an exciton diffusion length of the interface will be able to reach it before recombining, which limits the organic layer thickness to 10-40 nm. Assuming an absorption coefficient of 10^5 cm^{-1} , an exciton diffusion length of 15 nm and a double pass through the organic layer, only 45 % of the incident light will be absorbed which is far from ideal. To solve this problem the bulk heterojunction architecture was developed.^[27] Here the donor and acceptor are blended together to form a phase separated bicontinuous network of donor and acceptor as shown in Figure 2.8b. This increases the interfacial area and increases the number of excitons that are within range of the interface. It should be noted that the situation depicted in Figure 2.8b is highly simplified. In many blends the morphology is not a simple bi-phase of the donor and acceptor. Instead there can be crystalline and amorphous regions of the donor and acceptor individually as well as a mixed amorphous phase where the donor and acceptor are intimately intermixed.

2.2.4 Charge Separation

After exciton dissociation the electron and hole remain weakly bound due to the Coulomb interaction in what is known as a charge transfer (CT) or polaron pair (PP) state. In order to be extracted the electron and hole must be spatially separated until no longer bound. The driving force for charge separation in bulk heterojunction systems is still a contentious issue and under debate. A well supported theory is that in many high efficiency bulk heterojunction systems there is a spatial energy cascade which provides the driving force. Initial charge transfer to form CT states occurs in the finely intermixed

donor / acceptor phase and it has been shown that the states in this mixed phase are higher in energy, due to donor acceptor interactions and the amorphous nature, compared to the pure donor and acceptor phases.^[28-30] The energy difference between the pure and mixed phases drives electron and hole separation and breaks apart the CT state. Once fully separated the electron and hole can be transported through the pure phases to the electrodes.

Charge separation is in competition with several loss pathways and must outcompete them if a high PCE is to be obtained. The CT state can be lost by direct recombination back to the ground state which is known as geminate recombination. Another loss mechanism is through back electron transfer (BET). If the CT state is sufficiently long lived it will convert from its initial singlet multiplicity to triplet through spin mixing. If the triplet energy of the donor is lower than the CT state there will be an energetic driving force towards triplet exciton formation on the donor through BET, which is a terminal loss mechanism.^[31-34]

2.2.5 Charge Transport

After charge separation the electron and hole must navigate through the bulk heterojunction until they reach the desired electrode. The efficiency of this process is dependent on the charge carrier mobility, the morphology of the bulk heterojunction and the in-built field provided by the electrodes. There are many models to describe charge transport in organic semiconductors but the most ubiquitous is the Gaussian Disorder Model (GDM) developed by Bässler.^[35] As organic semiconductors are frequently disordered in nature, the transport through them is best described by a site to site hopping mechanism where the sites in question are the HOMO and LUMO energies of individual molecules or polymer segments for hole and electron transport respectively. In the GDM the energy of the hopping sites is described by a Gaussian distribution,^[35]

$$\rho(\varepsilon) = \frac{1}{\sqrt{2\pi\sigma^2}} \exp\left(-\frac{\varepsilon^2}{2\sigma^2}\right) \quad (2.1)$$

where ε is the energy relative to the centre of the distribution and σ is energetic disorder parameter and describes the extent of the energetic disorder in the system. The hopping rate between sites in this distribution is described using the Miller-Abrahams relation,^[36]

$$v_{ij} = v_0 \exp\left(-2\gamma a \frac{\Delta R_{ij}}{a}\right) \left\{ \begin{array}{l} \exp\left(-\frac{E_j - E_i}{kT}\right); \quad E_j > E_i \\ 1 \quad \quad \quad ; \quad E_j < E_i \end{array} \right\} \quad (2.2)$$

where v_0 is a scaling factor, ΔR_{ij} is the distance between the two sites, γ is an orbital overlap parameter, a is the average intersite distance and E is the site energy. Hops that are uphill in energy must be thermally activated and are weighted by the Boltzmann factor. For energetically downhill hops the weighting factor becomes unity. Due to the disordered nature of organic semiconductors there will be a distribution of intersite distances. To account for this an overlap parameter, $\Gamma = 2\gamma a$, is defined and given a Gaussian distribution of values with a width Σ , which is known as the spatial disorder parameter. Using the GDM the influence of electric field and temperature on the charge transport of carriers can be modelled.

To generate a voltage and current from a bulk heterojunction solar cell the electrons and holes must be selectively driven to opposite electrodes. If the bulk heterojunction was simply sandwiched between two electrodes made of the same material there would be no driving force for charge selectivity; electrons and holes would diffuse away from the interface by random hopping and have an equal probability of reaching either electrode. A driving force for charge selection can be provided by using two electrodes with different work functions. The work function of an electrode, Φ , is the energy required to eject an electron to the vacuum and is the difference in energy between the Fermi level and the vacuum level. The isolated energy levels of a bulk heterojunction and a high and low work function electrode are shown in Figure 2.9a. When these materials are brought

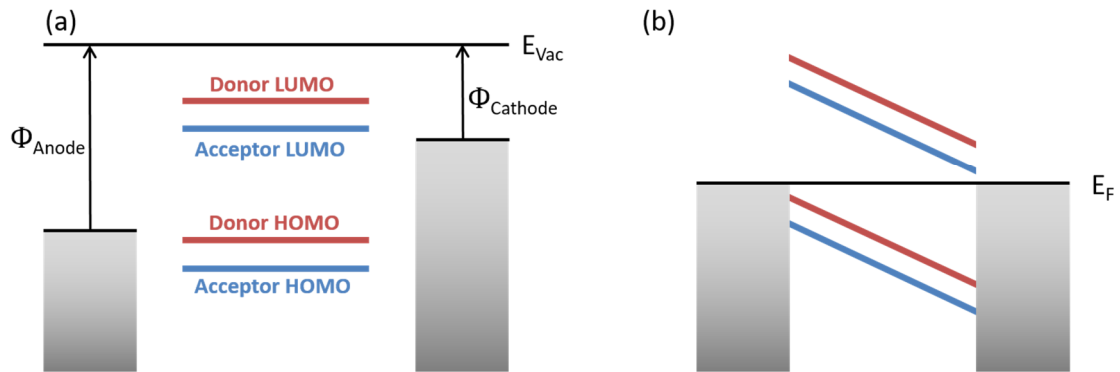


Figure 2.9 Energy level diagram of bulk heterojunction solar cell (a) before and (b) after contact of the materials.

together the Fermi level of the three materials aligns through electron transfer from the low work function electrode to the high work function electrode until equilibrium is obtained, which alters the energy level diagram as shown in Figure 2.9b. There is now an electric potential difference between the left and right hand sides of the energy level diagram equal to $\Delta\Phi/e$ where $\Delta\Phi$ is the difference in electrode work functions. This potential gives rise to an electric field inside the cell which causes a gradient in the HOMO and LUMO levels. After charge separation electrons will preferentially move towards the right and holes towards to left in order to minimise their energy which results in preferential collection of electrons at cathode and holes at the anode (Figure 2.9b). In high efficiency bulk heterojunction cells the charge selectivity can be further increased with the use electron and hole blocking layers to prevent charge collection at the wrong electrode.

During charge transport the electrons and holes have the potential to recombine. This recombination is termed non-geminate as the electron and hole originate from different excitons. There are two types of non-geminate recombination, bimolecular and monomolecular, and they are illustrated in Figure 2.10. In bimolecular recombination the electron and hole are both mobile and is typically modelled using Langevin theory which assumes that the rate limiting step is the diffusion of the electron and hole towards each other.^[37]

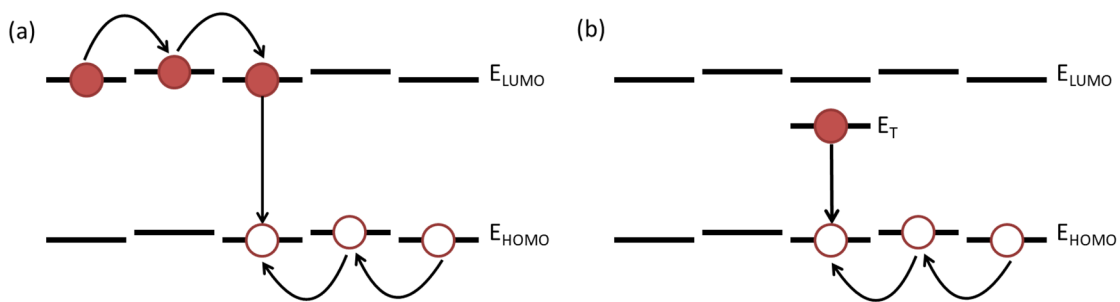


Figure 2.10 Schematic representation of non-geminate recombination through (a) bimolecular (Langevin) and (b) monomolecular (trap assisted) mechanisms.

Using Langevin theory the bimolecular recombination rate, R_L , is given by,

$$R_L = B_L(n_e n_h - n_i^2) \approx B_L n_e n_h \quad (2.3)$$

where n_e and n_h are the electron and hole density under illumination, n_i is the intrinsic carrier concentration due to thermal excitation and B_L is the recombination rate constant which is given by,

$$B_L = e \frac{\mu_n + \mu_h}{\epsilon_0 \epsilon_r} \quad (2.4)$$

where μ_n and μ_h are the electron and hole mobility respectively. As the photogenerated carrier densities are usually much greater than the intrinsic density, the n_i^2 term can be omitted and the bimolecular recombination rate is therefore second order in the photogenerated carrier concentration, hence the name. A simple Langevin analysis usually overestimates the bimolecular recombination in bulk heterojunction solar cells by several orders of magnitude, and a Langevin reduction factor γ is commonly added to Eq. 2.3 to account for the discrepancy.^[38] The deviation arises from the existence of donor and acceptor phases in a bulk heterojunction cell which is not taken into account by Langevin theory, which assumes a single homogenous material. The origin of the reduction is still under debate. Older models put forward the idea that the phase separation of donor and acceptor keeps the electrons and holes spatially separated and therefore lowers the encounter chance.^[38] However more recent developments suggest that it is the ability of the interfacial CT states, formed as a precursor to recombination, to dissociate back to free charge carriers that leads to the suppression of recombination.^[39]

The second type of non-geminate recombination is mediated through trap sites in the blend. A trap is a hopping site that has an energy significantly lower than the average energy of the distribution of hopping sites and can be considered a sub bandgap state with an energy between the HOMO and LUMO. A charge carrier which falls into a trap site therefore becomes localised to that site until it undergoes a thermally activated hop out of the site or recombines. The occupied trap site acts as recombination centre in the cell with the recombination most commonly described using Shockley, Read, and Hall (SRH) theory.^[40, 41] Under the assumption that trap filling occurs much faster than the recombination, the SRT recombination rate can be written as,^[42, 43]

$$R_{SRH} = \frac{(n_e n_h - n_i^2)}{\tau_e(n_e + n_{e,traps}) + \tau_h(n_h + n_{h,traps})} \quad (2.5)$$

where n_e and n_h are the density of mobile electrons and holes in the LUMO and HOMO of the donor and acceptor respectively, τ_e and τ_h are the recombination lifetime of mobile electrons and holes, and $n_{e,traps}$ and $n_{h,traps}$ are the density of trapped electrons and holes. In typical solar cell the number density of photogenerated carriers will be equal ($n_e \approx n_h \approx n$), and will be much greater than the intrinsic charge density ($n^2 \gg n_i^2$) and trap density ($n \gg n_{e,trap}, n_{h,trap}$). Under these assumptions Eq. 2.5 can be simplified to,

$$R_{SRT} = \frac{n}{\tau_{SRT}} \quad (2.6)$$

where $\tau_{SRT} = \tau_e + \tau_h$. The SRT recombination rate is therefore linear in charge carrier density, hence its alternate name of monomolecular recombination. In general the extraction time for charge carriers under the in-built field must be significantly shorter than τ_{SRT} and B_L^{-1} to avoid high recombination losses during charge transport. It is therefore important to use semiconductors with good mobility and optimise the morphology of the bulk heterojunction to allow rapid charge transport.

2.2.6 Charge Extraction

The final step in OPV operation is the extraction of the charge carriers to the external circuit where they can do work. In order to efficiently extract the carriers the work function of the electrode must be carefully chosen. The interface formed between a metal and a semiconductor depends on the energy difference between the Fermi level of the metal and the energy of the HOMO and LUMO. When the metal and semiconductor are brought together the Fermi level of both must align in equilibrium. Three interface scenarios are possible and are shown in Figure 2.11. The first scenario is when the Fermi level of the metal lies between the HOMO and LUMO of the semiconductor, $EA < \Phi_M < IP$ where EA is the electron affinity and IP is the ionisation potential, and is shown in Figure 2.11a. Here the difference between E_F and E_{LUMO} gives rise to an injection barrier, ϕ_e , for electrons into the LUMO of the semiconductor. Similarly the difference between E_F and E_{HOMO} defines the hole injection barrier, ϕ_h , into the HOMO of the semiconductor.

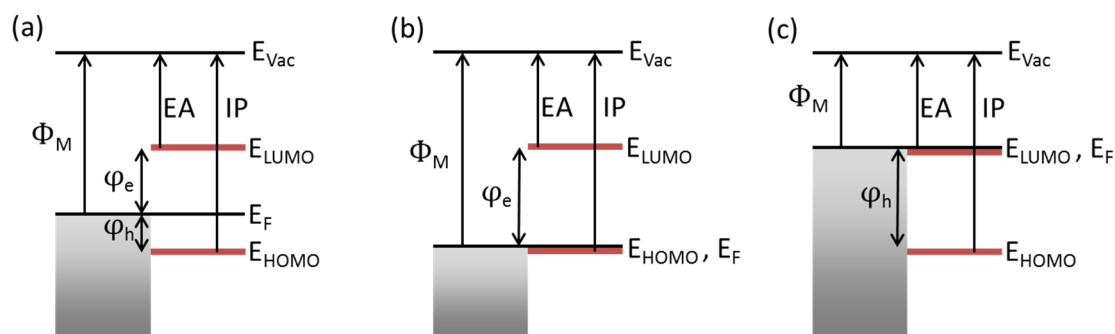


Figure 2.11 Energy level diagrams of metal-organic interfaces where (a) $EA < \Phi_M < IP$, (b) $\Phi_M > IP$ resulting in Fermi level pinning to E_{HOMO} and (c) $\Phi_M < EA$ resulting in Fermi level pinning to E_{LUMO} . Adapted from Tress.^[44]

The second scenario is when the Fermi level of the metal is lower in energy than the HOMO of the semiconductor, $\Phi_M > IP$, as shown in Figure 2.11b. Here electrons will be transferred from the HOMO of the semiconductor to metal until the Fermi level of the metal matches E_{HOMO} , which is known as Fermi level pinning.^[44] This results in a contact with no hole injection barrier, $\varphi_h = 0$, and a high electron injection barrier equal to the HOMO-LUMO splitting energy. Reciprocally when the Fermi level of the metal is higher in energy than the LUMO of the semiconductor, $\Phi_M < EA$, electrons will be transferred from the metal to LUMO of the semiconductor which pins the Fermi level to E_{LUMO} as shown in Figure 2.11c. Metal-organic interfaces are commonly described as either Schottky or ohmic. A Schottky contact is one with a high barrier for electron or hole injection resulting in an injection limited current. An ohmic contact has a small barrier for carrier injection (typically $\varphi < 0.1$ eV) and the current will be determined by the resistivity of the semiconductor. Fermi level pinning of the metal work function to the HOMO or LUMO of the semiconductor results in ohmic contacts for hole and electron injection respectively.

In organic photovoltaics we are obviously interested in extracting the charge carriers rather than injecting them. It is important to avoid injection barriers at metal semiconductor interface in a bulk heterojunction solar cell as they reduce the maximum voltage that is available from the cell. To obtain the highest possible voltage a low work function electrode that is ohmic to LUMO of the acceptor is therefore chosen for the cathode (electron extraction) and high work function electrode that is ohmic to the HOMO of the donor for the anode (hole extraction).

2.2.7 Generating Power

To generate power the solar cell must be connected to an external circuit where it can deliver power to a load. The current–voltage characteristics (J-V) of a solar cell connected to an external circuit is shown in Figure 2.12 and is divided into four quadrants. In the 1st and 3rd quadrants the solar cell consumes power from an external power supply and are used to explore the properties of the cell. In the 1st quadrant the cell is under forward bias and charge carriers are injected into the cell. In the 3rd quadrant photogenerated charge carriers are extracted under an applied reverse bias. The main area of interest is the 4th quadrant, as it is here where the cell generates electrical power. If the external circuit is open (infinite resistance) charges build up at the electrodes which creates a potential that prevents further current flow; this potential is known as the open circuit voltage (V_{OC}) and is the maximum voltage obtainable from the cell. If the external circuit is shorted (zero resistance) the maximum number of photogenerated charge carriers are extracted at the electrodes leading to a large current flow, known as the short circuit current. The photocurrent is proportional to the number of absorbed photons, and therefore to the area of the cell. It is therefore instructive to normalise current by cell area to obtain the short

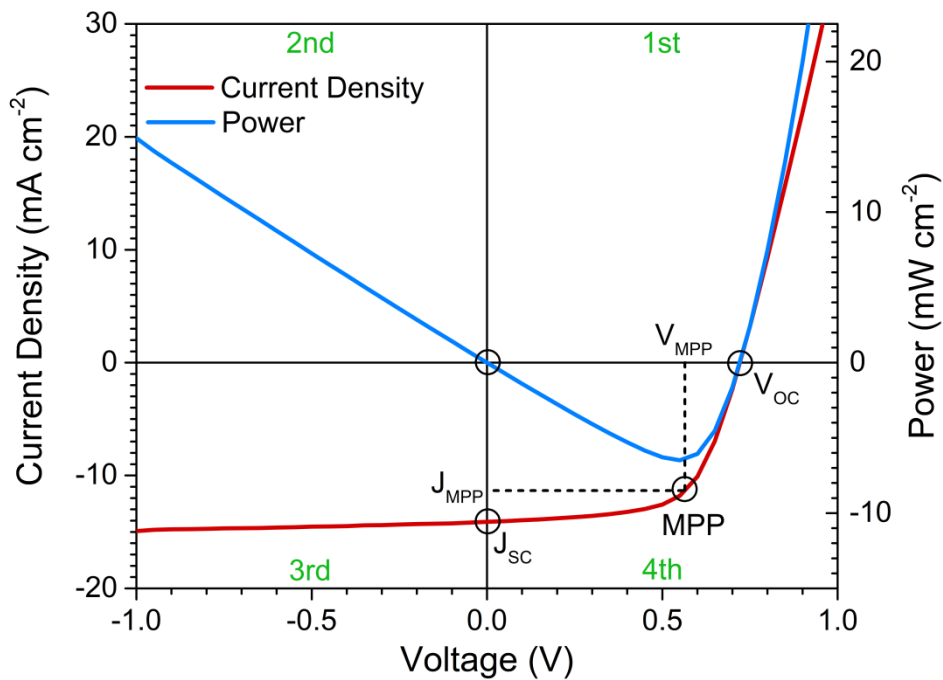


Figure 2.12 Current-voltage characteristics of solar cell under illumination.

circuit current density (J_{SC}). As power is given by the product of current and voltage the cell generates no electrical power at the above points. Instead the cell must be operated at the maximum power point (MPP) where the product of current and voltage yields maximum power (P_{MPP}). The power conversion efficiency (PCE) of the cell is given by dividing the maximum electrical output power by the incident optical power, P_{In} , on the cell.

$$PCE = \frac{P_{MPP}}{P_{In}} = \frac{V_{MPP}J_{MPP}}{P_{In}} = \frac{V_{OC}J_{SC}FF}{P_{In}} \quad (2.7)$$

It is informative to rewrite the PCE equation in terms of the V_{OC} , J_{SC} and a new parameter called the Fill Factor (FF). The FF is a measure of the quality of the solar cell and is the ratio of the maximum power (P_{MPP}) over the ideal maximum power ($V_{OC}J_{SC}$). Graphically the FF represents the squareness of the J-V curve. To obtain a high PCE the V_{OC} , J_{SC} and FF of the cell need to be optimised.

2.3 References

1. A. Köhler and H. Bässler, *Electronic Processes in Organic Semiconductors: An Introduction*. (Wiley-VCH, Weinheim, Germany, 2015).
2. C. H. Choi, M. Kertesz and A. Karpfen, The effects of electron correlation on the degree of bond alternation and electronic structure of oligomers of polyacetylene. *J. Chem. Phys.* **107** (17), 6712-6721 (1997).
3. C. J. Brabec, Organic photovoltaics: technology and market. *Sol. Energy Mater. Sol. Cells* **83** (2-3), 273-292 (2004).
4. Y. H. Liu, J. B. Zhao, Z. K. Li, C. Mu, W. Ma, H. W. Hu, K. Jiang, H. R. Lin, H. Ade and H. Yan, Aggregation and Morphology Control Enables Multiple Cases of High-Efficiency Polymer Solar Cells. *Nat. Commun.* **5**, 8 (2014).
5. Y. Y. Xiaofeng Lin, Li Nian, Hua Su, Jiemei Ou, Zhongke Yuan, Fangyan Xie, Wei Hong, Dingshan Yu, Mingqiu Zhang, Yuguang Ma, Xudong Chen, Interfacial Modification Layers Based on Carbon Dots for Efficient Inverted Polymer Solar Cells Exceeding 10% Power Conversion Efficiency. *Nano Energy* **26**, 216-233 (2016).
6. H. F. Yao, L. Ye, H. Zhang, S. S. Li, S. Q. Zhang and J. H. Hou, Molecular Design of Benzodithiophene-based Organic Photovoltaic Materials. *Chem. Rev.* **116** (12), 7397-7457 (2016).

7. S. Q. Zhang, L. Ye and J. H. Hou, Breaking the 10% Efficiency Barrier in Organic Photovoltaics: Morphology and Device Optimization of Well-Known PBDTTT Polymers. *Adv. Energy Mater.* **6** (11), 20 (2016).
8. J. Zhao, Y. Li, G. Yang, K. Jiang, H. Lin, H. Ade, W. Ma and H. Yan, Efficient organic solar cells processed from hydrocarbon solvents. *Nat. Energy* **1**, 15027 (2016).
9. D. Feldman, G. Barbose, R. Margolis, M. Bolinger, D. Chung, R. Fu, J. Seel, C. Davidson, N. Darghouth and R. Wiser, Photovoltaic System Pricing Trends, Historical, Recent, and Near-Term Projections 2015 Edition, (U.S. Department of Energy, 2015).
10. <http://nrel.gov/pv/assets/images/efficiency-chart.png>, Accessed 04/06/17.
11. C. L. Cutting, M. Bag and D. Venkataraman, Indoor light recycling: a new home for organic photovoltaics. *J. Mater. Chem. C* **4** (43), 10367-10370 (2016).
12. H. K. H. Lee, Z. Li, J. R. Durrant and W. C. Tsoi, Is organic photovoltaics promising for indoor applications? *Appl. Phys. Lett.* **108** (25), 5 (2016).
13. B. P. Jelle, C. Breivik and H. D. Rokenes, Building integrated photovoltaic products: A state-of-the-art review and future research opportunities. *Sol. Energy Mater. Sol. Cells* **100**, 69-96 (2012).
14. C. C. Chen, L. T. Dou, R. Zhu, C. H. Chung, T. B. Song, Y. B. Zheng, S. Hawks, G. Li, P. S. Weiss and Y. Yang, Visibly Transparent Polymer Solar Cells Produced by Solution Processing. *ACS Nano* **6** (8), 7185-7190 (2012).
15. M. A. Green and M. J. Keevers, Optical Properties of Intrinsic Silicon at 300 K *Prog. Photovoltaics* **3** (3), 189-192 (1995).
16. W. C. Dunlap and R. L. Watters, Direct Measurement of the Dielectric Constants of Silicon and Germanium. *Phys. Rev.* **92** (6), 1396-1397 (1953).
17. M. A. Green, Improved value for the silicon free exciton binding energy. *AIP Adv.* **3** (11), 15 (2013).
18. S. Torabi, F. Jahani, I. Van Severen, C. Kanimozhi, S. Patil, R. W. A. Havenith, R. C. Chiechi, L. Lutsen, D. J. M. Vanderzande, T. J. Cleij, J. C. Hummelen and L. J. A. Koster, Strategy for Enhancing the Dielectric Constant of Organic Semiconductors Without Sacrificing Charge Carrier Mobility and Solubility. *Adv. Funct. Mater.* **25** (1), 150-157 (2015).
19. K. Hummer and C. Ambrosch-Draxl, Oligoacene exciton binding energies: Their dependence on molecular size. *Physical Review B* **71** (8), 4 (2005).
20. I. H. Campbell, T. W. Hagler, D. L. Smith and J. P. Ferraris, Direct measurement of conjugated polymer electronic excitation energies using metal/polymer/metal structures. *Phys. Rev. Lett.* **76** (11), 1900-1903 (1996).

21. S. F. Alvarado, P. F. Seidler, D. G. Lidzey and D. D. C. Bradley, Direct determination of the exciton binding energy of conjugated polymers using a scanning tunneling microscope. *Phys. Rev. Lett.* **81** (5), 1082-1085 (1998).
22. J. Tsutsumi, H. Matsuzaki, N. Kanai, T. Yamada and T. Hasegawa, Charge Separation and Recombination of Charge-Transfer Excitons in Donor-Acceptor Polymer Solar Cells. *J. Phys. Chem. C* **117** (33), 16769-16773 (2013).
23. G. A. Chamberlain, Organic Solar-cells - A Review. *Solar Cells* **8** (1), 47-83 (1983).
24. C. W. Tang, Two-Layer Organic Photovoltaic Cell. *Appl. Phys. Lett.* **48** (2), 183-185 (1986).
25. G. J. Hedley, A. Ruseckas and I. D. W. Samuel, Light Harvesting for Organic Photovoltaics. *Chem. Rev.* **117** (2), 796-837 (2017).
26. O. V. Mikhnenko, P. W. M. Blom and T. Q. Nguyen, Exciton diffusion in organic semiconductors. *Energy Environ. Sci.* **8** (7), 1867-1888 (2015).
27. G. Yu, J. Gao, J. C. Hummelen, F. Wudl and A. J. Heeger, Polymer Photovoltaic Cells - Enhanced Efficiencies Via A Network Of Internal Donor-acceptor Heterojunctions. *Science* **270** (5243), 1789-1791 (1995).
28. F. C. Jamieson, E. B. Domingo, T. McCarthy-Ward, M. Heeney, N. Stingelin and J. R. Durrant, Fullerene crystallisation as a key driver of charge separation in polymer/fullerene bulk heterojunction solar cells. *Chem. Sci.* **3** (2), 485-492 (2012).
29. S. Shoaee, S. Subramaniyan, H. Xin, C. Keiderling, P. S. Tuladhar, F. Jamieson, S. A. Jenekhe and J. R. Durrant, Charge Photogeneration for a Series of Thiazolo-Thiazole Donor Polymers Blended with the Fullerene Electron Acceptors PCBM and ICBA. *Adv. Funct. Mater.* **23** (26), 3286-3298 (2013).
30. S. Sweetnam, K. R. Graham, G. O. N. Ndjawa, T. Heumuller, J. A. Bartelt, T. M. Burke, W. T. Li, W. You, A. Amassian and M. D. McGehee, Characterization of the Polymer Energy Landscape in Polymer:Fullerene Bulk Heterojunctions with Pure and Mixed Phases. *J. Am. Chem. Soc.* **136** (40), 14078-14088 (2014).
31. M. Liedtke, A. Sperlich, H. Kraus, A. Baumann, C. Deibel, M. J. M. Wirix, J. Loos, C. M. Cardona and V. Dyakonov, Triplet Exciton Generation in Bulk-Heterojunction Solar Cells Based on Endohedral Fullerenes. *J. Am. Chem. Soc.* **133** (23), 9088-9094 (2011).
32. H. Ohkita, S. Cook, Y. Astuti, W. Duffy, M. Heeney, S. Tierney, I. McCulloch, D. D. C. Bradley and J. R. Durrant, Radical ion pair mediated triplet formation in polymer-fullerene blend films. *Chem. Commun.* (37), 3939-3941 (2006).
33. C. Dyer-Smith, L. X. Reynolds, A. Bruno, D. D. C. Bradley, S. A. Haque and J. Nelson, Triplet Formation in Fullerene Multi-Adduct Blends for Organic Solar Cells and Its Influence on Device Performance. *Adv. Funct. Mater.* **20** (16), 2701-2708 (2010).

34. D. Veldman, T. Offermans, J. Sweelssen, M. M. Koetse, S. C. J. Meskers and R. A. J. Janssen, Triplet formation from the charge-separated state in blends of MDMO-PPV with cyano-containing acceptor polymers. *Thin Solid Films* **511**, 333-337 (2006).
35. H. Bassler, Charge Transport In Disordered Organic Photoconductors - A Monte-carlo Simulation Study. *Physica Status Solidi B-Basic Research* **175** (1), 15-56 (1993).
36. A. Miller and E. Abrahams, Impurity Conduction At Low Concentrations. *Phys. Rev.* **120** (3), 745-755 (1960).
37. P. Langevin, The recombination and mobilities of ions in gases. *Ann. Chim. Phys.* **28**, 433-530 (1903).
38. C. Deibel, A. Wagenpfahl and V. Dyakonov, Origin of reduced polaron recombination in organic semiconductor devices. *Physical Review B* **80** (7), 7 (2009).
39. T. M. Burke, S. Sweetnam, K. Vandewal and M. D. McGehee, Beyond Langevin Recombination: How Equilibrium Between Free Carriers and Charge Transfer States Determines the Open-Circuit Voltage of Organic Solar Cells. *Adv. Energy Mater.* **5** (11), 12 (2015).
40. W. Shockley and W. T. Read, Statistics Of The Recombinations Of Holes And Electrons. *Phys. Rev.* **87** (5), 835-842 (1952).
41. R. N. Hall, Electron-hole Recombination In Germanium. *Phys. Rev.* **87** (2), 387-387 (1952).
42. S. R. Cowan, W. L. Leong, N. Banerji, G. Dennler and A. J. Heeger, Identifying a Threshold Impurity Level for Organic Solar Cells: Enhanced First-Order Recombination Via Well-Defined PC84BM Traps in Organic Bulk Heterojunction Solar Cells. *Adv. Funct. Mater.* **21** (16), 3083-3092 (2011).
43. S. R. Cowan, A. Roy and A. J. Heeger, Recombination in polymer-fullerene bulk heterojunction solar cells. *Physical Review B* **82** (24), 10 (2010).
44. W. Tress, Organic Solar Cells: Theory, Experiment, and Device Simulation. (Springer International Publishing, 2014).

3 Electron Paramagnetic Resonance

This chapter provides a theoretical background in electron paramagnetic resonance. It focuses on describing the interactions of electrons with an applied magnetic field, their local environment and each other using spin Hamiltonians. Details on how to obtain EPR spectra are introduced in the following chapter.

3.1 An Electron in a Magnetic Field

In 1920 Stern & Gerlach performed their famous experiment and were the first,^[1-3] albeit unknowingly,^[4] to observe the quantisation of magnetic moment due to the intrinsic angular momentum of the electron. The theoretical foundation for their observations was later provided in 1925 by Goudsmit and Uhlenbeck who postulated that by assigning electrons an intrinsic angular momentum, the features of experimental spectra could be explained.^[5, 6] They named this intrinsic angular momentum ‘spin’, as they erroneously suggested that the rotation of the electron was the source of the angular momentum.^[5, 6] It is the interaction of this spin angular momentum with an applied magnetic field that is the essence of electron magnetic resonance spectroscopy.

The magnetic moment operator of a free electron $\hat{\boldsymbol{\mu}}_e$ is related to the spin angular momentum operator $\hat{\mathbf{S}}$ by,

$$\hat{\boldsymbol{\mu}}_e = -g_e \mu_B \hat{\mathbf{S}} \quad (3.1)$$

where μ_B is the Bohr magneton, and g_e is the free electron g-factor and is one of the most accurately known physical constants with a value of 2.00231930436182(52).^[7] Here g_e and μ_B are chosen to be positive and the negative sign is stated explicitly, and arises from the negative charge of the electron. When an electron is placed in a magnetic field \mathbf{B} the Zeeman interaction energy of the magnetic moment and the field is given by the following Hamiltonian,

$$\hat{H}_{eZ} = -\mathbf{B}' \cdot \hat{\boldsymbol{\mu}}_e \quad (3.2a)$$

$$\hat{H}_{eZ} = g_e \mu_B \mathbf{B}' \cdot \hat{\mathbf{S}} \quad (3.2b)$$

where ' denotes the transpose is being taken. By choosing \mathbf{B} to be aligned along the z-axis the Hamiltonian can be rewritten as,

$$\hat{H}_{eZ} = -B\hat{\mu}_{ez} \quad (3.3a)$$

$$\hat{H}_{eZ} = g_e\mu_B B\hat{S}_z \quad (3.3b)$$

where \hat{S}_z is the z component of the spin angular momentum operator. An electron is a spin $\frac{1}{2}$ particle and can exist in two spin states; commonly labelled the $|\alpha\rangle$ and $|\beta\rangle$ states which are degenerate in the absence of a magnetic field. Applying the \hat{S}_z to these states yields,

$$\hat{S}_z|\alpha\rangle = +\frac{1}{2}|\alpha\rangle \quad (3.4a)$$

$$\hat{S}_z|\beta\rangle = -\frac{1}{2}|\beta\rangle \quad (3.4b)$$

where $+\frac{1}{2}$ and $-\frac{1}{2}$ are the values of magnetic spin quantum number m_s of the $|\alpha\rangle$ and $|\beta\rangle$ states respectively. The energies of the states $|\alpha\rangle$ and $|\beta\rangle$ in a magnetic field are therefore given by the following expectation values.

$$\langle\alpha|\hat{H}|\alpha\rangle = +\frac{1}{2}g_e\mu_B B \quad (3.5a)$$

$$\langle\beta|\hat{H}|\beta\rangle = -\frac{1}{2}g_e\mu_B B \quad (3.5b)$$

Application of a magnetic field breaks the degeneracy of the $|\alpha\rangle$ and $|\beta\rangle$ states as the energy of the electron is lower when its magnetic moment is aligned parallel to the applied field and higher when it is anti-parallel. The energy separation between the two states is proportional to the strength of the applied field and is known as the Zeeman splitting.

By applying electromagnetic radiation of appropriate frequency ν , transitions between the two states can be induced. The resonance condition of these transitions is given by the following.

$$h\nu = g_e\mu_B B \quad (3.6)$$

Fulfilling this resonance condition and using it to obtain information on the system under study is the essence of electron magnetic resonance spectroscopy.

3.2 What is the g-factor?

In the previous section the response of an isolated electron to a magnetic field was introduced. However the electrons of interest are located in molecular orbitals and will therefore experience a small amount of orbital angular momentum in addition to the spin angular momentum. The total magnetic moment operator of the electron is then the sum of orbital and spin angular momentum contributions and given by,

$$\hat{\boldsymbol{\mu}} = -\mu_B(\hat{\mathbf{L}} + g_e\hat{\mathbf{S}}) \quad (3.7)$$

where $\hat{\mathbf{L}}$ is the orbital angular momentum operator. In addition the spin and orbital angular momentum are coupled through a spin-orbit coupling term,

$$\lambda\hat{\mathbf{L}}'\cdot\hat{\mathbf{S}} \quad (3.8)$$

where λ is magnitude of the spin-orbit coupling. Using Eq. 3.7 and 3.8 the spin Hamiltonian of an electron in a magnetic field (Eq. 3.2) can be modified to include the orbital contribution.

$$\hat{H}_{eZ} = \mu_B\mathbf{B}'\cdot(\hat{\mathbf{L}} + g_e\hat{\mathbf{S}}) + \lambda\hat{\mathbf{L}}'\cdot\hat{\mathbf{S}} \quad (3.9)$$

In principle one could stop here and describe systems based on the above Hamiltonian. However from a practical standpoint it is instead more convenient to define a new variable g-factor g which includes the orbital angular momentum contribution. Using this approach the electron Zeeman interaction Hamiltonian can be rewritten as the following.

$$\hat{H}_{eZ} = g\mu_B\mathbf{B}'\cdot\hat{\mathbf{S}} \quad (3.10)$$

Details on the mathematical steps to transform Eq. 3.9 to 3.10 can be found in Weil & Bolton.^[8] The deviation between g and g_e depends on the strength of spin-orbit coupling. The new EPR resonance condition is simply obtained by replacing g_e by g .

$$h\nu = g\mu_B B \quad (3.11)$$

Organic semiconducting molecules and polymers generally have a low symmetry and the spin-orbit coupling is therefore anisotropic; g will therefore vary depending on the relative orientation of \mathbf{B} and the molecule or polymer under study. To describe this anisotropy, g takes the form of a 2nd rank tensor.

$$\mathbf{g} = \begin{pmatrix} g_{xx} & g_{xy} & g_{xz} \\ g_{yx} & g_{yy} & g_{yz} \\ g_{zx} & g_{zy} & g_{zz} \end{pmatrix} \quad (3.12a)$$

However it is more commonly diagonalised by transformation into the g principal axis reference frame,

$$\mathbf{g} = \begin{pmatrix} g_x & 0 & 0 \\ 0 & g_y & 0 \\ 0 & 0 & g_z \end{pmatrix} \quad (3.12b)$$

where g_x , g_y , and g_z are the principal values of the g -tensor. The principal values of the g -tensor contain information on the electronic structure and symmetry of the spin environment and serve as a unique fingerprint of the paramagnetic species under study. An isotropic g -factor can also be defined, which is the average of the three principal values.

$$g_{iso} = \frac{1}{3}(g_x + g_y + g_z) \quad (3.13)$$

When quickly referencing the g -factor of a paramagnetic species it is common to quote the g_{iso} rather than the full tensor.

For samples with a high degree of orientation, such as a single crystal, the observed g -factor is dependent on the relative orientation of the magnetic field axis and the g principal axis. However organic semiconductors are generally amorphous or polycrystalline and will therefore be randomly oriented with respect to the magnetic field. As a result, the three principal values of the g -tensor are observed simultaneously in the EPR spectrum which is known as a powder average. The powder spectra of a spin $\frac{1}{2}$ species with different symmetries of spin environment is shown in Figure 3.1

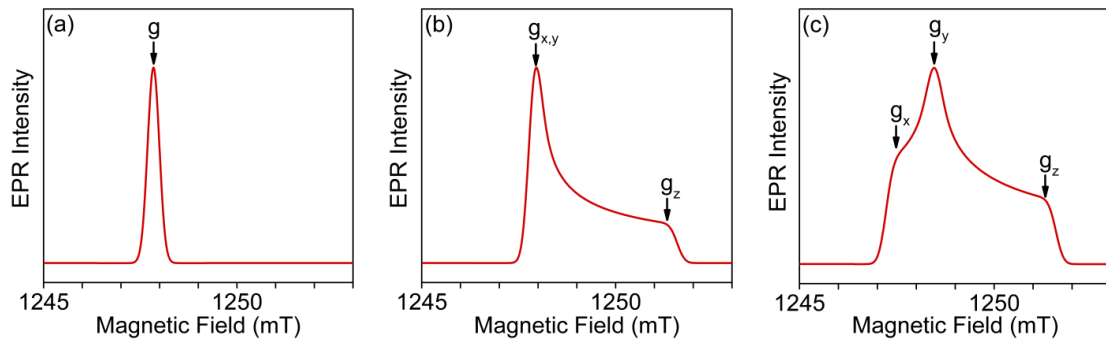


Figure 3.1 Simulation of powder EPR spectrum for a single spin $\frac{1}{2}$ species with (a) cubic g -tensor, (b) axial g -tensor and (c) rhombic g -tensor.

If the spin environment has cubic symmetry the three principal values will be equal ($g_x = g_y = g_z$) and the EPR spectrum will be composed of a single line (Figure 3.1a). A single line spectrum is also obtained in liquid solutions where the three principal values are motionally averaged to yield a single isotropic value, g_{iso} . If two of the principal values are equal and one different ($g_x = g_y \neq g_z$) the spin environment has axial symmetry and the powder EPR spectrum will contain two peaks (Figure 3.1b). In the lowest symmetry case all three g-factors are different and the spin environment has rhombic symmetry, resulting in an EPR spectrum with three peaks as shown in Figure 3.1c. Therefore by measuring an EPR spectrum the principal values of the g-tensor can be obtained and the electronic structure of the spin environment determined.

3.3 Interactions with Magnetic Nuclei

Nuclei with a non-zero nuclear spin quantum number I possess an intrinsic nuclear spin angular momentum and an associated nuclear magnetic moment. Many of these magnetically active nuclei are present in organic semiconductors, such as ^{14}N , ^{31}P , ^{19}F and most importantly ^1H which guarantees that the EPR spectrum of any organic semiconductor will be influenced by the nuclei.

3.3.1 Nuclear Zeeman Interaction

Magnetic nuclei interact with the magnetic field in the same way as an electron. The Zeeman interaction of a nuclear spin with the magnetic field is given by,

$$\hat{H}_{nZ} = g_n \mu_N \mathbf{B}' \cdot \hat{\mathbf{I}} \quad (3.14)$$

where g_n is the nuclear g-factor, μ_N is the nuclear magneton and $\hat{\mathbf{I}}$ is the nuclear spin angular momentum operator. This interaction is completely analogous to that discussed in the previous section and is the foundation of NMR spectroscopy. This interaction has little or no influence in most EPR spectroscopy due to conservation of angular momentum which normally imposes a $\Delta m_I = 0$ selection rule during the EPR transition, and the nuclear spin state therefore remains unchanged. One notable exception is the occurrence of nuclear spin-flip satellites which are discussed in detail in Section 5.5.5.

3.3.2 Nuclear Hyperfine Interaction

Of greater interest for EPR spectroscopy is the coupling between the electron and nuclear spins which is called the hyperfine interaction. The presence of a nearby nuclear spin alters the energy of the electron spin levels. The hyperfine interaction Hamiltonian of an electron spin coupled to k nuclei is given by,

$$\hat{H}_{hf} = \sum_k \hat{\mathbf{S}}' \cdot \mathbf{A} \cdot \hat{\mathbf{I}}_k \quad (3.15)$$

where \mathbf{A} is the hyperfine interaction tensor that describes the coupling between the electron and nuclear spins. \hat{H}_{hf} is composed of two separate interactions, one isotropic and the other anisotropic, with different physical origins.

$$\hat{H}_{hf} = \hat{H}_{hf_Fermi} + \hat{H}_{hf_Dip} \quad (3.16)$$

The isotropic part is known as the Fermi contact interaction and arises because the probability density of an electron in an s orbital is non-zero at the nucleus. The finite probability that the electron is located at the nucleus gives rise to the interaction between the electron and nuclear magnetic moments. The Fermi contact interaction is given by,

$$\hat{H}_{hf_Fermi} = \frac{2\mu_0}{3} g\mu_B g_n \mu_N |\psi(0)|^2 \hat{\mathbf{S}}' \cdot \hat{\mathbf{I}} \quad (3.17a)$$

$$\hat{H}_{hf_Fermi} = A_{iso} \hat{\mathbf{S}}' \cdot \hat{\mathbf{I}} \quad (3.17b)$$

where A_0 is the isotropic hyperfine coupling constant. The coupling constant is proportional to the electron density at the nucleus and is given by,

$$A_{iso} = \frac{2\mu_0}{3} g\mu_B g_n \mu_N |\psi(0)|^2 \quad (3.18)$$

where μ_0 is the vacuum permeability and $|\psi(0)|^2$ is the probability that the electron is at the nucleus.

The anisotropic part of the hyperfine interaction is due to dipolar coupling between the electron and nuclear magnetic moments. The dipolar hyperfine interaction Hamiltonian is given by,

$$\hat{H}_{hf_Dip} = \frac{\mu_0}{4\pi} g\mu_B g_N \mu_N \left[\frac{\hat{\mathbf{S}}' \cdot \hat{\mathbf{I}}}{r^3} - \frac{3(\hat{\mathbf{S}}' \cdot \mathbf{r})(\hat{\mathbf{I}} \cdot \mathbf{r})}{r^5} \right] \quad (3.19)$$

where \mathbf{r} is the vector between the electron and the coupled nucleus. Following spatial integration, the two interactions can be collectively described through the hyperfine interaction tensor \mathbf{A} which analogously to \mathbf{g} can be written in a general form (Eq. 3.20a) or diagonalised by transformation into the \mathbf{A} principal axis reference frame (Eq. 3.20b).

$$\mathbf{A} = \begin{pmatrix} A_{xx} & A_{xy} & A_{xz} \\ A_{yx} & A_{yy} & A_{yz} \\ A_{zx} & A_{zy} & A_{zz} \end{pmatrix} \quad (3.20a)$$

$$\mathbf{A} = \begin{pmatrix} A_x & 0 & 0 \\ 0 & A_y & 0 \\ 0 & 0 & A_z \end{pmatrix} \quad (3.20b)$$

In general the principal axes of \mathbf{g} and \mathbf{A} are not parallel; however in organic molecules and polymers the g anisotropy is typically small and the relative orientation of \mathbf{g} and \mathbf{A} is therefore not crucial. It is sometimes convenient to split \mathbf{A} into its isotropic and anisotropic parts,

$$\mathbf{A} = A_{iso} \mathbf{1}_3 + \mathbf{T} \quad (3.21)$$

where $\mathbf{1}_3$ is the 3x3 identity matrix and \mathbf{T} is the dipolar hyperfine interaction tensor.

The effect of magnetic nuclei on the EPR spectrum of a single electron is shown in Figure 3.2, where it has been assumed that the hyperfine interaction is isotropic only. The EPR spectrum of an electron with a single well defined g -factor is a Lorentzian (Figure 3.2a). Interaction with an $I = 1/2$ nucleus such as ^1H splits the energy of each electron spin level into two, resulting in two possible EPR transitions and a doublet EPR spectrum (Figure 3.2b). Similarly interaction with an $I = 3/2$ nucleus like ^{14}N will result in a triplet EPR spectrum (Figure 3.2c). Frequently the electron will interact with multiple nuclei which splits the EPR spectrum into $2NI+1$ lines where N is the number of coupled nuclei. The EPR spectrum of an electron coupled to 8 nuclei with the equal A_{iso} is shown in Figure 3.2d. In organic semiconductors there is an abundance of protons and other magnetic nuclei and the electron and hole will therefore almost always be coupled to many nuclei.

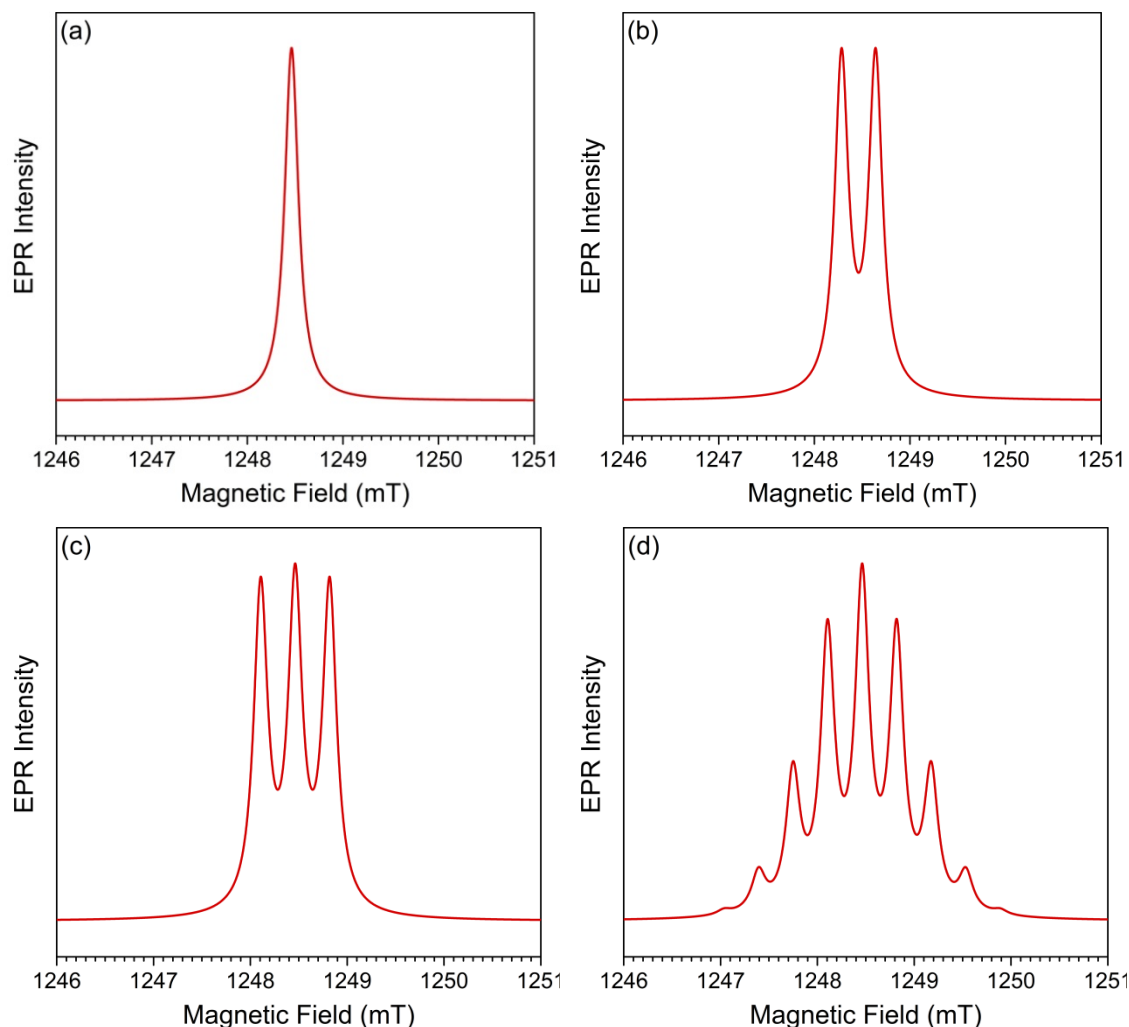


Figure 3.2 Simulation of EPR spectrum for a single spin $\frac{1}{2}$ interacting with (a) no magnetic nuclei, (b) single $I = \frac{1}{2}$ nucleus, (c) single $I = \frac{3}{2}$ nucleus, and (d) eight $I = \frac{1}{2}$ nuclei.

Due to the small hyperfine coupling constants and the large number of coupled nuclei, the hyperfine splitting in the EPR spectrum of organic semiconductors is generally not resolved. Instead the many hyperfine lines will overlap resulting in inhomogeneous broadening and a Gaussian lineshape in the EPR spectrum. In order to observe these small couplings directly, hyperfine spectroscopy methods such as electron nuclear double resonance spectroscopy (ENDOR) have to be used, which is discussed in Section 4.3.3.

3.4 Electron-Electron Interactions

In systems where there are multiple unpaired electrons in close proximity the spins of the electrons will interact. These interactions are of great importance in OPV systems when the electron and hole are in close proximity, such as excitons and polaron pairs, resulting

in large interaction energies. The electron spins interact through two distinct mechanisms, Heisenberg exchange and dipolar coupling, which will be introduced here.

3.4.1 Exchange Interaction

The exchange interaction arises from the difference in energy between symmetric and anti-symmetric spatial wave function overlap of electron wave functions. The isotropic exchange interaction between two electrons is given by,

$$\hat{H}_{ex} = -2J\hat{\mathbf{S}}'_A \cdot \hat{\mathbf{S}}_B \quad (3.22)$$

where $\hat{\mathbf{S}}_A$ and $\hat{\mathbf{S}}_B$ are the electron spin angular momentum operator of electrons A and B and J is the isotropic electron exchange coupling constant. J can be approximated using the following exchange integral,^[8]

$$J = \langle \phi_a(A)\phi_b(B) | \frac{e^2}{4\pi\epsilon_0 r} | \phi_a(A)\phi_b(B) \rangle \quad (3.23)$$

where ϕ are the spatial wave functions of the two electrons and r is the electron separation. In the case of two electrons there are four possible spin states. The simplest way of representing these states is a product of the individual spin states and is known as the product basis,

$$\begin{aligned} |1\rangle &= |\alpha_A\alpha_B\rangle \\ |2\rangle &= |\alpha_A\beta_B\rangle \\ |3\rangle &= |\beta_A\alpha_B\rangle \\ |4\rangle &= |\beta_A\beta_B\rangle \end{aligned} \quad (3.24)$$

where α and β (see Eq. 3.4) are the spin down and spin up states and the subscript specifies which electron. The Hamiltonian in Eq. 3.22 can be rewritten in matrix form using the product state basis.

$$\hat{H}_{ex} = \frac{1}{4} \begin{pmatrix} -2J & 0 & 0 & 0 \\ 0 & 2J & -4J & 0 \\ 0 & -4J & 2J & 0 \\ 0 & 0 & 0 & -2J \end{pmatrix} \quad (3.25)$$

The eigenvectors and eigenvalues of \hat{H}_{ex} define the singlet triplet basis and have the following form.

$$\begin{aligned}
|T_+\rangle &= |\alpha_A\alpha_B\rangle & E_{T+} &= -\frac{1}{2}J \\
|S\rangle &= \frac{1}{\sqrt{2}}[|\alpha_A\beta_B\rangle - |\beta_A\alpha_B\rangle] & E_S &= \frac{3}{2}J \\
|T_0\rangle &= \frac{1}{\sqrt{2}}[|\alpha_A\beta_B\rangle + |\beta_A\alpha_B\rangle] & E_{T0} &= -\frac{1}{2}J \\
|T_-\rangle &= |\beta_A\beta_B\rangle & E_{T-} &= -\frac{1}{2}J
\end{aligned} \tag{3.26}$$

It can be seen from Eq. 3.26 that there are three eigenstates with energy $-\frac{1}{2}J$ and one state with energy $\frac{3}{2}J$. The three eigenstates with equal energy form the triplet state, they have total spin $S = 1$ and their wave functions are symmetric under spin exchange. The state with energy $\frac{3}{2}J$ is the singlet state which has a total spin $S = 0$ and is antisymmetric under exchange of spins. The singlet and triplet states are therefore separated in energy by exchange coupling constant J . In the majority of organic systems $J > 0$ and the triplet states therefore lie lower in energy than their singlet counterparts. It should be noted that there is not a standard definition of J and it may be defined as double or opposite sign to the convention used here. Now that states with total spin $S = 0$ and $S = 1$ have been found, it is convenient to rewrite the exchange interaction in Eq. 3.22 in terms of the total spin operator $\hat{\mathbf{S}} = \hat{\mathbf{S}}_A + \hat{\mathbf{S}}_B$.

$$\hat{H}_{ex} = -J \left(\hat{\mathbf{S}}^2 - \frac{3}{2} \right) \tag{3.27}$$

3.4.2 Dipolar Interaction

As the name implies the dipolar interaction arises from the dipole-dipole interaction between the magnetic moments of the two electrons. This is the same principle as the anisotropic hyperfine interaction discussed earlier. The dipolar interaction between two electron spins is given by,

$$\hat{H}_{dip} = \frac{\mu_0}{4\pi} g_1 g_2 \mu_B^2 \left[\frac{\hat{\mathbf{S}}'_A \cdot \hat{\mathbf{S}}_B}{r^3} - \frac{3(\hat{\mathbf{S}}'_A \cdot \mathbf{r})(\hat{\mathbf{S}}'_B \cdot \mathbf{r})}{r^5} \right] \tag{3.28}$$

where g_1 and g_2 are the g factors of the two electrons, \mathbf{r} is the inter electron vector. By expanding the scalar products and integrating over space, the dipolar interaction Hamiltonian can be rewritten,

$$\hat{H}_{dip} = \hat{\mathbf{S}}' \cdot \mathbf{D} \cdot \hat{\mathbf{S}} = 2\hat{\mathbf{S}}'_A \cdot \mathbf{D} \cdot \hat{\mathbf{S}}_B \quad (3.29)$$

where $\hat{\mathbf{S}}$ is the total spin angular momentum operator ($\hat{\mathbf{S}} = \hat{\mathbf{S}}_A + \hat{\mathbf{S}}_B$) and \mathbf{D} is dipolar coupling tensor. \mathbf{D} takes the form of second rank tensor and can be written in a general form or diagonalised by transformation into the principal axis reference frame.

$$\mathbf{D} = \begin{pmatrix} D_{xx} & D_{xy} & D_{xz} \\ D_{yx} & D_{yy} & D_{yz} \\ D_{zx} & D_{zy} & D_{zz} \end{pmatrix} \quad (3.30a)$$

$$\mathbf{D} = \begin{pmatrix} D_x & 0 & 0 \\ 0 & D_y & 0 \\ 0 & 0 & D_z \end{pmatrix} \quad (3.30b)$$

\mathbf{D} is traceless and the dipolar interaction can therefore be described using two independent parameters D and E ,^[9]

$$D = \frac{3}{2}D_z \quad (3.31a)$$

$$E = \frac{1}{2}(D_x - D_y) \quad (3.31b)$$

which are known as the Zero Field Splitting (ZFS) parameters. By convention D and E are defined so that the z -axis of \mathbf{D} is along the direction of largest dipolar coupling $D_z \geq D_x \geq D_y$. The magnitude of D describes of the strength of dipolar interaction and is proportional to the distance between the interacting spins. E is the rhombicity and characterises the deviation of the dipolar interaction from axial symmetry. The dipolar coupling has no influence on the singlet state but causes the energies of the three triplet sublevels break degeneracy. The zero field energies of the triplet levels are given by,

$$\begin{aligned} U_x &= -D_x = \frac{1}{3}D - E \\ U_y &= -D_y = \frac{1}{3}D + E \\ U_z &= -D_z = -\frac{2}{3}D \end{aligned} \quad (3.32)$$

If the spin distribution is isotropic then there is no minimum energy orientation for the electron positions and all three levels will have equal energy (Figure 3.3a). If the spin distribution is oblate, squashed along z-axis, then the dipolar interaction will be minimised when the electrons lie the xy plane (T_z) and are able to maximise their

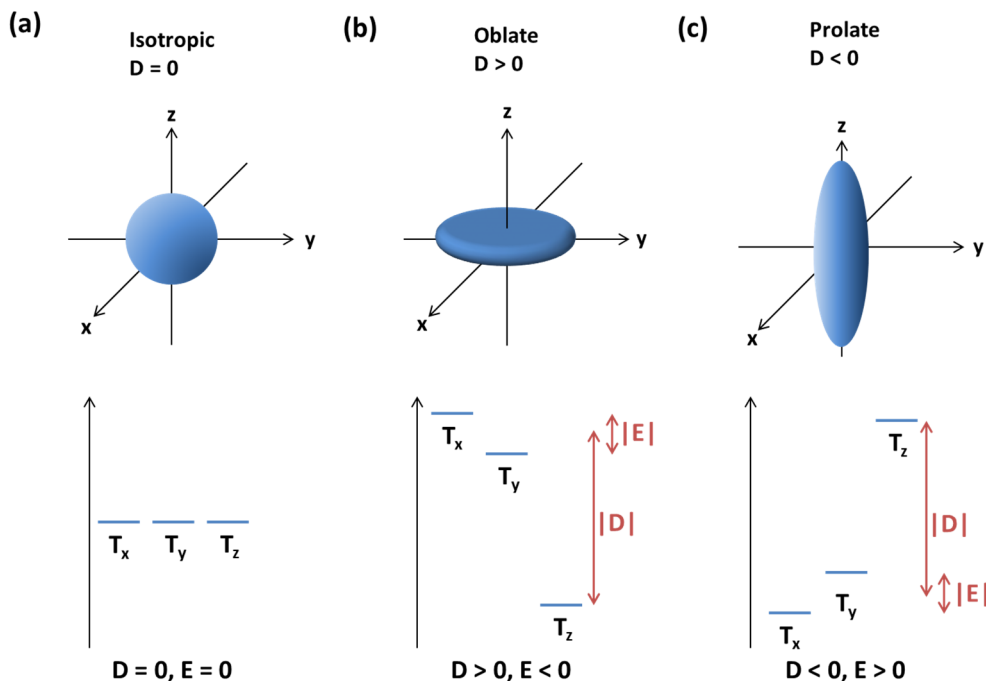


Figure 3.3 Influence of the shape of the spin density distribution on the Zero Field Splitting of the triplet sublevels.

separation apart. The T_z level therefore lies lowest in energy as shown in Figure 3.3b. Similarly a prolate spin distribution, elongation along the z-axis, results in a raising of the T_z level. If the spin distribution is circularly symmetric in the xy plane the T_x and T_y levels will be degenerate; otherwise there will be splitting of the T_x and T_y by E . Using D and E the dipolar interaction Hamiltonian can be rewritten in to yield,

$$\hat{H}_{dip} = D \left(\hat{S}_z^2 - \frac{1}{3} \hat{S}^2 \right) + E (\hat{S}_x^2 - \hat{S}_y^2) \quad (3.33)$$

3.4.3 Spin Correlated Radical Pair

By combining the various interactions introduced thus far a general Hamiltonian for two interacting electrons in a magnetic field can be written,

$$\hat{H} = \hat{H}_{eZ,A} + \hat{H}_{eZ,B} + \hat{H}_{ex} + \hat{H}_{dip} \quad (3.34a)$$

$$\hat{H} = g_A \mu_B B + g_B \mu_B B - J \left(\hat{\mathbf{S}}^2 - \frac{3}{2} \right) + \frac{3}{2} D_z \left(\hat{\mathbf{S}}_z^2 - \frac{1}{3} \hat{\mathbf{S}}^2 \right) \quad (3.34b)$$

where it has been assumed that the two electrons have isotropic g-factors, there are no hyperfine interactions and the dipolar coupling between the two electrons is purely axial. Under the action of the Zeeman, exchange and dipolar interactions the singlet-triplet basis states introduced in Eq. 3.26 are no longer eigenstates of the system. The new eigenstates and eigenenergies of the system can be found by writing the Hamiltonian in matrix form and diagonalising. The matrix form of the Hamiltonian in the singlet-triplet basis is given by,^[10-13]

$$\hat{H} = \begin{pmatrix} \omega - \frac{J}{2} + \frac{D_z}{2} & 0 & 0 & 0 \\ 0 & \frac{3J}{2} & Q & 0 \\ 0 & Q & -\frac{J}{2} - D_z & 0 \\ 0 & 0 & 0 & -\omega - \frac{J}{2} + \frac{D_z}{2} \end{pmatrix} \quad (3.35)$$

where the Zeeman interaction energy of each electron has been written in terms of its transition frequency,

$$\begin{aligned} \omega_A &= \frac{g_A \mu_B B}{h} & \omega_B &= \frac{g_B \mu_B B}{h} \\ \omega &= \frac{1}{2}(\omega_A + \omega_B) & Q &= \frac{1}{2}(\omega_A - \omega_B) \end{aligned} \quad (3.36)$$

and J and D_z are in frequency units. The eigenvectors and eigenenergies of \hat{H} are,

$$\begin{aligned} |1\rangle &= |T_+\rangle & \omega_1 &= \omega - \frac{J}{2} + \frac{D_z}{2} \\ |2\rangle &= \cos(\alpha)|S\rangle + \sin(\alpha)|T_0\rangle & \omega_2 &= +\Omega + \frac{J}{2} - \frac{D_z}{2} \\ |3\rangle &= -\sin(\alpha)|S\rangle + \cos(\alpha)|T_0\rangle & \omega_3 &= -\Omega + \frac{J}{2} - \frac{D_z}{2} \\ |4\rangle &= |T_-\rangle & \omega_4 &= -\omega - \frac{J}{2} + \frac{D_z}{2} \end{aligned} \quad (3.37)$$

and Ω and α are defined as,

$$\Omega^2 = Q^2 + \left(J + \frac{D_z}{2}\right)^2 \quad (3.38a)$$

$$\tan(2\alpha) = \frac{Q}{\left(J + \frac{D_z}{2}\right)} \quad (3.38b)$$

The eigenvectors of Eq. 3.37 define a new basis set which is commonly called the spin correlated radical pair (SCRCP) basis. It can be seen that T_+ and T_- states from the singlet-triplet basis carry over unchanged while the S and T_0 states are mixed together to yield two new mixed states 2 and 3. The extent of mixing is described by the mixing angle α which is defined by Eq. 3.38b. When the exchange coupling is very large ($J \gg Q$) then S - T_0 mixing will be suppressed, $\alpha \rightarrow 0$, and states 2 and 3 tend towards the pure S and T_0 respectively. In the opposite extreme when the coupling interactions between the spins are very weak ($J, D_z \ll Q$) then $\alpha \rightarrow \pi/4$ and states 2 and 3 become $\alpha_A\beta_B$ and $\beta_A\alpha_B$, signifying that the spins are completely independent. The SCRCP basis is useful to describe states with coupling strengths between these two extremes.

3.5 Application to Organic Photovoltaics

3.5.1 Photoinduced Excited States

The charge separation processes from the ground state to free charge carriers in a bulk heterojunction OPV cell is shown in Figure 3.4. Upon photon absorption a strongly bound exciton is formed. In an exciton the electron and hole are in close proximity resulting in a large exchange interaction and the decoupling of the singlet and triplet manifolds; the exciton therefore exists in a pure singlet or pure triplet state. Due to conservation of angular momentum the photogenerated exciton is always formed in the singlet state. After the exciton diffuses to the donor acceptor interface primary electron transfer occurs to yield a charge separated state. In this thesis, this state will be referred to as the primary polaron pair (PP). This is equivalent to the interfacial charge transfer (CT) state commonly referred to literature. Ideally the electron and hole then spatially separate through secondary electron and hole transfer generating less strongly bound PPs and ultimately fully separated polarons. The electron and hole will frequently be referred to

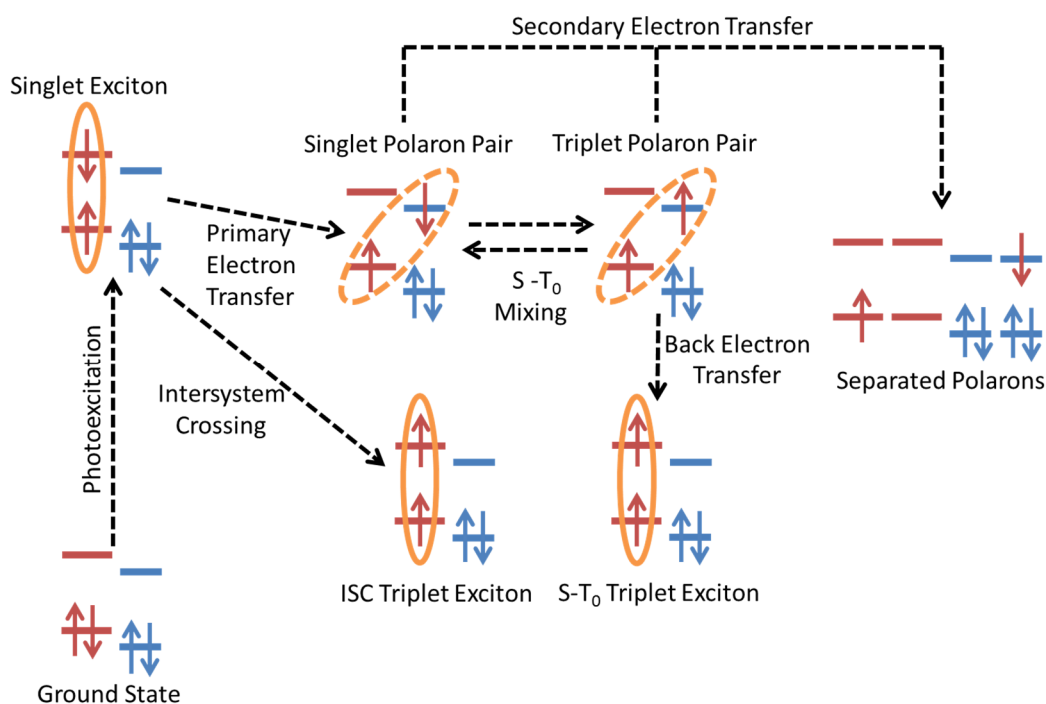


Figure 3.4 Charge Separation pathways in a bulk heterojunction OPV. The donor energy levels are shown in red and those of the acceptor in blue.

as the positive polaron (P^+) and negative polaron (P^-) respectively throughout this thesis. In organic semiconductors there will be a distortion of the molecule or polymer segment that an electron or hole resides on. A polaron is a quasiparticle of a charge and the distortion of the surroundings due to that charge. In EPR spectroscopy the term polaron is particularly well suited as it emphasises that the paramagnetic species detected is the entire positively or negatively charged molecule or polymer segment with associated spin-orbit coupling and hyperfine interactions. In addition to free polaron formation there are other unwanted pathways such as recombination to the singlet ground state and triplet exciton formation. With the exception of the singlet exciton, the states depicted in Figure 3.4 are EPR active which makes EPR spectroscopy a powerful tool to probe the excited states in OPV cells. Each of these EPR active states will now be discussed in detail.

3.5.2 Polaron Pair

The primary polaron pair lifetime in a typical OPV bulk heterojunction solar cell is on the order of picoseconds.^[14] However the time resolution of a time-resolved EPR measurement (TR-EPR), as will be discussed in further detail in Section 4.35, is at best 100 ns. The primary and intermediate polaron pairs (partially separated through electron and hole transfer) are therefore not observable using TR-EPR. Instead it is polaron pairs that have undergone many electron and hole transfer steps and have lifetimes in the hundreds of nanoseconds range that will be observed during a TR-EPR measurement. These long lived TR-EPR observable states are termed secondary polaron pairs.

From an EPR perspective a secondary polaron pair consists of two interacting spin $\frac{1}{2}$ species. The energy levels of this system in a magnetic field are given by the SCRP eigenstates introduced in Eq. 3.37. There are four allowed transitions ($\Delta m_s = \pm 1$) between these four eigenstates,

$$\begin{aligned}
 \omega_{12} &= \omega - \Omega - J + D_z \\
 \omega_{34} &= \omega - \Omega + J - D_z \\
 \omega_{13} &= \omega + \Omega - J + D_z \\
 \omega_{24} &= \omega + \Omega + J - D_z
 \end{aligned}
 \tag{3.39}$$

The energy levels and EPR stick spectrum of the polaron pair are shown in Figure 3.5. It can be seen that the spectrum consists of a pair of doublets separated by 2Ω with a doublet splitting of $2J - 2D_z$. In the absence of exchange and dipolar coupling the spectrum will collapse into two lines, shown by the dotted lines, which is the EPR spectrum of two non-interacting polarons.

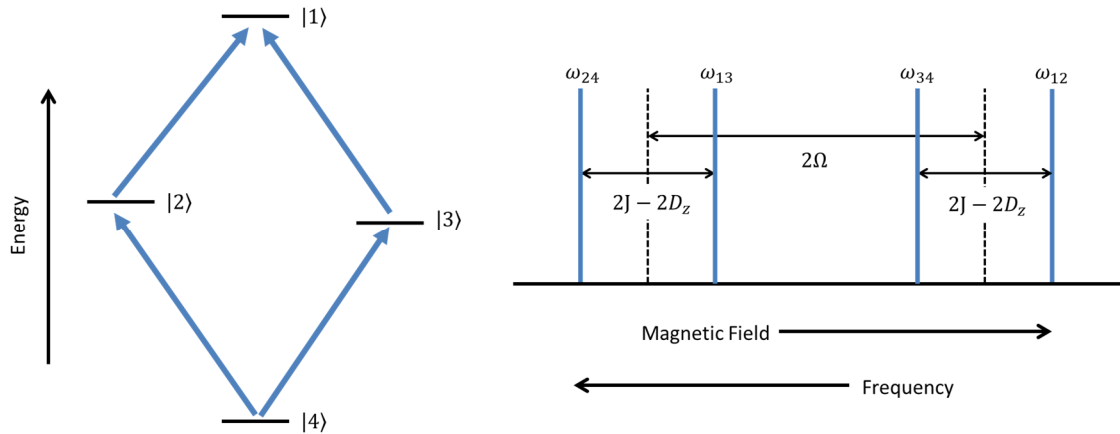


Figure 3.5 Energy levels and stick spectrum of secondary polaron pair with Boltzmann population. The ordering has assumed $J > 0$ and $D < 0$.

The spectrum shown in Figure 3.5 assumes that the energy levels have standard thermal populations given by Boltzmann statistics. However the polaron pair is generated from a singlet exciton and due to conservation of angular momentum the only states that can be populated are those with some singlet character. Therefore only states 2 and 3 will be populated, with average populations proportional to $\cos^2(\alpha)$ and $\sin^2(\alpha)$ respectively. The EPR spectrum of singlet populated polaron pair is shown in Figure 3.6. It can be seen that the non-Boltzmann population gives rise to spectrum that contains alternating absorption (blue) and emission (red) components. The relative intensity of each transition is proportional to the product of the population difference of the two states and the transition probability given by Fermi's golden rule. Propagating these populations and probabilities yields four transitions with equal intensity with two in emission and two in absorption.^[13] An EPR spectrum exhibiting emission and absorption components is said to be polarised. The polarisation mechanism just described is commonly called the spin

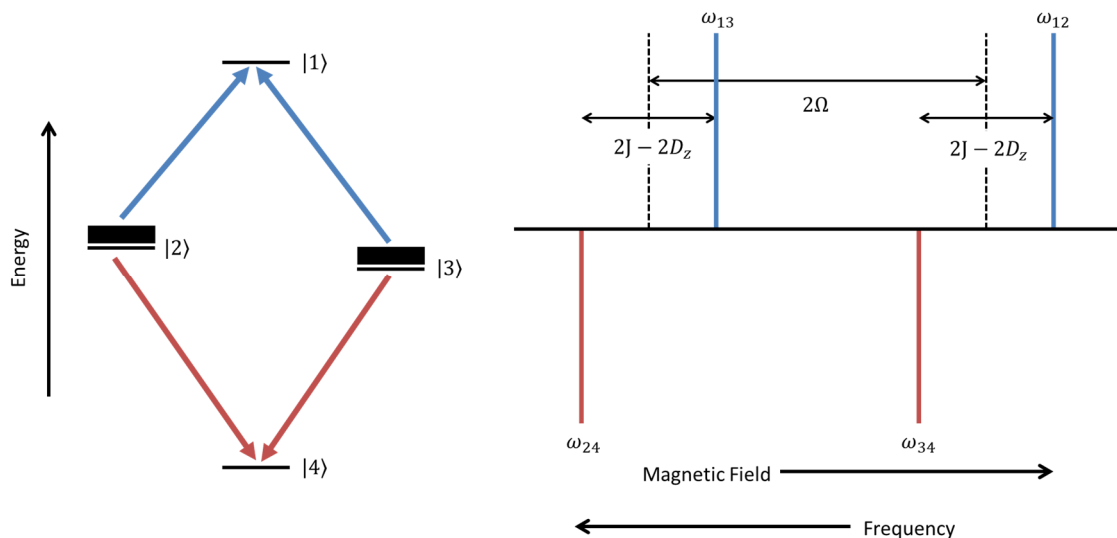


Figure 3.6 Energy levels and stick spectrum of secondary polaron pair with excess population in the states with some singlet character. The ordering has assumed $J > 0$ and $D < 0$. Emission is shown in red and absorption in blue.

correlated radical pair mechanism (SCRPM). It is a specific type of chemically induced dynamic electron polarisation (CIDEP).

A secondary polaron pair detected in a TR-EPR measurement is therefore expected to have an EAEA or AEAE polarisation pattern depending on the signs of J and D_z . The SCRPM assumes that the polarisation of the polaron pair is wholly generated during the TR-EPR measurement. This assumption is valid as long as the primary and intermediate polaron pairs that precede the secondary separate sufficiently rapidly so as not to allow significant S- T_0 mixing to occur.^[15, 16] If there is a long lived primary or intermediate polaron pair the polarisation of the secondary polaron pair will be distorted due to polarisation built up during the separation process that carries over to the secondary polaron pair. This polarisation build up can be explained using a closely related CIDEP mechanism known as the radical pair mechanism (RPM).^[13] The RPM essentially makes the opposite assumption to the SCRPM. It is assumed that the polarisation observed during a TR-EPR measurement arises wholly from polarisation built up during the separation and that there is no interaction between the polarons at the time of measurement.

Assuming the spins are not interacting at the time of measurement the polarisation is given by population difference of the α and β uncoupled basis states of each polaron. The polarisation is therefore given by,^[13]

$$\begin{aligned}\varphi_A &= \frac{1}{N} (N(\beta_A\beta_B) + N(\beta_A\alpha_B) - N(\alpha_A\beta_B) - N(\alpha_A\alpha_B)) \\ \varphi_B &= \frac{1}{N} (N(\beta_A\beta_B) + N(\alpha_A\beta_B) - N(\beta_A\alpha_B) - N(\alpha_A\alpha_B))\end{aligned}\tag{3.40}$$

where φ_A and φ_B are polarisations of polaron A and B. The origin of this polarisation can be visualised by considering the transition frequencies given by Eq. 3.39. When there is no interaction between the spins, J and D_z are zero and there are now two pairs of degenerate transitions,

$$\begin{aligned}\omega_{12} &= \omega_{34} = \omega - Q = \omega_B \\ \omega_{13} &= \omega_{24} = \omega + Q = \omega_A\end{aligned}\tag{3.41}$$

which are just the transition energies of each independent polaron. States 1 to 4 are now the uncoupled product states obtained when $\alpha \rightarrow \pi/2$ and defined in Eq. 3.24.

The energy levels and stick spectrum of this situation is shown in Figure 3.7. Assuming an initial singlet state, only states $|2\rangle$ and $|3\rangle$ will be populated after electron transfer. In the absence of $S-T_0$ mixing during charge separation the populations of states $|2\rangle$ and $|3\rangle$ will be $\cos^2(\alpha)$ and $\sin^2(\alpha)$ respectively and the transition probability for ω_{12} and ω_{34} is $\sin^2(\alpha)$ and $\cos^2(\alpha)$ respectively. The transition intensity is given by the product of the population difference and the transition probability, and therefore the ω_{12} and ω_{34} transitions will have the same intensity of $\sin^2(\alpha)\cos^2(\alpha)$.^[13] However one transition is in emission and the other in absorption, and these transitions will therefore cancel. The same situation applies to the ω_{13}, ω_{24} transitions and therefore no polarised EPR spectrum will result. If $S-T_0$ mixing occurs during separation of the polaron pair, the population of states $|2\rangle$ and $|3\rangle$ are perturbed from their initial values and the ω_{12}, ω_{34} and ω_{13}, ω_{24} transitions therefore do not cancel completely and an EPR spectrum with EA or AE polarisation results. This is illustrated in the right panel of Figure 3.7 where the dotted stick lines show the magnitude of each transition and the solid lines show the net polarisation.

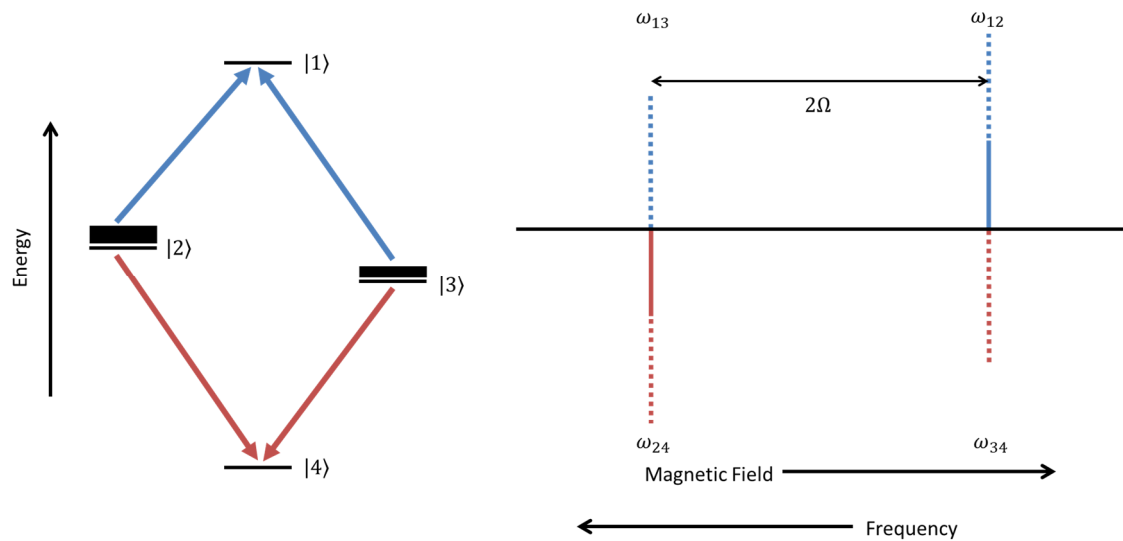


Figure 3.7 Energy levels and stick spectrum of separated polaron pair where polarisation has built up during. The ordering has assumed $J > 0$ and $D < 0$. Emission is shown in red and absorption in blue.

The polarisation pattern exhibited by many OPV blends is a combination of the polarisation arising from both the SCRPM and RPM, as would be expected for a sequential electron transfer system.^[15, 16] If the primary and intermediate polaron pairs separate rapidly then negligible polarisation will build up during charge separation the polarisation pattern of the observable secondary polaron pair is EAEA as expected from the SCRPM. If charge separation is slower the primary or intermediate polaron pairs can be long enough lived for significant $S-T_0$ mixing to occur which will distort the polarisation pattern of the observable secondary polaron pairs from EAEA towards EA. The slower the charge separation the more $S-T_0$ mixing that can occur and greater the distortion.^[15, 16]

3.5.3 Free Polarons

After the positive and negative polaron have separated they can be treated independently and each will give rise to its own EPR signal. When the EPR spectrum is recorded in the standard manner (not timed with the laser flash) any polarisation that built up during the separation will have decayed and the spin states of each polaron will have a standard Boltzmann population, and the EPR transitions will therefore be purely absorptive. In OPV blends the positive polaron will be located on the electron donor and the negative polaron on the acceptor. The EPR spectrum will therefore consist of two components with different g -factors and linewidths corresponding to the different local environment of the

positive and negative polarons. The light induced EPR spectrum of the classic P3HT:PC₆₁BM blend is shown in Figure 3.8. Recording the spectrum at 9.8 GHz (Figure 3.8a) shows two peaks corresponding to the positive and negative polaron. In order to obtain more information from the spectrum it is beneficial to record the spectrum at a higher microwave frequency which separates the components of the g-tensor in magnetic field and enables the principal values to be resolved as shown in Figure 3.8b.

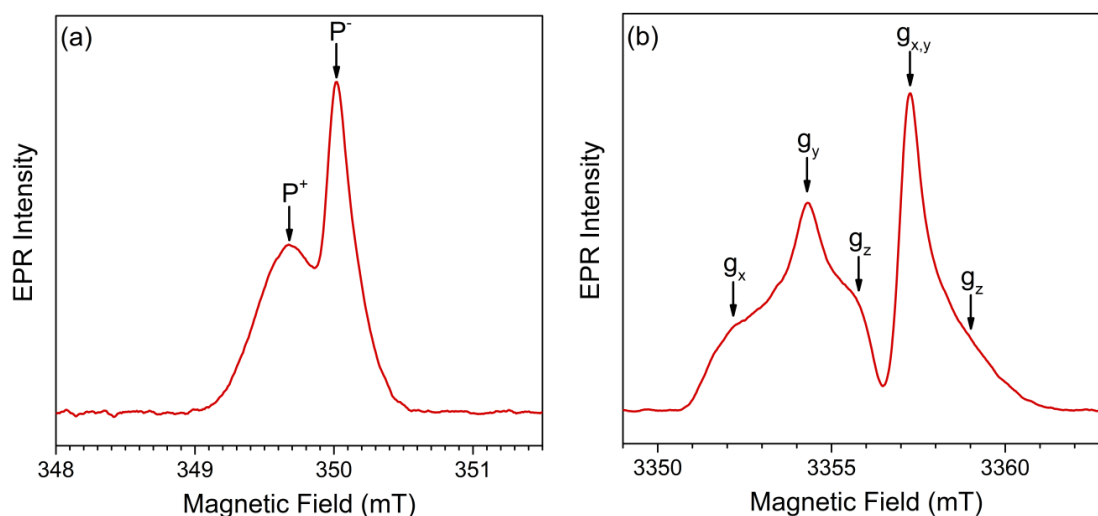


Figure 3.8 Light induced EPR spectrum of P3HT:PC₆₁BM at (a) 9.8 GHz and (b) 94 GHz.

3.5.4 Triplet Excitons

Triplet excitons are a potential loss mechanism in OPV cells and their presence can be detected using EPR. A triplet exciton consists of an electron and hole in close proximity which form a tightly bound neutral quasi particle with total spin $S = 1$. The spins of the electron and hole will interact through exchange and dipolar coupling. Due to the close proximity of the electron and hole the exchange coupling interaction is very large ($J \gg Q$) and $\alpha \rightarrow 0$ (Eq. 3.37). States $|2\rangle$ and $|3\rangle$ therefore become the pure singlet $|S\rangle$ and triplet states respectively $|T_0\rangle$. This is the strong coupling regime and the exciton exists in either the pure singlet or pure triplet state and EPR transitions between these states are forbidden. All photogenerated excitons will initially be in the singlet state due to conservation of angular momentum during photoexcitation; however the singlet exciton

is EPR silent. Instead EPR is able to detect triplet excitons by exciting transitions within the three triplet sublevels as shown in the top panel of Figure 3.9.

Due to the close proximity of the electron and hole the EPR spectrum of a triplet exciton is dominated by the dipolar interaction introduced in Section 3.4.2. The shape of the triplet exciton spectrum is determined by the zero field splitting parameters D and E (Eq. 3.31) which describe the symmetry of the triplet exciton distribution. The triplet exciton spectrum will normally be a powder average of all possible orientations of the molecule or polymer segment with respect to the magnetic field. The origin of the triplet exciton EPR spectrum is illustrated in Figure 3.9. The position of the transitions between the three sublevels is dependent on the relative orientation of the molecule, more specifically the dipolar principal axis reference frame, and the applied magnetic field. In the upper panel of Figure 3.9 the energies of the triplet sublevels and transition positions when the magnetic field is aligned along the three principal axis of the dipolar principal axis frame are shown. Assuming that the molecule or polymer is randomly orientated in the magnetic field the triplet spectrum shown in the lower panel of Figure 3.9 is built up by averaging across every possible orientation. Figure 3.9 also shows how the magnitudes

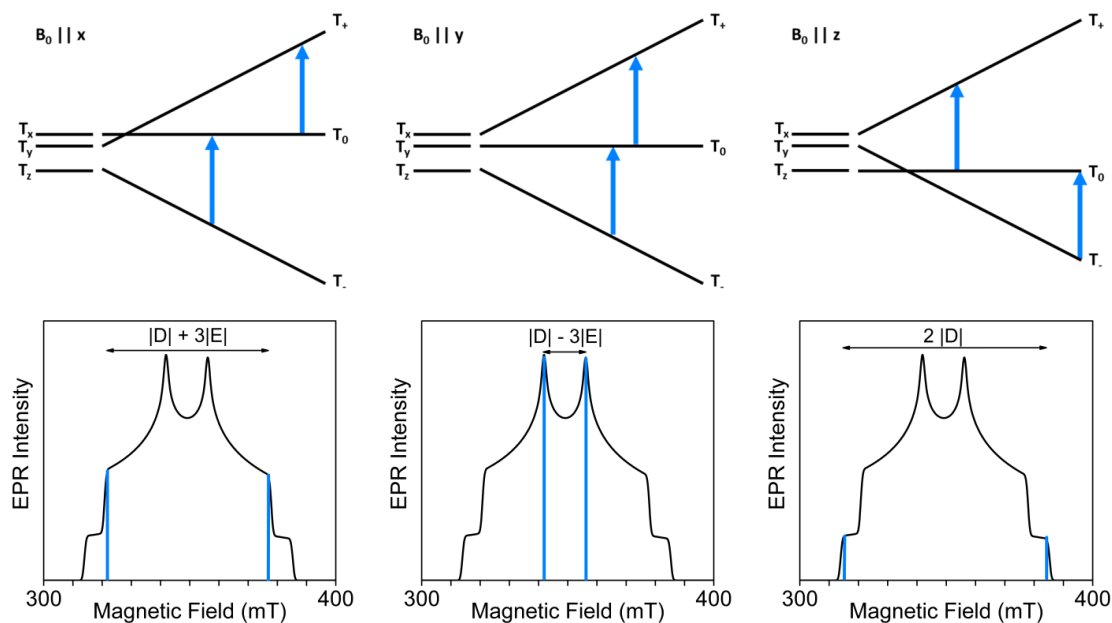


Figure 3.9 Origin of the triplet exciton spectrum assuming a Boltzmann of the triplet sublevels. The upper panel shows the energy of the triplet sublevels when the magnetic field is orientated along the three principal axis of the dipolar principal axis reference frame. The lower panel shows how the transitions at these three orientations build up the powder spectrum. The energies of the triplet levels are such that $D > 0$ and $E < 0$. Adapted from Richert et. al.¹⁷¹

of D and E can be obtained from the turning points of the triplet exciton spectrum and which serve as a finger print. It is important to emphasise that only the magnitudes of D or E can be obtained from the EPR spectrum; it provides no insight into the sign. The spectra shown in Figure 3.9 assume that the triplet levels T_+ , T_0 , and T_- are populated with a Boltzmann distribution and all transitions are therefore absorptive. In practise this never occurs as the triplet exciton is a short lived species and the population of the triplet levels will crucially depend on how the triplet was formed. The populations will therefore deviate from a Boltzmann population which results in polarisation of triplet exciton spectrum.

As shown back in Figure 3.4 there are two pathways to generate a triplet exciton, intersystem crossing (ISC) from the singlet exciton and back electron transfer (BET) from the polaron pair. These two processes result in different populations of the triplet sublevels and the pathway can therefore be identified from the polarisation pattern of the triplet exciton spectrum. The two routes are shown as a Jablonski diagram in Figure 3.10. In the ISC route a singlet exciton is generated on either the donor or acceptor and before it has a chance to reach the donor acceptor interface it undergoes intersystem crossing to the triplet state. Intersystem crossing occurs because the spin-orbit coupling results in a mixing of the singlet and triplet states. The spin-orbit coupling interaction is anisotropic and the singlet-triplet mixing will therefore vary in the x, y and z directions of the

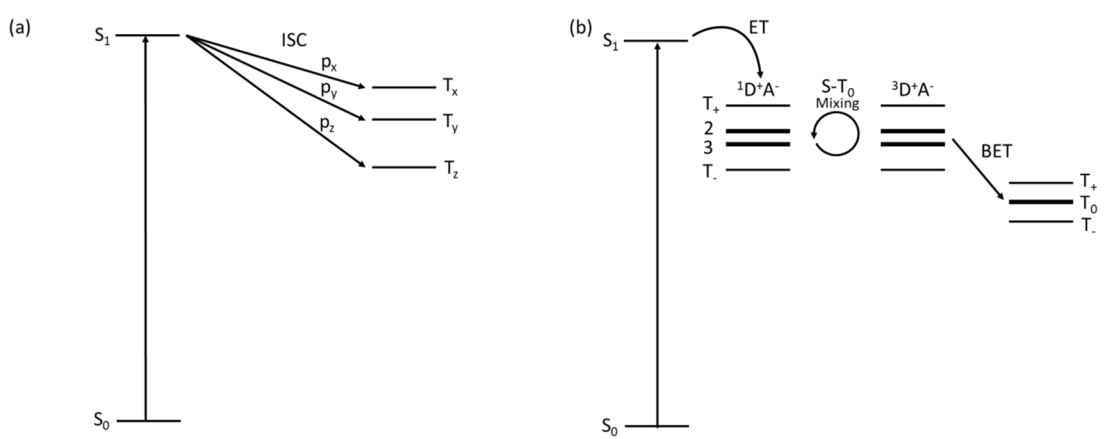


Figure 3.10 Jablonski diagram of (a) ISC and (b) BET triplet exciton formation pathways.

molecule. The zero field triplet sublevels are therefore populated differently depending on the spin-orbit coupling in that direction as illustrated in Figure 3.10a. The population of the high field states T_+ , T_0 , and T_- is determined by propagating the population of the zero field states to high field. Assuming that B_0 is along the z axis of the dipolar reference frame the population of the high field states is given by,^[17]

$$p_0 = p_z$$

$$p_+ = \frac{1}{2}(p_x + p_y) \quad (3.42)$$

$$p_- = \frac{1}{2}(p_x + p_y)$$

where p_i is the population of each state. Analogous conversions exist when the magnetic field is oriented along the other two axes. The polarisation of the triplet exciton spectrum arising from selective population of the zero field sublevels through ISC is shown in Figure 3.11. The energy of the triplet levels is shown in the upper panel of Figure 3.11, where it has been assumed that the T_x level has been preferentially populated through ISC ($p_x > p_y, p_z$). The relative populations of the zero field and high field triplet sublevels are

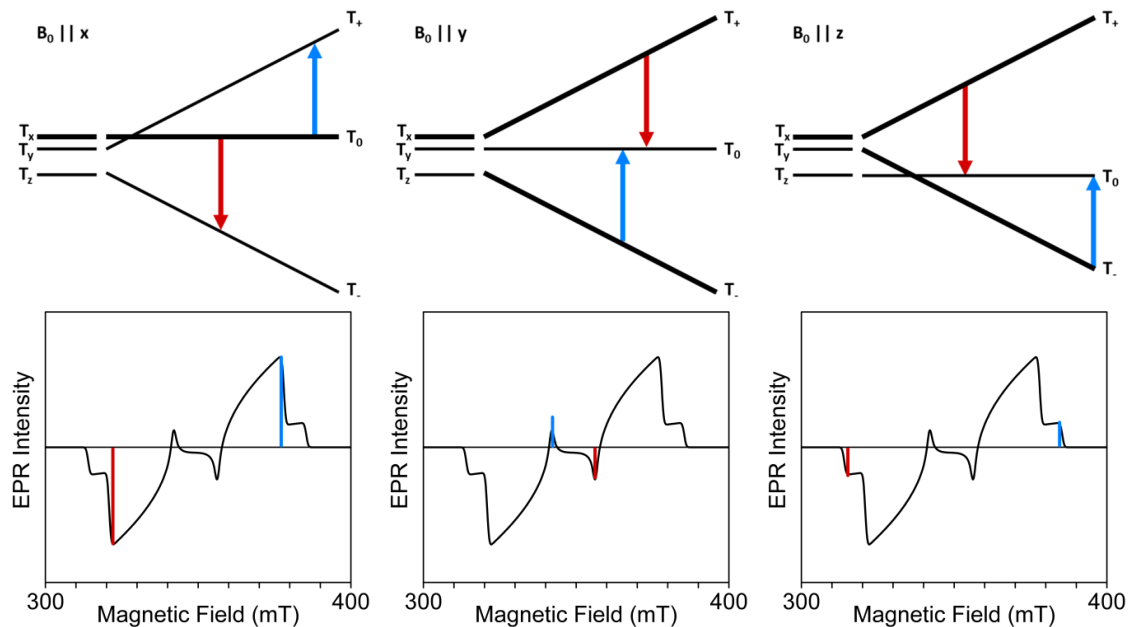


Figure 3.11 Polarisation of triplet exciton spectrum from ISC. It has been assumed that there is preferential ISC into the T_x level. The relative population of the levels is indicated by the thickness of the lines. The energies of the triplet levels are such that $D > 0$ and $E < 0$. Adapted from Richert et al.^[17]

shown by the thickness of the lines. It can be seen that selective population of T_x gives rise to both absorption and emission transitions between the triplet sublevels. This gives rise to a polarised triplet exciton EPR spectrum as shown in the lower panel. The polarisation pattern of this triplet exciton is EEAEAA; many different ISC polarisation patterns are possible depending on the relative populations of the zero field levels and the sign of D .

The second route of triplet exciton formation is back electron transfer from the polaron pair. Depending on the community this is also called the $S-T_0$ triplet or the recombination triplet. The origin of the selective population is illustrated in Figure 3.10b. A singlet exciton is generated in either the donor or acceptor which reaches the interface and electron transfer occurs generating a singlet polaron pair. As discussed in Section 3.5.2 $S-T_0$ mixing shifts population between the S and T_0 states and the polaron pair therefore acquires triplet character. A triplet exciton can then be generated by transfer of an electron back to the donor molecule (BET). In the polaron pair only the T_0 sublevel is populated through $S-T_0$ mixing and this population carries over, resulting in a triplet exciton where the T_0 is selectively populated as shown in Figure 3.10b. This is the crucial difference

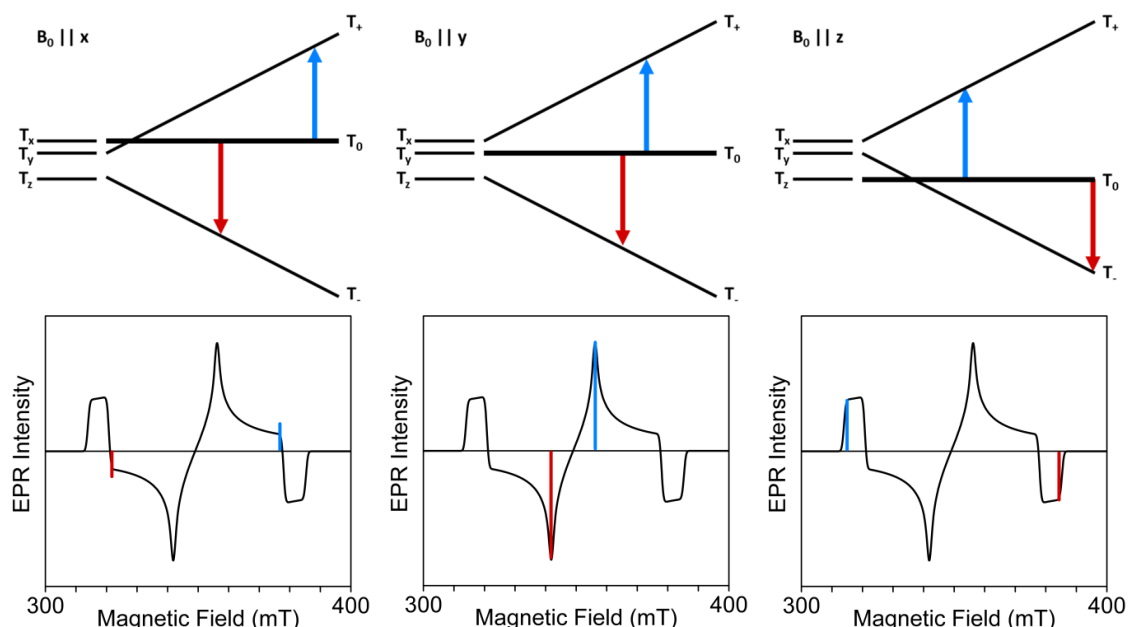


Figure 3.12 Polarisation of triplet exciton spectrum arising from the BET mechanism which preferentially populates the T_0 sublevel. The relative population of the levels is indicated by the thickness of the lines. The energies of the triplet levels are such that $D > 0$ and $E < 0$. Adapted from Richert et al.^[17]

between the ISC and BET polarisation mechanisms. In ISC the zero field states are populated unequally and the populations then propagated to the high field states while in the BET mechanism the high field states are populated directly. The energy levels and polarisation pattern resulting from this mechanism are shown in Figure 3.12. When $D > 0$ the triplet exciton has an AEEAAE pattern and the inverse when $D < 0$. This polarisation pattern is unique to BET, it cannot be generated through any combination zero field state populations. The polarisation pattern of the triplet exciton detected in a TR-EPR measurement can therefore be used to identify the pathway by which the exciton was generated. No other form of spectroscopy can so clearly distinguish the two mechanisms.

3.6 References

1. W. Gerlach and O. Stern, Der experimentelle Nachweis des magnetischen Moments des Silberatoms. *Z. Phys.* **8** (1), 110-111 (1922).
2. W. Gerlach and O. Stern, Der experimentelle Nachweis der Richtungsquantelung im Magnetfeld. *Z. Phys.* **9** (1), 349-352 (1922).
3. W. Gerlach and O. Stern, Das magnetische Moment des Silberatoms. *Z. Phys.* **9** (1), 353-355 (1922).
4. F. Weinert, Wrong theory—right experiment: The significance of the Stern–Gerlach experiments. *Stud. Hist. Philos. Mod. Phys.* **26** (1), 75-86 (1995).
5. G. E. Uhlenbeck and S. Goudsmit, Spinning Electrons and the Structure of Spectra. *Nature* **117**, 264-265 (1926).
6. G. E. Uhlenbeck and S. Goudsmit, Ersetzung der Hypothese vom unmechanischen Zwang durch eine Forderung bezüglich des inneren Verhaltens jedes einzelnen Elektrons. *Naturwissenschaften* **13**, 953-954 (1925).
7. P. J. Mohr, D. B. Newell and B. N. Taylor, CODATA recommended values of the fundamental physical constants: 2014. *Rev. Mod. Phys.* **88** (3), 73 (2016).
8. J. A. Weil and J. R. Bolton, Electron Paramagnetic Resonance Elementary Theory & Practical Applications, 2nd ed. (John Wiley & Sons, Hoboken, NJ, USA, 2007).
9. C. P. Poole, H. A. Farach and W. K. Jackson, Standardization of Convention for Zero-Field Splitting Parameters. *J. Chem. Phys.* **61** (6), 2220-2221 (1974).
10. P. J. Hore, D. A. Hunter, C. D. McKie and A. J. Hoff, Electron-Paramagnetic Resonance of Spin-correlated Radical Pairs in Photosynthetic Reactions. *Chem. Phys. Lett.* **137** (6), 495-500 (1987).

11. C. D. Buckley, D. A. Hunter, P. J. Hore and K. A. McLauchlan, Electron-Spin-Resonance of Spin-Correlated Radical Pairs. *Chem. Phys. Lett.* **135** (3), 307-312 (1987).
12. G. L. Closs, M. D. E. Forbes and J. R. Norris, Spin-Polarized Electron-Paramagnetic Resonance-Spectra of Radical Pairs in Micelles - Observation of Electron-Spin Spin Interactions. *J. Phys. Chem.* **91** (13), 3592-3599 (1987).
13. A. J. Hoff, *Advanced EPR: Applications in Biology and Biochemistry*. (Elsevier, NY, USA, 1989).
14. D. A. Vithanage, A. Devizis, V. Abramavicius, Y. Infahsaeng, D. Abramavicius, R. C. I. MacKenzie, P. E. Keivanidis, A. Yartsev, D. Hertel, J. Nelson, V. Sundstrom and V. Gulbinas, Visualizing Charge Separation in Bulk Heterojunction Organic Solar Cells. *Nat. Commun.* **4**, 6 (2013).
15. J. Niklas, S. Beaupre, M. Leclerc, T. Xu, L. P. Yu, A. Sperlich, V. Dyakonov and O. G. Poluektov, Photoinduced Dynamics of Charge Separation: From Photosynthesis to Polymer-Fullerene Bulk Heterojunctions. *J. Phys. Chem. B* **119** (24), 7407-7416 (2015).
16. J. Niklas and O. Poluektov, Charge Transfer Processes in OPV Materials as Revealed by EPR Spectroscopy. *Adv. Energy Mater.* **7** (10), 1602226 (2017).
17. S. Richert, C. E. Tait and C. R. Timmel, Delocalisation of photoexcited triplet states probed by transient EPR and hyperfine spectroscopy. *J. Magn. Reson.* **280**, 103-116 (2017).

4 Experimental Methods

In this chapter the sample preparation procedures and experimental techniques used throughout the thesis are discussed. In addition, further magnetic resonance theory is provided that is specific to conventional EPR and electrically detected EPR spectroscopy.

4.1 OPV Fabrication

4.1.1 Substrate Cleaning

A clean substrate is essential for efficient and reproducible OPV operation. The substrates were cleaned by ultrasonication in a hot 3% Hellmanex III (Sigma Aldrich) aqueous solution for 10 minutes, and the substrates rinsed several times with deionised water to ensure the complete removal of Hellmanex III residue. This was followed by ultrasonication in acetone for 5 minutes and isopropanol for 5 minutes. The substrates were then blown dry with nitrogen. Immediately prior to film deposition, the substrates were plasma ashed in an oxygen plasma at 80 W for 3 minutes (Plasma Technology MiniFlecto) which removes organic contaminants and improves the wettability of the substrate.

4.1.2 Film Deposition

Solutions of the desired semiconductor were prepared inside a nitrogen glovebox and left to stir at 50 °C until dissolved. The majority of films were prepared using spin coating, where the substrate is held in place with a vacuum and the solution deposited on top of it. The substrate is then accelerated to the desired rotation speed and spun until dry. By varying the rotation speed and concentration of the semiconductor solution, the thickness of the deposited film can be controlled. Typical parameters to achieve ~100 nm thick polymer:fullerene films were 25 mg cm⁻³ and 1500 rpm.

4.1.3 Contact Deposition

The top electrode was deposited using thermal evaporation through a shadow mask. The most common top contact used in this thesis was 20 nm of calcium (Ca) followed by 80 nm of aluminium (Al). The Ca layer provides an ohmic contact to the LUMO of most organic semiconductors. To increase electrical stability and to protect the Ca layer, it is capped with a thick layer of Al. Ca was evaporated from a tungsten crucible at a rate of

0.1 nm s⁻¹. The Al was evaporated from a tungsten coil packed with Al wire at a rate of 0.1-0.3 nm s⁻¹. The film thickness was monitored using quartz crystal monitors. The chamber pressure was in the range of 1-4 x 10⁻⁶ mbar for all evaporations. Lithium fluoride (LiF) and gold were evaporated in a similar manner to the above when required, using a tungsten crucible and boat respectively.

4.2 J-V Characterisation

4.2.1 Cell Fabrication

Substrates fabricated solely for J-V characterisation were 12 x 12 mm with a central 4 mm strip of indium tin oxide (ITO) (Xinyan Technology Ltd). The substrates were cleaned and the desired layers and top contact deposited as described in Section 4.1. The top electrode consisted of three 2 mm wide strips, perpendicular to the ITO, and thus defining three independent pixels per substrate with an area of 8 mm² (4 mm x 2 mm).

4.2.2 Measuring Solar Cell Performance

Solar cell performance is determined by measuring the current-voltage (J-V) characteristics while the cell is illuminated by artificial sunlight. The performance of the cell naturally depends on the intensity and wavelength of illumination source. To obtain results relevant to real world performance and to allow different institutions to meaningfully compare results, a standard illumination spectrum and intensity is used. The universally adopted reference spectrum is defined by the American Society for Testing and Materials (ASTM) and named ASTM G173-03.^[1] ASTM G173-03 defines two standard terrestrial solar spectral irradiance distributions, AM1.5G for flat panel PV technology which is of interest here, and AM1.5D which is used for solar concentrators. The AM1.5G reference spectrum is shown in Figure 4.1 and is representative of the solar spectrum once it has travelled 1.5 times through the atmosphere, corresponding to an angle where the sun is 41.81° above the horizon.

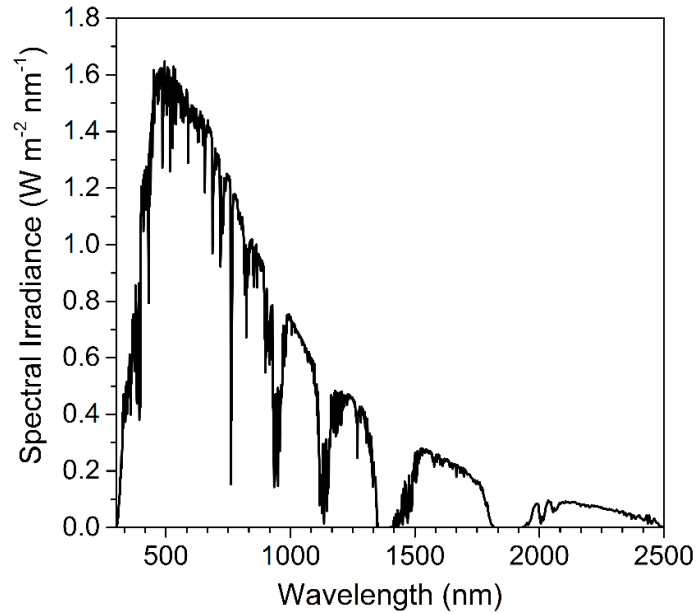


Figure 4.1: AM1.5G Reference Spectrum. Data obtained from NREL.^[2]

A Class AAA solar simulator (Sciencetech, SS150-AAA) with an AM1.5G filter was used to generate a close approximation to the terrestrial solar spectrum for cell testing. Before each measurement the irradiance at the cell position was set to 100 mW cm^{-2} (1 sun) using a calibrated silicon reference cell (Newport). A shadow mask with holes matching the dimensions and location of the three pixels was placed over the cell to avoid light absorbed outside of the defined pixel area contributing to the photocurrent. The J-V characteristics were measured using a Keithley 2400 SourceMeter controlled by a LabVIEW interface. The voltage across the cell was swept from -1 V to +1 V and the current measured. The current was divided by the pixel area to give the current density, J . Figure 4.2 shows a typical J-V characteristic of an OPV solar cell, in this case PTB7:PC₇₁BM, obtained using this setup. The P_{MPP} was determined by the minimum (P_{MPP} is negative due to the negative sign convention of the current in the 4th quadrant) value of the product of J and V . The PCE of the cells was then calculated from the P_{MPP} divided by the power incident on the cell, given by the product of the irradiance and pixel area. The J_{SC} is given by the current density when the voltage is zero, while the V_{OC} is determined from a linear fit between the points above and below $J = 0$. The fill factor is calculated by P_{MPP} over the product of V_{OC} and J_{SC} .

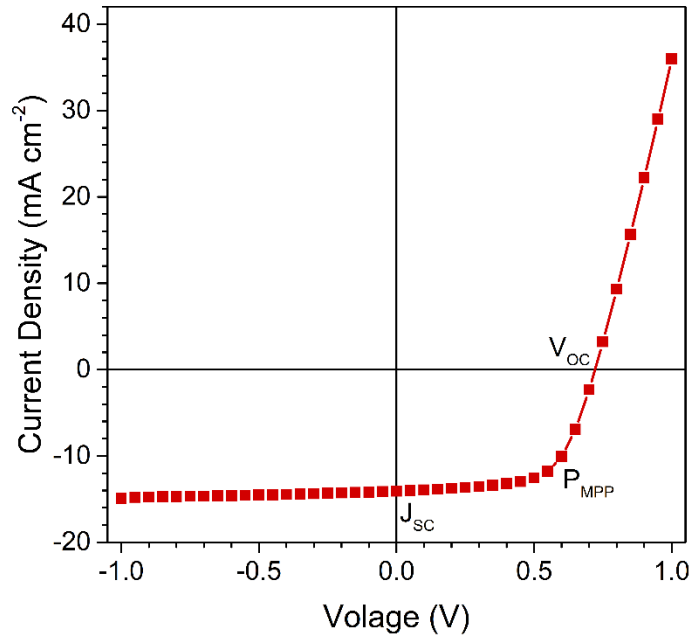


Figure 4.2: J-V characteristic of a PTB7:PC₇₁BM solar cell under 1 Sun illumination.

4.2.3 Intensity Dependent J-V

Additional information on the performance of the cell can be gained by measuring the J-V characteristics as a function of light intensity. This was achieved using a white light LED (Cree) and custom driver connected to a voltage pulse generator that was controlled by a LabVIEW interface. I am grateful to Dr. Bernd Ebenhoch for building this setup and writing the control software. The software sets the pulse generator voltage to generate a specific light intensity and the voltage applied to the cell is swept from -1 V to +1 V and the current measured. The voltage on the pulse generator is then changed to alter the light intensity and the applied voltage sweep repeated, which builds up a sequence of J-V curves over a two order of magnitude range of light intensity.

One important point is that the spectrum of the LED obviously differs substantially from the AM1.5G solar spectrum. Thus, when the LED intensity is set to “1 Sun” (100 mW cm⁻²) the effective intensity seen by the solar cell may be substantially different than the intensity experienced if the AM1.5G simulator had been used. To compensate for this, the J_{sc} of the cell when measured under LED - 1 Sun was compared to the J_{sc} obtained when the cell was measured under AM1.5G Simulator - 1 Sun. The ratio of these two values was used to scale the LED intensities to the correct value.

The main use of this technique is to investigate the type of recombination occurring in the cell; bimolecular or monomolecular. The influence of light intensity on the short circuit current can be described using,

$$J_{SC} = \alpha I^\beta \quad (4.1)$$

where I is the light intensity, α is a scaling prefactor and β describes the linearity of the response. If $\beta = 1$ the J_{SC} scales linearly with light intensity which is the expected behaviour in the absence of recombination loss, as more photons equals more electrons and holes. The J_{SC} will only break from linearity if there is a loss mechanism that scales greater than first order with the number of charge carriers. The primary mechanism that exhibits this behaviour is bimolecular recombination which as previously shown in Eq. 2.3, is second order in charge carrier concentration. The exponent β therefore provides a measure of the degree of bimolecular recombination occurring inside the cell. A β of unity means no bimolecular recombination is occurring while lower values signify increasing bimolecular recombination losses.^[3-6] The exponent can be easily obtained by measuring the J-V of the solar cell over a range of light intensities and plotting the J_{SC} versus light intensity on a log-log scale as shown in Figure 4.3a. By plotting on a double log scale β switches from the exponent to the gradient of the slope. It can then be easily obtained by applying a linear regression to the data.

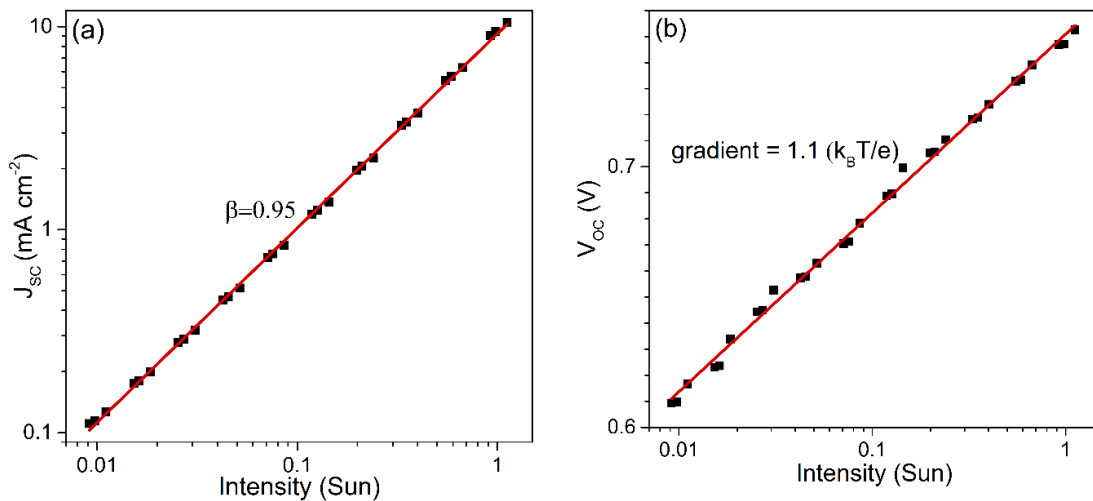


Figure 4.3 Variable light intensity characterisation of a PTB7:PC₇₁BM solar cell. (a) J_{sc} against light intensity on a double log scale. (b) V_{oc} against light intensity on a natural log scale.

To estimate the monomolecular recombination losses inside the cell a similar approach can be adopted. The solar cell is an intrinsic semiconductor, with a Fermi level in the

centre of the bandgap. When the cell is illuminated, electrons are promoted to LUMO and holes generated in the HOMO. This results in the creation of two new quasi Fermi levels with energies of E_F^h and E_F^e for holes and electrons respectively. The population of electrons and holes under illumination is given by,^[7, 8]

$$n_e = N \exp\left(-\frac{E_{LUMO} - E_F^e}{k_B T}\right) \quad (4.2a)$$

$$n_h = N \exp\left(-\frac{E_F^h - E_{HOMO}}{k_B T}\right) \quad (4.2b)$$

where N is the density of states. Taking the product of these two populations yields,

$$\begin{aligned} n_e n_h &= N^2 \exp\left(\frac{E_{HOMO} - E_{LUMO} + E_F^e - E_F^h}{k_B T}\right) \\ &= N^2 \exp\left(-\frac{E_{Gap}}{k_B T}\right) \exp\left(\frac{E_F^e - E_F^h}{k_B T}\right) \end{aligned} \quad (4.3)$$

where E_{Gap} is the difference in energy between the HOMO and LUMO. Assuming that the contacts are ohmic, as discussed in section 2.2.6, the V_{OC} will be given by the difference in energy of the electron and hole quasi Fermi energies and Eq. 4.3 can be rewritten as,

$$n_e n_h = N^2 \exp\left(-\frac{E_{Gap}}{k_B T}\right) \exp\left(\frac{eV_{OC}}{k_B T}\right) \quad (4.4)$$

where e is the elementary charge. At open circuit the charge recombination rate R and charge generation rate must G be in equilibrium, $G = R$. Assuming that all the recombination at open circuit is bimolecular it can be written,

$$G = R = B_L n_e n_h \quad (4.5)$$

where the term on the right hand side is the bimolecular recombination rate introduced in Eq. 2.3. Inserting Eq. 4.5 into Eq. 4.4 and rearranging, the open circuit voltage is given by Eq. 4.6.^[3, 8]

$$V_{OC} = \frac{E_{Gap}}{e} - \frac{k_B T}{e} \ln\left(\frac{B_L N^2}{G}\right) \quad (4.6)$$

The generation rate G depends on the intensity of the incident light while B_L and N^2 are independent of light intensity. A plot of light intensity on a natural log scale against V_{OC} will therefore have a gradient of $\frac{k_B T}{e}$ if the recombination at open circuit is purely bimolecular. A gradient exceeding $\frac{k_B T}{e}$ reveals that the recombination is greater than can be obtained solely by bimolecular processes. The gradient can therefore be used as a measure of the degree of monomolecular (trap-assisted) recombination occurring in the cell as shown in Figure 4.3b. The greater the deviation is away from $\frac{k_B T}{e}$ the greater the monomolecular recombination losses.

4.3 Electron Paramagnetic Resonance Spectroscopy

4.3.1 The EPR Spectrometer

An EPR spectrometer consists of three key components; the microwave bridge, a magnet, and a microwave resonator. A simplified diagram of an EPR spectrometer is shown in Figure 4.4. The microwave bridge is responsible for the detection and generation of the microwaves. The microwaves from the bridge are coupled into a microwave resonator in order to improve sensitivity of the spectrometer. Inside the resonator a standing wave is generated which enhances the strength of the microwave magnetic field at the sample. To induce a Zeeman splitting of the spin energy levels an electromagnetic or superconducting magnet is used to generate a strong static magnetic field. By adjusting the current through the magnet coils the strength of magnetic field and the Zeeman splitting can be varied.

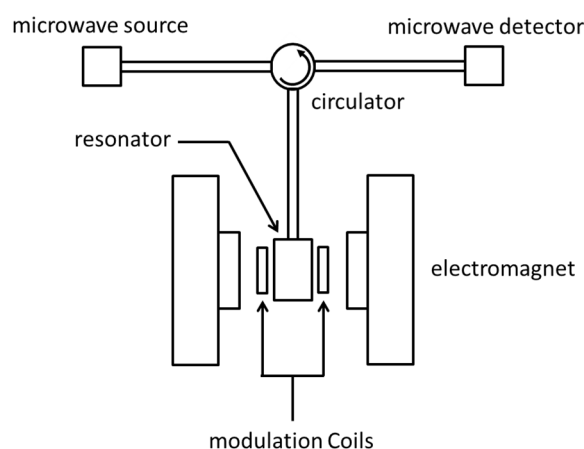


Figure 4.4 Simplified schematic of a cwEPR spectrometer.

EPR spectrometers can be grouped by two criteria; their operating frequency and whether they use continuous wave or pulsed microwaves. The most common EPR frequency is 9.8 GHz (also called X-Band). Spectrometers operating at higher frequencies are becoming increasingly common as they offer improved sensitivity and allow transitions which may be overlapping at lower frequencies to be resolved. In terms of operating mode, continuous wave spectrometers have greater sensitivity than pulsed and may be used at room temperature which makes them well suited for the rapid screening samples or looking for small signals. Pulse spectrometers are technically more complicated, require a better theoretical understanding and must be used at low temperature to increase relaxation times. However they can provide a wealth of additional information using advanced pulse sequences such as coupling to nuclei and other electron spins. The EPR spectra presented in this thesis were recorded across a varied range of EPR spectrometers that were spread across three different institutions; the University of Dundee, University of St Andrews and Argonne National Laboratory. The operating frequencies, mode, resonators and locations of the spectrometers used are summarised in Table 4.1.

Table 4.1 Spectrometers and resonators used for EPR spectroscopy.

Spectrometer	Frequency	Resonator	Mode	Location
Bruker EMX	9.8 GHz (X-Band)	Cavity (ER 4123SHQE)	CW	Dundee
Bruker Elexsys E580	9.8 GHz (X-Band)	Dielectric ring (EN 4118X-MD4)	CW / Pulsed	St Andrews & Argonne
Bruker Elexsys E580	34 GHz (Q-Band)	Dielectric ring (ER5106QT-2W)	CW / Pulsed	St Andrews
HIPER ^[9]	94 GHz (W-Band)	N/A	Pulsed	St Andrews
The Can ^[10, 11]	130 GHz (D-Band)	TE ₀₁₁	Pulsed	Argonne

4.3.2 Continuous Wave EPR

As discussed in Section 3.1 an applied magnetic field, B_0 , will break the degeneracy of the $|\alpha\rangle$ and $|\beta\rangle$ spin states with an energy splitting proportional to the magnetic field strength. A magnetic dipole transition between $|\alpha\rangle$ and $|\beta\rangle$ states can be induced by applying a perpendicular electromagnetic field, B_1 , oscillating at frequency such that the photon energy matches the Zeeman splitting energy as defined in Eq. 4.7.

$$h\nu = g\mu_B B_0 \quad (4.7)$$

In a continuous wave EPR spectrometer the sample is continuously irradiated by microwaves at a fixed frequency ν and experiences a magnetic field B_1 oscillating at that frequency inside the resonator. The coupling between the incoming microwaves and the resonator is adjusted so that no microwaves are reflected from the resonator (critical coupling). The magnetic field B_0 is then swept and when Eq. 4.7 is satisfied microwaves are absorbed by the sample which changes the impedance of the resonator and microwaves are reflected from the resonator. These reflected microwaves are then recorded as a function of magnetic field to form the EPR spectrum.

In order to improve the signal to noise ratio a lock in amplifier (phase sensitive detection) is almost always used. Phase sensitive detection can be achieved by either modulating the incoming microwaves or the static magnetic field B_0 . The latter approach is employed by the majority of CW spectrometers including the ones used in this thesis. Field modulation of the EPR signal is achieved using Helmholtz coils placed in the walls of the resonator which generate a sinusoidally oscillating magnetic field (typically 100 kHz) with amplitude B_{mod} that is parallel to the main field B_0 . The influence of the field modulation on the detected EPR signal is shown in Figure 4.5. When 100 kHz field modulation with amplitude B_{mod} is used the microwaves reflected from the resonator at static field position B_0 are modulated at 100 kHz with a maximum amplitude proportional to the gradient of the EPR lineshape over the field range $B_0 - \frac{B_{mod}}{2}$ to $B_0 + \frac{B_{mod}}{2}$. The reflected microwaves are converted to current by the microwave detector which is passed into the lock in amplifier. The lock in amplifier filters out signals which are not modulated

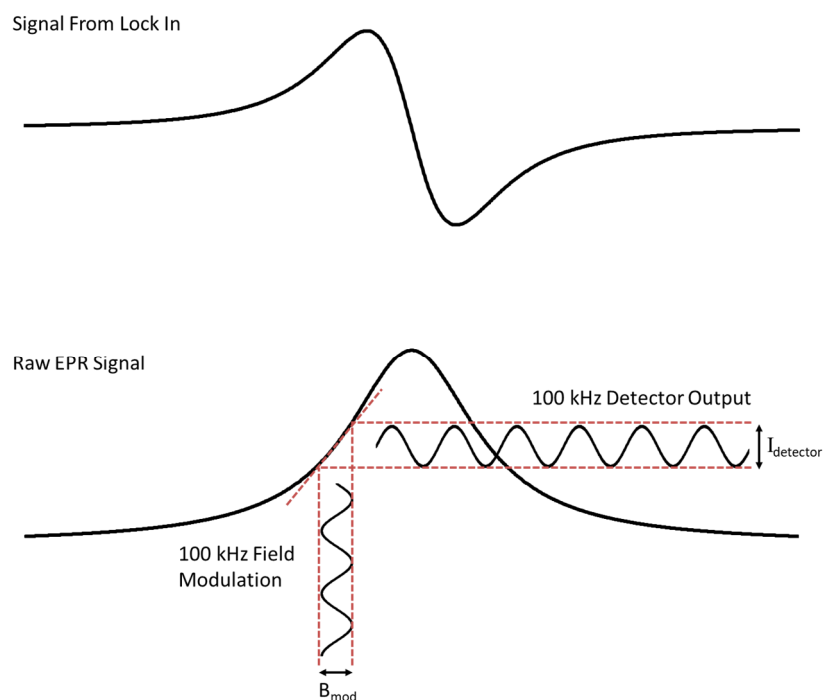


Figure 4.5 Effect of field modulation on the EPR signal. Adapted from Weil & Bolton.^[12]

at 100 kHz, thereby improving the signal to noise ratio. The output from the lock in amplifier at each field position is proportional to the gradient of true EPR response so the detected signal is the first derivative of the EPR response. For this reason CW EPR spectra are commonly shown as a first derivative. Larger values of B_{mod} will improve the signal to noise ratio. However as B_{mod} increases it will begin to smooth out the sharper features of the spectrum and cause broadening of the linewidth. There is therefore a trade-off between accurate spectral reproduction and signal to noise ratio.

4.3.3 Pulsed EPR

In a pulsed spectrometer the microwaves pass through a pulse forming unit which creates microwave pulses lasting several to hundreds of nanoseconds. These pulses are then amplified using a travelling wave tube (TWT) amplifier before being directed into the resonator.

To describe the action of the microwave pulses on the sample it is more intuitive to move away from the quantum mechanical picture of individual spins towards a more visual semi classical description using magnetic moments and bulk magnetisation of the sample.

When a magnetic field B_0 is applied the magnetic moment of each spin experiences a torque and will therefore precess around B_0 at the Larmor frequency which is given by,

$$\omega_L = \frac{g\mu_B B_0}{\hbar} = \gamma B_0 \quad (4.8)$$

where γ is the gyromagnetic ratio. Electrons where the spin magnet moment lies parallel to the applied field are lower in energy than those that lie antiparallel. There will therefore be an excess of electrons in the parallel state as given by a Boltzmann distribution. Averaging over N spins in the sample a net magnetic moment per unit volume can be defined,

$$\mathbf{M} = \frac{1}{V} \sum_{i=1}^N \boldsymbol{\mu}_i \quad (4.9)$$

where \mathbf{M} is the magnetisation of the sample. Assuming that the magnetic field B_0 is applied along the z-direction, as is convention, there will therefore be a net magnetisation along the z-axis. Each individual magnetic moment will still precess around the z-axis at ω_L but as there is no preferential orientation in the x-y plane there is no x-y component of \mathbf{M} and it points directly along the z-axis.

A microwave pulse consists of a short burst of linearly polarised microwaves where the magnetic field vector of the microwave pulse inside the resonator \mathbf{B}_1 is perpendicular to the static field \mathbf{B}_0 . Any linearly polarised electromagnetic wave can be mathematically decomposed into two counter rotating circularly polarised components (see Figure 4.6a), which is easier to visualise. Assuming \mathbf{B}_1 is polarised along the x-axis the two circularly polarised components of \mathbf{B}_1 will rotate at $\pm \omega_0$ around the z-axis where ω_0 is the angular microwave frequency as shown in Figure 4.6a alongside the magnetisation vector. The action of the microwave pulse on the magnetisation is simplified by moving to a reference frame which rotates at ω_0 which is shown in Figure 4.6b. In this rotating frame there is a static component of \mathbf{B}_1 along the x-axis and a component moving at $-2\omega_0$ which can be ignored. Assuming that the microwaves are resonant with the processing spins, $\omega_0 = \omega_L$, the rotating frame also removes the precession of the magnetic moments around the z-axis. If there is no precession then the static field \mathbf{B}_0 disappears in the rotating frame and only the influence of \mathbf{B}_1 on \mathbf{M} needs to be considered.

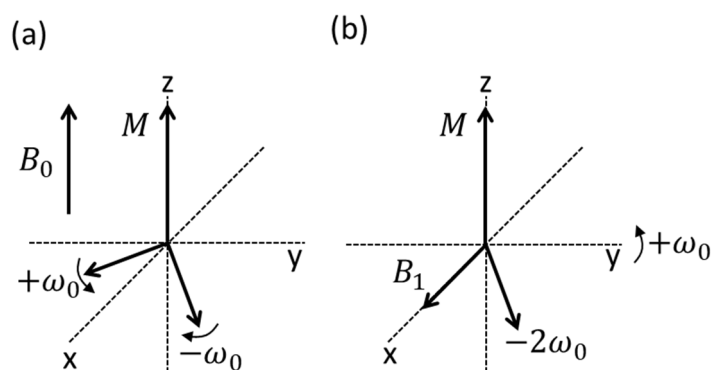


Figure 4.6 The microwave magnetic field in (a) laboratory reference frame and (b) rotating reference frame. Adapted from Weber.^[13]

The magnetisation will experience a torque due to \mathbf{B}_1 and will therefore rotate around \mathbf{B}_1 at,

$$\omega_1 = \gamma B_1 \quad (4.10)$$

where ω_1 is known as the Rabi frequency. The extent of the rotation of \mathbf{M} is determined by the length and strength of the microwave pulse magnetic field. This is characterised by the tip angle of the microwave pulse,

$$\alpha = \gamma B_1 \tau_p \quad (4.11)$$

where τ_p is the length of the microwave pulse. Pulses are named after their tip angle. One of the most common pulses is a $\pi/2$ which rotates the magnetisation from pointing along +z direction to the along $-y$ direction. Similarly a π pulse rotates the magnetisation from +z to $-z$ and so on.

It can be seen from Eq. 4.11 that there are many different combinations of B_1 and τ_p that can generate pulses with the same tip angle. While a short high B_1 pulse or long low B_1 pulse can cause the same rotation of \mathbf{M} they differ in their excitation bandwidth. The excitation bandwidth of a rectangular pulse is approximately given as 1 over the pulse length.

$$\text{Excitation Bandwidth} \approx \frac{1}{\tau_p} \quad (4.12)$$

The excitation bandwidth determines how large an area of the EPR spectrum is simultaneously excited at each field position. This is particularly important when

investigating systems with two overlapping EPR resonances such as positive and negative polarons in the donor and acceptor phases of bulk heterojunction solar cells. If excitation of single species is desired such as in an ENDOR or T_1 experiment smaller excitation bandwidths are desirable. Small excitation bandwidths are achieved using long low power pulses which are called selective or soft pulses while short high powers have a large excitation bandwidth are called non-selective or hard pulses.

Free Induction Decay (FID)

The simplest pulse sequence that can be implemented is applying a single $\pi/2$ pulse to the system which flips the magnetisation into the x-y plane. In the rotating frame this is not particularly interesting but in the laboratory frame the magnetisation is now rotating around the z-axis in the x-y plane. This rotating magnetisation generates microwave signal called the free induction decay (FID) which can be detected.

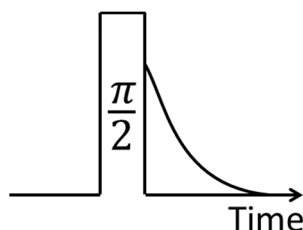


Figure 4.7: FID after microwave pulse.

Relaxation

The magnetisation does not rotate around the z-axis forever and decays through two mechanisms. When a $\pi/2$ pulse is applied the sample is no longer in thermal equilibrium and over time this energy will be dissipated from the spins to the lattice and the magnetisation will decay exponentially back towards the +z direction as shown in Figure 4.8 This decay is known as spin-lattice relaxation or longitudinal relaxation and has a characteristic time constant T_1 .

The second type of relaxation is transverse, where the magnetisation vector fans out in the x-y plane as shown in Figure 4.8. This fanning out will cause the transverse magnetisation to decay to zero. The fanning out of the magnetisation is caused by several different mechanisms such as spin-spin interactions resulting in spin flip flops This is known as spin-spin relaxation and has characteristic time constant T_2 .

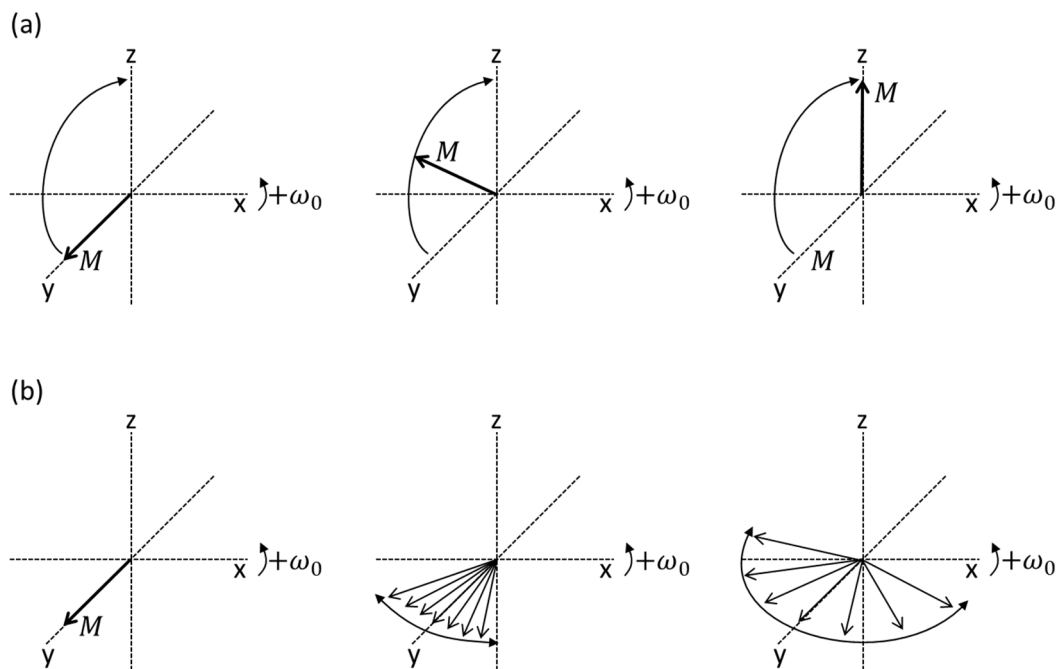


Figure 4.8 Longitudinal (a) and transverse relaxation (b) of the magnetisation after a $\pi/2$ pulse.

T_2 is generally much shorter than T_1 and it is therefore this loss of transverse magnetisation that is responsible for the decay of the FID. The rapid decay of the transverse magnetisation poses an issue for detecting the microwaves emitted by the system after a pulse due to spectrometer deadtime. After the microwave pulse the resonator will dissipate microwave power (also called ringing) over a period of time that depends on the Q-factor of the resonator. The sensitive microwave detector must be protected from this high microwave power ringing. There is therefore a period of time, called the deadtime, after the microwave pulse where no microwave emission from the sample can be detected. This is a problem as the FID generally decays away before the deadtime has ended. The solution to this problem is to use spin echoes.

Hahn Echo

By applying a $\pi/2$ followed by a π pulse the decaying transverse magnetisation can be refocused and recovered at a later time. The $\pi/2$ pulse rotates the magnetisation vector into the x-y plane. The magnetisation is then left to fan out for a period τ and a π pulse applied which flips the magnetisation components by 180° so that they are now a mirror image of prior to the pulse. As the magnetisation components are still travelling in the same direction as prior to the pulse, they will refocus and converge at time τ after the π

pulse creating an echo of the earlier transverse magnetisation which can be detected. The value of τ is chosen such that the echo appears after the deadtime. This sequence is called a Hahn Echo and is the foundation of many advanced pulse experiments.

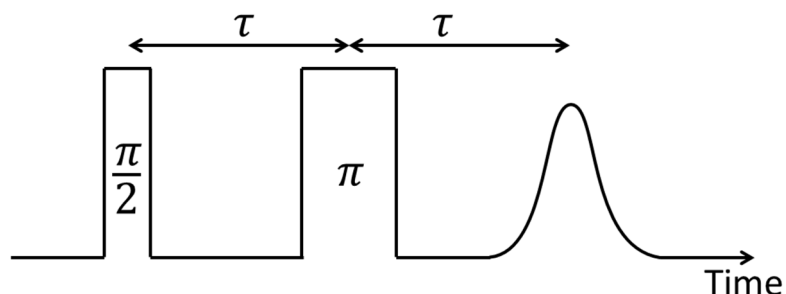


Figure 4.9: Hahn Echo Pulse Sequence

Stimulated Echo

The Hahn sequence is not the only method to generate an echo. A series of three $\pi/2$ pulses gives rise to the so called stimulated echo. This pulse sequence is necessary for some types of ENDOR experiment as will be discussed shortly. Note that the situation is more complicated than presented here as there will be additional (unwanted) echoes. This applies to all pulse sequences with more than two pulses.



Figure 4.10: Stimulated Echo Pulse Sequence

Inversion Recovery

The T_1 relaxation time of a material can be measured using the inversion recovery pulse sequence. The magnetisation is first flipped to the $-z$ direction by a π pulse and will start to relax back towards $+z$ due to spin-lattice relaxation. The progress of this relaxation can be monitored using a Hahn echo at time T after the inversion pulse. By repeating this

measurement over a range of T the recovery of the magnetisation (height of the echo) versus time can be obtained and T_1 calculated.

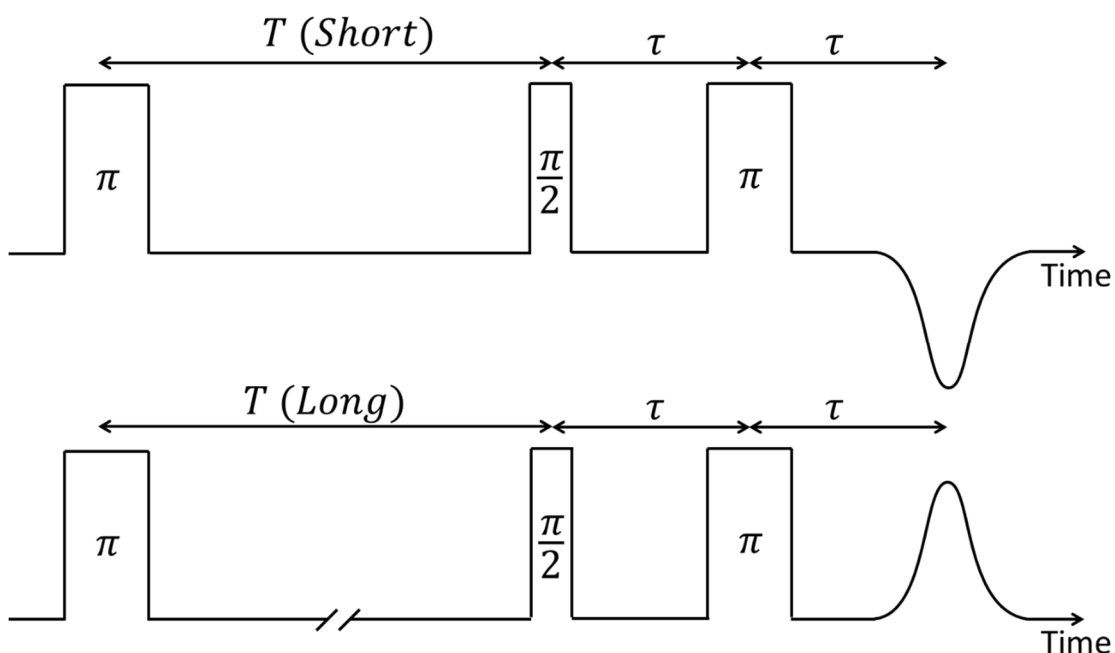


Figure 4.11: Inversion Recovery Pulse Sequence. The upper panel shows the resulting echo at short interval T and the lower panel at long T .

ENDOR

Electron nuclear double resonance spectroscopy (ENDOR) is used to probe the interaction of the electron spins with magnetic nuclei in the sample which are coupled through the hyperfine interaction. This is achieved by applying microwaves and radio waves in a single double resonance experiment which interact with the electrons and nuclei respectively. There are two commonly used ENDOR pulse sequences Davies,^[14] and Mims,^[15] which are described in turn.

Davies Pulse Sequence

The Davies ENDOR sequence is shown in Figure 4.12 and consists of a microwave and radio wave part. The microwave part is essentially equivalent to the inversion recovery sequence except that T is now kept constant. To explain the ENDOR sequence, consider

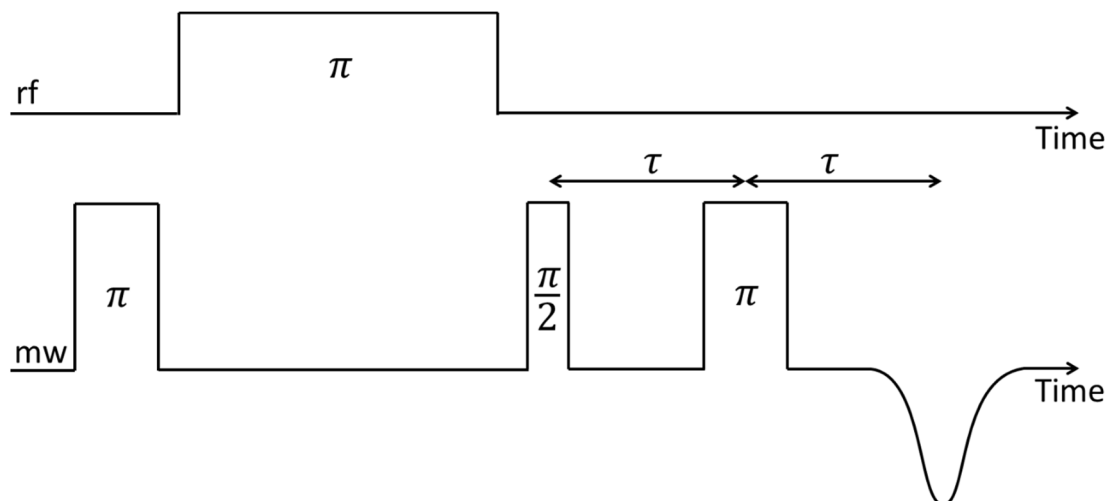


Figure 4.12 Davies ENDOR pulse sequence.

the simplest hyperfine coupled system consisting of a spin $\frac{1}{2}$ electron spin coupled to a spin $\frac{1}{2}$ nuclear spin. The four energy levels of this system are shown in Figure 4.13. There are two possible EPR transitions (vertical) and two NMR transitions (diagonal). At thermal equilibrium the two lower states will be preferentially populated as shown by the black bars. Upon application of a selective (see Eq. 4.13) π MW pulse that is resonant with the leftmost transition the population is shifted from the $|\beta\alpha\rangle$ to the $|\alpha\alpha\rangle$ state (Figure 4.13b). This inverts the magnetisation and an inverted echo would be detected using the Hahn read out sequence. By applying a π RF pulse that is resonant with one of the nuclear transitions population is shifted from the $|\alpha\alpha\rangle$ to the $|\alpha\beta\rangle$ state (Figure 4.13c). As the intensity of the inverted echo is proportional to the population difference between the $|\beta\alpha\rangle$ and $|\alpha\alpha\rangle$ states, the application of a resonant RF pulse suppresses the inverted echo. In a Davies ENDOR experiment the MW pulse is kept constant, the frequency of the RF swept, and the intensity of the inverted echo recorded as a function of RF frequency. As the RF resonant frequency depends on the interaction between the electron and nuclear spins the strength of the hyperfine coupling interaction is revealed.

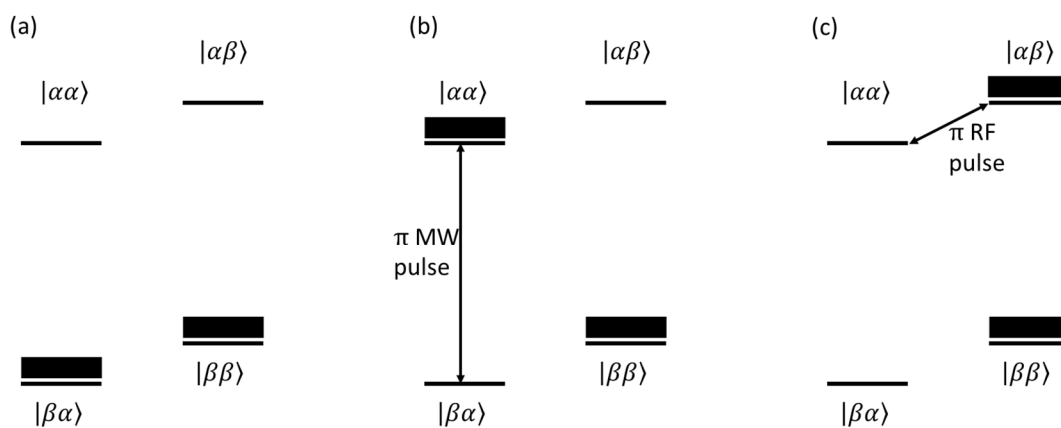


Figure 4.13 Energy levels of a $S=1/2, I=1/2$ spin system. The black bars indicate the excess population (a) in thermal equilibrium, (b) after a selective MW π pulse, and (c) after RF π pulse. The first letter in the ket is the electron spin state and the second is the nuclear spin state. Adapted from Gemperle and Schweiger.^[16]

Mims Pulse Sequence

The Mims pulse sequence is based on the stimulated echo pulse sequence as shown in Figure 4.14. The first $\pi/2$ pulse rotates the magnetisation into the x-y plane which is left to fan out over time τ . Application of the second $\pi/2$ rotates the magnetisation components so that they are now in the x-z plane (assuming B_1 is along x as in Figure 4.6). The transverse magnetisation components will then decay swiftly, leaving only longitudinal magnetisation remaining. Applying a $\pi/2$ readout pulse will convert the longitudinal magnetisation to transverse and the components will refocus at time τ after the pulse,

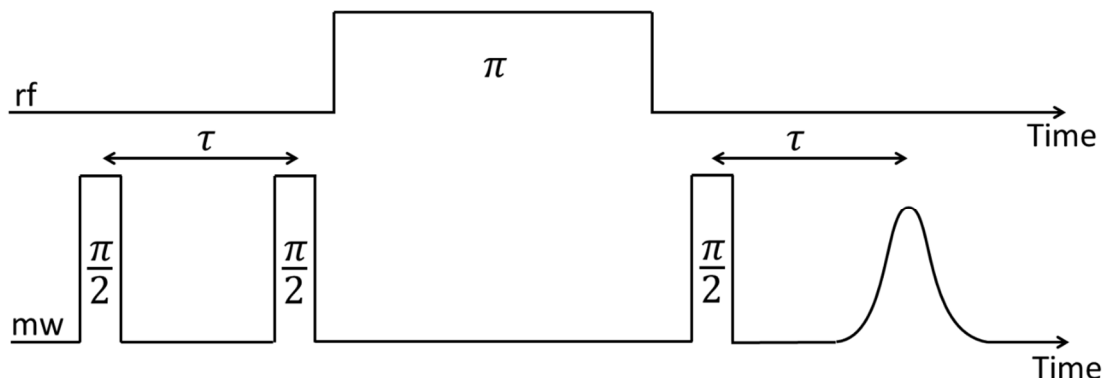


Figure 4.14 Mims ENDOR pulse sequence.

generating an echo. The application of a π RF pulse resonant with one of the NMR transitions changes the rotation speed of that magnetisation component which prevents it from refocusing at time τ after the $\pi/2$ and decreases the height of the echo. The ENDOR spectrum is therefore obtained in a similar manner to Davies, varying the RF frequency and monitoring the height of the stimulated echo.

4.3.4 Light Induced EPR (LEPR)

The photogeneration of charge is a key process in photovoltaic cells. This can be studied using LEPR where the OPV blend is illuminated prior or during the EPR measurement. The most common light source used for LEPR measurements in this thesis was 532 nm from a frequency doubled Nd:YAG pulsed at 10 (Surelite Continuum) or 20 Hz (INDI, Newport). The light from the laser was coupled into a fibre which terminated at the optical access port of the EPR resonator. At cryogenic temperatures the recombination of charge carriers is slow and the pulsed laser builds up a steady state population of charge carriers after illuminating for several minutes. The laser is then left running and CW or pulsed EPR spectra recorded.

4.3.5 Time-Resolved EPR (TR-EPR)

TR-EPR is a pump probe experiment where the EPR spectrum is recorded a short time after an optical pump pulse. The method of TR-EPR used throughout this thesis is direct detection. Direct detection is a type of cwEPR experiment where the field modulation is disabled and the transient evolution of the cwEPR spectrum recorded as a function of time after the laser flash.

The TR-EPR measurements were achieved using the same Nd:YAG source as above. The cwEPR spectrum was recorded as a function of time after the laser flash using the transient recorder (SpecJet) of the E580 spectrometer. The triggering of the laser and the transient recorder was controlled using a delay generator (Stanford DG535). The time resolution of the setup is limited by the quality factor of the resonator,^[17] and is of order 100 ns.

4.3.6 Field Calibration

Obtaining accurate g-factors is crucial as they serve as a fingerprint for the paramagnetic species under study. The g-factor depends on the magnetic field and the microwave frequency (Eq. 3.12). The microwave frequency can be easily measured to high degree of accuracy during each experiment using a microwave frequency counter. Accurate measurement of the magnetic field at the sample position is more difficult. Every EPR spectrometer contains a Hall probe to measure the magnetic field created by the electromagnet. However the Hall probe is located outside of the microwave resonator. As a result there is a non-negligible difference in magnetic field strength between the Hall probe and that experienced by the sample inside the resonator. To accurately determine the magnetic field at the sample position, a calibration sample was used.

By measuring the EPR spectrum of a paramagnetic sample which possesses a narrow linewidth with an accurately known g-factor, the magnetic field at the sample position can be easily calculated using Eq. 3.12. The reference sample used to calibrate the magnetic field of the various EPR spectrometers used throughout this thesis was nitrogen doped C_{60} , $N@C_{60}$ for short.^[18] $N@C_{60}$ is a type of endohedral fullerene which consists of a standard C_{60} fullerene cage with a nitrogen atom located inside. $N@C_{60}$ is a $S = 3/2$, $I = 1$ spin system due to the three unpaired electrons in nitrogen and the $I = 1$ nuclear spin of ^{14}N which has 99.6 % abundance. Due to the high symmetry of $N@C_{60}$ there are no appreciable zero field splitting interactions between the three electrons, and the transitions between the four $S = 3/2$ levels are therefore degenerate.^[19] The spin system can therefore be modelled as $S = 1/2$, $I = 1$.

The 9.8 GHz EPR spectrum of the $N@C_{60}$ sample is shown in Figure 4.15 (black line). It consists of characteristic triplet of sharp lines which is the EPR signature of $N@C_{60}$ and arises from the hyperfine coupling to $I = 1$. In addition there is a broad central feature which is due to a $C_{60}-O-O-C_{60}$ radical that builds up in the sample after prolonged exposure to light and ambient atmosphere.^[20] This build up is benign as it does not change the g-factor of the $N@C_{60}$,^[20] and the field position of the $N@C_{60}$ resonance can be accurately determined using the two outer lines of the triplet. The system was simulated using the literature g-factor of 2.0022(3) for $N@C_{60}$,^[20, 21] and a hyperfine coupling

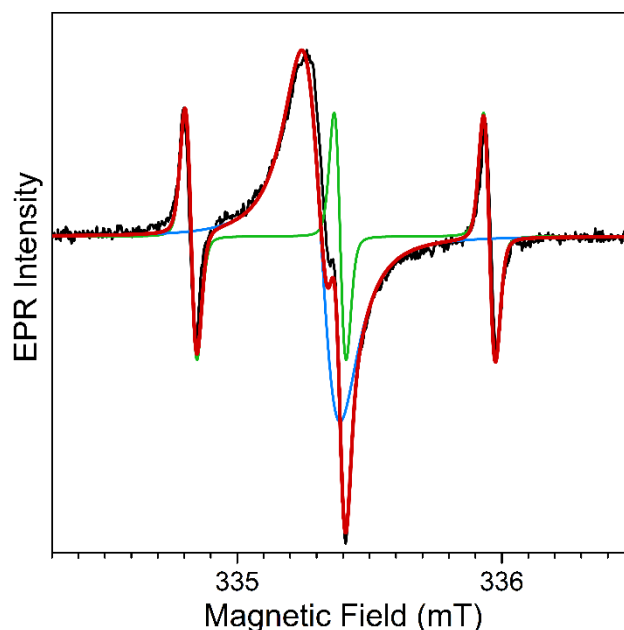


Figure 4.15 EPR spectrum of N@C₆₀ calibration sample recorded at 9.8 GHz at RT. The experimental spectrum is shown in black, the N@C₆₀ triplet in green, the impurity in blue and the total simulation in red.

constant of 15.8 MHz. The magnetic field axis of the experimental spectrum was shifted until the experimental and simulated spectra achieved optimum overlay. The magnitude of axis shift required gives the difference in field between the Hall probe and the sample position and this field correction factor can then be applied to all spectra measured on that spectrometer.

4.4 Electrically Detected Magnetic Resonance Spectroscopy

4.4.1 Introduction

While a powerful technique, conventional EPR spectroscopy suffers from two key shortfalls when investigating processes in organic solar cells. The first is that conventional EPR has a sensitivity of around 10^{10} spins which is generally too low to reliably study thin films (~ 100 nm) of organic semiconductors.^[12, 22, 23] For this reason most EPR studies on OPV systems use thick films (> 1 μm) or frozen solutions in order to increase the signal to noise of the measurement. Given the importance of film morphology in OPV this approach raises questions of the relevance these results to operation of a thin film OPV cell. Secondly conventional EPR is sensitive to every paramagnetic species in the sample regardless of whether those species are involved in the operation of the cell. This makes it difficult to determine whether the detected species are relevant to the performance of the cell or a minority species with no impact on cell

efficiency. The solution to these problems is to replace the microwave detection with electrical detection which is known as Electrically Detected Magnetic Resonance (EDMR). In EDMR a working semiconductor device is placed inside the resonator and the change in the current (or voltage) at resonance detected. Current detection greatly improves the sensitivity of the measurement which enables thin film semiconductor devices to be measured.^[22-25] In addition since only those species which directly influence the current can be detected, the observed species must be relevant to the operation of the device.

The most forthcoming example of a spin dependent process is charge carrier recombination. If the electron and hole are both ‘spin up’, i.e in a triplet configuration, then the recombination is forbidden due to conservation of angular momentum (first panel of Figure 4.16) By applying microwaves resonant with the electron in the LUMO a spin flip can be induced, enabling the recombination to occur and causing a change in the current through the sample which can be detected. Other current influencing spin-dependent mechanisms are also possible such as spin dependent hopping and scattering.^[25]

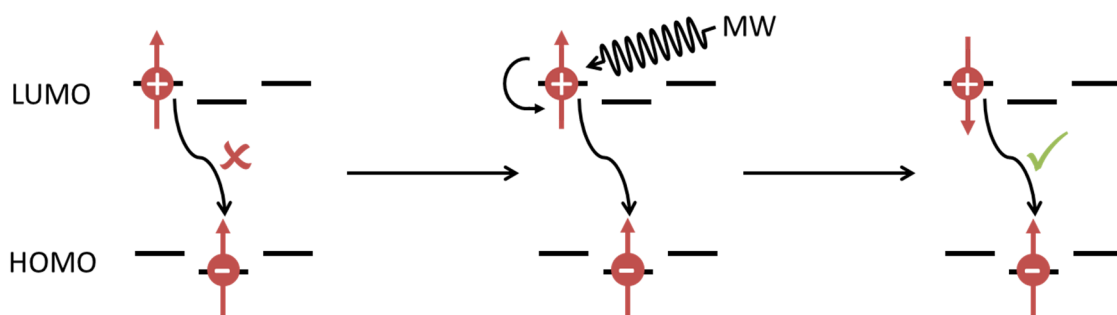


Figure 4.16 Spin dependent recombination process.

The first EDMR measurement was performed by Maxwell and Honig,^[26] and was attributed to the spin dependent scattering of charge carriers. The first recombination EDMR response was observed a few years later by Lepine.^[27] A model was needed to quantify these new observations. Lepine suggested a simple thermal polarisation model analogous to conventional EPR where the spin dependent recombination change is proportional to the population difference between the two Zeeman levels. Subsequent experiments revealed that the observed current changes at resonance were larger than

could be explained by Lepine's model. Many more models were developed throughout the 1970s but could not reconcile the theoretical predictions with the experimental observations, for example the lack of temperature dependence.^[28] In 1978 Kaplan, Solomon and Mott presented a new model (the KSM model) which is the basis of the majority of EDMR models to date.^[29]

The KSM model is based on the formation of intermediate spin pairs prior to recombination. After forming an intermediate pair partners must either recombine or dissociate, and cannot interact with other species while in the pair. The EDMR response arises from the conversion of the intermediate pairs from a triplet to a singlet spin configuration at resonance which increases the recombination rate causing a detectable change in current. Since its inception the KSM model has been developed further by many authors. One of the most important of these developments was presented by Boehme and Lips,^[25, 28] who generalised the KSM model and provided the first understanding of the dynamic evolution of the current response following a microwave pulse (pEDMR). This intermediate pair model is presented in an abridged format in the following section.

4.4.2 Intermediate Pair Model

Consider two spin $\frac{1}{2}$ particles, an electron and hole, forming an intermediate pair prior to recombination. In general the electron and hole will have different g -factors and there will be exchange and dipolar coupling between them. The Hamiltonian and eigenstates describing this intermediate pair in a magnetic field is simply that of the SCRP introduced in Section 3.4.3. The occupation of the four states can be described using the density matrix formalism where the population of each state is given by its corresponding density matrix element ρ_{ii} . The creation and annihilation pathways of the four states are shown in Figure 4.17. Prior to resonance the system is in a steady state with a constant generation rate of charge carriers, i.e. constant current. The carriers can either be created through electrical injection or illumination to generate a photocurrent. In the steady state, intermediate pairs will be generated at a constant rate G and it is assumed that the generation rate for the four intermediate pair states is equal, with a rate of $G/4$. An equal generation rate for the four states is a valid assumption as long as the recombination is non-geminate. The intermediate pairs may dissociate back to free electrons and holes with

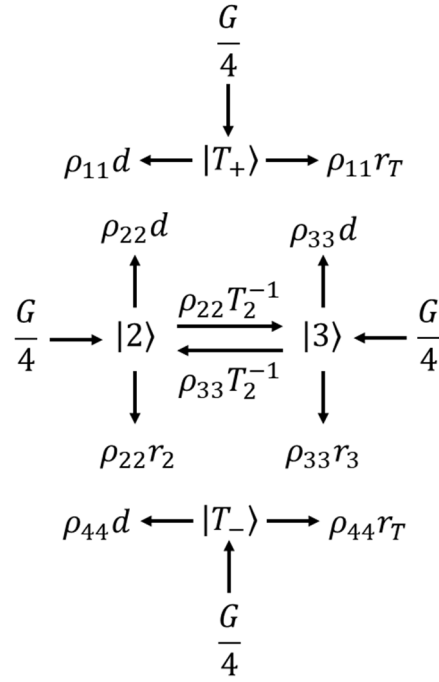


Figure 4.17 Eigenstates of the intermediate pair model with their respective generation, recombination, relaxation and dissociation rates. Adapted from Boehme & Lips.^[25]

a rate constant d which is assumed equal for the four states. In addition pairs in states 2 and 3 can interconvert through spin-spin relaxation with rate constant $1/T_2$. The probability for a pair to recombine depends on the spin permutation symmetry of the pair. Pure singlet states will recombine with rate constant r_s and pure triplet states with r_T . The triplet recombination rate is assumed to be small but finite due to non-negligible spin-orbit coupling. The pure triplet states $|T_+\rangle$ and $|T_-\rangle$ will therefore recombine with rate constant r_T while the recombination rate of the mixed states $|2\rangle$ and $|3\rangle$ is dependent on the singlet and triplet content of the pair as given by the following expression.^[25]

$$r_i = r_s |\langle i|S\rangle|^2 + r_T |\langle i|T_0\rangle|^2 \quad (4.14)$$

The values of r_2 and r_3 will therefore depend on the mixing angle which is determined by g-factors of the electron and hole and the strength of dipolar and exchange coupling between them (see SCRP Eq. 3.38).

At resonance the conductivity of sample will change from its steady state value. The time dependent conductivity change following excitation of the sample with a resonant microwave pulse is given by,^[25]

$$\Delta\sigma(t) = \sigma(t) - \sigma^s = e[\Delta n_e(t)\mu_e + \Delta n_h(t)\mu_h] \quad (4.15)$$

where σ^s is the steady state conductivity and Δn_e and Δn_h are the time dependent changes in electron and hole density. In Eq. 4.15 it is assumed that the resonant microwave pulse alters the electron and hole density in the sample, i.e the spin dependent mechanism is recombination. If the spin-dependent mechanism is instead due to a process such as scattering or hopping then Eq 4.15 would be changed such that the electron and hole densities remains constant and the mobility of the carriers is changed by the resonant microwaves. The changes of the electron and hole densities are given by summing over the change in density matrix element of the four eigenstates,^[25]

$$\Delta n_e(t) = \tau_L d \sum_{i=1}^4 [\rho_{ii}(t) - \rho_{ii}^s] \quad (4.16)$$

$$\Delta n_h(t) = -\tau_L \sum_{i=1}^4 r_i [\rho_{ii}(t) - \rho_{ii}^s]$$

where τ_L is the charge carrier lifetime. Combining Eq. 4.15 and Eq. 4.16 the change in conductivity following a resonant microwave pulse can be written as follows.^[25]

$$\Delta\sigma(t) = e\tau_L d\mu_e \sum_{i=1}^4 [\rho_{ii}(t) - \rho_{ii}^s] \left(1 - \frac{r_i \mu_h}{d \mu_e}\right) \quad (4.17)$$

Since $r_T \ll r_S$ the steady state populations of the four intermediate pair eigenstates are not equal. The two pure triplet states will be dominantly populated and states 2 and 3 which have singlet character, $\rho_{11,44}^s \gg \rho_{22,33}^s$. The effect of resonant microwaves is therefore to shift the population from $\rho_{11,44}$ to $\rho_{22,33}$.

4.4.3 cwEDMR

In a continuous wave (cwEDMR) experiment the microwaves are continuously applied and the populations of four eigenstates will reach a new equilibrium when spins in the pair are on-resonance with the microwaves. This on-resonance equilibrium will have excess population in states 2 and 3 compared to the off-resonance equilibrium. The difference between the two will depend on the microwave power used (strength of B_1 field). This change in population at resonance will alter the recombination rate and current at resonance which can be detected. In practise the cwEDMR spectra were obtained in a

similar manner to cwEPR spectra. The resonator was critically coupled and the change in current recorded as a function of the magnetic field. The microwave power and field modulation amplitude were chosen so that power and modulation broadening effects were avoided (unless otherwise stated).

4.4.4 pEDMR

pEDMR Transient

In a pulsed (pEDMR) experiment a short high power microwave pulse is used to coherently manipulate the spins in the intermediate pairs. The spins in the intermediate pairs will precess under the B_1 field of the microwave pulse which alters the spin permutation symmetry of the pair over time. Looking at Eq. 4.17; after the pulse has ended ($t = 0$) the four density matrix elements will no longer be equal to their steady state values ($\rho_{ii}(0) \neq \rho_{ii}^s$). As a result the recombination rate and sample current will also be perturbed from their steady state values ($\sigma(0) \neq \sigma^s$). Due to the different recombination rates of spin pairs in the four eigenstates, the populations of the four density matrix elements will slowly relax back to their steady state values over a microsecond timescale. During this population relaxation the current will also relax back towards the steady state in accordance with Eq. 4.17. This current relaxation after the microwave pulse can be detected and is known as pEDMR transient. An example of a pEDMR transient is shown in Figure 4.18. The current relaxation after the microwave pulse is recorded at each field position. These transient slices are then combined to build up the two dimensional pEDMR transient shown by the colour plot, where blue is the steady state current. The EDMR lineshape can be visualised in two ways. By observing a cross section of the pEDMR transient at constant time, the evolution of the EDMR lineshape following the microwave pulse can be obtained. Alternatively the integral of the pEDMR transient can be calculated to give the overall time integrated EDMR lineshape which is shown in the top of Figure 4.18.

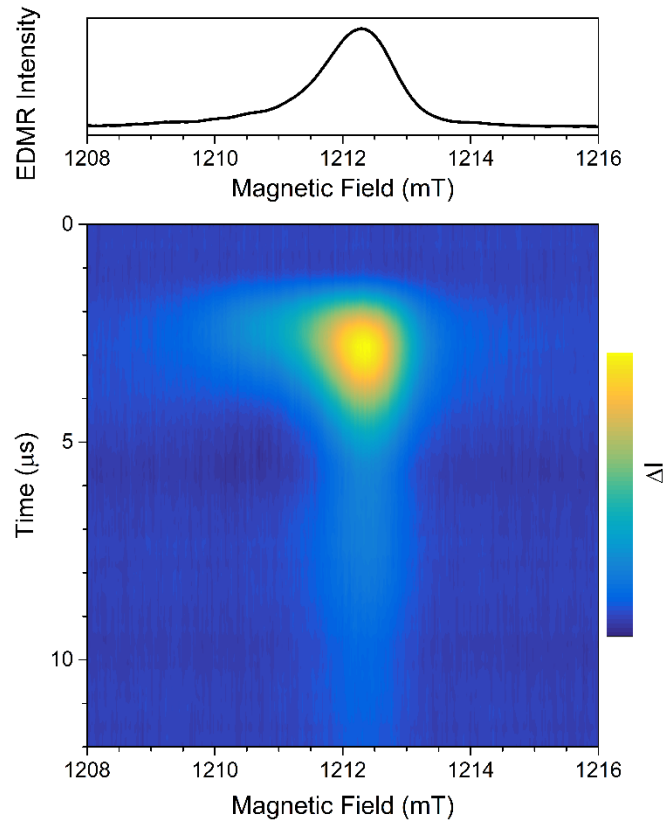


Figure 4.18 Example of a pEDMR transient and integrated spectrum.

pEDMR Rabi Oscillation

Important information on the nature of the spin can be revealed by observing the coherent motion of the spins during the microwave pulse. This spin motion occurs on timescale of nanoseconds which is too fast to monitor directly. However it has been shown that the integrated charge, Q , of the pEDMR transient is proportional to the population of the spin states the moment that microwave pulse ends, $\rho(0)$.^[25] This effectively makes Q a measure of the spin permutation symmetry of the spin pairs at the end of the microwave pulse. The coherent motion of the spins during the pulse can therefore be elucidated by monitoring the variation of Q as a function of microwave pulse length which is known as a spin-Rabi oscillation experiment.

The concept of a spin-Rabi measurement is shown in Figure 4.19. The microwave pulse length is incremented over a 2 to 1000 ns range. The current transient after each microwave pulse is integrated over a chosen time domain. The choice of time domain is not crucial as long as there is only a single spin-dependent process, and the portion with

the best signal to noise is therefore used. A plot of Q against the pulse length reveals the spin-Rabi oscillation of the spins in the pair.

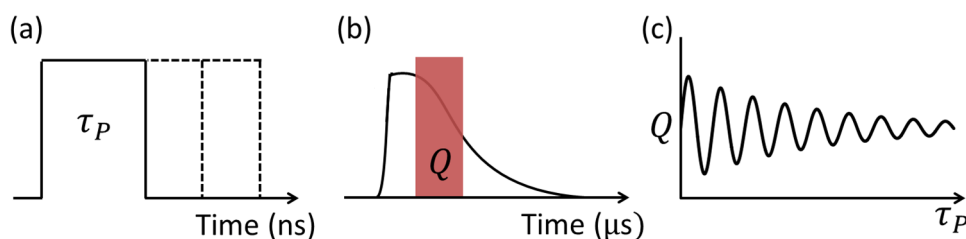


Figure 4.19 Rabi oscillation experiment. (a) The microwave pulse length is incremented. (b) A section of the pEDMR current transient is integrated. (c) The oscillation of the integrated charge reveals the coherent motion of the spin pairs during the microwave pulse; a spin-Rabi oscillation. Adapted from Schnegg et al.^[30]

4.4.5 EDMR Substrate Fabrication

Substrates for EDMR measurements require a non-conventional geometry which had to be fabricated. The substrates have to be suitably narrow to fit inside the X-band and Q-band EPR tubes which have internal diameters of 3.2 and 2.4 mm respectively. Secondly they have to be sufficiently long, such that the connections and wires to the external circuit can be made outside of the microwave resonator to avoid perturbation of the microwave modes and loss of Q factor.

X-Band EDMR substrates were fabricated by first patterning the ITO electrode through photolithography and wet etching. A 50 x 50 mm square of ITO coated soda-lime glass (Xinyan Technology Ltd) was rinsed with IPA and dried with nitrogen. The substrate was preheated at 120 °C to remove any residual water and Microposit S1813 G2 photoresist (Rohm & Haas) was spin-coated at 4000 rpm for 30 s. The substrate was soft baked at 120°C for 30 s. The photoresist was then exposed to UV light for 4 s through a photomask using a mask aligner. The exposed substrate was immersed in diluted Microposit Developer 351 (Rohm & Haas); four parts DI water and one part developer. It was then dried with nitrogen and baked at 120°C for 10 minutes. The exposed resist was removed by rinsing the substrate in acetone, leaving the desired electrode pattern. To etch the ITO surface, the substrate was immersed in hydrochloric acid (37 %) for around 15 minutes and successful ITO removal checked using a multimeter. The large substrate was then diced into multiple 50 mm x 2.8 mm substrates using a computer controlled dicing saw

(MicroAce 66, Loadpoint Ltd). During cutting the substrate was held in place using low adhesive dicing tape and a vacuum chuck.

Q-Band substrates were prepared in a similar manner to that described above with the exception that the ITO coated soda-lime glass was replaced by ITO coated fused quartz (UQG Optics Ltd). This change was necessary as we found that the use of soda-lime glass substrates severely diminished the Q factor of the resonator at Q-Band and prohibited critical coupling. The Q-Band substrates were also diced narrower, 50 mm x 2.1 mm, to accommodate the smaller bore size of the Q-Band resonator.

4.4.6 EDMR Cell Fabrication

The EDMR substrates were cleaned using the methods described in Section 4.1.1 and the geometry is shown in Figure 4.20a. The substrate was attached to a 10 mm x 10 mm square of glass using double sided tape for ease of spin coating and the desired layers spin coated to yield Figure 4.20b. The substrates were then transferred to a thermal evaporator and the metal top contact deposited as shown in Figure 4.20c. The overlap of the ITO and metal contact defines the active area of the cell, which was 1.5 mm x 5 mm. The quality of spin coated films on such narrow substrates tends to be poor, due to the close proximity of the substrate edges. By defining a small active area in the centre of the substrate the most uniform section of the film was used. It can be seen from Figure 4.20c that metal was also deposited on top of the ITO electrode. The purpose of this was to lower the series resistance of the cell as the long and narrow ITO electrode would have a resistance

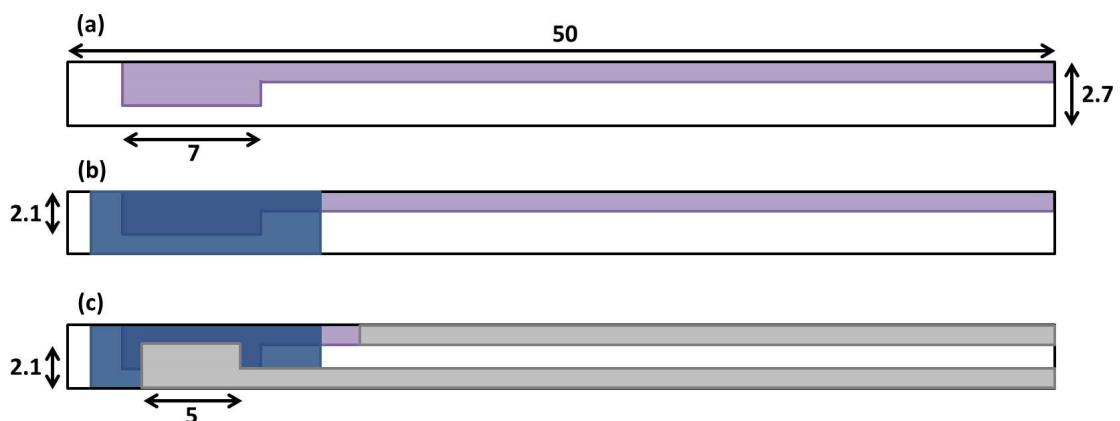


Figure 4.20: Fabrication of EDMR OPV Cells. The ITO electrode is shown in purple, the active layer in blue and the metallic top contact in grey. Dimensions are for X-Band. Q-Band substrates were of a similar design but had a smaller width.

of $\sim 800 \Omega$ which would limit the fill factor of the cell. The metal contact thickness was kept at 100 nm or below, which is lower than the microwave skin depth at the microwave frequencies used and therefore limits the perturbation of the microwave modes.

Organic semiconductors are susceptible to degradation through reactions with oxygen and moisture and the cells must therefore be encapsulated. The EDMR cells were encapsulated inside the glovebox by attaching a 10 mm x 2.5 mm piece of microscope coverslip over the active area using a UV curing epoxy (Norland 68). To connect the cells to the external circuit, they were removed from the glovebox and first attached to a small piece of double sided copper coated board as shown in Figure 4.21. A file was used to remove the copper and create a recess at one end of the board and the substrate was bonded into this recess using cyanoacrylate glue. The anode and cathode were connected to opposite faces of the circuit board using silver paint (RS Components Ltd.). The circuit board was then soldered to a miniature shielded two core cable (Industrifil).

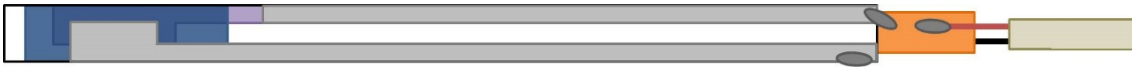


Figure 4.21: Connection of EDMR cells to the external circuit.

4.4.7 EDMR Cell Testing

After fabrication the J-V characteristics of every fabricated cell was measured in the dark and under the solar simulator using the method outlined in Section 4.2.2. The only notable difference is that due to unique geometry of the EDMR substrate a shadow mask was not used during the measurements; however this is not critical as the J-V characteristics were used for routine screening as opposed to accurate determination of cell efficiencies.

4.4.8 EDMR Setup

EDMR measurements were carried out on three spectrometers which are detailed in Table 4.2.

Table 4.2 Spectrometers and resonators used for EDMR spectroscopy.

Spectrometer	Frequency	Resonator	Mode
Bruker EMX	9.8 GHz	Cavity resonator (ER 4123SHQE)	CW
Bruker Eleksys E580	9.8 GHz	Dielectric ring resonator (EN 4118X-MD4)	CW & Pulsed
Bruker Eleksys E580	34 GHz	Dielectric ring resonator (ER5106QT-2W)	CW & Pulsed
HIPER ^[9]	94 GHz	N/A	Pulsed

To record the change in current at resonance the current detection hardware needs to be interfaced into the spectrometer. To achieve this the miniature shield two core cable attached to the EDMR cell was soldered into a junction box which connected each core wire to the inner core of a BNC cable and the braided shield was connected to the outer (ground) of the BNC cables. The two BNC cables were then attached to the dual inputs of a custom current to voltage converter (Elektronik-Manufaktur Mahlsdorf). This current to voltage converter was designed by the Lips group for EDMR spectroscopy,^[31, 32] and has a balanced input design that removes common mode noise and therefore suppresses electrical noise picked up from the external environment. The first stage of the converter is a transimpedance amplifier which converts the change in current to a change in voltage. This is followed by a low pass filter which separates the DC component, an adjustable band pass filter which provides noise suppression and ends with by a final gain stage to adjust the signal to the desired level for the spectrometer input. For CW measurements lock in detection was used and the output of the amplifier was therefore fed into the external input of the lock in amplifier of the EMX or E580. For pulsed measurements the output was connected to the transient recorder (digital oscilloscope) of the E580 or the ADC card of HIPER.

For mounting inside the spectrometer the EDMR cells were secured inside a borosilicate glass NMR tube for 9.8 GHz measurements and a quartz EPR tube for 34 GHz measurements. The use of glass NMR tubes was simply a matter of economics as they are a factor of ten cheaper than quartz tubes and do not influence the performance at 9.8 GHz. At 34 GHz the glass tubes are too lossy and prevented critical coupling of the resonator, and quartz tubes were therefore used instead. The samples were then positioned inside the resonator so that the centre of cell was located at the resonator centre. For 94 GHz measurements the cell was placed in a custom sample holder.

For 'light-on' measurements at 9.8 GHz the photocurrent was generated using a white light LED mounted on a heatsink and positioned just outside the resonator. For 34 GHz measurements the white light LED was used initially but due to the very small optical access of the ER5106QT-2W resonator, little light entered the resonator and the photocurrent was therefore small and signal to noise during measurements was poor. The illumination source was therefore changed to a diode laser mounted on an optical bread board with two steering mirrors and a focusing lens. The beam was then steered until the photocurrent reached a maximum. Different wavelengths of light were tested and laser versus white light illumination cross checked at 9.8 GHz but no difference in EDMR response was found and the different illumination sources are therefore justified. For 94 GHz the white light LED was mounted inside the custom holder. For dark measurements the carriers were injected into the cell using the inbuilt voltage source of the custom current-voltage converter which had a range of -5 V to +5 V.

The EDMR measurement setup is shown in Figure 4.22. In a typical cwEDMR measurement the cell would first be loaded into the resonator and rotated to minimise the induction current from the field modulation coils. At certain angles the cell acts as an antenna and picks up a large oscillation current at the modulation frequency. This current is benign except that it is orders of magnitude larger than the spin dependent current change we are trying to detect and can cause the amplifier to clip or overload the input to the spectrometer. The cell was therefore rotated inside the resonator, while monitoring an oscilloscope connected to the AC output of the amplifier, until the pickup is minimised. The illumination intensity or drive voltage is then adjusted to give the desired DC current

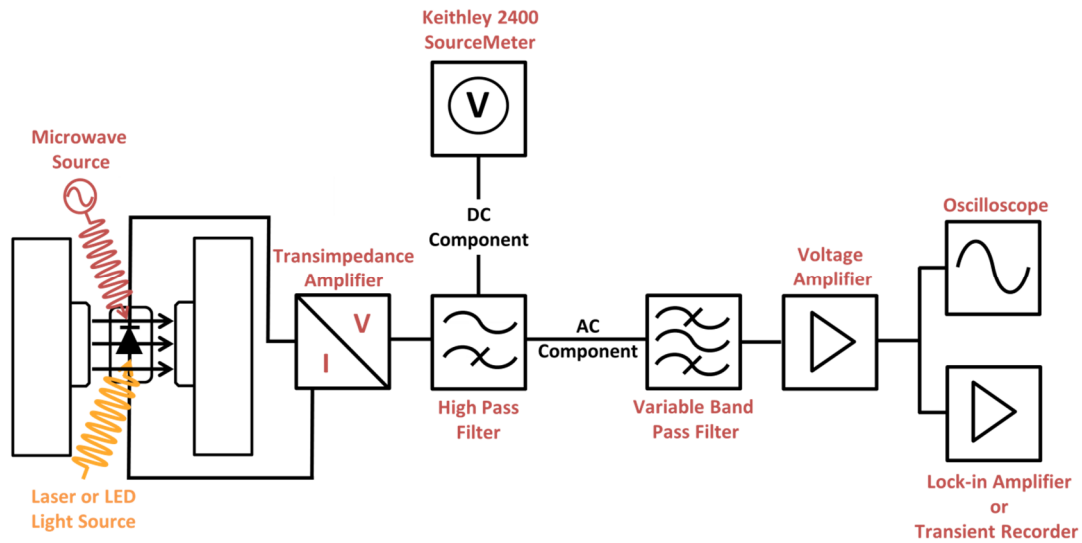


Figure 4.22 EDMR measurement setup.

which was monitored using a Keithley 2400 SourceMeter connected to the DC output (split off using the high pass filter) of the transimpedance amplifier. Using the conversion factor of the amplifier the DC current through the cell can therefore be monitored. To account for differences in impedance in the two inputs to the amplifier, the amplifier can be ‘balanced’ using a dial to control the relative weight of each input. This dial was adjusted while monitoring the AC output of the amplifier on the oscilloscope until the noise was at a minimum. An appropriate amplifier gain was then chosen so that that the signal was not overloading the input to the lock-amplifier. A similar procedure was used for pEDMR measurements except that the noise was minimised while monitoring the pEDMR trace on the transient recorder of the E580 and the gain chosen to avoid clipping in the transient recorder.

4.5 Time of Flight

4.5.1 Principle of ToF

Time of Flight (ToF) is a method to measure the mobility of electrons and holes travelling in a semiconductor. In ToF the semiconductor of interest is sandwiched between two electrodes and the time taken for photogenerated carriers to cross the semiconductor layer is measured. A typical ToF setup is shown in Figure 4.23, where the configuration shown is for the measurement of electron mobility. A short laser pulse is used to generate a sheet of electrons and holes near the ITO electrode. The applied bias creates an electric field within the semiconductor which causes the electrons and holes to drift in opposite directions. The ITO electrode is biased negatively and the Ca/Al positively and the holes are therefore quickly collected by the ITO electrode while the electrons drift across the semiconductor layer and are collected at the Ca/Al electrode. The time taken for the electrons to cross the sample, known as the transit time, t_{tr} , is determined by monitoring the transient photocurrent on an oscilloscope. For hole mobility measurements the situation is identical except that the charges are photogenerated by the laser through the Ca/Al electrode.

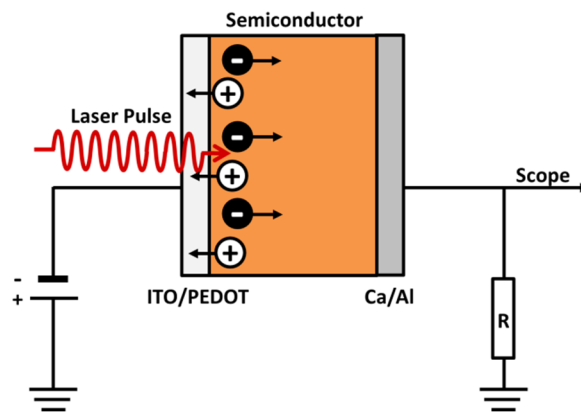


Figure 4.23 Schematic of the ToF method. In the orientation shown the electron mobility is measured. Adapted from Köhler & Bäessler.^[33]

While in principle a very simple technique, several conditions have to be satisfied for a successful ToF measurement:^[33, 34]

1. The RC time constant of the detection circuit must be significantly smaller than the transit time, $RC \ll t_{tr}$, otherwise the measured transit time is artificially increased.

2. The photogenerated charge carrier sheet must be spatially confined. The sample thickness d therefore must be much greater than the absorption depth of the laser pulse into the film. This can be quantified as $d \gg \ln(10)/\alpha$, where α is the absorption coefficient of the semiconductor. 90 % of the laser light will be absorbed within $\ln(10)/\alpha$, which is typically around several hundred nanometres in most organic semiconductors. The film thickness therefore needs to be a micron at minimum and the laser wavelength should coincide with the maximum of α . Failure to satisfy this condition will result in carrier generation throughout the film resulting in a broad distribution of arrival times and over estimation of the mobility.
3. Charge carrier injection must be avoided. Injected carriers of the opposite sign to those being measured will result in recombination of carriers while drifting across the film which will prevent determination of the transit time. To avoid injection ToF is always performed in a reverse bias configuration. The ITO/PEDOT electrode, which typically forms an Ohmic contact to the HOMO and a Schottky to the LUMO, is biased negatively which prevents electron injection into the LUMO. The analogous situation occurs at the Ca/Al electrode for preventing hole injection. More generally the transit time must be shorter than the time it takes for the measured carrier to relax to the ground state, $t_{tr} < t_{\sigma} = \epsilon_0 \epsilon_r / \sigma$, where σ is the conductivity and t_{σ} is the dielectric relaxation time of the semiconductor.
4. The concentration of photogenerated charge carriers is kept low enough to prevent distortion of the electric field. A general guideline to satisfy this requirement is that the number of photogenerated carriers is around 5-10 % of the capacitor charge, $Q_{photo} \ll CV$, where C is the cell capacitance and V is the applied voltage. Failure to satisfy this requirement may result in screening of the electric field by the carriers.

The shape of an idealised photocurrent transient during a ToF measurement is shown in Figure 4.24. Following photoexcitation through the ITO a sheet of electrons and holes are generated in the cell near the ITO electrode, which begin to drift under the applied field. This causes an initial spike in the photocurrent that rapidly decays. The reason for this rapid decay is twofold. Initially both electrons and holes are contributing to the photocurrent but the holes are quickly removed from the system through the ITO electrode causing a corresponding decrease in photocurrent. In addition the charge carriers are initially generated high in their density of states and

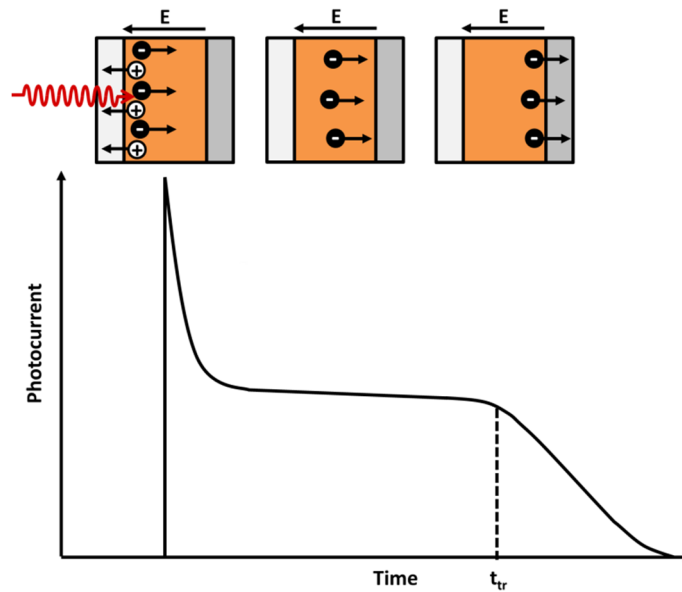


Figure 4.24 Origin of the ToF photocurrent transient and transit time.

therefore can more easily hop and have a high initial mobility. The carriers rapidly thermalise towards the equilibrium tail of the density of states which lowers the mobility and the photocurrent. Once in equilibrium the electrons drift across the sample with constant velocity giving rise to a plateau region in the photocurrent. As the electrons begin to reach the Ca/Al electrode the photocurrent decreases. As there is a distribution of electron energies and mobilities, the electrons do not arrive simultaneously and the photocurrent therefore has a finite decay time which is known as the tail. The knee between the plateau and tail regions defines the transit time of the electrons and from this time their mobility can be calculated using the following relation,

$$\mu = \frac{d^2}{Vt_{tr}} \quad (4.18)$$

where V is the applied voltage and d is the sample thickness.

The photocurrent transient shown in Figure 4.24 occurs if the transport is non-dispersive which means that the carriers traverse the film without spreading out. Unfortunately many organic semiconductors exhibit dispersive transport where the charge carrier packet spreads out as it crosses the film. Dispersive transport arises due to the nature of hopping transport through disordered media (see GDM in Section 2.2.5). There is a distribution of hopping site energies and the time a carrier spends on a site before hopping to the next is dependent on the energy difference between that site and its neighbours. As the carriers

hop through this energetic landscape some carriers will be energetically fortunate and traverse it quickly while others will become temporarily trapped. The current will therefore decrease as the carriers cross the film and there will be a large distribution in arrival times. An example of a dispersive transient is shown in Figure 4.25a where it can be seen there is no distinction between the plateau and tail regions which makes determining the transit time difficult.

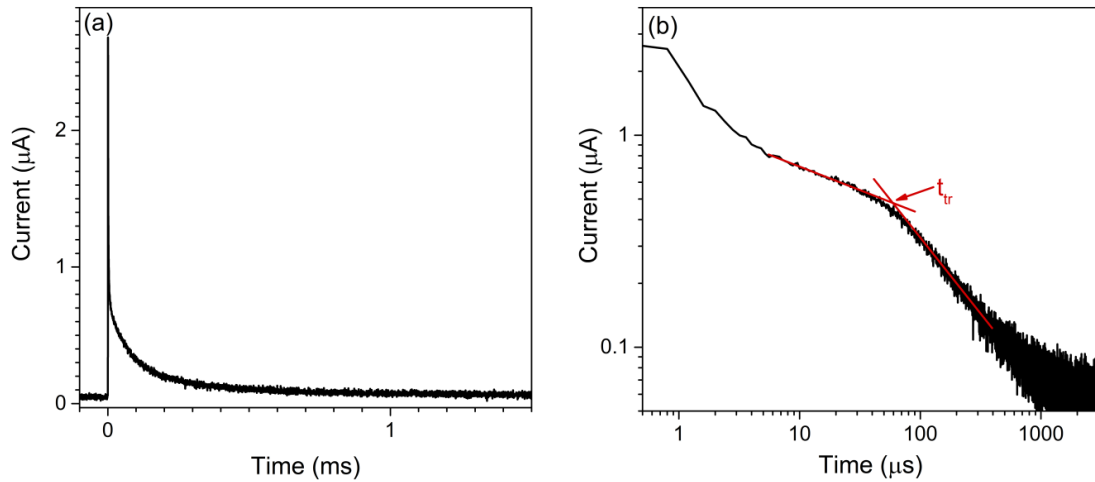


Figure 4.25 Example of a dispersive ToF photocurrent transient in (a) linear scale and (b) double logarithmic scale.

Dispersive ToF transients are therefore commonly analysed in accordance with Scher-Montroll formalism which describes the transient using a power law that changes exponent once carriers start to be arrive at the electrode,^[35]

$$\begin{aligned} I_{Photo}(t) &\sim t^{-(1-\alpha)}, & t < t_{tr} \\ I_{Photo}(t) &\sim t^{-(1+\alpha)}, & t > t_{tr} \end{aligned} \quad (4.19)$$

where α is a parameter that describes the dispersity of the transient. By plotting the transient on a double logarithmic plot the change in exponent transforms into a change in gradient and the knee of this gradient change is the transit time. The transit time can therefore be accurately determined by the intersection of two linear fits as shown in Figure 4.25b.

4.5.2 ToF Cell Fabrication

ToF requires organic layer thicknesses of several microns (see point 2 in the previous section). It is difficult to deposit films thicker than several hundred nanometres using spin coating and the organic layers were therefore deposited using drop casting. A flat surface

is crucial to achieve uniform drop cast films and the substrates were therefore placed on a custom metal platform with three adjustable legs. The height of legs was adjusted until the platform was level which was monitored by a bull's eye spirit level mounted on the platform. The substrate was then covered in a layer of solution and left to dry. Film quality is generally improved by allowing the solvent to slowly evaporate. Higher boiling point solvents such as dichlorobenzene, trichlorobenzene and tetrachloroethane are therefore favourable. The evaporation rate can be further controlled by covering the drying substrates with a watch glass.

After organic layer deposition the top electrode is deposited. This is undertaken in a similar manner to standard solar cells (Section 4.1.3) except that the cathode needs to be kept thin for hole mobility measurements as the electrode needs to be optically transparent to the laser pulse. A standard choice of cathode is Ca/Al and a good compromise between optical transparency and electrical stability is achieved using 10 nm of calcium followed by 20 nm of aluminium.

A final note is that the cell is left unencapsulated. Knowing the thickness of the organic layer accurately is crucial for an accurate determination of the mobility (Eq. 4.18). A reference cell cannot be used as the drop casting method produces films with large variations in thickness. The cell is therefore left unencapsulated so that the thickness of each pixel can be accurately measured after the measurement.

4.5.3 ToF Measurement

The cell is placed inside a cryostat (Oxford Instruments Optistat) and pumped down to 1×10^{-4} mbar to prevent degradation during the measurement. The cell is connected to the external circuit shown in Figure 4.26. The cell was biased using a low noise high voltage power supply (Farnell Instruments E350) which has a maximum output voltage of 350 V. The relative polarity of the cell and power supply was always chosen so that the cell was in reverse bias (positive voltage applied to the cathode) to prevent injection of charge carriers into the semiconductor. The top switch decouples the cell from the voltage source and grounds it to dissipate any charge build up. The lower switch switches between two detection loops with different methods of current to voltage conversion. In

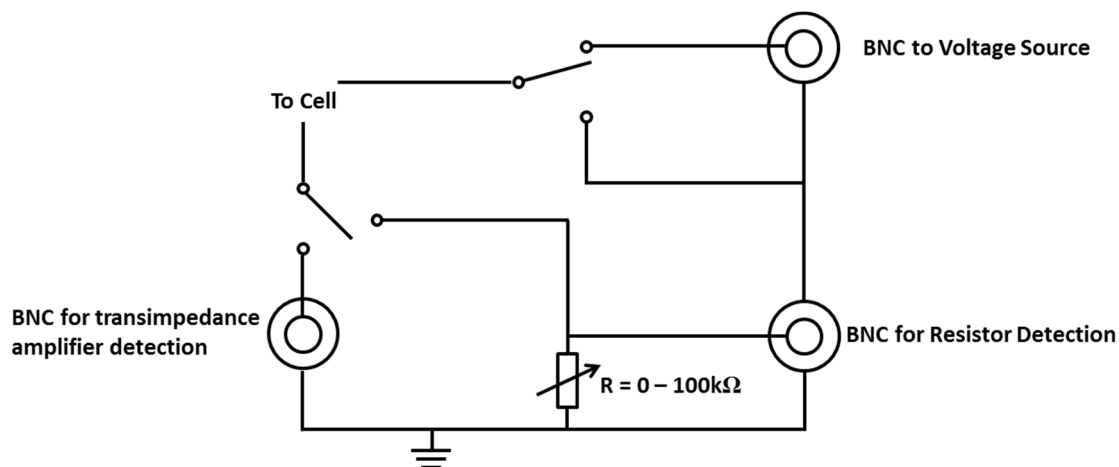


Figure 4.26 Time of flight detection circuit.

the loop on the right the current transient from the cell flows through a variable resistor and then to ground. An oscilloscope is connected across this resistor to measure the change in voltage with time. The loop on the left has no resistor and is for use with a transimpedance amplifier which converts the small change in current into a large voltage change that is then monitored on the oscilloscope. The transimpedance amplifier was used for nearly all measurements as it offers far superior signal to noise than the resistor. The resistor was mainly used to calibrate the magnitude of the photocurrent transient.

In order to minimise the absorption depth of the laser pulse it is important that the pump wavelength is as close as possible to the absorption maximum of material under study. Dye lasers are a simple method that enable access to a wide range of wavelengths. A basic dye laser was therefore constructed and is shown schematically in Figure 4.27. The pump laser is the 2nd harmonic of an Nd:YAG (Surelite Continuum). A cylindrical lens is used to form the beam into a narrow strip that is approximately the same width as the dye cuvette when it reaches it. The laser dye chosen was Pyridine 1 (Sirah) which absorbs strongly at 532 nm and emits in the 670 nm to 720 nm range. The Pyridine 1 was dissolved in DMSO at a concentration of 0.9 mg cm⁻³. At this concentration the pump laser is absorbed within several millimetres. The pump laser excites a strip of Pyridine 1 close to the front wall of the cuvette which fluoresces and the side walls of the cuvette act as an optical cavity, creating a laser. As laser light is out-coupled from both sides of the

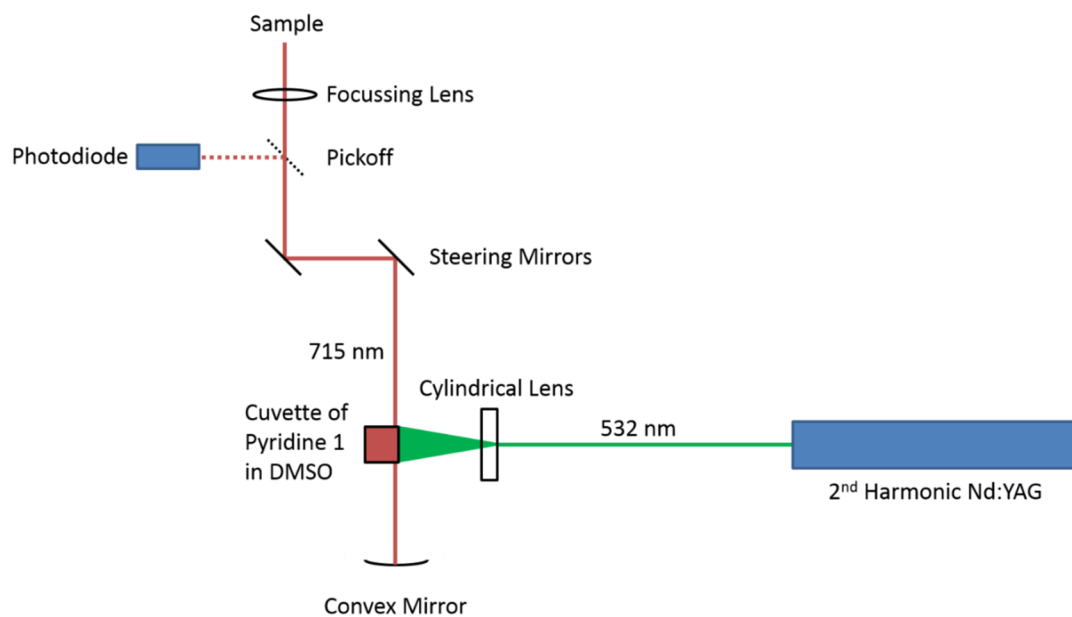


Figure 4.27 Nd:YAG pumped dye laser for TOF excitation.

the cuvette, a convex mirror was placed at one side to direct light out coupled to the ‘wrong’ side back through the dye cuvette. The beam then passes through a pickoff mirror which is used to trigger the oscilloscope and finally focused onto a specific pixel of the cell under study. The wavelength and FWHM of the dye laser was characterised using a spectrometer (OceanOptics) as shown in Figure 4.28. The peak wavelength is 714 nm and the FWHM is 11 nm.

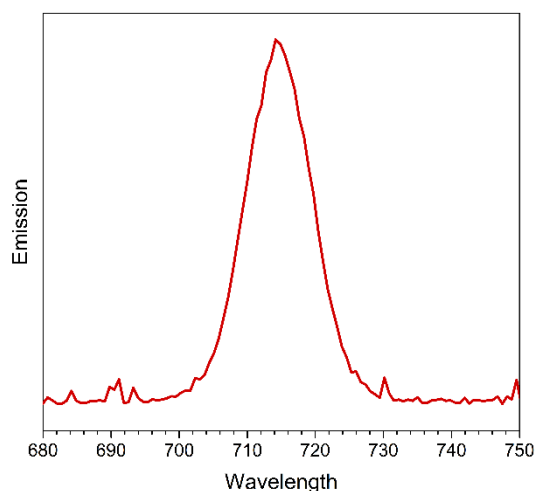


Figure 4.28 Lasing output of Pyridine 1 dye laser pumped using pulsed 532 nm.

4.5.4 Thickness Measurement

The thickness of each pixel was measured using a surface profiler (Veeco Dektak 150). Three scratches were made across each pixel and the difference in height between the scratch and the film measured at nine points on each pixel and the mean value calculated.

4.6 References

1. ASTM G173-03(2012), Standard Tables for Reference Solar Spectral Irradiances: Direct Normal and Hemispherical on 37° Tilted Surface, ASTM International, West Conshohocken, PA, 2012, www.astm.org.
2. <http://rredc.nrel.gov/solar/spectra/am1.5>, Accessed 16/02/17.
3. A. K. K. Kyaw, D. H. Wang, V. Gupta, W. L. Leong, L. Ke, G. C. Bazan and A. J. Heeger, Intensity Dependence of Current-Voltage Characteristics and Recombination in High-Efficiency Solution-Processed Small-Molecule Solar Cells. *ACS Nano* **7** (5), 4569-4577 (2013).
4. B. Ebenhoch, S. A. J. Thomson, K. Genevicius, G. Juska and I. D. W. Samuel, Charge carrier mobility of the organic photovoltaic materials PTB7 and PC71BM and its influence on device performance. *Org. Electron.* **22**, 62-68 (2015).
5. I. Riedel, J. Parisi, V. Dyakonov, L. Lutsen, D. Vanderzande and J. C. Hummelen, Effect of temperature and illumination on the electrical characteristics of polymer-fullerene bulk-heterojunction solar cells. *Adv. Funct. Mater.* **14** (1), 38-44 (2004).
6. S. R. Cowan, A. Roy and A. J. Heeger, Recombination in polymer-fullerene bulk heterojunction solar cells. *Physical Review B* **82** (24), 10 (2010).
7. W. Tress, *Organic Solar Cells: Theory, Experiment, and Device Simulation*. (Springer International Publishing, 2014).
8. L. J. A. Koster, V. D. Mihailetschi, R. Ramaker and P. W. M. Blom, Light intensity dependence of open-circuit voltage of polymer : fullerene solar cells. *Appl. Phys. Lett.* **86** (12), 3 (2005).
9. P. A. S. Cruickshank, D. R. Bolton, D. A. Robertson, R. I. Hunter, R. J. Wyld and G. M. Smith, A kilowatt pulsed 94 GHz electron paramagnetic resonance spectrometer with high concentration sensitivity, high instantaneous bandwidth, and low dead time. *Rev. Sci. Instrum.* **80** (10), 15 (2009).
10. A. Y. Bresgunov, A. A. Dubinskii, V. N. Krimov, Y. G. Petrov, O. G. Poluektov and Y. S. Lebedev, Pulsed EPR in 2-mm Band. *Appl. Magn. Reson.* **2** (4), 715-728 (1991).
11. O. G. Poluektov, L. M. Utschig, S. L. Schlesselman, K. V. Lakshmi, G. W. Brudvig, G. Kothe and M. C. Thurnauer, Electronic Structure of the P-700 Special Pair From

- High-frequency Electron Paramagnetic Resonance Spectroscopy. *J. Phys. Chem. B* **106** (35), 8911-8916 (2002).
12. J. A. Weil and J. R. Bolton, *Electron Paramagnetic Resonance Elementary Theory & Practical Applications*, 2nd ed. (John Wiley & Sons, Hoboken, NJ, USA, 2007).
 13. R. T. Weber, *ELEXSYS E580 User's Manual*. (Bruker BioSpin Corporation 2005).
 14. E. R. Davies, A New Pulse Endor Technique. *Phys. Lett. A* **47** (1) (1974).
 15. W. B. Mims, Pulsed Endor Experiments. *Proc. R. Soc. London, Ser. A* **283** (1395), 452-& (1965).
 16. C. Gemperle and A. Schweiger, Pulsed Electron Nuclear Double-resonance Methodology. *Chem. Rev.* **91** (7), 1481-1505 (1991).
 17. M. D. E. Forbes, J. Peterson and C. S. Breivogel, Simple Modification of Varian E-Line Microwave Bridges for Fast Time-Resolved EPR Spectroscopy. *Rev. Sci. Instrum.* **62** (11), 2662-2665 (1991).
 18. T. A. Murphy, T. Pawlik, A. Weidinger, M. Hohne, R. Alcala and J. M. Spaeth, Observation of atomlike nitrogen in nitrogen-implanted solid C-60. *Phys. Rev. Lett.* **77** (6), 1075-1078 (1996).
 19. A. Popov, *Endohedral Fullerenes: Electron Transfer and Spin*. (Springer International Publishing, 2017).
 20. M. Eckardt, R. Wieczorek and W. Harneit, Stability of C-60 and N@C-60 under thermal and optical exposure. *Carbon* **95**, 601-607 (2015).
 21. B. Pietzak, M. Waiblinger, T. A. Murphy, A. Weidinger, M. Hohne, E. Dietel and A. Hirsch, presented at the Symposium A on Fullerenes and Carbon Based Materials, at the European-Materials-Research-Society 1997 Meeting, Strasbourg, France, 1997 (unpublished).
 22. F. Kraffert, R. Steyrlleuthner, C. Meier, R. Bittl and J. Behrends, Transient electrically detected magnetic resonance spectroscopy applied to organic solar cells. *Appl. Phys. Lett.* **107** (4), 5 (2015).
 23. C. J. Cochrane and P. M. Lenahan, Spin counting in electrically detected magnetic resonance via low-field defect state mixing. *Appl. Phys. Lett.* **104** (9), 5 (2014).
 24. D. R. McCamey, H. Huebl, M. S. Brandt, W. D. Hutchison, J. C. McCallum, R. G. Clark and a. R. Hamilton, Electrically detected magnetic resonance in ion-implanted Si : P nanostructures. *Appl. Phys. Lett.* **89** (18), --- (2006).
 25. C. Boehme and K. Lips, The Investigation of Charge Carrier Recombination and Hopping Transport with Pulsed Electrically Detected Magnetic Resonance Techniques. In: *Charge Transport in Disordered Solids with Applications in Electronics*. (Wiley, Chichester, England, 2006).

26. R. Maxwell and A. Honig, Neutral Impurity Scattering Experiments in Silicon With Highly Spin Polarized Electrons. *Phys. Rev. Lett.* **17** (4), 188-& (1966).
27. D. J. Lepine, Spin Dependent Recombination on Silicon Surface. *Physical Review B* **6** (2), 436-& (1972).
28. C. Boehme and K. Lips, Theory of time-domain measurement of spin-dependent recombination with pulsed electrically detected magnetic resonance. *Physical Review B* **68** (24), 19 (2003).
29. D. Kaplan, I. Solomon and N. F. Mott, Explanation of the large spin-dependent recombination effect in semiconductors. *J. Physique Lett.* **39**, 51-54 (1978).
30. A. Schnegg, J. Behrends, M. Fehr and K. Lips, Pulsed electrically detected magnetic resonance for thin film silicon and organic solar cells. *Phys. Chem. Chem. Phys.* **14** (42), 14418-14438 (2012).
31. J. Behrends, Spin-dependent Transport and Recombination in Solar Cells studied by Pulsed Electrically Detected Magnetic Resonance. *Thesis* (2009).
32. J. Behrends, A. Schnegg, M. Fehr, A. Lambertz, S. Haas, F. Finger, B. Rech and K. Lips, Electrical detection of electron spin resonance in microcrystalline silicon pin solar cells. *Philos. Mag.* **89** (28-30), 2655-2676 (2009).
33. A. Köhler and H. Bässler, *Electronic Processes in Organic Semiconductors: An Introduction*. (Wiley-VCH, Weinheim, Germany, 2015).
34. A. Kokil, K. Yang and J. Kumar, Techniques for characterization of charge carrier mobility in organic semiconductors. *J. Polym. Sci. Pt. B-Polym. Phys.* **50** (15), 1130-1144 (2012).
35. H. Scher, M. F. Shlesinger and J. T. Bendler, Time-Scale Invariance in Transport and Relaxation. *Phys. Today* **44** (1), 26-34 (1991).

5 Air Exposure Induced Recombination in PTB7:PC₇₁BM Solar Cells as Studied by Electrically Detected Magnetic Resonance

5.1 Introduction

In this chapter a study of trap assisted recombination pathways in PTB7:PC₇₁BM cells processed under ambient atmosphere is presented. Current voltage characterisation was combined with continuous wave and pulsed electrically detected magnetic resonance to spectroscopically identify recombination sites that form in the blend during ambient processing. The work presented here forms the basis of the paper Air Exposure Induced Recombination in PTB7:PC₇₁BM Solar Cells.^[1]

The efficiency of PTB7:PC₇₁BM cells containing the solvent additive DIO is reduced when processed under ambient atmosphere. Light intensity dependent current-voltage analysis reveals that exposure to ambient atmosphere results in a substantial increase in trap-assisted recombination losses. To identify the source of the recombination, the pristine and air exposed cells were analysed using EDMR spectroscopy. EDMR spectroscopy reveals a pronounced increase in the spin-dependent component of the photocurrent of cells exposed to both ambient atmosphere and DIO. Using pulsed EDMR spin-Rabi oscillation measurements, two weakly coupled spin ½ species are shown to be primarily responsible for the spin-dependent photocurrent. Selective injection of charge carriers shows that the two spin ½ species are electrons and holes undergoing recombination. In order to identify the location of the recombination sites in the blend EDMR spectroscopy of the neat components, PTB7 and PC₇₁BM, was undertaken. Comparison of the blend spectrum to those of the neat components enables the primary spin-dependent transition to be assigned to trapped electrons on the PC₇₁BM recombining with holes on the PTB7.

5.2 Background

As of 2017 OPV cells with efficiencies exceeding 10 % are routinely reported,^[2-8] which is an important step in achieving the 10/10 target for OPV cells, 10 % efficiency and 10 years lifetime, which is seen as a prerequisite for commercialisation While cell

efficiencies have steadily improved many of the high efficiency donor / acceptor systems have been shown to lack intrinsic stability and are also susceptible to extrinsic degradation via reactions with oxygen and moisture.^[9] Fully understanding and solving the various degradation mechanisms is crucial if OPV cells are to reach commercialisation.

The focus of this investigation is on the ambient stability of the blend of the polymeric donor poly([4,8-bis[(2-ethylhexyl) oxy]benzo[1,2-b:4,5-b] dithiophene-2,6-diyl]) (PTB7) with the fullerene derivative phenyl-C₇₁-butric acid methyl-ester (PC₇₁BM) which has achieved PCEs of over 9 %.^[10] Closely related derivatives in the same BDT based polymer family such as PTB7-Th have obtained PCEs of over 10 %.^[11] The PTB7:PC₇₁BM system therefore serves as an archetypal modern and high performance polymer:fullerene blend. The PTB7:PC₇₁BM system has been extensively studied and there have been several previous investigations into its ambient stability. Under illumination in ambient atmosphere PTB7 was shown to undergo photo-oxidation due to singlet oxygen generation mediated through oxygen quenching of PTB7 triplets.^[12] This was explored further using Raman spectroscopy and density functional theory calculations which identified the photo-oxidation reaction to be the formation of hydroxyl groups on the benzodithiophene units of PTB7.^[13] It was also shown that cell efficiency is reduced when stored under ambient atmosphere in the dark.^[14]

Like all OPV blend systems the PCE of PTB7:PC₇₁BM is critically dependent on the nanoscale morphology of the bulk heterojunction that is created during film deposition. To achieve optimum morphology a high boiling point solvent additive diiodooctane (DIO) is routinely employed to optimise the morphology. DIO has been shown to reduce fullerene aggregate size and promote the formation of narrow elongated PTB7 and PC₇₁BM domains which aids charge extraction and improves the PCE by a factor of 2.^[15] Earlier stability studies did not explore the role that the DIO might play in cell stability and focused on the donor and acceptor only. Recently several studies have highlighted the poor cell stability when residual DIO is left in the active layer after cell fabrication.^[16-19] The influence of DIO on the ambient processing capability of PTB7:PC₇₁BM cells has also been explored. The PCE of PTB7:PC₇₁BM cells were observed to decrease substantially when spin-coated under ambient atmosphere rather than the inert atmosphere of a glovebox.^[20, 21] The cause of this performance drop was initially

unknown but it was later shown through XPS and FT-IR spectroscopy that DIO promotes oxidation of the PC₇₁BM.^[22] Ambient processability is an important area of study in the road to commercialisation as one of the key advantages of OPV over other thin film PV technologies is their solution processability, enabling high throughput and low cost roll-to-roll processing.^[23] Such large area processing will occur under ambient atmosphere, rather than the low oxygen and moisture environment of a glovebox used for research cells.^[20] OPV blends must therefore be capable of ambient processing without loss of performance.

While previously reported spectroscopy provides excellent insight into the observed degradation, it does not provide a direct link to changes in cell performance. Conversely electrical studies on working cells are insensitive to the origin of the performance loss. The goal of this research was to bridge this divide by combining photovoltaic characterisation with electrically detected spectroscopy to investigate the source of the performance loss in PTB7:PC₇₁BM solar cells when processed under ambient atmosphere.

5.3 Materials

5.3.1 PTB7

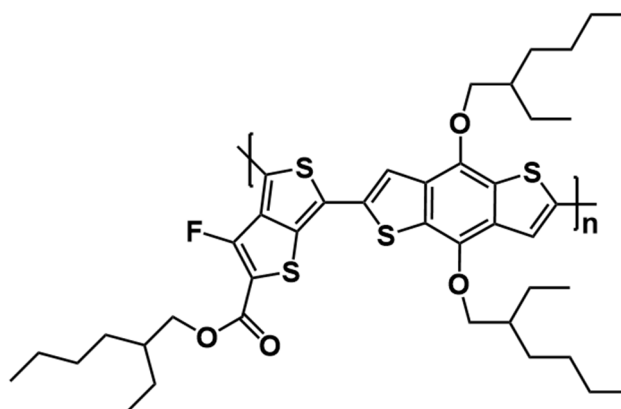


Figure 5.1 PTB7 chemical structure

Poly([4,8-bis[(2-ethylhexyl) oxy]benzo[1,2-b:4,5-b] dithiophene-2,6-diyl]) (PTB7) is a low bandgap polymeric donor. The alternating electron rich (benzodithiophene) and electron deficient (thienothiophene) units lower the band gap, resulting is greater

absorption of the solar spectrum than earlier donor designs. When blended with PC₇₁BM it was the first OPV material system to achieve a PCE of over 7%.^[24] PTB7 was purchased from 1-Material (OS0007) and used without further purification.

5.3.2 PC₇₁BM

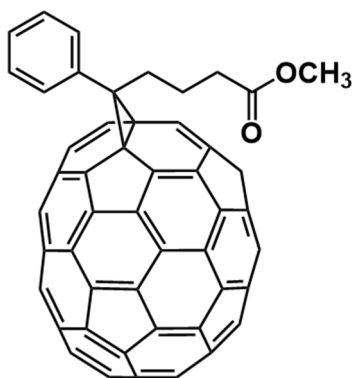


Figure 5.2 PC₇₁BM chemical structure

[6,6]-Phenyl-C₇₁-butyric acid methyl ester (PC₇₁BM) is soluble fullerene derivative widely used as the electron acceptor in high efficiency OPV cells. The asymmetry of PC₇₁BM cage results in enhanced optical absorption compared with PC₆₁BM, enabling greater photon harvesting.^[25, 26] PC₇₁BM was purchased from Solenne (> 99 % purity) and used without further purification.

5.3.3 DIO

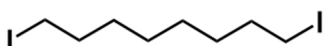


Figure 5.3 DIO chemical structure

1,8-diodooctane is a high boiling point solvent that is used as an additive to improve the morphology of several OPV blend systems. In PTB7:PC₇₁BM the addition of DIO prevents the formation of large fullerene clusters which improves the PCE by a factor of 2.^[15] DIO was purchased from Sigma Aldrich (250295-5G) with a purity of 98 % and containing copper as a stabiliser. It was used without further purification.

5.4 Experimental

5.4.1 Sample Preparation

Substrates for J-V characterisation were prepared as outlined in Section 4.2.1. For EDMR spectroscopy the substrate preparation and cell design described in Section 4.4.1 was used. For ambipolar and hole rich cells a bottom contact of PEDOT:PSS (Heraeus Clevis P VP AI 4083) was spin-coated at 4000 rpm. The substrates were then annealed on a hotplate at 120 °C for 20 min to remove residual water. In electron rich cells a 1 nm layer of LiF was thermally evaporated onto the ITO substrate in place of the PEDOT:PSS. PTB7 and PC₇₁BM were dissolved in anhydrous chlorobenzene in a 1:1.5 weight ratio to give a total concentration of 20 mg cm⁻³ inside a nitrogen filled glovebox and stirred at 50 °C for 6 hours. For cells processed using the solvent additive 1,8-Diiodooctane, 3% by volume of DIO was added to the solution 10 minutes prior to spin-coating.

To fabricate pristine cells the PTB7:PC₇₁BM solution was spin-coated at 1000 rpm inside a nitrogen glovebox and the cells left to dry for 10 minutes. Air exposed cells were spin-coated at 1000 rpm under ambient atmosphere and left to dry for 10 minutes under the ambient atmosphere. Single component cells were fabricated in a similar manner to the above, using concentrations of 20 mg cm⁻³ and 5 mg cm⁻³ for PC₇₁BM and PTB7 in chlorobenzene respectively. The top electrodes were deposited by thermal evaporation. These were 20 nm calcium followed by 80 nm aluminium for ambipolar cells; 1 nm LiF followed by 80 nm aluminium for electron rich cells and 100 nm of gold for hole rich cells. Following contact deposition the cells were encapsulated as described in Section 4.4.5.

5.5 Results

5.5.1 J-V Characterisation

PTB7:PC₇₁BM cells were fabricated under inert atmosphere (pristine) and ambient atmosphere (air exposed), with and without the solvent additive DIO. The J-V characteristics of the cells were measured under AM1.5G illumination and are shown in Figure 5.4. When the cells were processed using DIO the average PCE of the pristine cells was 6.1(3) % while the air exposed cells had an average PCE of 1.7(2) %, which is

a 73 % reduction in efficiency. Looking at Figure 5.4a it can be seen that the air exposed cells have a steep slope in the 3rd quadrant (negative voltage and negative current) which results in loss of J_{SC} and fill factor (see Table 5.1). A 3rd quadrant slope indicates that more charge carriers are being extracted as the negative voltage is increased, which suggests that charge recombination is outcompeting charge extraction. This strongly implies that air exposure has increased charge carrier recombination losses inside the cell. The reduction in fill factor and J_{SC} together with a small drop of the V_{OC} is responsible for the loss of PCE of the air exposed cells.

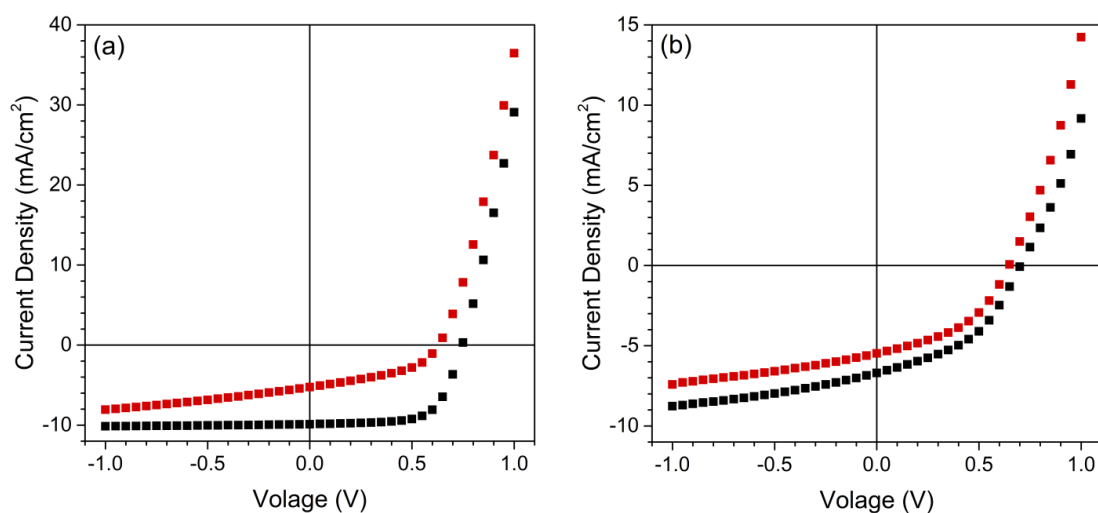


Figure 5.4 J-V characteristics of pristine (black) and air exposed (red) PTB7:PC₇₁BM cells. (a) Cells were processed using DIO. (b) Cells were processed without DIO.

For comparison pristine and air exposed PTB7:PC₇₁BM cells were processed without the solvent additive DIO. The pristine cells had a PCE of 2.2(1) % compared to 1.5(1) % for the air exposed, a 31 % reduction in PCE. The J-V curves of the pristine cells and air exposed cells are similar as shown in Figure 5.4b. Both exhibit a steep 3rd quadrant slope and low fill factor due to poor charge extraction. Such a shape is typical of cells with an unoptimised morphology, and is expected when PTB7:PC₇₁BM cells are processed without a solvent additive. The 31 % reduction in PCE when DIO free cells are processed under ambient atmosphere is significantly less than the 73 % reduction obtained for DIO containing cells. This result suggests that DIO enhances the performance loss when PTB7:PC₇₁BM cells are processed under ambient atmosphere. To gain further insight into the source of the performance loss variable light intensity J-V analysis was used.

Table 5.1 Variation of PTB7:PC71BM cell parameters with processing environment

Exposure	DIO	PCE (%)	FF (%)	J_{SC} (mA cm ⁻²)	V_{OC} (V)
Pristine	Yes	6.1(3)	65	13.0	0.74
Air Exposed	Yes	1.7(2)	43	5.5	0.59
Pristine	No	2.2(1)	46	6.6	0.72
Air Exposed	No	1.5(1)	43	5.3	0.66

J-V curves of DIO processed cells were recorded over a range of light intensities. As explained in Section 4.2.3 the bimolecular recombination loss at short circuit can be estimated by plotting the J_{SC} versus light intensity on a log-log scale as shown in Figure 5.5a while monomolecular recombination losses can be estimated by plotting the natural logarithm of the light intensity versus V_{OC} as shown in Figure 5.5b. The data in Figure 5.5a was fitted with a power law $J_{SC} = aI^b$, where I is the light intensity and b is a measure of the degree of bimolecular recombination, the lower the value of b the greater the recombination. Averaged across multiple cells the value of b was 0.956(1) for pristine cells and 0.936(3) for air exposed cells. The similarity in the value of b between pristine and air exposed cells suggests that processing the cells under ambient atmosphere does not appreciably increase the bimolecular recombination loss. Linear fits were applied to

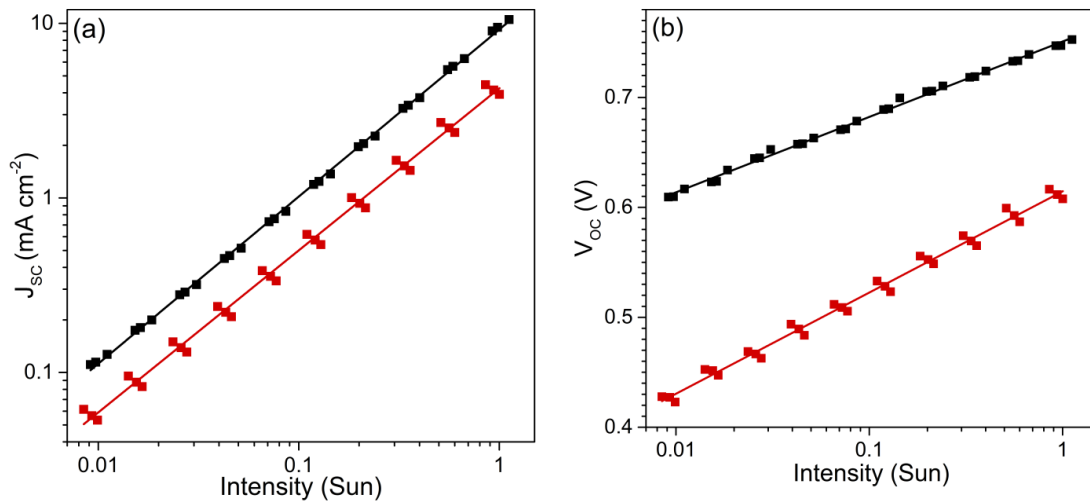


Figure 5.5 J-V characteristics of pristine (black) and air exposed (red) PTB7:PC71BM solar cells as function of light intensity. Cells were processed using DIO. (a) J_{SC} versus light intensity on log-log plot to estimate bimolecular recombination losses. (b) V_{OC} versus light intensity on semi log plot to estimate monomolecular recombination.

the data in Figure 5.5b. A slope of kT/e corresponds to zero monomolecular (trap-assisted) recombination losses, higher gradients signify increased losses. The average gradient was 1.16(1) kT/e for pristine cells and 1.52(1) kT/e for air exposed. The substantially higher gradient when cells are processed under ambient atmosphere indicates that the air exposure creates trap sites inside the cell which serve as recombination centres. This increased trap assisted recombination is likely the source of the PCE reduction when PTB7:PC₇₁BM cells are processed under ambient atmosphere. In order to gain further insight into these recombination centres, EDMR spectroscopy was used.

5.5.2 Influence of Processing Environment on EDMR of PTB7:PC₇₁BM Cells

The EDMR spectra of PTB7:PC₇₁BM cells processed under different environments were measured at 9.8 GHz. The cells were illuminated with a white light LED at short circuit and the change in the photocurrent recorded. The EDMR spectra of three PTB7:PC₇₁BM cells processed under different environments are shown in Figure 5.6. The light intensity was adjusted so that the photocurrent was 20 μ A in all measurements and the spectra were recorded using the same microwave power and field modulation amplitude. Cells processed under the nitrogen atmosphere of the glovebox exhibit a weak EDMR response around $g \approx 2$. Cells processed under ambient atmosphere without DIO exhibit a similar response in both magnitude and lineshape. However when cells are processed under ambient atmosphere using DIO the EDMR response increases by around a factor of 50. These measurements were repeated across more than 20 cells spread across 4 fabrication runs and this trend was observed in all instances. This increase in the EDMR signal when both DIO and air are present correlates with the large reduction in PCE when DIO containing cells are processed under ambient atmosphere. This suggests that the combination of DIO and oxygen causes a chemical change in the blend which lowers the PCE and gives rise to a strong spin-dependent mechanism in the photocurrent. This spin-dependent mechanism is likely the trap assisted recombination identified in the variable light intensity J-V characterisation. The correlation between increasing EDMR response and lower PCE is in agreement with previous EPR studies which showed that the stronger

the EPR intensity arising from radical species the lower the cell performance.^[27-29]

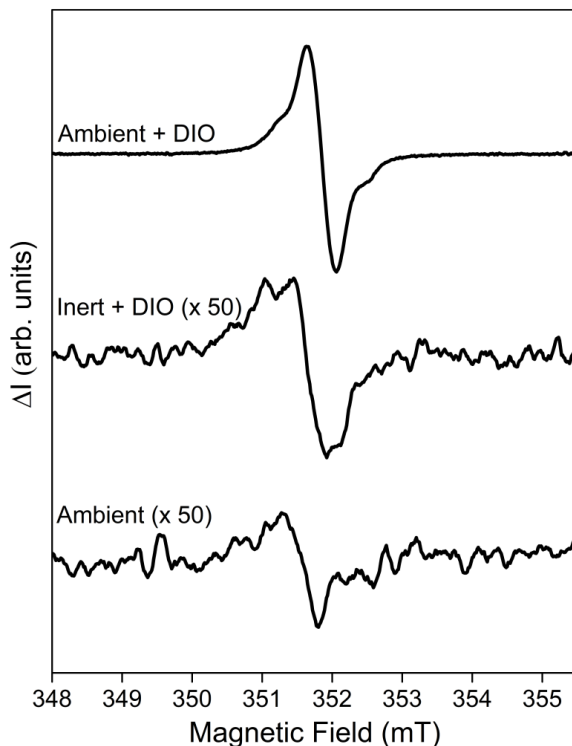


Figure 5.6 ED MR spectra of PTB7:PC₇₁BM cells processed under different environments. The spectra were recorded under short circuit conditions with white light illumination using continuous wave 9.8 GHz microwave irradiation.

The cwED MR spectra shown in Figure 5.6 were recorded with field modulation and phase sensitive detection using a lock in amplifier. While this greatly improves the signal to noise it also obscures the sign of the ED MR response as the phase information is lost in the electrical detection circuit. The absolute magnitude of the current change is also obscured as there are unknown gain stages in the spectrometer and the magnitude is dependent on the choice of field modulation amplitude. To obtain this information the change in the photocurrent of the ‘ambient + DIO’ cell at resonance was monitored using a Keithley 2400 source measure unit. The off resonance photocurrent was 20.03 μA which decreased to 19.96 μA during resonance. The spin dependent component of the photocurrent is therefore around 50 nA which gives a relative current change of order 1×10^{-3} . The current change in the two other cells could not be measured using this method

due to their weaker signal. However their relative current change can be inferred from Figure 5.6 to be around $\sim 2 \times 10^{-5}$.

The decrease in photocurrent at resonance is consistent with a spin-dependent recombination mechanism. At equilibrium prior to resonance the electron-hole pairs undergoing non-geminate recombination will have a predominately triplet character, since those with singlet character will recombine and be removed from the system. At resonance the singlet content of the pairs will be increased (Section 4.4.2). An increase in singlet content results in an increase in recombination rate and a decrease in the photocurrent resonance. While the observed decrease in photocurrent supports a recombination mechanism it is not conclusive as other spin-dependent mechanisms can also give rise to a decreasing current at resonance.^[30]

Obtaining a reliable spectral fit at using an EDMR spectrum taken at a single frequency is difficult and will have a large uncertainty.^[31] EDMR spectra were therefore taken at three microwave frequencies in order to increase the accuracy of the spectral simulation as shown in Figure 5.7. The 9.8 GHz and 34 GHz spectra were recorded using cwEDMR while the 94 GHz was obtained by pEDMR; this spectrum was then pseudomodulated by taking the first derivative. The spectra were taken using low microwave power to prevent a distortion of lineshape due to power broadening.^[32] The simulation is based on two Gaussian distributions which is the expected resonance response from two inhomogeneously broadened spin $\frac{1}{2}$ species that form a spin-pair in an organic semiconductor.^[31, 33-35] The g-factor that each Gaussian distribution is centred on are those which gave the most accurate simulation of the experimental data over the three frequencies. The experimental spectra are best simulated using Gaussian distributions with centres of $g = 2.0022(2)$ (blue) and $2.0026(2)$ (green). At 9.8 GHz the Gaussians centred on $2.0022(2)$ and $2.0026(2)$ have FWHM of $0.22(2)$ mT and $0.40(2)$ mT respectively. As the microwave frequency is increased the Gaussians broaden, reaching a FWHM of $1.48(2)$ mT and $2.30(2)$ mT at 94 GHz.

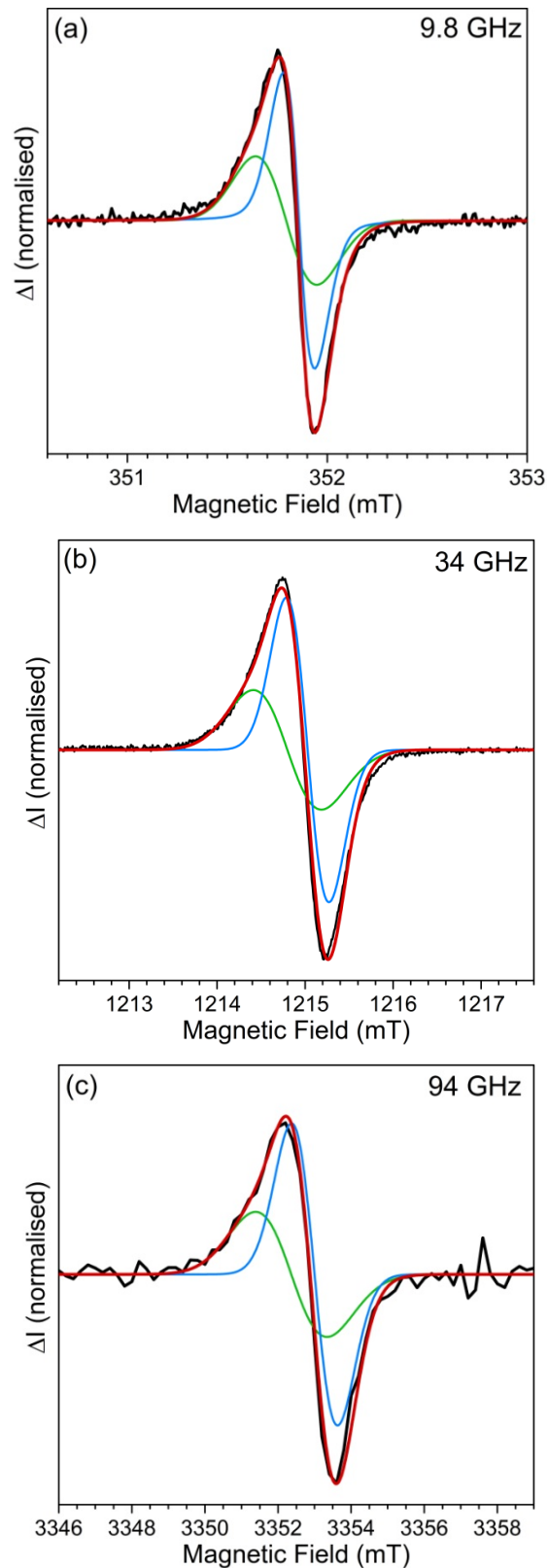


Figure 5.7 EDMR spectra of degraded PTB7:PC₇₁BM cells. The spectra were recorded under short circuit conditions with white light illumination. The experimental spectra are shown in black, the total simulation in red and the underlying components in blue and green. (a) CW 9.8 GHz spectrum. (b) CW 34 GHz spectrum. (c) pseudo-modulated pulse 94 GHz spectrum.

The EDMR spectra are fit remarkably well at all three microwave frequencies using the two symmetric Gaussian distributions. As discussed in Section 3.2 the conventional light induced EPR spectra of organic semiconductors generally exhibit anisotropy due to the relative orientation of the anisotropic molecule or polymer segment and the applied magnetic field. The g-tensors of light induced electrons and holes in the PTB7:PC₇₁BM blend has been previously measured using high field EPR, which showed that they are both anisotropic with rhombic symmetry.^[36, 37] The conventional light induced EPR spectra of electrons and holes in PTB7:PC₇₁BM would exhibit asymmetry from anisotropy even at 9.8 GHz and the principal values (turning points of the spectrum) of the g-tensor would be clearly resolved at 94 GHz. However in the EDMR spectra there is no indication of the principal values even at 94 GHz. This suggests that the g-tensors of the species detected here are either; more isotropic than those detected in conventional EPR or the inhomogeneous broadening (A-strain and g-strain) is so large that the principal values are smoothed out with no clear turning corresponding turning points in the spectrum. Given the increase in EDMR signal with air exposure, the species detected here almost certainly correspond to electrons or holes localised to defects in the blend and therefore may bear little resemblance to the EPR spectra of light induced electrons and holes at cryogenic temperatures. The simulation of the spectra using isotropic g-factors and symmetric Gaussians or Lorentzians is well supported by previous EDMR studies on organic semiconductor systems. The two members of the spin pair giving rise to the EDMR response have been accurately simulated using a double Gaussian or Lorentzian fits in the majority of previous EDMR studies of organic systems, even when some of the organic materials are known to possess an asymmetric EPR lineshape.^[31, 34, 35, 38-44] Introducing some anisotropy into the spectral fit does improve the residuals of the fits in Figure 5.7. However it has to be applied in a purely subjective manner due to the strong overlap of the two components and does not provide any new physical insight. Double isotropic fits were therefore used for all simulations in this study and should be considered a first order approach that captures the essence of the lineshape and the rough location of the two components.

The EDMR linewidth in organic semiconductors arises from two sources of inhomogeneous broadening. The first is unresolved hyperfine coupling to local nuclear magnetic moments and is field independent. The second is spin-orbit coupling which

gives rise to a distribution in the g-factor and is proportional to the magnetic field strength. This total linewidth σ_{tot} can be written, following the approach of Joshi et al,^[31] as a geometric addition of the two components,

$$\sigma_{tot} = \sqrt{\sigma_{hyp}^2 + \alpha^2 B_0^2} \quad (5.1)$$

where σ_{hyp} is the field independent contribution from unresolved hyperfine coupling, α quantifies broadening due to spin-orbit coupling and B_0 is the magnetic field. The spin-orbit coupling term is responsible for the large increase in linewidth of the EDMR spectra as microwave frequency is increased. The linewidths of the two Gaussians are plotted in Figure 5.8 as a function of magnetic field. The dotted lines are an approximate fit using Eq 5.1 and should be treated with caution as there are insufficient data points to accurately simulate the magnetic field dependence; however they serve as a useful guide to the eye.

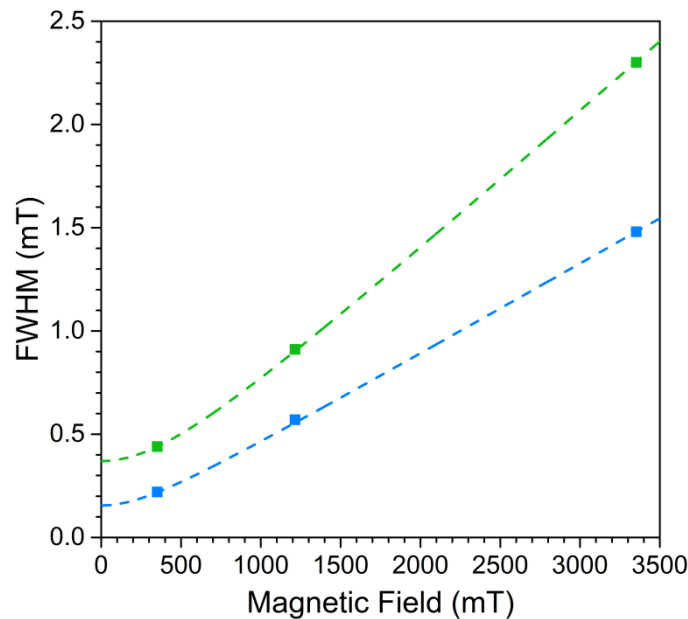


Figure 5.8 Magnetic field dependence Gaussian linewidths. The squares are the linewidths obtained from simulation of the experimental spectra at the three microwave frequencies. The dotted line is fit using Eq 5.1. The Gaussian distribution centred on 2.0022(2) is shown in blue and the 2.0026(2) distribution in green.

The value of σ_{hyp} can be estimated from the y-axis intercept and it can therefore be seen that the 2.0026(2) (green) distribution has a larger hyperfine broadening than the 2.0022(2) (blue) distribution. This indicates that the 2.0022(2) species is less strongly coupled to the surrounding nuclei. This suggest that the species at 2.0022(2) may be more delocalised than that at 2.0026(2) but this is far from conclusive.

5.5.3 Power Saturation

The influence of microwave power on the intensity and lineshape of the EDMR spectrum was investigated. The variation of the 9.8 GHz EDMR lineshape and magnitude with increasing microwave power is shown in Figure 5.9. At microwave powers below 5 mW the EDMR lineshape is accurately described by the two Gaussians discussed in the previous section, and the magnitude of the EDMR response increases linearly with microwave power as can be seen from the linear fit through the first three points. As the microwave power is increased beyond 5 mW the resonance enters the saturation regime. This results in a break from linearity and power broadening of the EDMR spectrum. In the saturation regime the lineshape of the two distributions are no longer described by pure Gaussians but rather pseudo-Voigtians; a linear combination of a Gaussian and a Lorentzian. As the power is increased the Lorentzian character becomes increasingly dominant and at powers over 100 mW the lineshape is most accurately simulated using pure Lorentzians. Increasing the microwave power beyond 100 mW results in no further increase of the resonance magnitude, as can be seen from the plateau in Figure 5.9b, and instead only further broadens the lineshape.

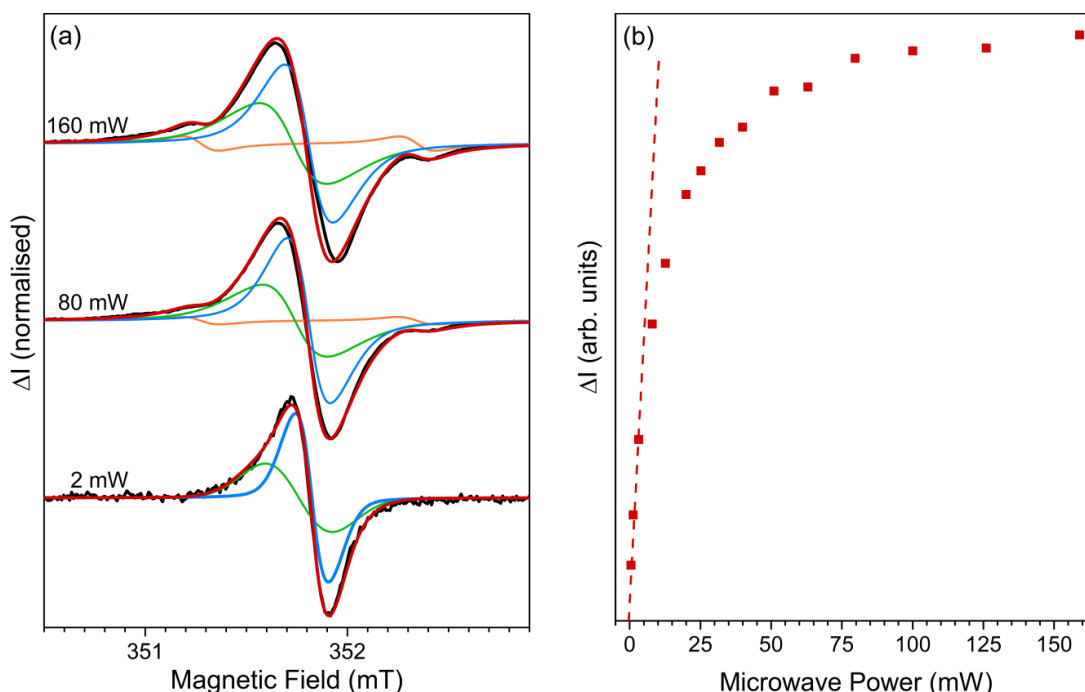


Figure 5.9 Effect of microwave power on the lineshape and magnitude of the 9.8 GHz EDMR spectrum of degraded PTB7:PC₇₁BM. (a) Variation of the lineshape with microwave power. The experimental spectra are shown in black, the total simulation in red, the 2.0022(2) in blue, 2.0226(2) in green and spin flip satellites in orange. (b) The variation of the maximum current change with microwave power.

5.5.4 Spin Flip Satellites

It is evident from Figure 5.9a that power broadening is not the only change in the EDMR lineshape. As the microwave power is increased two sharp peaks located either side of the main line become increasingly pronounced. The peaks are equidistant from the resonance centred on 2.0022(2) suggesting that they are coupled to the central line. The weak intensity, equidistance from the centre, and increased relative amplitude at low microwave powers suggests they are spin flip satellites.

Spin flip satellites were first observed by Zeldes et al.^[45] and the theoretical foundation provided by Trammel,^[46] and arise from the simultaneous flipping of the electron and a neighbouring nuclear spin during the EPR transition. The exact theory of these transitions is mathematically demanding and can be found elsewhere.^[46-49] Here a simplified theory is presented in order to illustrate the origin of the satellites. Consider a system containing a single electron and nucleus with $I = \frac{1}{2}$ such as a proton. The spin Hamiltonian of this system is given by,

$$\hat{H} = \hat{H}_{eZ} + \hat{H}_{nZ} + \hat{H}_{hf} \quad (5.2a)$$

$$\hat{H} = g\mu_B \mathbf{B}' \cdot \hat{\mathbf{S}} - g_N \mu_N \mathbf{B}' \cdot \hat{\mathbf{I}} + \hat{\mathbf{S}}' \cdot \mathbf{A} \cdot \hat{\mathbf{I}} \quad (5.2b)$$

The four possible spin states of the system are:

$$|\alpha(e), \alpha(n)\rangle \quad |\alpha(e), \beta(n)\rangle \quad |\beta(e), \alpha(n)\rangle \quad |\beta(e), \beta(n)\rangle \quad (5.3)$$

where the α and β are the spin up and spin down states and e and n signify if the spin states is that of the electron or nucleus. Applying \hat{H} to these states, taking the g-factor and hyperfine coupling to be isotropic, yields the following energies to first order:^[50]

$$U_{\alpha(e), \alpha(n)} = +\frac{1}{2} g_e \mu_B B - \frac{1}{2} g_N \mu_N B + \frac{1}{4} A_0 \quad (5.4a)$$

$$U_{\alpha(e), \beta(n)} = +\frac{1}{2} g_e \mu_B B + \frac{1}{2} g_N \mu_N B - \frac{1}{4} A_0 \quad (5.4b)$$

$$U_{\beta(e), \alpha(n)} = -\frac{1}{2} g_e \mu_B B - \frac{1}{2} g_N \mu_N B - \frac{1}{4} A_0 \quad (5.4c)$$

$$U_{\beta(e), \beta(n)} = -\frac{1}{2} g_e \mu_B B + \frac{1}{2} g_N \mu_N B + \frac{1}{4} A_0 \quad (5.4d)$$

The energy level diagram is shown in Figure 5.10, where the ordering is such that the hyperfine coupling term is smaller than the nuclear Zeeman term. In the transitions shown in blue the electron magnetic moment is changed while the nuclear magnetic moment remains unchanged ($\Delta M_S = 1, \Delta M_I = 0$). These are the standard EPR allowed transitions and have energies given by Eq 5.5.

$$U_{\alpha(e),\alpha(n)} - U_{\beta(e),\alpha(n)} = g_e \mu_B B + \frac{1}{2} A_0 \quad (5.5a)$$

$$U_{\alpha(e),\beta(n)} - U_{\beta(e),\beta(n)} = g_e \mu_B B - \frac{1}{2} A_0 \quad (5.5b)$$

In organic semiconductors the hyperfine coupling is weak and the two transitions are therefore not resolved in the EDMR spectrum. Instead the interaction of the electron with many surrounding protons causes an envelope of these transitions, leading to inhomogeneous broadening of the resonance and giving rise to the Gaussian distributions simulated in the previous section.

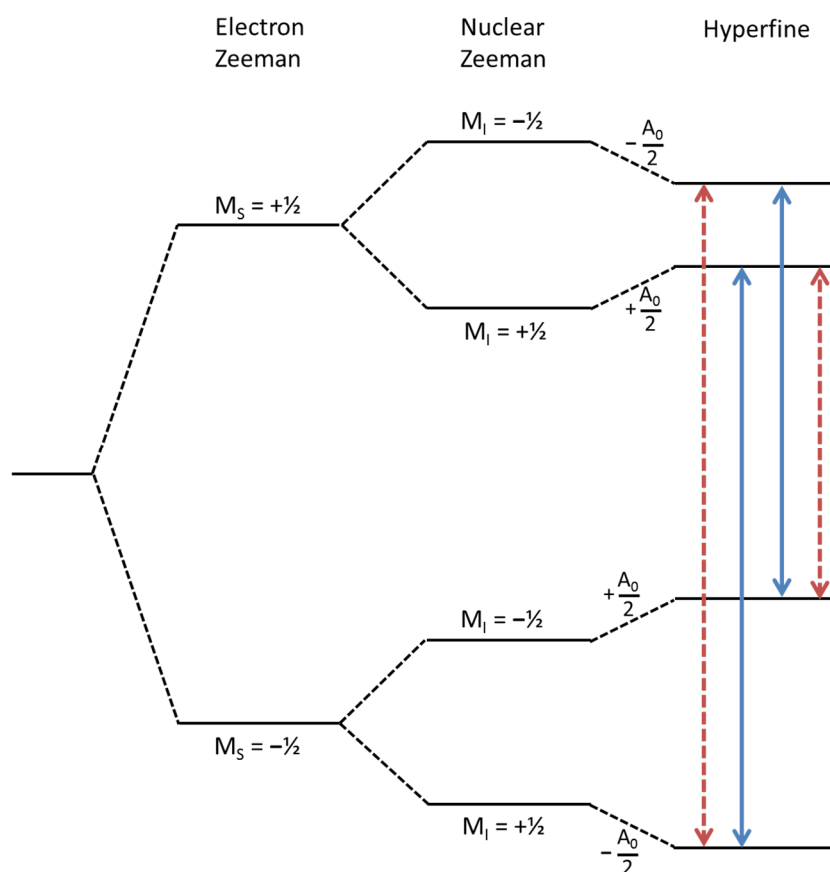


Figure 5.10 Energy levels of a $S = 1/2, I = 1/2$ system. Hyperfine coupling is assumed to be isotropic only. Allowed transitions are shown in blue and forbidden in red. Adapted from Weil & Bolton.^[50]

The red transitions in Figure 5.10 are those where both electron and nuclear magnetic moment changes ($\Delta M_s = 1$, $\Delta M_I = 1$). These transitions are forbidden due to conservation of angular momentum and therefore not observable in the vast majority of EPR measurements. However as the electron and nuclear magnetic moments will be coupled this selection rule is relaxed and weak transitions can be seen under certain circumstances. The energies of these “forbidden” transitions are given by Eq. 5.6.

$$U_{\alpha(e),\alpha(n)} - U_{\beta(e),\beta(n)} = g_e\mu_B B - g_N\mu_N B \quad (5.6a)$$

$$U_{\alpha(e),\beta(n)} - U_{\beta(e),\alpha(n)} = g_e\mu_B B + g_N\mu_N B \quad (5.6b)$$

Comparing Eq. 5.5 and Eq. 5.6 it can be seen that forbidden transitions have energies of $g_N\mu_N B$ above and below the central allowed transition. It is these forbidden transitions that give rise to the nuclear spin flip satellites. Converting energy difference to magnetic field units, the expected spacing between the centre transition and the satellites is given by Eq. 5.7.

$$\Delta B_{sat} = \frac{g_N\mu_N B}{g_e\mu_B} \quad (5.7)$$

The experimental spectra shown in Figure 5.9a were most accurately simulated using Lorentzian lineshapes equidistant from the 2.0022(2) distribution. The spacing between the 2.0022(2) distribution and the satellites was 0.51(2) mT. Using Eq 5.7 a spacing of 0.51 mT corresponds to a g_N of approximately 5.5 which is the nuclear g-factor of a proton. This supports the argument that the satellites arise from nuclear spin-flips, specifically the flips of nearby protons.

To provide further evidence that the satellite lines arise from nuclear spin flip transitions, the power dependence of the satellite lines was investigated. Experimental spectra were recorded over a range of microwave powers and the lineshape simulated at each power. The integrated intensities of the simulated central 2.0022(2) distribution and the satellite lines are plotted in Figure 5.11 as a function of microwave power. The integrated intensity of the centre line breaks from linearity at low microwave powers due, as discussed in the previous section, to saturation of EDMR transition. In contrast the intensity of the satellite lines remains linear over the full range of microwave powers. As nuclear spin flip

transitions are ‘forbidden’ the transition rate is much smaller than for the central line and the satellite transitions therefore require higher microwave power to saturate. The lack of power saturation in Figure 5.11 is further proof that the satellites arise from nuclear spin flips.

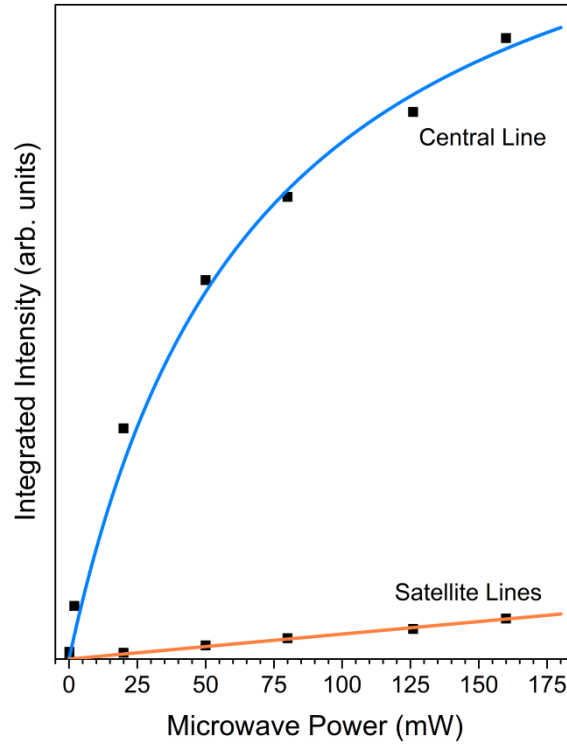


Figure 5.11 Integrated intensity of central and satellite lines as a function of microwave power. Data points are the integrated intensities of the components in the spectral simulations.

Based on Eq. 5.7 the distance between the satellites and central line increases with magnetic field and the centre-satellite separation should therefore be greater in 34 GHz and 94 GHz EDMR spectra. However from the full theory developed by Trammel,^[46] the intensity of the satellites is inversely proportional to the square of the magnetic field:

$$\frac{I_{sat}}{I_{centre}} \propto \frac{g_e^2 \mu_B^2}{B_0^2 r^6} \quad (5.8)$$

where I_{sat} and I_{centre} are the integrated intensity of the centre and the satellite lines and r is distance between the electron and nucleus. The spin flip satellite intensity at 34 GHz and 94 GHz would therefore be 8 % and 1 % of the intensity obtained at 9.8 GHz respectively. For this reason no satellite transitions were able to be observed in the 34 GHz and 94 GHz EDMR spectra.

The presence of a spin flip satellite suggests that one of the spin pair partners is in close proximity to a hydrogen nucleus. A search of the literature yielded only two previous reports of electrically detected spin flip satellites, both by Hiromitsu et al.^[51, 52] The first report was EDMR spectroscopy of H₂-phthalocyanine:C₆₀ bilayer solar cells. Two independent EDMR resonances at 2.0018(2) and 2.0010(2) were detected and attributed to electron hole recombination at two different recombination sites. The 2.0018 resonance had associated proton spin flip satellites and was therefore assigned to be in close proximity to the H₂-phthalocyanine. However this interpretation was cast into doubt upon measuring the EDMR spectrum of a cell containing only the C₆₀ layer.^[52] Here they observed an EDMR resonance at 2.0020(2) which also had associated proton spin flip satellites. The origin of these protons is not clear as C₆₀ does not contain hydrogen. They are simply referred to as impurity protons in the paper but their suspected origin is not discussed. Based on the observation of satellites in C₆₀ they suggest that the proton spin flip satellites observed in the H₂-phthalocyanine:C₆₀ cell may also be due to these impurity protons. These earlier results are obviously relevant to the work presented in this chapter as the proton spin flip satellites observed here are centred on a resonance with similar g-factor and PC₇₁BM is a similar material to C₆₀. However it is difficult to draw any conclusions based on this earlier work without knowing the origin or chemical nature of proton impurity sites.

5.5.5 Breakdown of the Simulation at High Powers

At the highest microwave powers the three component fit (two central distributions plus satellite component) becomes increasingly poor at reproducing the experimental lineshape. This can be seen from Fit 1 in Figure 5.12, where there is a lack of spectral density on the low field side using a three component simulation. This inability to reproduce the experimental spectra at high powers suggests that there is, at least, one additional EDMR transition present. The simplest refinement of the simulation that can be made to improve the fit is an additional broad resonance centred on 2.0038(3) which is shown in magenta in Fit 2 in Figure 5.12. This fit is obviously not unique but gave the best improvement with only the addition of a single component.

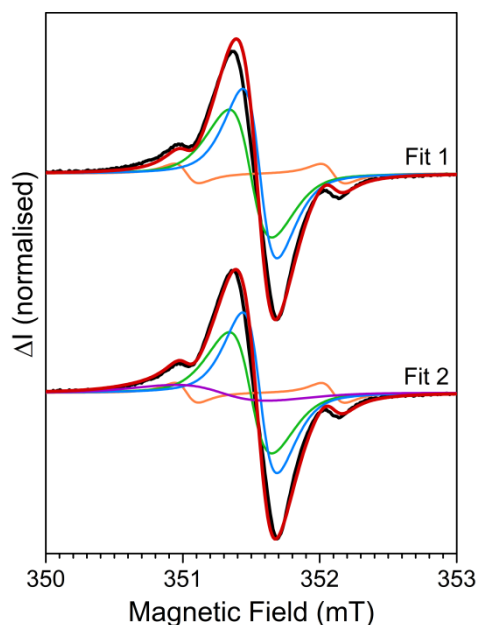


Figure 5.12 Breakdown of the three component fit at high microwave powers. Experimental spectra (black line) were recorded at 200 mW. The total simulation is shown in red, the 2.0022(2) in blue, 2.0226(2) in green, spin flip satellites in orange, and the additional 2.0038(3) component in magenta.

5.5.6 Pulsed EDMR

To further explore the nature of the EDMR transitions and gain insight to underlying mechanism pulsed EDMR spectroscopy was employed. pEDMR transients of the degraded cell were recorded as a function of magnetic field at 9.8 GHz and 34 GHz. The pEDMR transient after a 300 ns 34 GHz pulse is shown in Figure 5.13a. The microwave pulse causes a decrease in the photocurrent which returns to its steady state value by 15 μ s as shown by the colour map. At times greater than 6 μ s the EDMR lineshape can be accurately simulated using two pseudo Voight distributions with equal intensities centred on 2.0022(2) and 2.0026(2), as shown in Figure 5.13c, in agreement to spectral fitting obtained from the cwEDMR. The pseudo Voight lineshape of the distributions arises from the high pulse power used to acquire the spectrum which introduced a small degree of power broadening and distortion of the lineshape towards Lorentzian.^[32] The relative intensity of the distributions remains equal at all times indicating that both distributions have the same dynamic behaviour. The fact both distributions exhibit the same dynamics lends further support to the proposal that the distributions are involved in the same spin-dependent process and represent the constituent members of a spin-pair.^[34, 40] At short times ($t < 5 \mu$ s) there is an additional broad distribution centred on 2.0038(3)

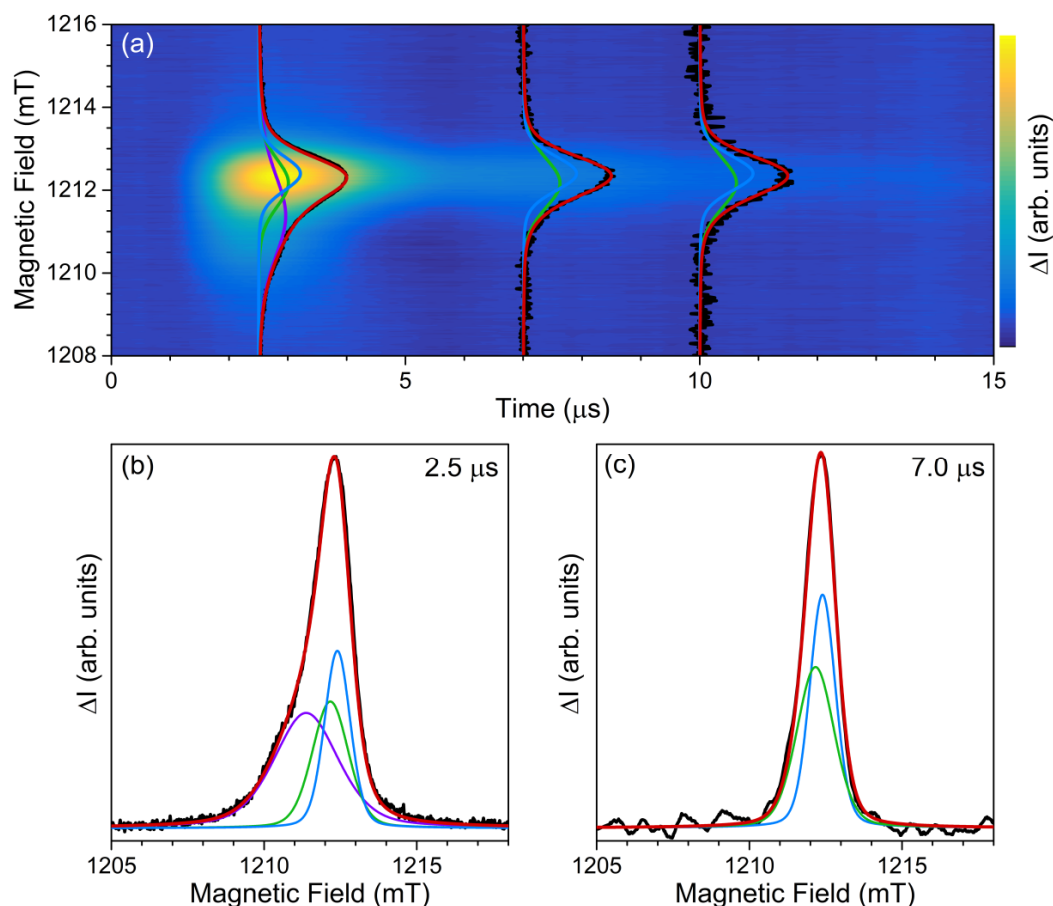


Figure 5.13 Pulse EDMR spectra recorded under short circuit conditions with illumination at room temperature. (a) Current transient following a 34 GHz 300 ns microwave pulse at $t = 0$. The colour plot denotes the change in photocurrent from the steady state. Line plots are superimposed to show the lineshape at different times. The experimental data is shown in black, the total simulation in red and the underlying components in blue, green and magenta. (b) Lineshape at 2.5 μs . (c) Lineshape at 7.0 μs .

as shown in Figure 5.13b. The 2.0038(3) distribution decays rapidly and has returned to the steady state value by 5 μs . This is almost certainly the same distribution that improved the fit of the high power cwEDMR spectrum in section 5.5.5. The fact it decays rapidly gives it small time integrated intensity in relation to the 2.0022(2) and 2.0026(2) distributions and therefore a weak cwEDMR response.

Figure 5.14 shows slices of the pEDMR transient at $t = 2.5 \mu\text{s}$ at different pulse powers. As the pulse power is decreased the weight of the 2.0038(3) distribution decreases relative to the 2.0022(2) and 2.0026(2) distributions indicating that it has different power saturation behaviour. This is in agreement to the cwEDMR spectra where the 2.0038(3) distribution was only visible at the highest microwave powers. The fact that the 2.0038(3) distribution exhibits different decay dynamics and power saturation behaviour from the

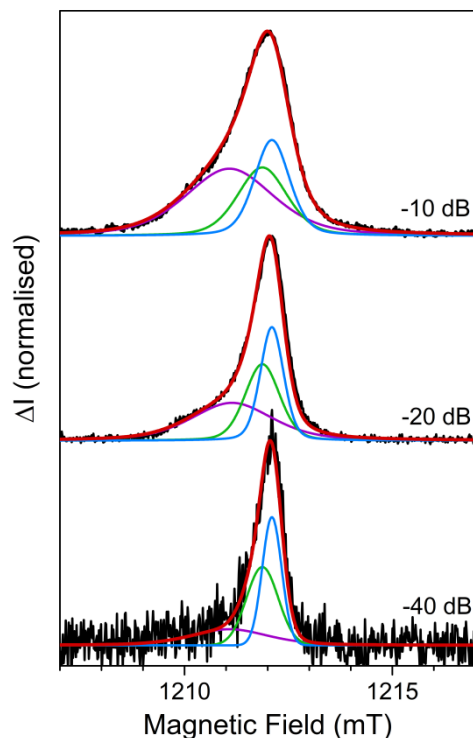


Figure 5.14 Variation of the pEDMR spectrum with microwave power. The spectra were recorded using 34 GHz 300 ns microwave pulses. Experimental spectra are shown in black, the total simulation in red and the underlying components in blue, green and magenta. All spectra are from a slice of the transient at $t = 2.5 \mu\text{s}$.

2.0022(2) and 2.0026(2) distributions reveals that it must correspond to a second independent spin dependent process.

5.5.7 Rabi Oscillation

To gain further information on the underlying mechanism, the spin nutation during the microwave pulse was explored. This was achieved using a Rabi oscillation experiment where the pulse length is varied and the EDMR transient integrated to obtain the charge, Q . As discussed in Section 4.4.4 the dynamics of the spin pair during the microwave pulse can be observed by integrating the pEDMR transient to obtain Q and plotting Q as a function of pulse length.

The pulse length was varied from 2 ns to 600 ns at nine microwave powers covering a 16 dB range. The Rabi Oscillation of Q at different microwave powers is shown in Figure 5.15. It can be seen that as the B_1 field becomes stronger the Rabi oscillation frequency, Ω , increases in accordance with the on resonance Rabi equation,

$$\Omega = \gamma B_1 \quad (5.9)$$

where γ is the gyromagnetic ratio of one member of the spin pair. Figure 5.15 also shows

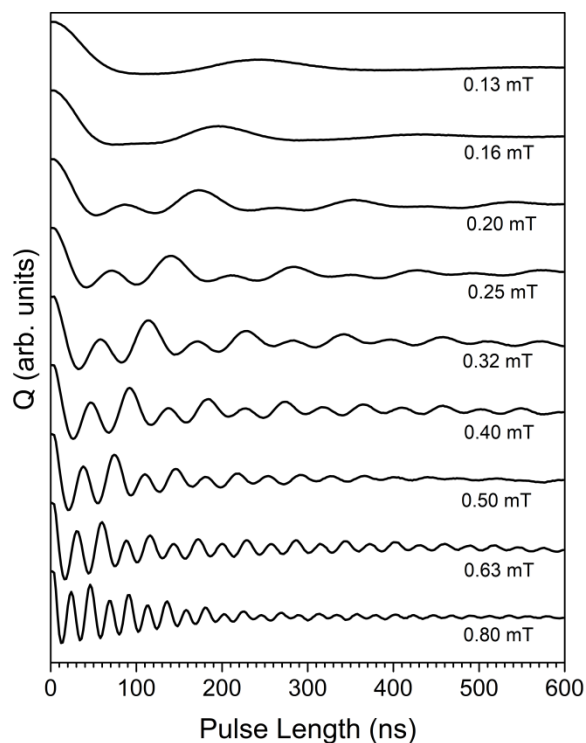


Figure 5.15 pEDMR Rabi oscillation spectra were recorded using 9.8 microwave pulses at short circuit. The B_1 field strength is listed below each oscillation.

that the Rabi oscillations appear to be composed of at least two frequencies. To more clearly analyse the oscillations, they were Fourier transformed to reveal the underlying frequency components. An example Fourier transform at a B_1 of 0.63 mT is shown in Figure 5.16. It reveals there are two prominent frequency components, one double the other. In addition there is a weak component close to zero frequency. There are two possible origins of this low frequency component, improper background subtraction and a spin beat difference oscillation. When the spin-pair contains two spins with different g-factors the spins will have slightly different Rabi frequencies which can give rise to an oscillation at the difference in Rabi frequency of the two spins. The presence of this low frequency oscillation has been predicted theoretically by Glenn et al,^[53] and observed experimentally by Schooten et al.^[42] However a frequency component close to zero can also be caused by imperfect background subtraction before taking the Fourier transform and is known as the DC component. Various methods of pre-processing were tried to accurately remove background drift of the Rabi oscillation experiment output but none were perfect. It could be seen that the height of low frequency component was dependent

on the background subtraction method used. It can therefore not be said definitively if the low frequency component arises from the beat difference oscillation or drifts in background during the Rabi oscillation experiment and the low frequency components are therefore neglected in the remaining analysis.

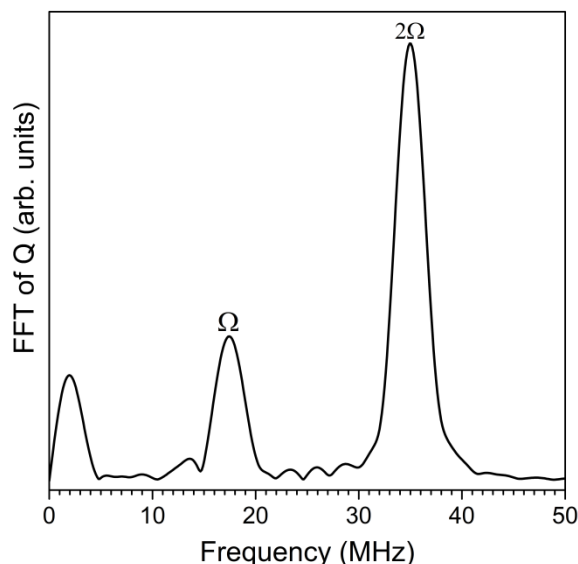


Figure 5.16 Fourier transform of the Rabi oscillations at $B_1 = 0.63$ mT.

The Fourier transform at each B_1 field was calculated and combined to create the colour plot shown in Figure 5.17. It can be seen from Figure 5.17 that frequency of both components varies linearly with B_1 field strength. Linear best fits (dashed lines) were applied, revealing a factor of 2 difference in the slopes and thus confirming that higher frequency component is double the frequency of the lower at all B_1 fields. At low B_1 the amplitude of the Ω component is greater than the 2Ω component. As B_1 is increased the spectral density shifts from the Ω to the 2Ω component and at the highest B_1 fields the Fourier transform is dominated by the 2Ω component. A double frequency component in the Rabi oscillation occurs when both spins in the pair are manipulated by the microwave pulse and oscillate simultaneously under the B_1 field.^[30, 41, 53] A double frequency component is expected under two scenarios,^[39, 53]

1. Weak exchange coupling and non-selective excitation ($J < \delta\omega < \gamma B_1$)
2. Strong exchange coupling ($\delta\omega \ll J$)

where $\delta\omega$ is the difference between the Larmor frequencies of the two spins in the pair and J is the exchange coupling constant. These scenarios can be distinguished by the behaviour of the intensity of the Ω and 2Ω components as B_1 is increased.

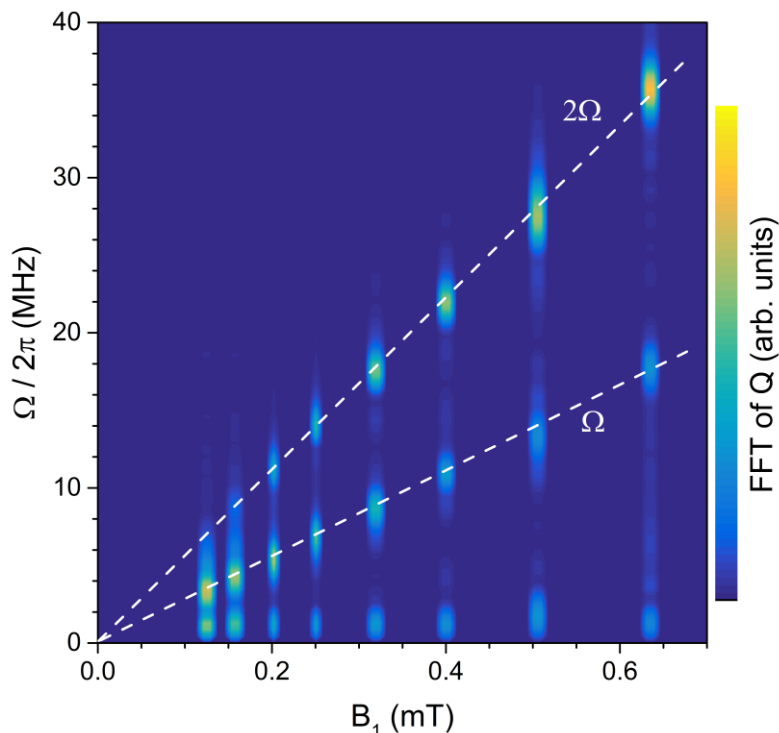


Figure 5.17 Plot of the Fourier transform of the Rabi oscillation as a function of B_1 field strength.

When exchange coupling is strong (scenario 2) the singlet and triplet manifolds in the spin pair are decoupled. At resonance microwaves promote transitions between the three triplet levels at a frequency of 2Ω . The magnitude of the 2Ω component in this case is independent of B_1 and always larger than the Ω component.

When exchange coupling is weak (scenario 1) the action of the microwave pulse depends on the strength of B_1 . At low B_1 the excitation bandwidth of the microwave pulse is narrow and only one spin in the pair is rotated during the pulse, and oscillation between the singlet and triplet states occurs at Ω . As B_1 is increased the excitation bandwidth broadens and both spins in the pair can be rotated simultaneously. This effectively decouples the singlet and triplet manifolds as the spins are now locked to triplet state, and oscillations will occur between the three triplet levels at 2Ω . It can be seen from Figure 5.17 that the magnitude of the 2Ω component is weak at low B_1 and increases in strength with increasing B_1 , hence the exchange coupling is weak. This spin-locking at high B_1

can also be seen by observing the change in pEDMR lineshape and Rabi frequency as a function of static magnetic field (B_0).

The Fourier transform of a field swept Rabi oscillation experiment is shown in Figure 5.18. It can be seen that the 2Ω component is only present in the centre of the spectrum where the overlap of the distributions of the two spins in the pair is greatest. This supports the assignment of weak coupling as the spins only precess together in the centre of the spectrum when they can both be simultaneously excited.

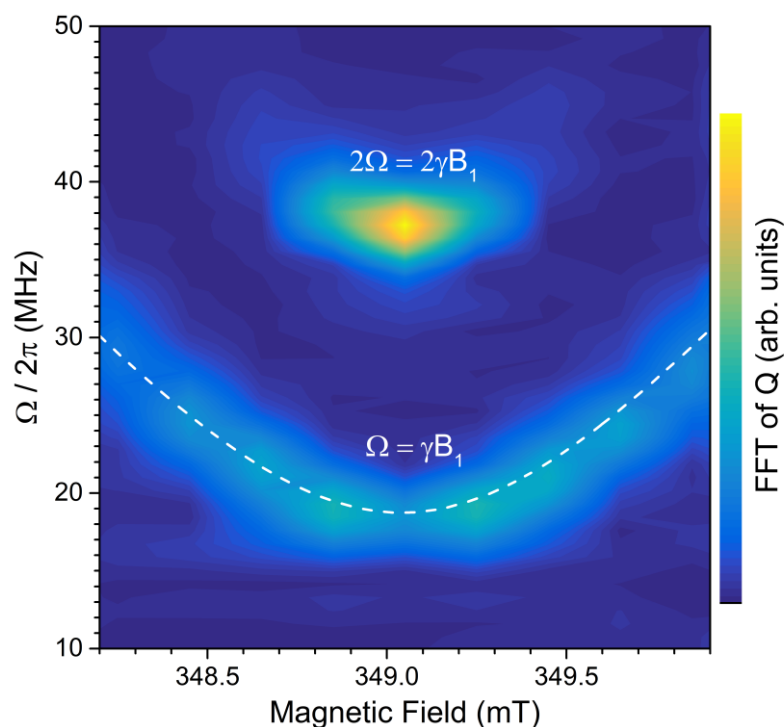


Figure 5.18 Plot of the Fourier transform of the Rabi oscillation as a function of B_0 field position.

A similar effect is seen when looking at the change in lineshape of the pEDMR spectrum as B_1 is increased. Time slices of the 9.8 GHz pEDMR transient at three values of B_1 are shown in Figure 5.19. At low B_1 (green) the EDMR transient is composed of a single sharp peak. As the B_1 field strength is increased the FWHM of the spectrum increases due to power broadening and a dip appears in the centre of the spectrum. This central dip is due to the increasing magnitude of the central 2Ω component seen in Figure 5.18 as B_1 is increased. The dip arises because spin-locking impedes the conversion of triplet spin pairs to singlet pairs and the magnitude of the EDMR response is proportional to this

conversion. The EDMR response is therefore quenched when spin-locking occurs, giving rise to central dip in the spectrum.

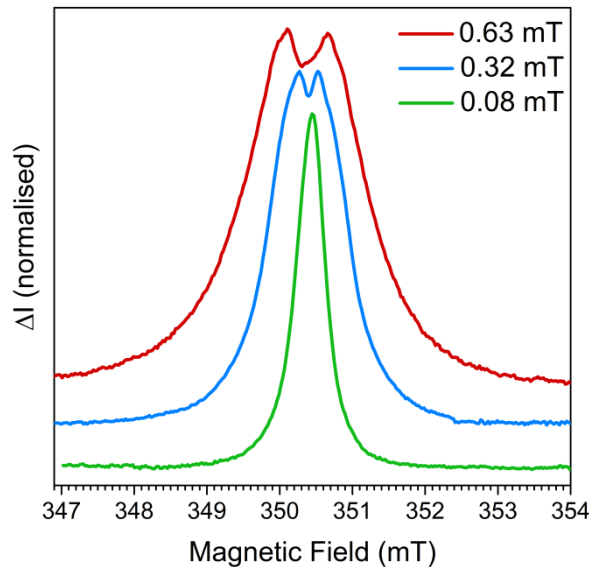


Figure 5.19 Time slice of the 9.8 GHz pEDMR transient at three B_1 field strengths.

The Rabi data shown thus far has all been at 9.8 GHz. At 9.8 GHz the low field distribution centred on 2.0038(3) severely overlaps with the spin-pair distributions and may contribute to the Rabi oscillations. However its time averaged intensity is significantly weaker than that of the spin-pair and the influence should be minimal. In order to further explore the origin of the 2.0038(3) Rabi Oscillation experiments were attempted at 34 and 94 GHz, however neither were successful. This was likely a combination of poor B_1 inhomogeneity and weaker B_1 field strength in these higher frequency measurements.

5.5.8 Selective Injection of Carriers

So far it has been shown that the EDMR response of degraded PTB7:PC71BM solar cells is primarily composed of two weakly interacting spin $\frac{1}{2}$ species forming a spin pair. While the decrease of the photocurrent at resonance is compatible with a recombination mechanism in the intermediate pair model it is not conclusive. It has been shown spin-dependent transport and recombination can both give rise to enhancing or quenching EDMR responses.^[30, 43] The sign of EDMR response therefore cannot be used to unambiguously assign the underlying mechanism and the two spin $\frac{1}{2}$ species forming the spin pair could equally be two like charged species involved in a transport process or an

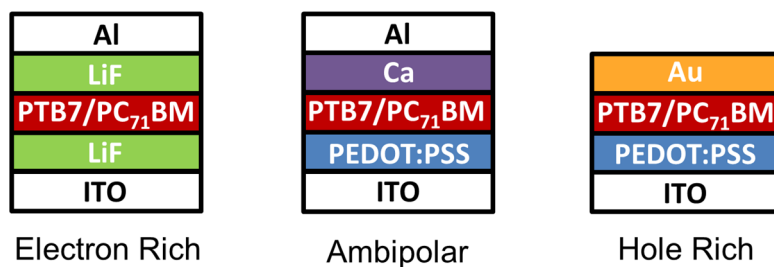


Figure 5.20 Electrode configurations of PTB7:PC₇₁BM cells.

electron and hole undergoing recombination. One method to determine which of these scenarios is taking place is selective injection of charge carriers. In order to control the injection of carriers, three types of PTB7:PC₇₁BM cell were fabricated with different choices of anode and cathode, the structures of which are shown in Figure 5.20. The reference configuration, which was used during the previous measurements in this chapter, uses a calcium / aluminium cathode and a PEDOT:PSS / ITO anode. The Fermi levels of various electrodes and the HOMO and LUMO levels of PTB7 and PC₇₁BM are shown in Figure 5.21. As the Fermi level of a calcium cathode is higher (less negative) than the LUMO of PC₇₁BM an Ohmic contact is formed due to Fermi level pinning (see Section 2.2.6), allowing efficient electron injection. At the anode, the work function of PEDOT:PSS is about equal to the HOMO of PTB7 resulting in an approximately ohmic contact and efficient hole injection. When this cell structure is placed under forward bias (PEDOT:PSS biased positively and calcium negatively) there will therefore be efficient injection of both electrons and holes into the cell and the current will be ambipolar.

The Fermi level of gold is ~1 eV lower (more negative) than the LUMO of PC₇₁BM. Using gold as the cathode will therefore result in large energetic barrier for electron injection. When a cell using PEDOT:PSS as the anode and gold as the cathode is placed under forward bias, the current will be dominated by holes. To create an electron rich cell the calcium and PEDOT:PSS interlayers were replaced by a thin (~1 nm) layer of lithium fluoride. Lithium fluoride functions differently from the other electrode materials mentioned, in that it modifies the energy level alignment of the materials it is located between. Lithium fluoride preferentially aligns so that the F⁻ points towards the electrode surface while the Li⁺ points towards the organic, creating an interface dipole that raises the effective Fermi level of the electrode.^[54] Placing a layer of lithium fluoride under the

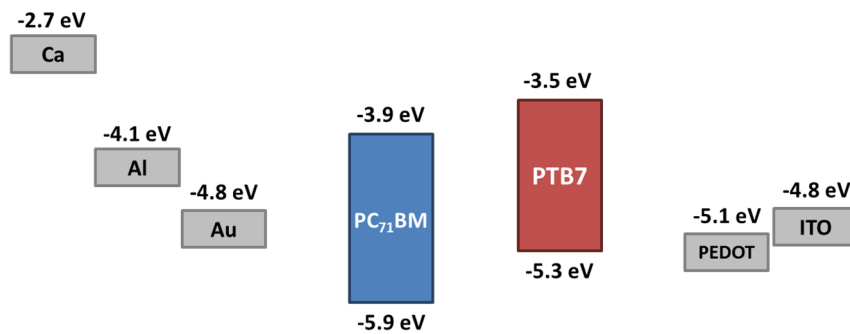


Figure 5.21 Energy levels and electrode Fermi levels.^[55-58]

aluminium raises the effective Fermi level of the aluminium by over 1 eV allowing an ohmic contact to be formed to the LUMO of PC₇₁BM.^[59] Similarly the lithium fluoride layer will raise the effective Fermi level of the ITO electrode resulting in a large energy separation between the ITO and the HOMO of the PTB7 which results in a large energetic barrier for hole injection. Therefore when this structure is placed under forward bias the majority carrier in the cell will be electrons.

If the EDMR mechanism is due to the recombination of electrons and holes the EDMR response of a cell will be greatest when both carriers are present in equal numbers. If the carriers are not present equally the generation rate of the spin-pairs and therefore the magnitude of the EDMR response will be determined by the minority carrier generation rate. The nature of the EDMR mechanism can therefore be elucidated by measuring the EDMR response of the ambipolar, electron rich and hole rich cells. The cwEDMR spectrum of the three cell types were each recorded under two conditions; at short circuit under illumination and under forward bias in the dark. The results are shown in Figure 5.22. When the charge carriers are photogenerated there will be an equal number of electrons and holes created in the cell and photogenerated spectra therefore act as a useful reference where both charge carriers must be present in equal numbers. The light intensity and forward bias voltage were adjusted so that current through the cells was 20 μ A, for photogeneration and injection spectra respectively. Looking at Figure 5.22 it can be seen that in the case of the ambipolar cell the magnitude of the photogenerated and injection spectra are approximately equal in magnitude. Contrast this with the electron and hole rich cells where the injection spectra are weaker by around a factor 10 compared to the photogenerated spectra. As the magnitude of the EDMR response is greatest when the charge carriers are photogenerated or through ambipolar injection, the primary EDMR

mechanism must involve both electrons and holes. It can therefore be concluded that the two weakly coupled spin $\frac{1}{2}$ species identified previously are electrons and holes undergoing recombination.

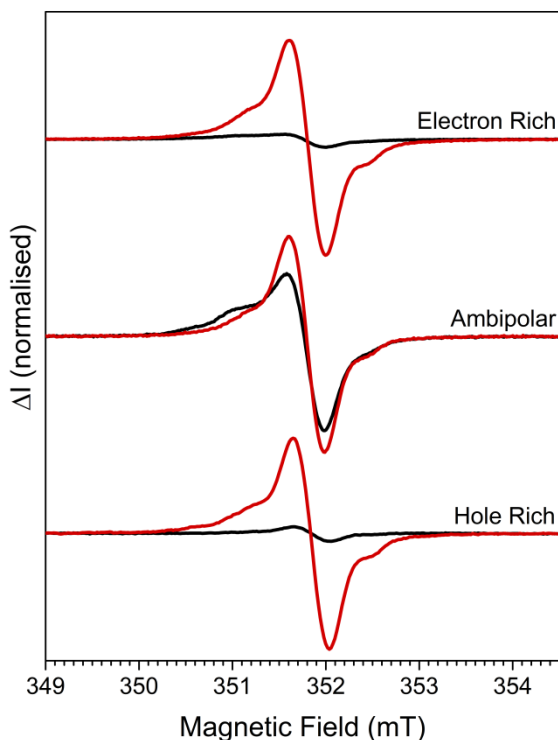


Figure 5.22 Comparison of photogenerated (red) and injected (black) degraded PTB7:PC₇₁BM 9.8 GHz cwEDMR spectra using different electrode configurations. For each electrode configuration the photogenerated and injection spectra have been normalised to the height of the photogenerated spectrum. The spectra were acquired under high (200 mW) microwave power and large modulation amplitude to achieve acceptable signal to noise ratio for all spectra. This results in power broadening and smoothing of the sharper features.

5.5.9 An Aside: Lineshape of the Injection Spectra

It is clear from Figure 5.22 that the lineshape of the injected and photogenerated ambipolar spectra is not equivalent. This can be more clearly seen in Figure 5.23 where the injected and photogenerated spectra have been normalised. Figure 5.23 shows that when the charge carriers in the ambipolar and electron rich cells are created by injection there is a substantial increase in spectral density on the low field side of the spectrum. In contrast the photogenerated and injection spectra for the hole rich cell are approximately equivalent.

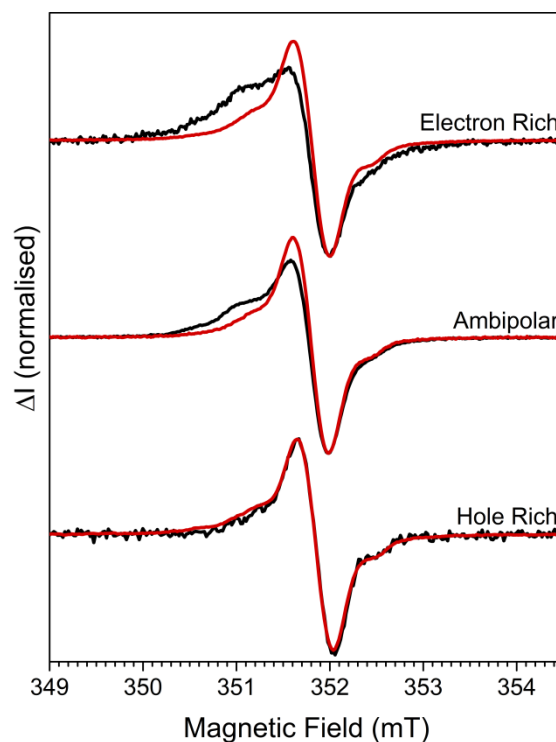


Figure 5.23 Normalised comparison of photogenerated (red) and injected (black) degraded PTB7:PC₇₁BM 9.8 GHz cwEDMR spectra using different electrode configurations.

To further investigate the source of this lineshape change, spectra of the ambipolar cell were recorded using different injection voltages and microwave powers and a small selection of these spectra are shown in Figure 5.24. The spectra can be roughly simulated by including two additional distributions centred at 2.0037(3) (magenta) and 2.0074(2) (orange) with FWHM of 1.02(5) mT and 0.35(3) mT and Voigtian and Gaussian lineshapes respectively. These distributions are additional to the spin pair and associated satellites previously introduced, which are shown collectively in blue. The distribution centred on 2.0037(3) has similar g -factor and linewidth to the short lived distribution observed in the pEDMR transient and in the cwEDMR at high microwave power at $g = 2.0038(3)$. It is highly likely that all three correspond to the same species and will therefore be named as 2.0038(3) from hereon. The distribution centred on 2.0074(2) appears to be unique to the injection spectra or is only present with a very low intensity when the carriers are photogenerated. This indicates that injection of the carriers likely leads to additional spin dependent mechanisms. It can be seen from Figure 5.24 that the relative intensity of the 2.0074(2) and 2.0037(3) distributions increases with respect to the spin-pair as the forward bias voltage is increased. It is difficult to draw a conclusion from this observation as the behaviour of the injection electrodes as a function of voltage

is not known. It is likely that changing the bias voltage perturbs the electron and hole injection balance and alters the relative population of electrons and holes in the cell. The fact that the balance is not perfect, i.e the electrodes are not both perfectly ohmic, is supported by the fact that the ambipolar injection spectrum is marginally less intense than the photogenerated in Figure 5.22. Ultimately the minor variation in relative intensity between the spin-pair and the 2.0038(3) distribution with injection voltage and electrode choice is insignificant. Instead the main insight is that Figure 5.22 shows that the mechanism involving the 2.0038(3) distribution must also require both electrons and holes, as the 2.0038(3) distribution is heavily suppressed in the hole rich and electron rich injection spectra. The 2.0038(3) distribution therefore also corresponds to a recombination mechanism.

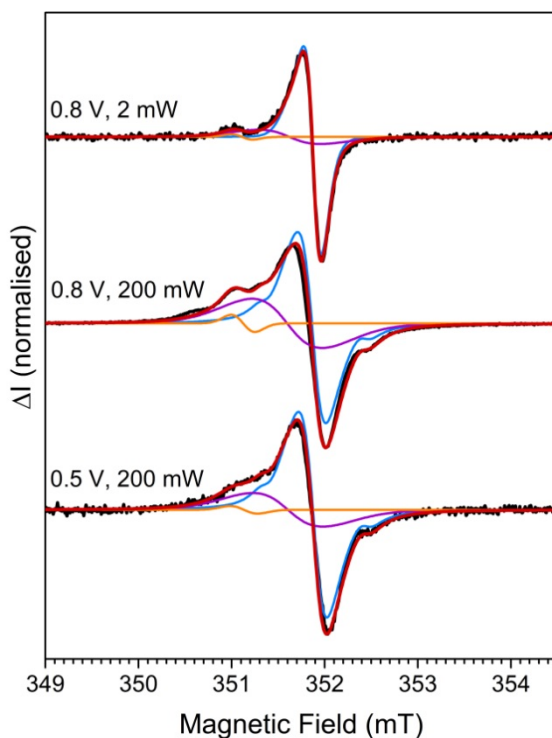


Figure 5.24 Comparison of EDMR spectra of ambipolar PTB7:PC71BM cells recorded using different injection voltages and microwave powers. Experimental spectra are shown in black, the total simulation in red, the spin-pair in blue and the injection induced features in magenta and orange.

5.5.10 Single Component Cells

The EDMR response has shown to be comprised of electrons and holes undergoing recombination. However the measurements so far have offered no insight into the location of the electrons and holes involved in the EDMR mechanism inside the cell. In order to

elucidate the location of the spins, cells containing the individual components of the blend, PTB7 and PC₇₁BM, were fabricated.

PC₇₁BM

The cwEDMR spectrum of an air exposed PC₇₁BM cell is shown in Figure 5.25. The spectrum can be accurately simulated using two Gaussian distributions centred on 2.0025(2) (green) and 2.0028(2) (blue) with FWHM of 0.38(2) and 1.00(2) mT, respectively. In contrast to the double Gaussian fits used earlier in this chapter the integrated intensities of Gaussian distributions used here are not equal. The two Gaussians therefore do not simply correspond to the two members of a spin pair, but instead likely belong to two independent transitions. Similar spectra containing two Gaussian distributions with different weights have been observed in air exposed films of PC₆₁BM by Morishita et al.^[34]

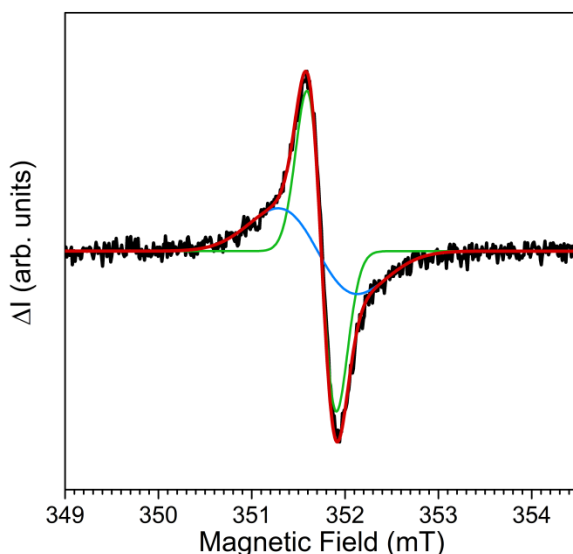


Figure 5.25 9.8 GHz cwEDMR spectrum of air exposed PC₇₁BM. The charge carriers were generated using a forward bias of 1.6 V to give a current of 20 μ A.

The variation of the cwEDMR spectrum when PC₇₁BM films are exposed to air during fabrication is shown in Figure 5.26. When PC₇₁BM films are exposed to air during processing the magnitude of the cwEDMR spectrum increases by around a factor 6. This demonstrates that PC₇₁BM films are sensitive to ambient atmosphere, and the room temperature cwEDMR response of PC₇₁BM cells is therefore due to a spin dependent process that occurs at ambient atmosphere induced defects. Fullerenes are well known to be susceptible to oxidation, and a variety of fullerene oxygen complexes have been

reported.^[60-62] The g-factors observed here of 2.0025(2)/28(2) are similar to the previous air exposed PC₆₁BM EDMR study with $g = 2.0030(2)$,^[34] and EPR studies on oxygen exposed C₆₀ films which reported fullerene oxygen complexes at $g = 2.0026(3)$.^[63-65] The air exposed cwEDMR spectrum of PC₇₁BM is therefore attributed to charge carriers located at oxidised PC₇₁BM. It is also clear from Figure 5.26 that the lineshape of the two red curves is not equivalent. This is further evidence of multiple independent spin-dependent processes occurring in the cell. Different samples have different populations of spin centres contributing to each process which alters the lineshape. The inert and air processed PC₇₁BM cells used to obtain Figure 5.26 did not contain the solvent additive DIO. In section 5.5.2 it was shown that exposure of DIO containing PTB7:PC₇₁BM films to ambient atmosphere during processing resulted in factor of 50 enhancement of the cwEDMR signal. In contrast the cwEDMR spectrum of PTB7:PC₇₁BM films fabricated without DIO were insensitive to the choice of processing environment, leading to the conclusion that DIO is a crucial agent in the degradation process. An effort was therefore made to investigate the role that DIO plays in the degradation of neat PC₇₁BM cells.

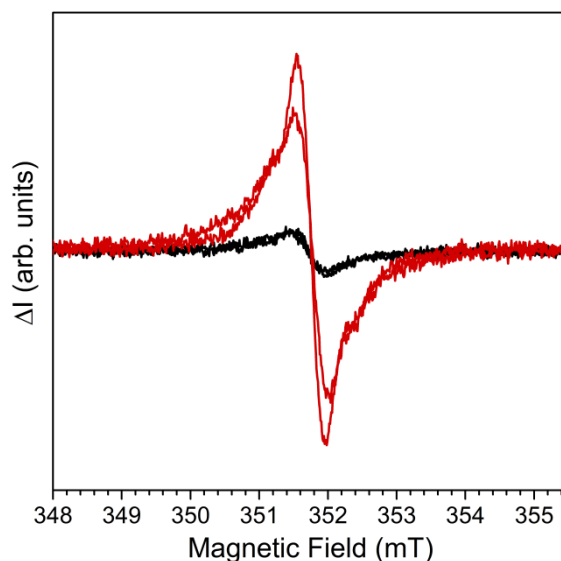


Figure 5.26 cwEDMR spectrum of PC₇₁BM at 9.8 GHz. The charge carriers were generated using a forward bias of 1.6 V to give a current of 20 μ A. Spectra of inert processed films are shown in black and air exposed films in red.

Numerous attempts were made to fabricate PC₇₁BM films containing DIO as a solvent additive. However it was found that even a small volume of DIO severely hinders the film formation of PC₇₁BM. Using the standard 3% by volume of DIO, no continuous film of PC₇₁BM was formed after spin coating. When the DIO concentration was reduced to 1 %

a continuous film was able to be formed, however the films contained pin holes which grew in size over a period of several minutes and rendered the films unusable. A stable PC₇₁BM film could only be formed when the DIO concentration was reduced to 0.3 %. cwEDMR spectra of air exposed 0.3 % DIO and 0.0 % DIO PC₇₁BM cells were measured but no difference in the cwEDMR spectra could be observed. This result is not surprising at such low DIO concentrations as very little DIO is in each film. Due to the low concentration it is not safe to draw a conclusion on the effect that DIO has on the EDMR response of PC₇₁BM. To summarise, it can be concluded that the EDMR response of PC₇₁BM is driven by exposure to oxygen. However it was not possible to determine if the addition of DIO would accelerate this degradation due to the poor film formation.

PTB7

The cwEDMR spectrum of an air exposed PTB7 cell is shown in Figure 5.27. The spectrum can be simulated with reasonable accuracy using a pseudo-Voigt distribution centred on 2.0037(2) with a FWHM of 1.35(2) mT. The simulation captures the bulk lineshape but it is clear from Figure 5.27 that it does not reproduce the finer detail of the experimental spectrum. The fine structure and pseudo-Voigt lineshape of the spectrum suggests that it is composed of multiple overlapping transitions, likely corresponding to multiple independent spin dependent processes in the cell.

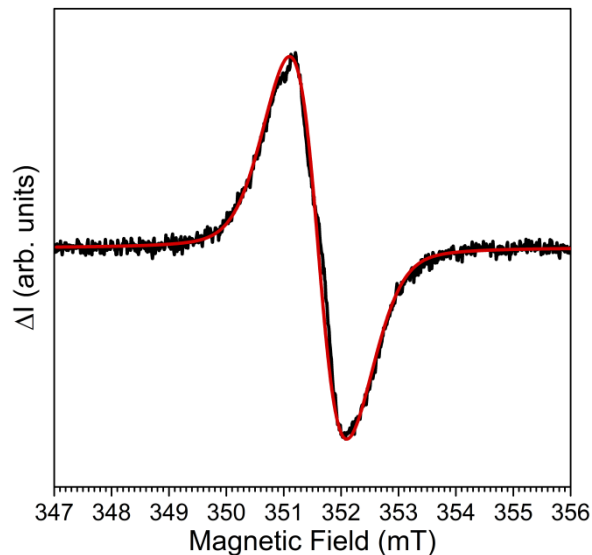


Figure 5.27 cwEDMR of PTB7 at 9.8 GHz. The charge carriers were generated using a forward bias of 1.7 V to give a current of 50 μ A . The experimental spectrum is shown in black and the simulation in red.

The effect of ambient atmosphere on the cwEDMR spectrum of PTB7 cells is shown in Figure 5.28. The cells were fabricated using DIO as the additive and exposed to ambient atmosphere during fabrication in similar manner to the blend. It can be seen from Figure 5.28 that exposure of the PTB7 films to ambient atmosphere has little effect on the cwEDMR of the cells, with the lineshape and magnitude of the pristine and air exposed cells being approximately equal. This suggests that exposure of PTB7 to ambient atmosphere does not lead to the formation of electrically active defects inside the cell.

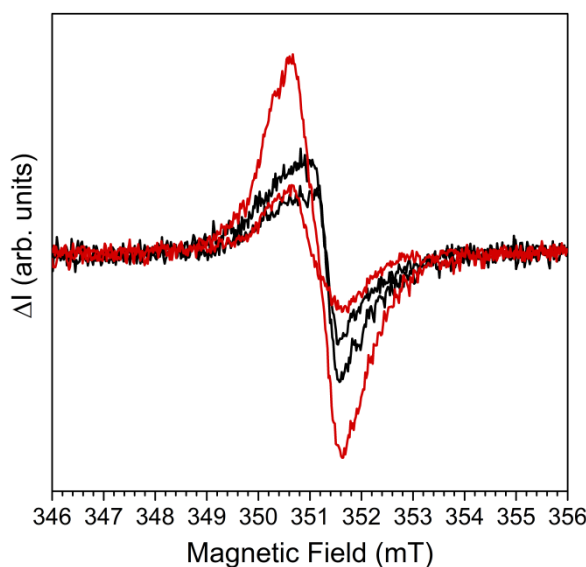


Figure 5.28 cwEDMR of PTB7 at 9.8 GHz. The charge carriers were generated using a forward bias of 1.2 to 1.5 V to give a current of 20 μ A. Spectra of inert processed films are shown in black and air exposed in red.

During the course of this investigation several different material batches of PTB7 were used. In Figure 5.29 a normalised comparison of the cwEDMR spectrum of these different PTB7 batches is shown. It can be seen from Figure 5.29 that while the cwEDMR spectra of the different PTB7 batches have the approximately the same g-factor and overall linewidth, there is substantial variation in their lineshape, despite the fact the PTB7 used is nominally equivalent. The variation of the lineshape with PTB7 batch suggests that the room temperature cwEDMR response of PTB7 arises wholly or partially from pre-existing defects in the PTB7 such as synthesis impurities. The different batches of PTB7 likely have different concentrations and differing types of defects, giving rise to a variation in the intensity of overlapping EDMR transitions which manifests as changes in lineshape. This observation is in agreement with previous EPR studies of PTB7 which

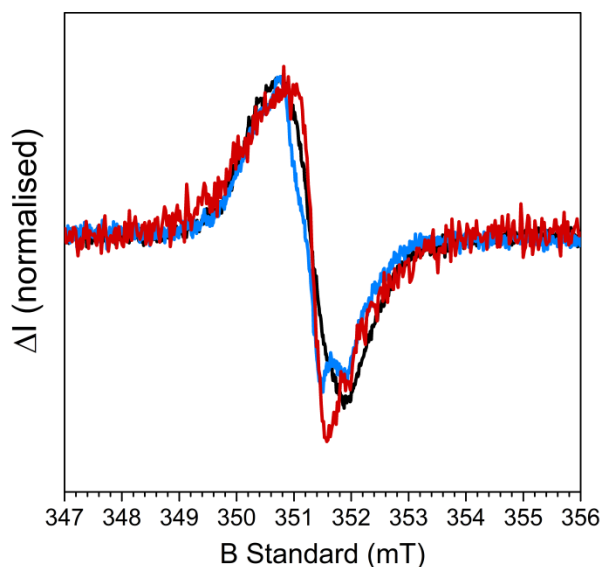


Figure 5.29 cwEDMR of PTB7 at 9.8 GHz. The charge carriers were generated using a forward bias of 1.5 - 1.7 V. The three colours correspond to three different batches of PTB7 used over the course of the investigation.

showed that the number of paramagnetic defects on the PTB7 varies with the molecular weight of the polymer batch.^[29] A build-up of similar paramagnetic defects were also detected when films of PTB7 were exposed to light for extended periods of time.^[66] While this does not impact the results of this study, caution should be used when interpreting the EDMR spectrum of organic semiconductors, as the EDMR resonance may correspond to a minority process occurring on a defect site rather than the majority processes in the pristine material.

5.5.11 Location of the Recombination Sites in the blend

The Spin Pair at $g = 2.0022(2) / 2.0026(2)$

A comparison of the cwEDMR lineshape of PC₇₁BM, PTB7 and the blend is shown in Figure 5.30. The spectrum of PTB7 and the blend are highly dissimilar, with the spectrum of PTB7 being substantially broader and at a higher g-factor than the spin-pair resonance of the blend. The spectral dissimilarity leads to the conclusion that the spin-pair in the blend does not involve charge carriers localised at PTB7 defect sites. In contrast the cwEDMR spectra of PC₇₁BM and the spin-pair in the blend contain similar Gaussian distributions with centres of 2.0025(2) and 2.0026(2), and FWHM of 0.38(2) mT and 0.40(2) mT, respectively. The near equivalence of these Gaussian distributions in both g-factor and linewidth is strongly suggestive that both distributions correspond to the same

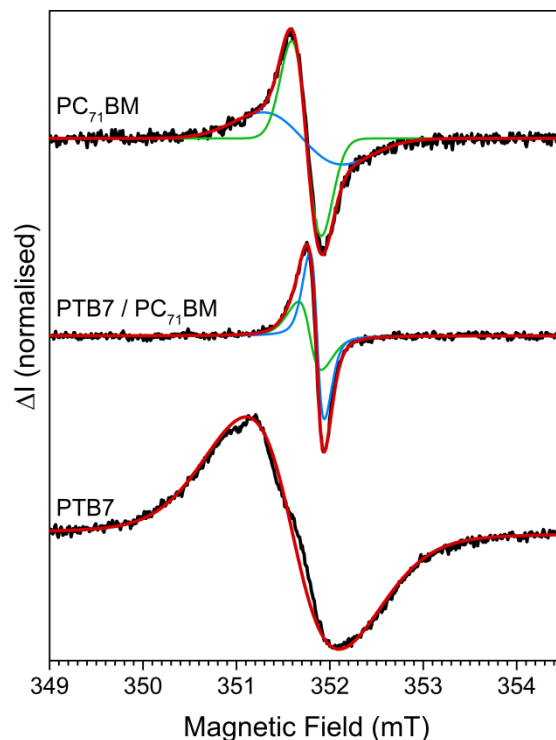


Figure 5.30 cwEDMR spectra of air exposed PC₇₁BM, PTB7:PC₇₁BM and PTB7 at 9.8 GHz. The charge carriers in PTB7 and PC₇₁BM were generated by injection under forward bias while carriers in the PTB7:PC₇₁BM were photogenerated.

species in the cell. It can therefore be concluded that the 2.0026(2) component of the spin-pair in the blend corresponds to either electrons or holes located on PC₇₁BM.

Based on the above assignment and the previous establishment that the spin-pair corresponds to recombination; there are three possible recombination mechanisms. These three mechanisms are: (1) the electron and hole are both located on the PC₇₁BM, (2) electrons are on the PTB7 and holes are on the PC₇₁BM, and (3) holes are on PTB7 and electrons on PC₇₁BM. Energetically mechanism 1 and 2 are unlikely to occur as the charge carriers originate from photoexcited excitons. After an exciton reaches the donor / acceptor interface and undergoes electron transfer, the electron is on the LUMO of PC₇₁BM and the hole on the HOMO of PTB7. The likelihood of holes then hopping from the HOMO of the PTB7 to the HOMO of the PC₇₁BM can be inferred from Boltzmann statistics. The relative population of two states at thermal equilibrium can be calculated using:

$$\frac{P_2}{P_1} = e^{\frac{E_1 - E_2}{k_B T}} \quad (5.8)$$

where P is the population of the state and E is the energy. From Figure 5.21 the HOMO of PTB7 is 600 meV above the HOMO of PC₇₁BM and kT at room temperature is approximately 26 meV. Using Eq 5.8 the population of holes on PC₇₁BM is a factor of 1×10^{-10} fewer than on PTB7. The hopping of electrons from the LUMO of PC₇₁BM to the LUMO of PTB7 is suppressed in a similar manner. As the spin dependent component of the photocurrent is at least 1×10^{-3} , the small number of carriers that may hop to the opposite phase cannot be responsible for the EDMR signal. Mechanisms 1 and 2 can therefore be ruled out. The 2.0022(2) distribution of the spin-pair can therefore be assigned to holes on PTB7.

In section 5.5.2 it was shown that the magnitude of the of the EDMR response of the blend increased by a factor of 50 when processed under ambient atmosphere in the presence of DIO. One of the partners in the spin-pair must therefore be localised to a defect that was created upon exposure to ambient atmosphere. In Figures 5.28 and 5.29 it was shown that EDMR response of neat PTB7 is not affected by exposure to ambient atmosphere but instead is influenced by the batch of PTB7 used. In contrast it was shown in Figure 5.26 that exposure to ambient atmosphere increases the EDMR magnitude of PC₇₁BM cells by a factor of 6 and the g -factor is consistent with oxidised PC₇₁BM. It is therefore concluded that the 2.0026(2) component of the spin-pair corresponds to electrons localised to oxidised PC₇₁BM. This assignment is consistent with reports that oxidation of the fullerene results in a lowering of the LUMO energy and the oxidised species can serve as electron trapping sites.^[67] It is also in agreement to the work of Lee et al.,^[22] who found that exposure of PTB7:PC₇₁BM films to both DIO and oxygen leads to epoxy group formation on the PC₇₁BM which could serve as a trap site. In summary the spin-pair signal in the blend is assigned to the recombination of trapped electrons located on oxidised PC₇₁BM (2.0026(2)) with mobile holes located on the PTB7 (2.0022(2)).

One discrepancy with the above assignment is the difference in g -factors obtained here to those previously reported for holes and electrons on PTB7 and PC₇₁BM using EPR spectroscopy.^[36, 37] The reported g_{iso} of electrons on PC₇₁BM is ~ 2.0036 .^[36, 37] While this is substantially different from the value of 2.0026(2) reported here this is not surprising if the electron is trapped on a oxidised fullerene cage. Modification of the fullerene cage

would result in different electron distribution and spin orbit coupling and therefore a different g-factor to electrons on 'pristine' PC₇₁BM is to be expected.

The g-factor obtained here of 2.0022(2) for holes on PTB7 is also different to the previous EPR report which found a g-factor of $g_{\text{iso}} = 2.0033$ ($g_x = 2.0045$, $g_y = 2.0031$, $g_z = 2.0023$).^[36] The origin of the difference between these values is not so clear. A similar discrepancy in g-factor was recently observed by Behrends et al. in their comparative EDMR and EPR study of P3HT:PC₆₁BM blends.^[68] In the EPR spectra the electron on PC₆₁BM has the distinctive axial g-tensor while the simulation of the electron on PC₆₁BM in the EDMR spectrum required an isotropic distribution centred on the g_z value of the EPR g-tensor. The difference between the EPR and EDMR spectra is yet not fully understood but may be due to the relative orientation of the polymer and fullerene molecules inside the film. A similar effect may be present here where the PTB7 value is centred on g_z component of the tensor. Another explanation is that the proximity of the hole to the trapped electron on the defect perturbs its local environment and g-factor.

The Broad Resonance at $g = 2.0038(3)$

As discussed previously the EDMR spectrum of the blend contains an additional broad resonance centred on 2.0038(3) with a FWHM of 1.1(1) mT that corresponds to a second independent transition in the blend. This resonance is highly similar in both g-factor and linewidth to the resonance of the PTB7 cells, namely 2.0037(2) with a FWHM of 1.35(2) mT. This similarity strongly suggests that the 2.0038(3) transition in the blend involves carriers on the PTB7. Like the spin pair above, the 2.0038(3) resonance is only present after the blend has been exposed to DIO and ambient atmosphere indicating that the underlying transition involves carriers localised to defect sites. In Figure 5.29 it was shown that EDMR spectrum of neat PTB7 films is dependent on the batch of PTB7 used, indicating that neat PTB7 resonance is wholly or partly due to defects on the PTB7. Based on the growth of the 2.0038(3) resonance when exposed to ambient atmosphere and the variation of the neat PTB7 spectrum with batch, the 2.0038(3) resonance is assigned to carriers trapped at defects on the PTB7. Under the spin-pair mechanism an EDMR transition should consist of two resonances. One possibility is that the 2.0038(3) distribution is a convolution of both resonances. Alternatively, the spin-pair partner may not be observable by EDMR, for example being too broad to be excited and detected in

EDMR. Due to the lack of information no mechanism can be definitively assigned. The most likely mechanism is recombination between holes trapped at defects on the PTB7 (the 2.0038 resonance) with mobile electrons on the PC₇₁BM which is unobservable or hidden in the baseline of the spectrum. It is interesting that the EDMR response of neat PTB7 cells was insensitive to exposure to DIO and ambient atmosphere. In contrast when the blend is exposed to the same conditions there is a resonance involving defect sites on the PTB7. This suggests that PTB7 is more susceptible to degradation when blended than when a neat component.

5.6 Conclusions

The degradation of PTB7:PC₇₁BM solar cells when exposed to ambient atmosphere was investigated using J-V characterisation and EDMR spectroscopy. When DIO containing PTB7:PC₇₁BM cells are fabricated under ambient atmosphere the PCE drops from 6.1(3) % to 1.7(2) %. Using J-V analysis the origin of this performance loss was determined to be increased trap assisted recombination. To gain further insight into the origin of trap assisted recombination EDMR spectroscopy was employed. The EDMR response of PTB7:PC₇₁BM is a factor of 50 greater in magnitude in cells fabricated using DIO under ambient atmosphere. This reveals that a strong spin dependent transition occurs in those cells which are exposed to both DIO and ambient atmosphere and is concomitant with the increased trap assisted recombination. The EDMR response is dominated by a spin-pair consisting of two Gaussian distributions centred on 2.0022(2) and 2.0026(2) and was determined to be weakly coupled electrons and holes undergoing recombination. Through comparison with neat component cells the recombination mechanism is assigned to electrons localised to traps on PC₇₁BM and mobile holes on the PTB7. In addition, there is a weaker resonance arising from degradation of the PTB7. This result shows that exposing DIO cast films to ambient atmosphere leads to the formation of defects on the PC₇₁BM which act as electron traps which results in increased recombination losses and lower PCE. The field should therefore move away from DIO towards more inert solvent additives in order to increase stability.

5.7 References

1. S. A. J. Thomson, S. C. Hogg, I. D. W. Samuel and D. J. Keeble, Air Exposure Induced Recombination in PTB7:PC71BM Solar Cells. *J. Mater. Chem. A* (2017).
2. J. B. Zhao, Y. K. Li, G. F. Yang, K. Jiang, H. R. Lin, H. Ade, W. Ma and H. Yan, Efficient organic solar cells processed from hydrocarbon solvents. *Nat. Energy* **1**, 7 (2016).
3. T. Liu, Y. Guo, Y. P. Yi, L. J. Huo, X. N. Xue, X. B. Sun, H. T. Fu, W. T. Xiong, D. Meng, Z. H. Wang, F. Liu, T. P. Russell and Y. M. Sun, Ternary Organic Solar Cells Based on Two Compatible Nonfullerene Acceptors with Power Conversion Efficiency > 10%. *Adv. Mater.* **28** (45), 10008-10015 (2016).
4. J. Huang, J. H. Carpenter, C. Z. Li, J. S. Yu, H. Ade and A. K. Y. Jen, Highly Efficient Organic Solar Cells with Improved Vertical Donor-Acceptor Compositional Gradient Via an Inverted Off-Center Spinning Method. *Adv. Mater.* **28** (5), 967-974 (2016).
5. J. D. Chen, C. H. Cui, Y. Q. Li, L. Zhou, Q. D. Ou, C. Li, Y. F. Li and J. X. Tang, Single-Junction Polymer Solar Cells Exceeding 10% Power Conversion Efficiency. *Adv. Mater.* **27** (6), 1035-1041 (2015).
6. D. Baran, T. Kirchartz, S. Wheeler, S. Dimitrov, M. Abdelsamie, J. Gorman, R. S. Ashraf, S. Holliday, A. Wadsworth, N. Gasparini, P. Kaienburg, H. Yan, A. Amassian, C. J. Brabec, J. R. Durrant and I. McCulloch, Reduced voltage losses yield 10% efficient fullerene free organic solar cells with > 1 V open circuit voltages. *Energy Environ. Sci.* **9** (12), 3783-3793 (2016).
7. S. Q. Zhang, L. Ye and J. H. Hou, Breaking the 10% Efficiency Barrier in Organic Photovoltaics: Morphology and Device Optimization of Well-Known PBDTTT Polymers. *Adv. Energy Mater.* **6** (11), 20 (2016).
8. Y. H. Liu, J. B. Zhao, Z. K. Li, C. Mu, W. Ma, H. W. Hu, K. Jiang, H. R. Lin, H. Ade and H. Yan, Aggregation and Morphology Control Enables Multiple Cases of High-Efficiency Polymer Solar Cells. *Nat. Commun.* **5**, 8 (2014).
9. W. R. Mateker and M. D. McGehee, Progress in Understanding Degradation Mechanisms and Improving Stability in Organic Photovoltaics. *Adv. Mater.* **29** (10), 1603940-n/a (2017).
10. Y. C. Cheng Gu , Zhongbo Zhang , Shanfeng Xue , Shuheng Sun , Chengmei Zhong , Huanhuan Zhang , Ying Lv , Fenghong Li , Fei Huang , and Yuguang Ma, Achieving High Efficiency of PTB7-Based Polymer Solar Cells via Integrated Optimization of Both Anode and Cathode Interlayers. *Adv. Energy Mater.* (2014).
11. S. H. Liao, H. J. Jhuo, P. N. Yeh, Y. S. Cheng, Y. L. Li, Y. H. Lee, S. Sharma and S. A. Chen, Single Junction Inverted Polymer Solar Cell Reaching Power Conversion Efficiency 10.31% by Employing Dual-Doped Zinc Oxide Nano-Film as Cathode Interlayer. *Scientific Reports* **4**, 7 (2014).

12. Y. W. Soon, H. Cho, J. Low, H. Bronstein, I. McCulloch and J. R. Durrant, Correlating triplet yield, singlet oxygen generation and photochemical stability in polymer/fullerene blend films. *Chem. Commun.* **49** (13), 1291-1293 (2013).
13. J. Razzell-Hollis, J. Wade, W. C. Tsoi, Y. Soon, J. Durrant and J. S. Kim, Photochemical stability of high efficiency PTB7:PC70BM solar cell blends. *J. Mater. Chem. A* **2** (47), 20189-20195 (2014).
14. B. Arredondo, M. B. Martin-Lopez, B. Romero, R. Vergaz, P. Romero-Gomez and J. Martorell, Monitoring degradation mechanisms in PTB7:PC71BM photovoltaic cells by means of impedance spectroscopy. *Sol. Energy Mater. Sol. Cells* **144**, 422-428 (2016).
15. G. J. Hedley, A. J. Ward, A. Alekseev, C. T. Howells, E. R. Martins, L. A. Serrano, G. Cooke, A. Ruseckas and I. D. W. Samuel, Determining the optimum morphology in high-performance polymer-fullerene organic photovoltaic cells. *Nat. Commun.* **4**, 10 (2013).
16. B. J. T. de Villers, K. A. O'Hara, D. P. Ostrowski, P. H. Biddle, S. E. Shaheen, M. L. Chabiny, D. C. Olson and N. Kopidakis, Removal of Residual Diiodooctane Improves Photostability of High-Performance Organic Solar Cell Polymers. *Chem. Mater.* **28** (3), 876-884 (2016).
17. W. Huang, E. Gann, Z. Q. Xu, L. Thomsen, Y. B. Cheng and C. R. McNeill, A facile approach to alleviate photochemical degradation in high efficiency polymer solar cells. *J. Mater. Chem. A* **3** (31), 16313-16319 (2015).
18. W. Kim, J. K. Kim, E. Kim, T. K. Ahn, D. H. Wang and J. H. Park, Conflicted Effects of a Solvent Additive on PTB7:PC71BM Bulk Heterojunction Solar Cells. *J. Phys. Chem. C* **119** (11), 5954-5961 (2015).
19. L. Ye, Y. Jing, X. Guo, H. Sun, S. Q. Zhang, M. J. Zhang, L. J. Huo and J. H. Hou, Remove the Residual Additives toward Enhanced Efficiency with Higher Reproducibility in Polymer Solar Cells. *J. Phys. Chem. C* **117** (29), 14920-14928 (2013).
20. N. Li and C. J. Brabec, Air-processed polymer tandem solar cells with power conversion efficiency exceeding 10%. *Energy Environ. Sci.* **8** (10), 2902-2909 (2015).
21. J. Noh, S. Jeong and J. Y. Lee, Ultrafast formation of air-processable and high-quality polymer films on an aqueous substrate. *Nat. Commun.* **7**, 9 (2016).
22. S. Lee, J. Kong and K. Lee, Air-Stable Organic Solar Cells Using an Iodine-Free Solvent Additive. *Adv. Energy Mater.* **6** (21), 9 (2016).
23. M. J. Griffith, N. A. Cooling, B. Vaughan, D. C. Elkington, A. S. Hart, A. G. Lyons, S. Quereshi, W. J. Belcher and P. C. Dastoor, Combining Printing, Coating, and Vacuum Deposition on the Roll-to-Roll Scale: A Hybrid Organic Photovoltaics Fabrication. *IEEE J. Sel. Top. Quantum Electron.* **22** (1), 14 (2016).

24. Y. Y. Liang, Z. Xu, J. B. Xia, S. T. Tsai, Y. Wu, G. Li, C. Ray and L. P. Yu, For the Bright Future-Bulk Heterojunction Polymer Solar Cells with Power Conversion Efficiency of 7.4%. *Adv. Mater.* **22**, E135 (2010).
25. J. Nelson, Polymer: fullerene bulk heterojunction solar cells. *Mater. Today* **14** (10), 462-470 (2011).
26. F. J. Zhang, Z. L. Zhuo, J. Zhang, X. Wang, X. W. Xu, Z. X. Wang, Y. S. Xin, J. Wang, W. H. Tang, Z. Xu and Y. S. Wang, Influence of PC60BM or PC70BM as electron acceptor on the performance of polymer solar cells. *Sol. Energy Mater. Sol. Cells* **97**, 71-77 (2012).
27. D. K. Susarova, N. P. Piven, A. V. Akkuratov, L. A. Frolova, M. S. Polinskaya, S. A. Ponomarenko, S. D. Babenko and P. A. Troshin, ESR spectroscopy as a powerful tool for probing the quality of conjugated polymers designed for photovoltaic applications. *Chem. Commun.* **51** (12), 2239-2241 (2015).
28. F. Fungura, W. R. Lindemann, J. Shinar and R. Shinar, Carbon Dangling Bonds in Photodegraded Polymer: Fullerene Solar Cells. *Adv. Energy Mater.* **7** (6), 11 (2017).
29. Z. Ding, J. Kettle, M. Horie, S. W. Chang, G. C. Smith, A. I. Shames and E. A. Katz, Efficient solar cells are more stable: the impact of polymer molecular weight on performance of organic photovoltaics. *J. Mater. Chem. A* **4** (19), 7274-7280 (2016).
30. C. Boehme and K. Lips, The Investigation of Charge Carrier Recombination and Hopping Transport with Pulsed Electrically Detected Magnetic Resonance Techniques. In: *Charge Transport in Disordered Solids with Applications in Electronics*. (Wiley, Chichester, England, 2006).
31. G. Joshi, R. Miller, L. Ogden, M. Kavand, S. Jamali, K. Ambal, S. Venkatesh, D. Schurig, H. Malissa, J. M. Lupton and C. Boehme, Separating hyperfine from spin-orbit interactions in organic semiconductors by multi-octave magnetic resonance using coplanar waveguide microresonators. *Appl. Phys. Lett.* **109** (10), 191-195 (2016).
32. C. Boehme and K. Lips, Theory of time-domain measurement of spin-dependent recombination with pulsed electrically detected magnetic resonance. *Physical Review B* **68** (24), 19 (2003).
33. R. Miller, K. J. van Schooten, H. Malissa, G. Joshi, S. Jamali, J. M. Lupton and C. Boehme, Morphology effects on spin-dependent transport and recombination in polyfluorene thin films. *Physical Review B* **94** (21), 15 (2016).
34. H. Morishita, W. J. Baker, D. P. Waters, R. Baarda, J. M. Lupton and C. Boehme, Mechanisms of spin-dependent dark conductivity in films of a soluble fullerene derivative under bipolar injection. *Physical Review B* **89** (12), 7 (2014).
35. C. Boehme, D. R. McCamey, K. J. van Schooten, W. J. Baker, S. Y. Lee, S. Y. Paik and J. M. Lupton, Pulsed electrically detected magnetic resonance in organic

- semiconductors. *Physica Status Solidi B-Basic Solid State Physics* **246** (11-12), 2750-2755 (2009).
36. J. Niklas, K. L. Mardis, B. P. Banks, G. M. Grooms, A. Sperlich, V. Dyakonov, S. Beaupre, M. Leclerc, T. Xu, L. P. Yu and O. G. Poluektov, Highly-Efficient Charge Separation and Polaron Delocalization in Polymer-Fullerene Bulk-Heterojunctions: A Comparative Multi-frequency EPR and DFT Study. *Phys. Chem. Chem. Phys.* **15** (24), 9562-9574 (2013).
 37. O. G. Poluektov, S. Filippone, N. Martin, A. Sperlich, C. Deibel and V. Dyakonov, Spin Signatures of Photogenerated Radical Anions in Polymer- Fullerene Bulk Heterojunctions High Frequency Pulsed EPR Spectroscopy. *J. Phys. Chem. B* **114** (45), 14426-14429 (2010).
 38. W. Harneit, C. Boehme, S. Schaefer, K. Huebener, K. Fostiropoulos and K. Lips, Room temperature electrical detection of spin coherence in C-60. *Phys. Rev. Lett.* **98** (21), 4 (2007).
 39. D. R. McCamey, K. J. van Schooten, W. J. Baker, S. Y. Lee, S. Y. Paik, J. M. Lupton and C. Boehme, Hyperfine-Field-Mediated Spin Beating in Electrostatically Bound Charge Carrier Pairs. *Phys. Rev. Lett.* **104** (1), 017601 (2010).
 40. W. J. Baker, D. R. McCamey, K. J. van Schooten, J. M. Lupton and C. Boehme, Differentiation between polaron-pair and triplet-exciton polaron spin-dependent mechanisms in organic light-emitting diodes by coherent spin beating. *Physical Review B* **84** (16), 7 (2011).
 41. S. Y. Lee, S. Y. Paik, D. R. McCamey, J. Yu, P. L. Burn, J. M. Lupton and C. Boehme, Tuning Hyperfine Fields in Conjugated Polymers for Coherent Organic Spintronics. *J. Am. Chem. Soc.* **133** (7), 2019-2021 (2011).
 42. K. J. van Schooten, D. L. Baird, M. E. Limes, J. M. Lupton and C. Boehme, Probing long-range carrier-pair spin-spin interactions in a conjugated polymer by detuning of electrically detected spin beating. *Nat. Commun.* **6**, 9 (2015).
 43. M. Kavand, D. Baird, K. van Schooten, H. Malissa, J. M. Lupton and C. Boehme, Discrimination between spin-dependent charge transport and spin-dependent recombination in pi-conjugated polymers by correlated current and electroluminescence-detected magnetic resonance. *Physical Review B* **94** (7), 11 (2016).
 44. A. Schnegg, J. Behrends, M. Fehr and K. Lips, Pulsed electrically detected magnetic resonance for thin film silicon and organic solar cells. *Phys. Chem. Chem. Phys.* **14** (42), 14418-14438 (2012).
 45. H. Zeldes and R. Livingston, Environmental Effect on Atomic Hydrogen Hyperfine Structure in Acids. *Phys. Rev.* **96** (6), 1702-1702 (1954).
 46. G. T. Trammell, H. Zeldes and R. Livingston, Effect of Environmental Nuclei In Electron Spin Resonance Spectroscopy. *Phys. Rev.* **110** (3), 630-634 (1958).

47. J. A. Weil and J. H. Anderson, Direct Field Effects in Electron Paramagnetic Resonance Hyperfine Spectra. *J. Chem. Phys.* **35** (4), 1410-& (1961).
48. B. L. Bales and E. S. Lesin, Use of Electron Paramagnetic Resonance Matrix Spin Flip Satellite Lines as a Tool in Structural Determination of Paramagnetic Centers in Disordered Solids. *J. Chem. Phys.* **65** (4), 1299-1304 (1976).
49. J. A. Weil and D. F. Howarth, Nuclear Spin-Flip Satellites in Electron Paramagnetic Resonance Spectroscopy. *Appl. Magn. Reson.* **38** (1), 85-93 (2010).
50. J. A. Weil and J. R. Bolton, Electron Paramagnetic Resonance Elementary Theory & Practical Applications, 2nd ed. (John Wiley & Sons, Hoboken, NJ, USA, 2007).
51. I. Hiromitsu, Y. Kaimori, M. Kitano and T. Ito, Spin-dependent recombination of photoinduced carriers in phthalocyanine/C-60 heterojunctions. *Physical Review B* **59** (3), 2151-2163 (1999).
52. I. Hiromitsu, M. Kitano, R. Shinto and T. Ito, Electrically detected electron spin resonance of Pt/C-60/In/Al Schottky-barrier cell. *Synth. Met.* **121** (1-3), 1539-1540 (2001).
53. R. Glenn, W. J. Baker, C. Boehme and M. E. Raikh, Analytical description of spin-Rabi oscillation controlled electronic transitions rates between weakly coupled pairs of paramagnetic states with $S=1/2$. *Physical Review B* **87** (15), 9 (2013).
54. C. J. Brabec, V. Dyakonov, J. Parisi and N. S. Sariciftci, Organic Photovoltaics- Concepts and Realization. (Springer-Verlag Berlin Heidelberg, NY, USA, 2003).
55. P. Cheng, Y. F. Li and X. W. Zhan, Efficient ternary blend polymer solar cells with indene-C-60 bisadduct as an electron-cascade acceptor. *Energy Environ. Sci.* **7** (6), 2005-2011 (2014).
56. J. S. Kim, B. Lagel, E. Moons, N. Johansson, I. D. Baikie, W. R. Salaneck, R. H. Friend and F. Cacialli, Kelvin probe and ultraviolet photoemission measurements of indium tin oxide work function: a comparison. *Synth. Met.* **111**, 311-314 (2000).
57. A. M. Nardes, M. Kemerink, M. M. de Kok, E. Vinken, K. Maturova and R. A. J. Janssen, Conductivity, work function, and environmental stability of PEDOT : PSS thin films treated with sorbitol. *Org. Electron.* **9** (5), 727-734 (2008).
58. W. M. Middleton and M. E. Van Valkenburg, Reference Data for Engineers: Radio, Electronics, Computer, and Communications 9th Ed. (Newnes, USA, 2001).
59. S. E. Shaheen, G. E. Jabbour, M. M. Morrell, Y. Kawabe, B. Kippelen, N. Peyghambarian, M. F. Nabor, R. Schlaf, E. A. Mash and N. R. Armstrong, Bright blue organic light-emitting diode with improved color purity using a LiF/Al cathode. *J. Appl. Phys.* **84** (4), 2324-2327 (1998).
60. F. Diederich, R. Ettl, Y. Rubin, R. L. Whetten, R. Beck, M. Alvarez, S. Anz, D. Sensharma, F. Wudl, K. C. Khemani and A. Koch, The Higher Fullerenes - Isolation

- and Characterization of C76, C84, C90, C94, and C70O, an Oxide of D5H-H70. *Science* **252** (5005), 548-551 (1991).
61. K. M. Creegan, J. L. Robbins, W. K. Robbins, J. M. Millar, R. D. Sherwood, P. J. Tindall, D. M. Cox, A. B. Smith, J. P. McCauley, D. R. Jones and R. T. Gallagher, Synthesis and Characterization of (C60)O, the 1st Fullerene Epoxide. *J. Am. Chem. Soc.* **114** (3), 1103-1105 (1992).
 62. D. Heymann and R. B. Weisman, Fullerene Oxides and Ozonides. *C. R. Chim.* **9** (7-8), 1107-1116 (2006).
 63. A. Colligiani and C. Taliani, ESR Study on the Doublet and Triplet Species Present in Pristine C-60 Fullerene Powder. *Chem. Mater.* **6** (10), 1633-1637 (1994).
 64. E. A. Katz, A. I. Shames, D. Faiman, S. Shtutina, Y. Cohen, S. Goren, W. Kempinski and L. Piekara-Sady, Do Structural Defects Affect Semiconducting Properties of Fullerene Thin Films? *Physica B-Condensed Matter* **273-4**, 934-937 (1999).
 65. P. Paul, K. C. Kim, D. Y. Sun, P. D. W. Boyd and C. A. Reed, Artifacts in the electron paramagnetic resonance spectra of C-60 fullerene ions: Inevitable C120O impurity. *J. Am. Chem. Soc.* **124** (16), 4394-4401 (2002).
 66. L. A. Frolova, N. P. Piven, D. K. Susarova, A. V. Akkuratov, S. D. Babenko and P. A. Troshin, ESR spectroscopy for monitoring the photochemical and thermal degradation of conjugated polymers used as electron donor materials in organic bulk heterojunction solar cells. *Chem. Commun.* **51** (12), 2242-2244 (2015).
 67. M. O. Reese, A. M. Nardes, B. L. Rupert, R. E. Larsen, D. C. Olson, M. T. Lloyd, S. E. Shaheen, D. S. Ginley, G. Rumbles and N. Kopidakis, Photoinduced Degradation of Polymer and Polymer-Fullerene Active Layers: Experiment and Theory. *Adv. Funct. Mater.* **20** (20), 3476-3483 (2010).
 68. F. Kraffert, R. Steyrlleuthner, C. Meier, R. Bittl and J. Behrends, Transient electrically detected magnetic resonance spectroscopy applied to organic solar cells. *Appl. Phys. Lett.* **107** (4), 5 (2015).

6 Polaron Electronic Structure, Charge Separation and Triplet Exciton Formation Pathways in All Molecular Solar Cells

6.1 Introduction

In this chapter steady state and time resolved EPR spectroscopy is used to investigate the polaron electronic structure, charge separation and triplet exciton formation pathways in the DTS family of small molecule solar cells. Using high frequency EPR the principal values of the g-tensors of the DTS molecules were determined for the first time. Comparison of the experimental values with those from DFT calculations and supporting ENDOR spectroscopy reveals that the positive polaron is delocalised over two to three units of the donor molecule which may lead to more efficient charge separation in these systems. Using TR-EPR the variation of charge separation across the DTS family was investigated, which reveals that charge separation is slower in the [1,2,5]thiadiazolo[3,4-c]pyridine donor blend compared with the fluorobenzothiadiazole donor blends. The slower charge separation in the [1,2,5]thiadiazolo[3,4-c]pyridine blend is accompanied by a higher population of triplet excitons formed by back electron transfer from the triplet polaron pair. This finding demonstrates that back electron transfer to the triplet of the donor is a loss mechanism in these molecular systems when charge separation is slow.

All experimental work presented in this chapter was undertaken at Argonne National Laboratory. The 9.8 GHz LEPR, ENDOR and TR-EPR measurements of DTS(FBTTh₂), DTG(F₂BTTh₂) and DTS(PTTh₂)₂ were obtained during my visit to ANL, where the sample preparation and EPR spectroscopy was jointly undertaken by Dr. Jens Niklas, Dr. Oleg Poluektov and myself. The 9.8 GHz EPR spectroscopy of DTS(F₂BTTh₂) and DTG(FBTTh₂) was carried out at a later date by Dr. Jens Niklas. The 130 GHz spectra were measured by Dr. Oleg Poluektov. The data processing, spectral fitting, and analysis of all experimental data was performed by me and is therefore included in this chapter. The work was also supported by DFT calculations undertaken by the group of Prof. Kirsty Mardis at Chicago State University. This chapter forms the basis of the paper “Charge Separation and Triplet Exciton Formation Pathways in Small Molecule Solar Cells as Studied by Time-resolved EPR Spectroscopy”^[1].

6.2 Background

Since the introduction of the bulk introduction concept,^[2] the field of organic photovoltaics has been dominated by blends of conjugated polymer donors with a fullerene based acceptor. Replacing the conjugated polymer donor with a small molecule has received increasing interest over the last decade.^[3] Switching from polymeric to small molecule donors is desired as they offer several potential advantages. Synthetically small molecules have a simpler work-up and are easier to purify than polymers which could reduce costs.^[3, 4] They have reduced batch to batch variation which enables the fabrication OPV cells with more reproducible performance.^[3] Furthermore they have well defined molecular structures which enable better energy level control and allow structure property relationships to be more easily established.^[5, 6] The efficiency of all molecular OPV cells has increased rapidly with PCEs of 8-10 % now being routinely achieved.^[3, 5, 7, 8] The charge separation and electronic excited states in these molecular systems have received far less attention than their polymeric counterparts, particularly from an EPR perspective. We therefore employed EPR spectroscopy combined with DFT calculations to explore the electronic states and charge separation dynamics in a blend of the DTS family of donors with PC₆₁BM. The DTS family has achieved widespread success with reported PCEs ranging from 6.7 to 8.3 % across the family.^[9, 10]

6.3 Materials

6.3.1 DTS Family of Small Molecule Donors

The DTS family of small molecule donors was developed by the Bazan group and are shown in Figure 6.1. The family utilises a donor/acceptor/donor/acceptor/donor framework which promotes intramolecular charge transfer and lowering of the bandgap, resulting in improved absorption characteristics. The central donor unit of the molecule is either a dithienosilole (DTS) or dithienogermole (DTG). The acceptor groups are either [1,2,5]thiadiazolo[3,4-c]pyridine (PT) or fluorobenzothiadiazoles with one (FBT) or two (F₂BT) fluorine electron withdrawing groups. Bithiophene units form the outer donors. DTS(PTTh₂)₂ was the first in the family and achieved an efficiency of 6.7 % when

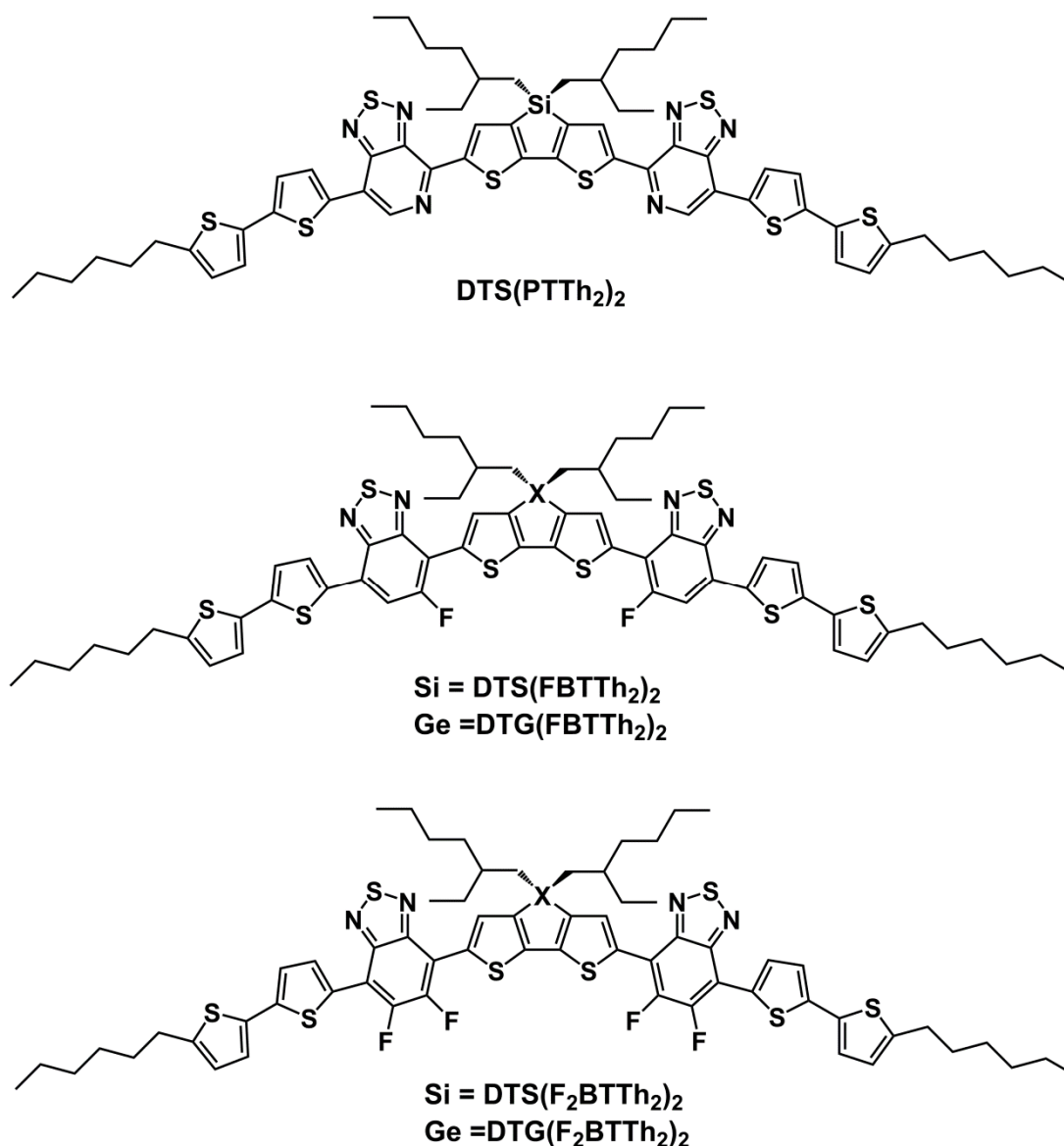


Figure 6.1 DTS family of small molecule electron donors.

blended with PC₇₁BM.^[9] This was followed DTS(FBTTh₂)₂ which replaced the PT acceptor units with FBT.^[11] The replacement of PT with FBT made the cells more compatible with the popular interlayer PEDOT:PSS as the basic PT unit tended to react with the acidic PEDOT:PSS. It also improved the efficiency to 7.0 %, which has later been optimised to over 8 %.^[10] An analogue of DTS(FBTTh₂)₂ was synthesised where the central silicon atom was replaced with germanium in the hopes that the increased C-Ge bond length would lead to better molecular ordering.^[12] This did not prove to be true and DTG(FBTTh₂)₂ achieved slightly lower performance than DTS(FBTTh₂)₂.^[12, 13] Two further analogues have been synthesised where an extra fluorine has been added to the

FBT groups in order to increase the electron withdrawing power, no cells using these analogues have been reported to date. All members of the DTS family used in this study were purchased from 1-Material and used without further purification.

6.3.2 PC₆₁BM

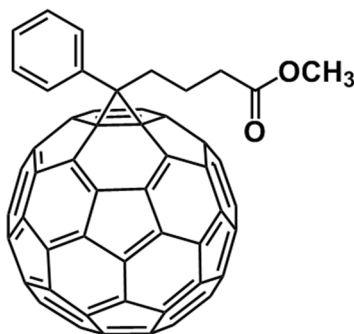


Figure 6.2 PC₆₁BM

[6,6]-Phenyl-C₆₁-butyric acid methyl ester (PC₆₁BM) is a soluble fullerene derivative that has been extensively used as the electron acceptor in OPV cells and is the archetypical acceptor molecule. PC₆₁BM was purchased from Sigma Aldrich (684449) had a purity of > 99.5 % and used without further purification.

6.4 Experimental

The donor molecule and PC₆₁BM were dissolved in anhydrous chlorobenzene in a 3:2 weight ratio to give a total concentration of 20 mg cm⁻³ inside a nitrogen drybox. For frozen solution samples, the solution was pipetted into quartz EPR tubes which were then sealed under nitrogen atmosphere using paraffin film and quickly transferred to spectrometer lab, while being kept in the dark, where they were flash frozen in liquid nitrogen. Film samples were prepared by pumping on the tube using a Schlenk line which slowly removed the solvent and left a thick film coating. The tubes were then sealed with paraffin film under a nitrogen atmosphere.

6.5 Results

6.5.1 9.8 GHz LEPR of DTS(FBTTh₂)₂:PC₆₁BM Blend

To observe the electronic excited states in these materials light induced EPR (LEPR) was used. In a high performance OPV cells the donor molecules under study are normally blended with PC₇₁BM due to its improved absorption coefficient compared with PC₆₁BM. However it has been shown that the negative polaron on PC₇₁BM spectrally overlaps with positive polaron of many common electron donors.^[14, 15] The donors were therefore blended with PC₆₁BM, which has a characteristically low g-factor compared with most organic radicals,^[15] in order to avoid spectral overlap of the positive and negative polarons which would have greatly complicated the interpretation of the spectra. PC₆₁BM is also a widely used acceptor in OPV cells with similar energy levels to PC₇₁BM and it has been shown that the replacement of PC₇₁BM by PC₆₁BM does not change the behaviour of the positive polaron on the donor.^[15] The results obtained in this study are therefore relevant to the blends used in high performance cells.

A 3:2 DTS(FBTTh₂)₂:PC₆₁BM solution was prepared in chlorobenzene and flash frozen in liquid nitrogen. The dark EPR spectrum is shown in Figure 6.3a and consists of several weak features centred close to $g = g_e$. The dark spectrum likely arises from a small number of paramagnetic defect sites in the sample. The sample was then illuminated using a white light source. The light on EPR spectrum is shown in Figure 6.3b and is approximately a

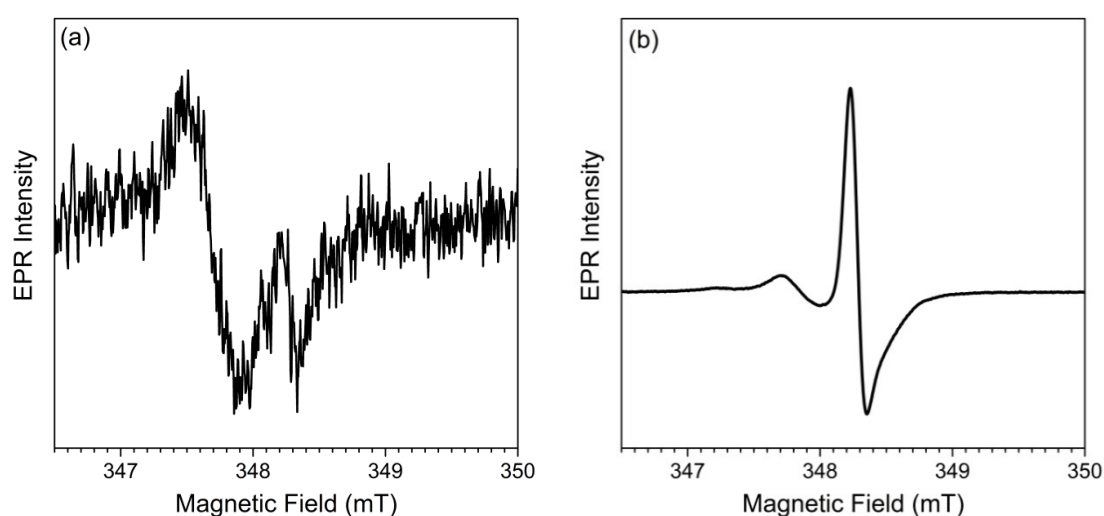


Figure 6.3 9.8 GHz EPR spectrum of DTS(FBTTh₂)₂:PC₆₁BM in (a) the dark and (b) under illumination. Spectra were recorded at 50 K in a frozen chlorobenzene solution.

factor of 50 stronger than the dark.

The spectrum was simulated using a broad low field component centred on $g \approx 2.0025$ (green) and a narrower high field line centred on $g \approx 1.9999$ (blue) as shown in Figure 6.4. The component centred on 2.0025 has a rhombic g-tensor while the high field component is axially symmetric. Based on previous EPR studies of donor:fullerene blends the high field component can be definitively assigned to negative polarons (P^-) residing on the $PC_{61}BM$, and the low field component centred on 2.0025 must therefore correspond to positive polarons (P^+) on the $DTS(FBTTh_2)_2$.^[15-20] The integrated intensity

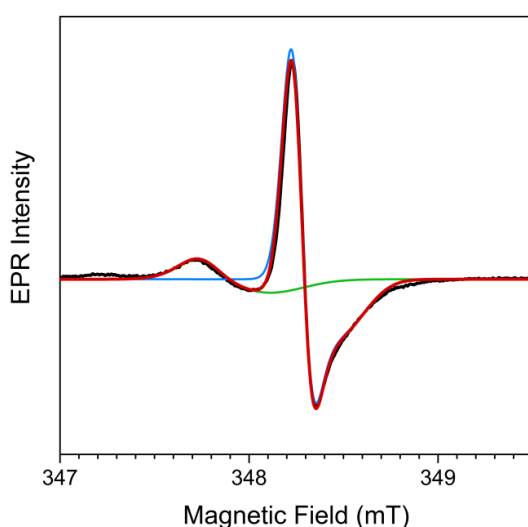


Figure 6.4 9.8 GHz LEPR spectrum of $DTS(FBTTh_2)_2:PC_{61}BM$ in chlorobenzene solution. The dark spectrum was subtracted from the light one. The experimental spectrum is shown in black, the P^+ sim in green, the P^- sim in blue and the total simulation in red.

of the P^+ component is 40 % of the P^- . This reduced intensity arises from the long spin lattice relaxation time of the donor which caused partial saturation of the P^+ resonance. It can be seen from Figure 6.4 that there is an additional bump on the extreme low field side of the spectrum that is not replicated by the simulation. This bump cannot be accommodated by extending the anisotropy of the P^+ g-tensor which suggests that it is a third independent component. This is supported by varying the microwave power as shown in Figure 6.5. At lower microwave power (blue) the height difference between the P^+ peak and the extra peak is greater than higher power (red). The different scaling behaviour with microwave power suggests that they are independent and the extra bump belongs to a third component. This low field bump is therefore assigned to impurities in

the supplied donor material. This is based on the observation of similar shoulder features previously in PTB7 (J. Niklas, personal communication, April 2015).

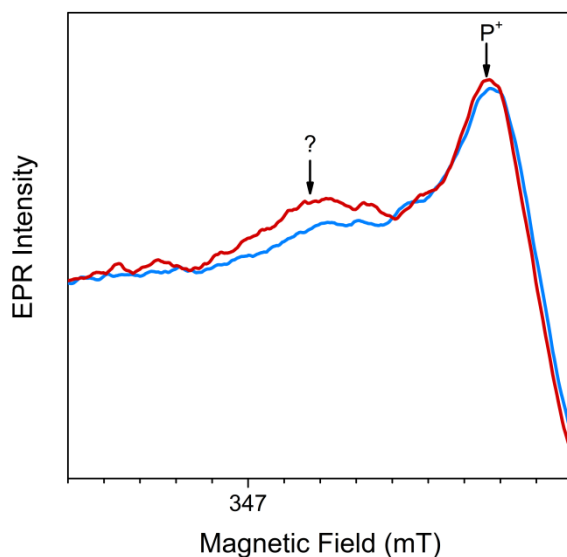


Figure 6.5 Influence of microwave power on the shoulder feature of the 9.8 GHz EPR spectrum of DTS(FBTTh₂)₂:PC₆₁BM

The illumination dynamics of the LEPR spectrum of DTS(FBTTh₂)₂:PC₆₁BM is shown in Figure 6.6. When the sample is first exposed to light the EPR intensity initially increases rapidly before reaching a plateau over the course of several minutes. The height of the plateau is determined by the competition between charge generation and bimolecular recombination in the sample. When charge generation and bimolecular recombination are in equilibrium the charge carrier concentration in the sample will remain constant and the EPR intensity therefore plateaus. After the light is switched off there is an initial rapid decay over several seconds followed by a much longer decay lasting hours. These two decay regimes are attributed to shallow and deep energetic traps in the sample and have been observed previously.^[21, 22] The charges in shallow traps are relatively mobile and therefore recombine bimolecularly (see Eq. 2.4) and are presumed responsible for the rapid decay. In contrast the charges in deep traps are immobile and recombination is expected to take place through a much slower tunnelling process which gives rise to the slow component in Figure 6.6.^[23] No difference in lineshape was observed when measuring with light on (shallow and deep) and after light (deep only) and all spectra were therefore recorded with light on to improve signal to noise.

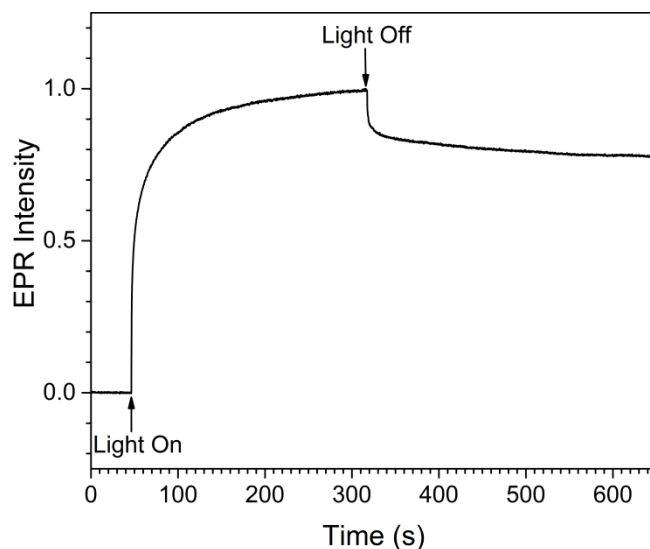


Figure 6.6 EPR Kinetics of DTS(FBTTh₂)₂:PC₆₁BM at 50 K. Spectrum was recorded while sitting at the maximum of the spectrum.

Film samples of DTS(FBTTh₂)₂:PC₆₁BM were also prepared. A comparison of the solution and film EPR spectrum recorded under the same experimental conditions is shown in Figure 6.7. The EPR spectrum of the film (red) and the frozen solution (blue) samples are similar. The only notable difference is in the width of the P⁻ component, which is narrower in the film. This is due to the fact that when in frozen solution the spectrum of P⁻ is broadened by weak coupling to ¹H on the solvent molecules and a shifting of the g_z value which is known to be very sensitive to the local environment.^[24]

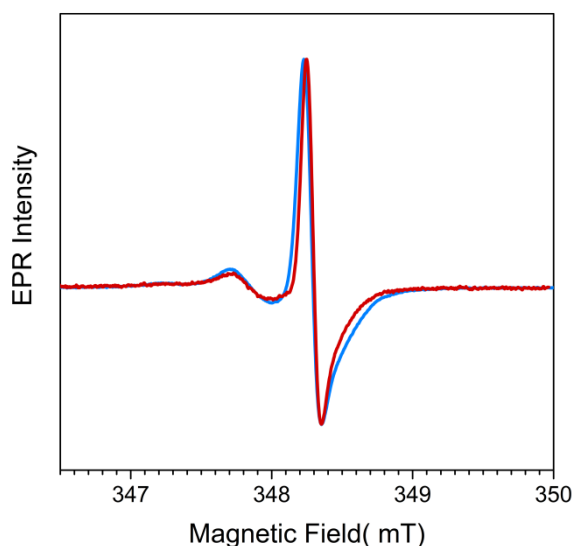


Figure 6.7 Comparison of solution and film 9.8 GHz EPR spectrum of DTS(FBTTh₂)₂:PC₆₁BM. The solution spectrum is shown in blue and the film in red. Both spectra were recorded at 50 K using the same experimental conditions.

6.5.2 9.8 GHz LEPR of donor:PC₆₁BM Blends

LEPR spectra of the other four donor materials blended with PC₆₁BM were also measured in both solution and film. In all cases a strong light induced EPR signal was detected consisting of a broad low field component centred around $g = 2.0025$ corresponding to P⁺ on the donor and the narrow high field signal of P⁻ on PC₆₁BM. The film and solution

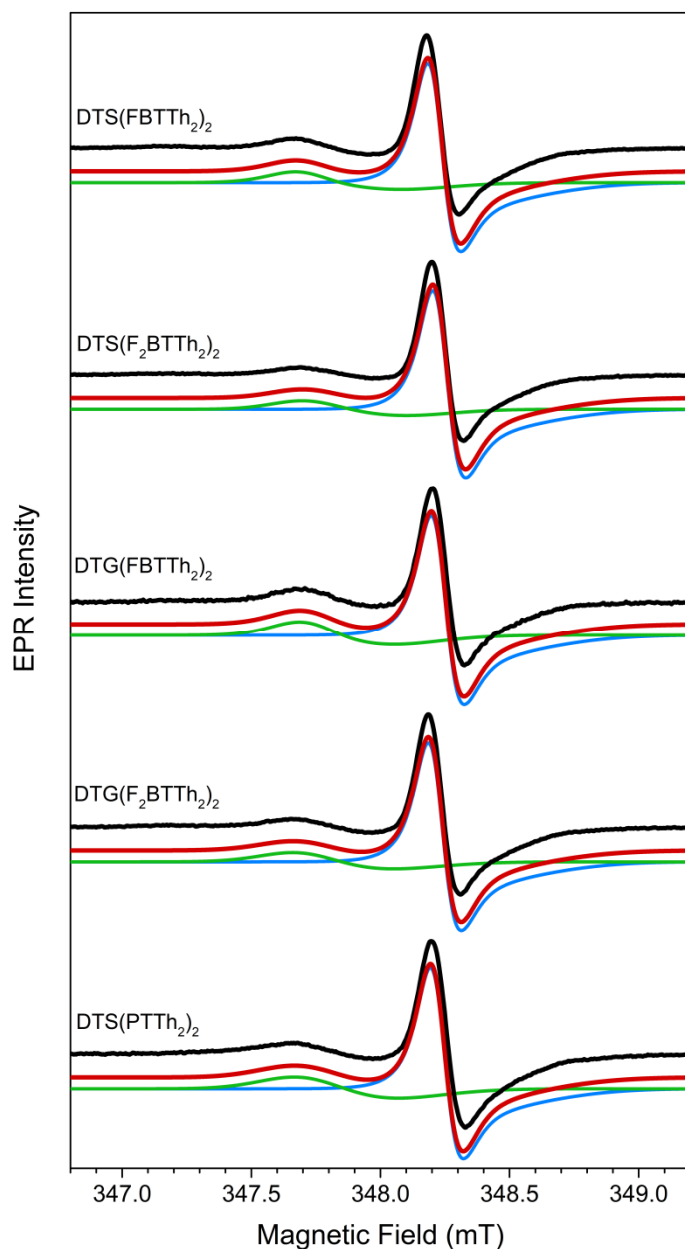


Figure 6.8 9.8 GHz LEPR spectra of dithienosilole and dithienogermole based donors blended with PC₆₁BM in frozen chlorobenzene solution at T = 50 K. The experimental spectra (black) are shown alongside theoretical simulations of the positive polaron residing on the donor (green), negative polaron on the PC₆₁BM (blue) and the superposition of both (red). Spectra were corrected to account for small differences in microwave frequency.

samples of the various blends all exhibited similar spectra and behaviour to the previously discussed DTS(FBTTh₂)₂:PC₆₁BM. The LEPR spectra of the five blends are shown in Figure 6.8 alongside their theoretical simulation. The four fluorobenzothiadiazole (FBT and F₂BT) appear to be almost identical within the limited resolution of 9.8 GHz LEPR. The DTS(PTTh₂)₂ spectrum is similar but it can be seen that the P⁺ component is noticeably broader than the other four. In order to gain further information about the electronic structure of the P⁺ on each donor, high field 130 GHz spectra were taken.

6.5.3 130 GHz LEPR of donor: PC₆₁BM

The 130 GHz LEPR spectra of the five donors blended with PC₆₁BM are shown in Figure 6.9. At 130 GHz the P⁺ and P⁻ components no longer overlap making the spectral fitting more reliable. Furthermore it can be seen that the anisotropy in the P⁺ g-tensor is resolved allowing the principal values of the g-tensor to be determined. The P⁻ on PC₆₁BM was essentially invariant across the five blends and could be accurately simulated using a nearly axial g-tensor with principal values of $g_x = 2.0006$, $g_y = 2.0004$, $g_z = 1.9989$; although the high degree of g-strain makes the g_z component difficult to determine accurately. These principal values are in good agreement to those previously reported in other donor:PC₆₁BM systems.^[14, 15, 17, 20, 24] The principal values of the g-tensors of P⁺ on the five donor molecules are summarised in Table 1. All donors exhibit a rhombic g-tensor with three clearly distinguished principal values. Looking at Table 6.1 it can be seen that the g-tensor is similar across the four fluorobenzothiadiazole donors. The replacement of silicon with germanium only induces a small shift (0.0002/3) in g_y to higher values. The insensitivity of the g-tensor to the replacement of silicon with

Table 6.1 Principal values of the polaron g-tensors. The relative error in the principal values is ± 0.0002 . The error in the g_z component of PC₆₁BM⁻ is larger, ± 0.0004 , due to the high g-strain.

Polaron	g_x	g_y	g_z
DTS(FBTTh ₂) ₂ ⁺	2.0035	2.0024	2.0017
DTS(F ₂ BTTh ₂) ₂ ⁺	2.0035	2.0023	2.0016
DTG(FBTTh ₂) ₂ ⁺	2.0034	2.0026	2.0016
DTG(F ₂ BTTh ₂) ₂ ⁺	2.0034	2.0027	2.0016
DTS(PTTh ₂) ₂ ⁺	2.0034	2.0024	2.0020
PC ₆₁ BM ⁻	2.0006	2.0004	1.9989

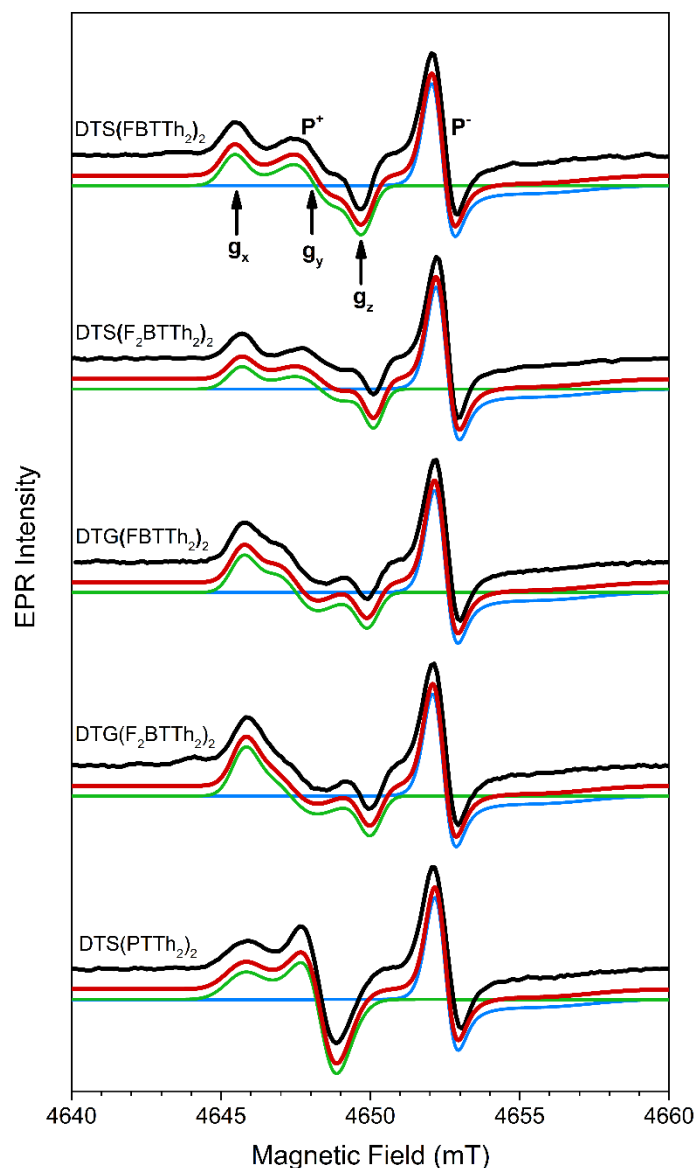


Figure 6.9 130 GHz LEPR spectra of dithienosilole and dithienogermole based donors blended with PC₆₁BM in frozen chlorobenzene solution at T = 50 K. The experimental spectra (black) are shown alongside theoretical simulations of the positive polaron residing on the donor (green), negative polaron on the PC₆₁BM (blue) and the superposition of both (red). Spectra were corrected to account for small differences in microwave frequency. The experimental spectra were pseudo modulated to give a first derivative lineshape.

germanium shows that the choice of central heteroatom has little influence on the electronic properties of the molecule. Similarly, the replacement of the FBT electron withdrawing group with F₂BT has no influence on the g-tensor. Comparing the g-tensor of DTS(PTTh₂)₂ to the fluorobenzothiadiazoles, it can be seen that DTS(PTTh₂)₂ is marginally less anisotropic with a higher g_z component of 2.0020.

6.5.4 ENDOR of DTS(FBTTh₂)₂:PC₆₁BM

The strength of the hyperfine interaction (hf) between the polaron and magnetic nuclei in the sample provides useful information on the extent of polaron delocalisation over the molecule. A more localised polaron will result in larger hf-coupling strengths. The magnetic nuclei present, in sufficient natural abundance, in the donor molecules under study are ¹H, ¹⁴N and ¹⁹F. The hyperfine couplings of P⁺ to magnetic nuclei are not resolved in the 9.8 GHz and 130 GHz LEPR spectra and pulsed ENDOR spectroscopy was therefore used to measure the hf-coupling strength.

The ENDOR spectra of P⁺ and P⁻ of DTS(FBTTh₂)₂:PC₆₁BM in frozen solution is shown in Figure 6.10. The ENDOR spectra were taken at two magnetic field positions, corresponding to the maxima of the P⁺ and P⁻ components of the field swept echo spectrum as shown in the inset of Figure 6.10. The ENDOR spectra are centred on the proton Larmor frequency which is 14.8 MHz at ~ 347 mT. The spectrum taken at the P⁺ field position consists of two broad overlapping peaks with a sharp peak in the centre. The two broad peaks correspond to hyperfine coupling to the P⁺. The central peak is due to hyperfine coupling to P⁻ and arises because the excitation width of the pulses in the ENDOR sequence is broad enough to excite a small number of P⁻. Reciprocally the P⁻ ENDOR spectrum is dominated by a sharp central peak and weaker broad wings for the reverse reason.

It can be seen that the P⁺ ENDOR spectrum is asymmetric with more spectral density on the low frequency side. This asymmetry arises from coupling to ¹⁹F which has a Larmor frequency of 13.9 MHz at 347 mT. The coupling to ¹⁹F suggests that some spin density is delocalised over the fluorines. The P⁺ was recorded using Mims and Davies pulse sequences (See Section 4.3.3). The Mims sequence has substantially better signal to noise than Davies but suffers from periodic blind spots which might obscure larger couplings. A low resolution Davies spectrum was therefore taken to check the linewidth. The Mims and Davies spectra have similar lineshapes and both give the same ¹H linewidth. The ¹⁹F coupling is more pronounced in the Davies spectrum as can be seen by the more obvious low frequency shoulder, but it is the same width. No coupling to ¹⁴N was detected.

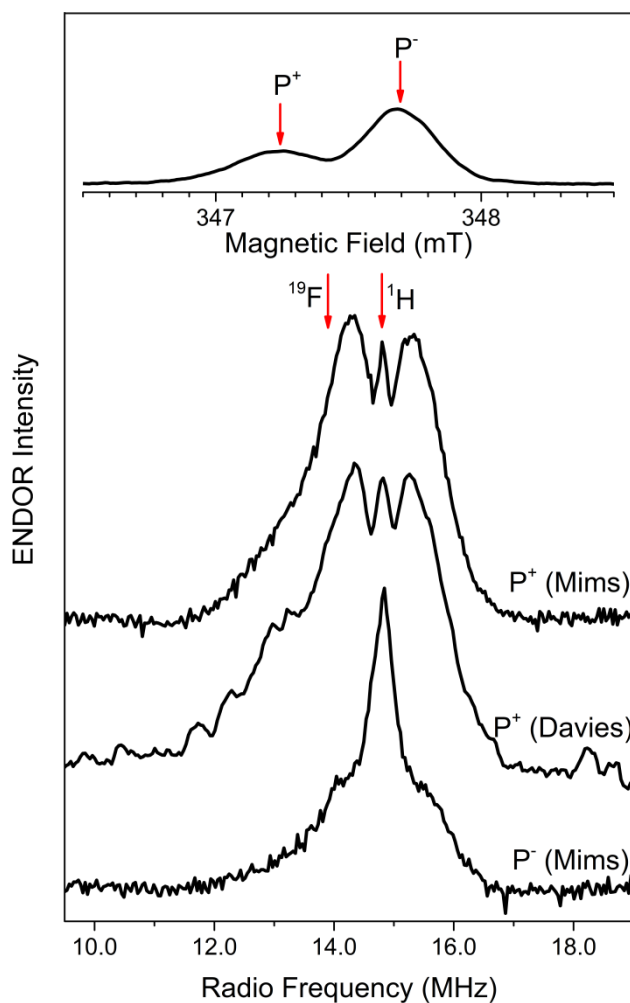


Figure 6.10 Light induced 9.8 GHz ENDOR spectra of DTS(FBTTh₂)₂:PC₆₁BM in frozen chlorobenzene solution at T = 50 K. The arrows in the main figure mark the Larmor frequency of ¹H and ¹⁹F at a magnetic field of 347 mT. The top inset shows the field swept echo spectrum and the positions where the ENDOR spectra were recorded.

The polaron delocalisation and distribution is best estimated using the coupling to ¹H. As explained in Section 3.3 the hyperfine interaction is composed of two parts; an isotropic contact interaction and an anisotropic part due to dipolar coupling. The dipolar coupling to ¹H in these systems is generally small and the width and shape of the spectrum can be described through the isotropic interaction. The greater the polaron spin density at a given magnetic nucleus the greater the strength of the isotropic hyperfine coupling to that nucleus. Increasing polaron delocalisation decreases the spin density at each nucleus, reducing the isotropic coupling. Increasing polaron delocalisation therefore lowers the largest detected hf-coupling which corresponds to a narrowing of the ENDOR spectrum. To avoid the contribution from ¹⁹F the strength of the ¹H coupling is best estimated using the distance from the centre of the spectrum to the high frequency side at half maximum,

and then doubling that value to give the FWHM. Using this definition the ^1H coupling has an associated FWHM of 2.4 ± 0.2 MHz which is similar to that reported for common donor polymers.^[24] The ENDOR spectra of a film sample of $\text{DTS}(\text{FBTTh}_2)_2\text{:PC}_{61}\text{BM}$ was also measured in order to check if the delocalisation of the polaron is altered by the transition from frozen solution to film. A comparison of the film (red) and frozen solution (black) ENDOR spectra is shown in Figure 6.11. The width of the film sample appears to be slightly narrower than the frozen solution but there is little difference. This shows that the P^+ delocalisation is effectively unchanged when moving from frozen solution to film.

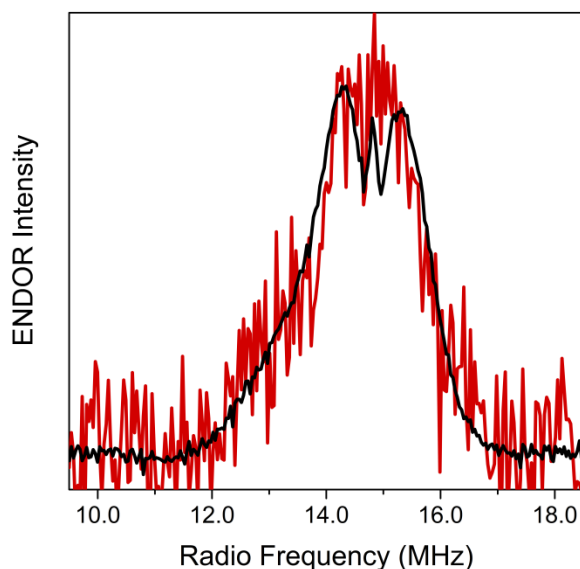


Figure 6.11 Light induced 9.8 GHz ENDOR spectra of $\text{DTS}(\text{FBTTh}_2)_2\text{:PC}_{61}\text{BM}$ in frozen chlorobenzene solution (black) and solution cast film (red) at $T = 50$ K.

6.5.5 ENDOR of donor: PC_{61}BM blends

ENDOR spectra of the remaining four donor: PC_{61}BM blends were recorded in frozen solution and film in a similar manner to the previous section. A comparison of the ENDOR spectra of P^+ in the five blends in frozen solution is shown in Figure 6.12 and the FWHM of the ^1H hyperfine coupling distributions listed in Table 6.2. The ENDOR spectra of P^+ on the four fluorobenzothiadiazole blends are similar in width, with a FWHM of 2.4 / 2.5 MHz which indicates that the polaron delocalisation is insensitive to the choice of heteroatom and to the number of fluorine substituents. It can be seen that the asymmetry due to the ^{19}F coupling is more pronounced in the F_2BT than the FBT as would be expected. The ENDOR spectrum of P^+ on $\text{DTS}(\text{PTTh}_2)_2$ is symmetric, as it

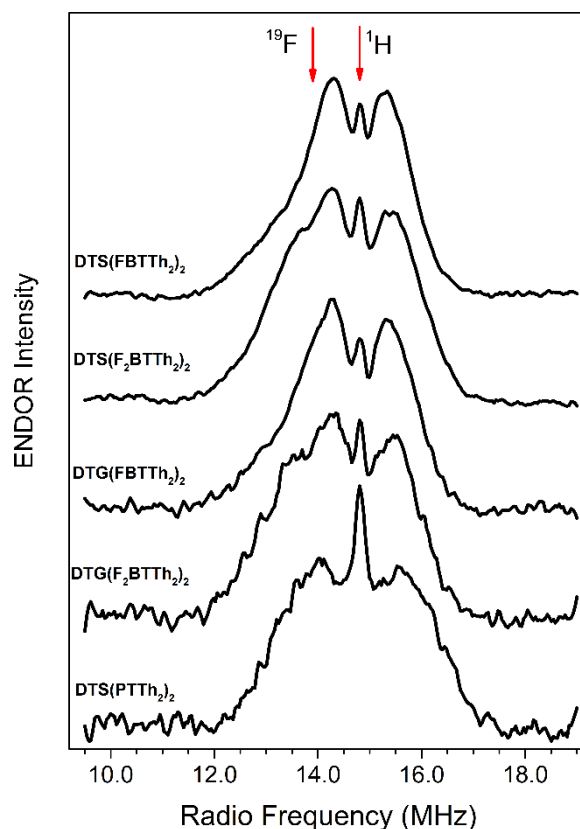


Figure 6.12 Light induced 9.8 GHz ENDOR spectra of dithienosilole and dithienogermole based donors blended with PC₆₁BM in frozen chlorobenzene solution at T = 50 K using the Mims pulse sequence. The arrows mark the Larmor frequency of ¹H and ¹⁹F at a magnetic field of 347 mT.

contains no fluorine, and is broader than the fluorobenzothiadiazoles with a FWHM of 3.2±0.2 MHz suggesting that the polaron is differently distributed on this donor molecule. The stronger hyperfine coupling in DTS(PTTh₂)₂:PC₆₁BM is in agreement with the larger linewidth of P⁺ seen in the 9.8 GHz LEPR spectrum.

Table 6.2 FWHM of the ¹H hyperfine coupling distribution in the ENDOR spectra.

Donor	¹ H FWHM
DTS(FBTTh ₂) ₂ ⁺	2.4±0.2
DTS(F ₂ BTTh ₂) ₂ ⁺	2.5±0.2
DTG(FBTTh ₂) ₂ ⁺	2.4±0.2
DTG(F ₂ BTTh ₂) ₂ ⁺	2.5±0.2
DTS(PTTh ₂) ₂ ⁺	3.2±0.2

6.5.6 Comparison of Experimental Results with DFT Calculations

DFT electronic structure calculations of P⁺ on the five donor molecules were performed by Prof. Kirsty Mardis and Mr. Christopher Mallares at Chicago State University. From these calculations spin density distributions, g-tensors and hyperfine coupling constants

of the donors were obtained. The calculated g-factors exhibited the same invariance with choice of heteroatom (Si or Ge) as seen in the experimental results. This is supported by the spin density plots (Figure 6.13) which show that there is no spin density on the central heteroatom and it is therefore not surprising that it does not influence the observed g-tensor.

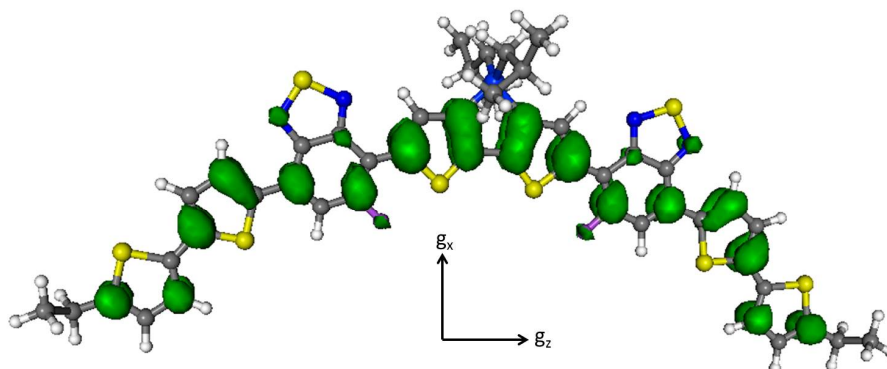


Figure 6.13 Optimised structure and spin density iso-surface of DTS(FBTTh₂)₂.

The donor molecules can adopt different conformations depending on the rotation of the thiophene units that make up the back bone. In a pure trans conformation the sulphur atom on each thiophene unit is on the opposite side to the sulphurs on adjacent thiophene units, as shown in Figure 6.13. In pure cis all sulphurs are on the same side, part trans and part cis conformations are also possible. DFT calculations showed that the pure trans conformation has the lowest energy, but the difference is not large enough to definitively select one conformation over another and there may therefore be a distribution of conformations present in the measured samples.

A comparison of the experimental and calculated principal values of DTS(FBTTh₂)₂ is shown in Table 6.3. Comparing the top three rows of Table 6.3 it can be seen that regardless of the conformation of the donor (cis or trans) the DFT calculations fail to reproduce the experimental principal values of DTS(FBTTh₂)₂. In general it seems that a cis conformation better reproduces the experimental g_x and g_y values while a trans conformation produces g_y and g_z values. Mixed cis/trans conformations produce similar principal values to the pure cis case. Even with the assumption of a distribution of

conformers in the experimental samples, the discrepancy between the calculated and measured g-factors is not resolved as g_x and g_z are underestimated in all cases.

Table 6.3 g-factors of DTS(FBTTh₂)₂ obtained by DFT electronic structure calculations

Structure	g_x	g_y	g_z
Experimental	2.0035	2.0024	2.0017
Monomer (cis)	2.0029	2.0023	2.0008
Monomer (trans)	2.0025	2.0022	2.0012
Dimer (cis)	2.0038	2.0025	2.0007
Dimer (trans)	2.0028	2.0024	2.0017

To reconcile this discrepancy, Mardis and Mallares constructed dimers with an overall +1 charge. The formation of such dimers was found to be energetically favourable, at least in the gas phase, and is in agreement with work by Reichenberger et al.,^[25] who showed that DTS(FBTTh₂)₂ forms aggregates when concentrated solutions are cooled. The principal values of the dimer models are listed in Table 6.3 and show improved agreement to the experimental values. Dimers in the cis conformation accurately reproduce g_x and g_y while trans conformation dimers reproduce g_y and g_z . While there is still a discrepancy it is a significant improvement over the monomer case which simultaneously underestimated g_x and g_z in all conformations. The calculated g-factors of dimers of the four other donor molecules showed similar improvement over the monomer case. Given the improvement obtained by the dimers, a trimer was also calculated. This was found to be energetically stable and had similar principal values to the dimer models. Therefore based on a comparison of the DFT and experimental principal values the, positive polaron is likely spread over a dimer or higher order aggregate in these systems.

Spin density plots of the dimer model (Figure 6.14) show that the spin density is distributed equally over both constituent molecules. A similar equal delocalisation of spin density is seen in the trimer. As discussed in Section 6.5.5 the isotropic hyperfine coupling constant is proportional to the spin density at the nucleus. Delocalisation of the polaron over a dimer or trimer will therefore reduce the hyperfine coupling constants to approximately one half and one third of the monomer values respectively. Consequently if the dimer/trimer formation suggested by the g-tensor comparison is correct, the ENDOR spectra of the donors should exhibit reduced hyperfine coupling constants.

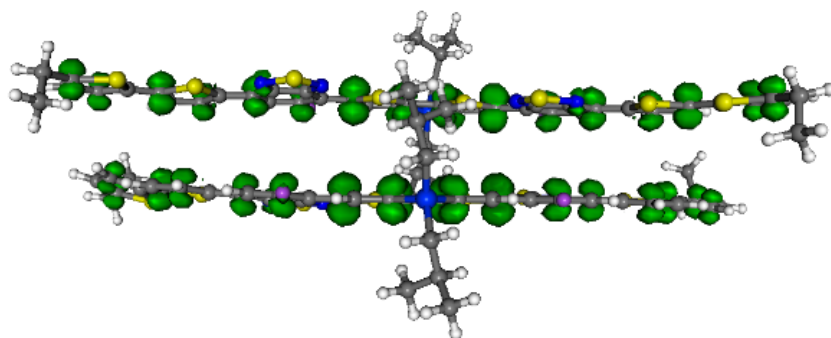


Figure 6.14 Optimised structure and spin density iso-surface of DTS(FBTTh₂)₂ dimer.

Mardis and Mallares calculated ¹H hyperfine coupling constants of the monomer, dimer and trimer of DTS(F₂BTTh₂)₂. Using these calculated values the ¹H ENDOR spectrum of DTS(F₂BTTh₂)₂ can be simulated. There are many small hyperfine couplings to ¹H on alkyl chains which do not influence the width of the ENDOR spectrum, these were discarded and the twelve ¹H with the largest hyperfine coupling were chosen for the simulation; all of which are on the conjugated backbone of the molecule. The influence of the relative orientation of the A and g tensors on the simulated spectra was checked and found to have no influence on the simulated spectra and the A and g frame were therefore chosen to be co-aligned. To accurately simulate the experimental ENDOR spectrum the quirks of the ENDOR measurement have to be taken into account. The Mims pulse sequence causes periodic suppression of the ENDOR intensity resulting in blind spots (holes) in the ENDOR spectrum. The Mims suppression function is given by,^[26, 27]

$$F_{ENDOR} \propto \sin^2(\pi A\tau) \quad (6.1)$$

where F_{ENDOR} is the ENDOR intensity, τ is the time interval between the first and second pulses in the Mims pulse sequence and A is the hyperfine coupling constant. Eq. 6.1 shows that there will be holes in the ENDOR spectrum at $A\tau = 0, 1, 2, \dots, n$. The interpulse separation used in the ENDOR experiments was 160 ns and the suppression caused by this pulse length is shown in Figure 6.15 by the green line. The black line is the pre-suppression simulated ¹H ENDOR spectrum using the twelve largest hyperfine coupling tensors obtained from the DFT calculation of the DTS(F₂BTTh₂)₂ monomer. The pre-

suppression simulation is dominated by a central peak corresponding to weakly coupled ^1H , however these couplings are removed by the Mims suppression resulting in a hole in the centre of the spectrum as shown by the red line. Theoretically the ENDOR intensity drops to zero at the holes but in general there is always a residual intensity present in the experimental spectra.

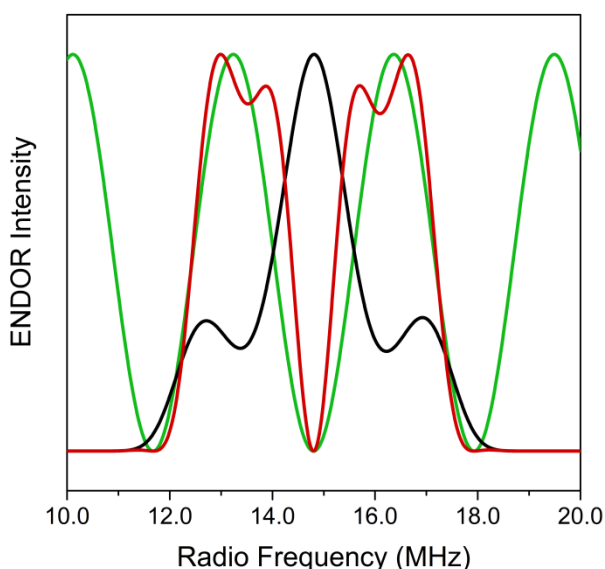


Figure 6.15 Influence of the Mims ENDOR suppression function on the ^1H simulation of $\text{DTS}(\text{F}_2\text{BTTh}_2)_2$. The unsuppressed ENDOR simulation is shown in black, the suppressed in red and the suppression function in green.

The experimental ENDOR spectrum of $\text{DTS}(\text{F}_2\text{BTTh}_2)_2$ together with ^1H ENDOR simulations of the monomer, dimer and trimer are shown in Figure 6.16. In order to reliably compare the width of experimental and simulated spectra the high frequency side of the spectra should be used as the reference in order to avoid the ^{19}F coupling which was not included in the simulations. It can be seen that the simulation using the monomer hyperfine coupling values severely overestimates the width of the ENDOR spectrum. In contrast the simulations using the dimer and trimer coupling values reproduce the experimental ENDOR width much more closely. Further agreement between the simulated and experimental spectra could be reached by tuning the suppression function so that the intensity does not fall to zero at the holes. The dimer appears to match the experimental spectrum with greater accuracy, with a similar FWHM to the experimental spectrum, while the trimer underestimates the width; however it is not possible to definitively choose between them. Given that the trimer appears to slightly underestimate

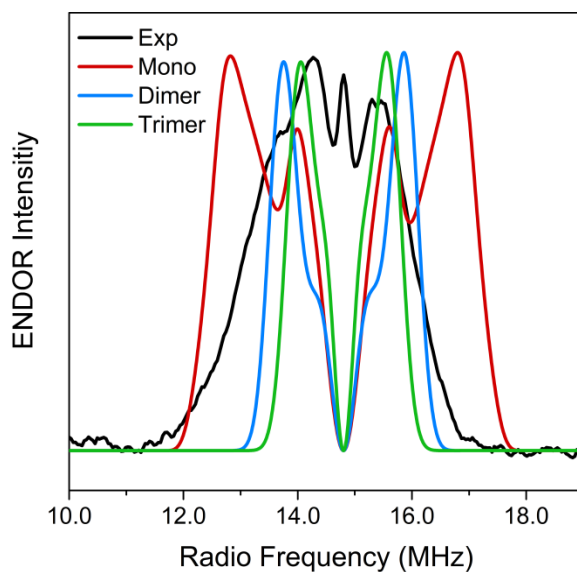


Figure 6.16 Comparison of experimental and simulated ^1H ENDOR spectra of $\text{DTS}(\text{F}_2\text{BTTh}_2)_2$. The experimental spectrum was recorded at 50 K in blend of $\text{DTS}(\text{F}_2\text{BTTh}_2)_2$: PC_{61}BM in frozen chlorobenzene solution. The simulated spectra were corrected to include suppression effects.

the width it is safe to conclude that the polaron is not delocalised over a higher order aggregate.

In summary, comparison of the experimental g -tensors with those from electronic structure DFT calculations suggests that the polaron is delocalised over a dimer or trimer. This delocalisation is supported by the reduced hyperfine coupling observed in the ENDOR spectra which is in good agreement with the dimer hyperfine values predicted by DFT. It was shown in Figure 6.11 that the width of the film and frozen solution ENDOR spectra are approximately equal and delocalisation of the polaron over a dimer, or possibly a trimer, is therefore also true for films. The PCE of a solar cell is dependent on the efficiency of charge separation of the polaron pairs formed at the donor / acceptor. Delocalisation of the donor polaron reduces the Coulomb binding energy in these pairs and will therefore aid charge separation and may be a contributing factor in the high efficiency achieved by these small molecule donors.

6.5.7 TR-EPR of Charge Separation

To obtain information on the charge separation dynamics of the polaron pair in these donor:PC₆₁BM systems, direct detection TR-EPR spectroscopy was performed. In this method the continuous wave EPR signal is recorded as a function of time after the laser flash without the use of field modulation as explained in Section 4.3.5. Direct detection TR-EPR spectra of the five blends in frozen chlorobenzene solution are shown in Figure 6.17. For roughly the first 500 ns after the laser flash the TR-EPR spectrum builds up. This build up time is controlled by the response of the resonator rather than an interesting sample dependent mechanism. The spectra shown in Figure 6.17 were then obtained by integrating the time trace from 500 ns after the laser flash to 600 ns after the laser flash. This is appropriate as the lineshape does not evolve during this integration period and the gain in signal to noise is substantial. The spectral lineshape remains approximately constant for the next 500 ns before evolving over a microsecond time scale. It is difficult, if not impossible, to obtain useful information from these later dynamics as they are

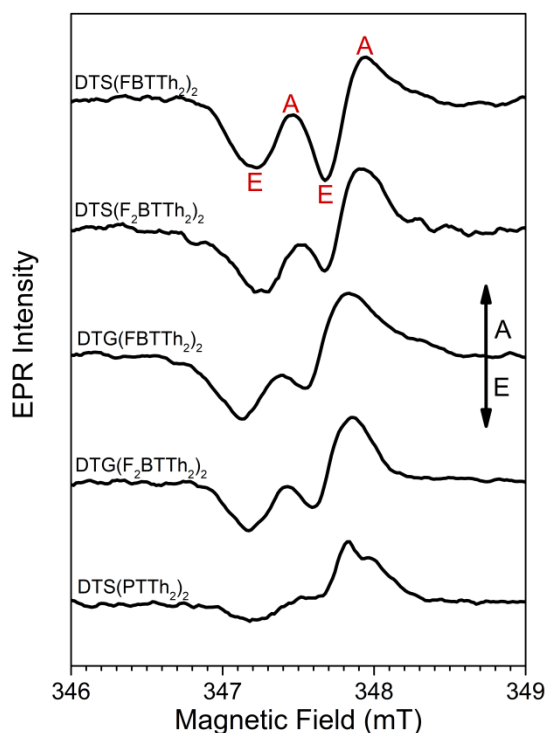


Figure 6.17 Continuous wave direct detection TR-EPR spectra of polaron pairs in dithienosilole and dithienogermole based donors blended with PC₆₁BM in frozen chlorobenzene solution at T = 50 K. The spectra were captured 500 ns after the laser flash and integrated over a 100 ns time period in order to improve the signal to noise. Positive going peaks correspond to microwave absorption (A) and negative to emission (E). Spectra have been background subtracted to remove the broad underlying triplet component and their positions corrected to account for changes in microwave frequency.

heavily influenced by the response of the detection circuitry, such as amplifier overshoot, inside the spectrometer. The TR-EPR analysis will therefore be based on the 500 ns snapshot. As will be explored in the following section there is also a broad triplet component in addition to signal of interest which causes a baseline distortion. The spectra shown in Figure 6.17 were therefore baseline corrected in order to remove the triplet signal.

Looking at Figure 6.17 it can be seen that the spectra consist of more than two peaks and therefore must be due to coupled spins. Furthermore the spectra are partly in microwave emission and partly in absorption signifying that there is a non-Boltzmann population of spin states. These characteristics indicate that the spectra correspond to a polaron pair undergoing charge separation. After the laser flash a singlet exciton is formed which will undergo electron (or hole) transfer to yield a singlet primary polaron pair. Sequential electron and/or hole transfer will then occur generating intermediate polaron pairs and ultimately secondary polaron pairs with lifetimes long enough to be observed with the 500 ns resolution of the TR-EPR experiment.

Assuming the sequential electron and hole transfer proceeds rapidly (<100 ps) the polarons are separated before magnetic interactions between the spins can cause S- T_0 mixing. Under this assumption the polarisation that is observed in the TR-EPR experiment should arise wholly from interactions in the observable secondary polaron pair and is therefore the EAEA pattern predicted by the SCRPM, as described in Section 3.5.2. It can be seen from Figure 6.17 that the spectra of the four fluorobenzothiadiazole donors all exhibit the same polarisation, a distorted EAEA pattern. This indicates that the polarisation is well described by the SCRPM and that the primary and intermediate polaron pairs separate sufficiently rapidly as to avoid S- T_0 mixing.

The spectrum of the DTS(PTTh₂)₂ exhibits a notably different polarisation than the fluorobenzothiadiazole donors that is closer to EA than EAEA. An EA polarisation pattern is predicted by the RPM. In the RPM magnetic interactions between the spins in the primary and intermediate polaron pairs cause S- T_0 mixing and a build-up of polarisation during charge separation (see Section 3.5.2). This built up of polarisation then carries over to the observable secondary polaron pair resulting in an EA polarisation pattern in the TR-EPR spectrum if the precursor state was singlet. In the context of

sequential electron transfer a distortion from EAEA towards EA occurs if there are long lived primary or intermediate polaron pair(s). It has been shown in analogous donor / acceptor biological systems that the longer the lifetime of the intermediate states the stronger the S-T₀ mixing and the greater the distortion from EAEA to EA.^[28] Applying this reasoning to the spectra in Figure 6.17 leads to the conclusion that charge separation in the four fluorobenzothiadiazole donors occurs on roughly the same timescale since they all exhibit a similar EAEA polarisation pattern. In contrast, charge separation in DTS(PTTh₂)₂ is slower as the spectrum is strongly distorted towards EA, suggesting that the separation process involves a long lived primary or intermediate polaron pair.

The film TR-EPR spectra shown in Figure 6.18 tell a similar story. The spectra of the FBT fluorobenzothiadiazole donors show a clear EAEA polarisation pattern in agreement with that in frozen solution. The pattern of the F₂BT donors is also EAEA but more heavily distorted than the solution case which may indicate that the morphology of films using the F₂BT donors is not as favourable as the FBT. The spectrum of DTS(PTTh₂)₂ is

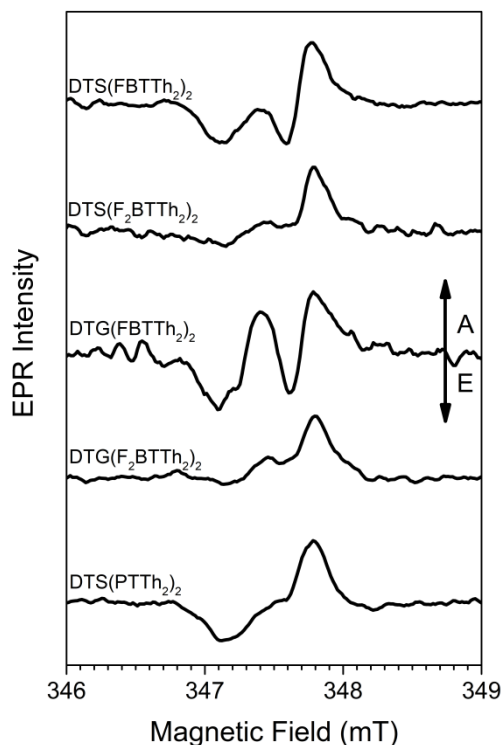


Figure 6.18 Continuous wave direct detection TR-EPR spectra of polaron pairs in dithienosilole and dithienogermole based donors blended with PC₆₁BM in solution cast films at T = 50 K. The spectra were captured 500 ns after the laser flash and integrated over a 100 ns time period in order to improve the signal to noise. Positive going peaks correspond to microwave absorption (A) and negative to emission (E). Spectra have been background subtracted to remove the broad underlying triplet component and their positions corrected to account for changes in microwave frequency.

similar to that obtained in frozen solution, suggesting that the slow charge separation in this blend carries over to films.

6.5.8 TR-EPR of Triplet Excitons

In order to obtain a more complete picture of the charge separation across this family of donor:PC₆₁BM blends the formation of triplet excitons was also investigated. The presence of triplet excitons are a strong indicator of inefficient charge separation in donor acceptor blends. If the photogenerated singlet exciton fails to reach the donor acceptor interface it may undergo ISC to the triplet state which is lower in energy.^[29] Alternatively singlet polaron pairs which take on triplet character through S-T₀ mixing can undergo back electron transfer (BET) to yield a triplet exciton on the donor. The triplet energy of many donors lies below the energy of the polaron pair so this process is energetically favourable and there is no energetic driving force for forward electron transfer to reoccur to break apart the exciton.^[29, 30] While back hole transfer can in principle occur, the triplet level of the acceptor is generally higher than the polaron pair which suppresses this mechanism.^[29, 31]

Direct detection TR-EPR spectra of triplet excitons in a frozen solution of the DTS(FBTTh₂)₂:PC₆₁BM blend are shown in Figure 6.19. There are two clear triplet signatures present in Figure 6.19 with substantially different widths of 90 mT and 25 mT. From previous studies of triplets in OPV blend systems the narrow feature can be assigned to triplet excitons on the PC₆₁BM.^[20, 32] The broad feature therefore must be triplet excitons on the DTS(FBTTh₂)₂. As discussed in Section 3.5.4 the ISC mechanism populates the zero field triplet states unequally due to different intersystem crossing rates to the three sublevels, while the BET mechanism selectively populates the high field T₀ state directly. The different triplet sublevel populations of these two pathways enable them to be distinguished through the polarisation pattern of the triplet spectrum. It can be seen from Figure 6.19 that the broad triplet has an EEAEAA pattern and the narrow triplet is AAAEEE, both of which indicate that the triplet excitons are generated through ISC.

In Figure 6.19a the simulation of the triplet exciton on PC₆₁BM using the ISC mechanism with $|D| = 290$ MHz and $|E| = 25$ MHz is shown in blue and reproduces the experimental lineshape with good accuracy. The simulation of the triplet exciton on DTS(FBTTh₂)₂

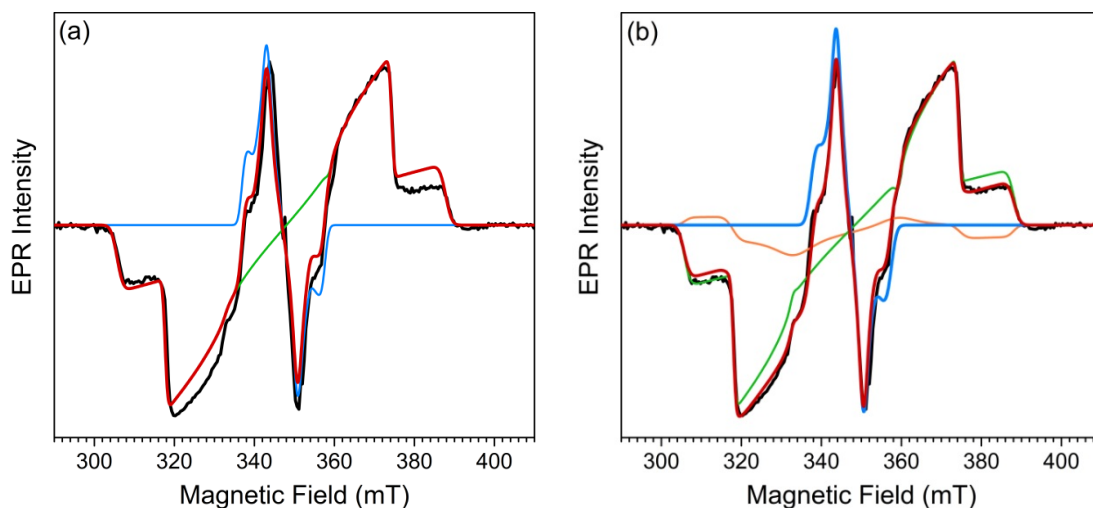


Figure 6.19 Continuous wave direct detection TR-EPR spectra of triplet excitons in DTS(FBTTh₂)₂:PC₆₁BM frozen chlorobenzene solution at T = 50 K. The spectra were captured 500 ns after the laser flash and integrated over a 100 ns time period in order to improve the signal to noise. Positive going peaks correspond to microwave absorption (A) and negative to emission (E). The experimental spectrum is shown in black, the total simulation in red, the ISC triplet on PC₆₁BM in blue, the ISC triplet on DTS(FBTTh₂)₂ in green and the BET triplet on DTS(FBTTh₂)₂ in orange. In (a) the spectrum fit using ISC mechanisms only while in (b) ISC and BET mechanisms are combined.

using the ISC mechanism with $|D| = 1150$ MHz and $|E| = 145$ MHz is shown in green in Figure 6.19a. While this simulation accurately reproduces the widths of the various transitions in the experimental spectrum, it fails to accurately reproduce their heights. The height of the outermost high field transition is overestimated by the simulation while the height of the central transition on the low field side is underestimated. By changing the population of the zero field sublevels the simulation can be tuned to accurately reproduce the heights of these two transitions but then the heights and polarisations of the other transitions are compromised. There is no combination of zero field sublevel populations (p_x , p_y , and p_z) that accurately reproduces the height and polarisation of all six transitions in the spectrum simultaneously.

In principle such a deviation between experiment and simulation could be explained by partial orientation effects, where the orientation of the molecules and the applied field is not random. However the sample measured in Figure 6.19 is a flash frozen chlorobenzene solution and orientation of the molecules should therefore be truly random. Instead the deviation is attributed to a certain fraction of the triplet excitons on DTS(FBTTh₂)₂ being generated through BET rather than ISC. By introducing BET excitons into the simulation (orange line), the simulated spectrum is now in excellent agreement to the experimental spectrum as shown in Figure 6.19b. The relative weight of the BET simulation component

required was 15 %, where the weight is calculated by the ratio of the integrated intensities of the BET and ISC DTS(FBTTh₂)₂ simulation components. This suggests that while most of the triplet excitons on DTS(FBTTh₂)₂ are created through ISC there is a substantial fraction generated through BET from the polaron pair.

The triplet exciton spectra of the other four blends were measured in a similar fashion and a comparison of the triplet spectra from the five blends is shown in Figure 6.20. All five blends exhibit similar triplet exciton TR-EPR spectra with a narrow component

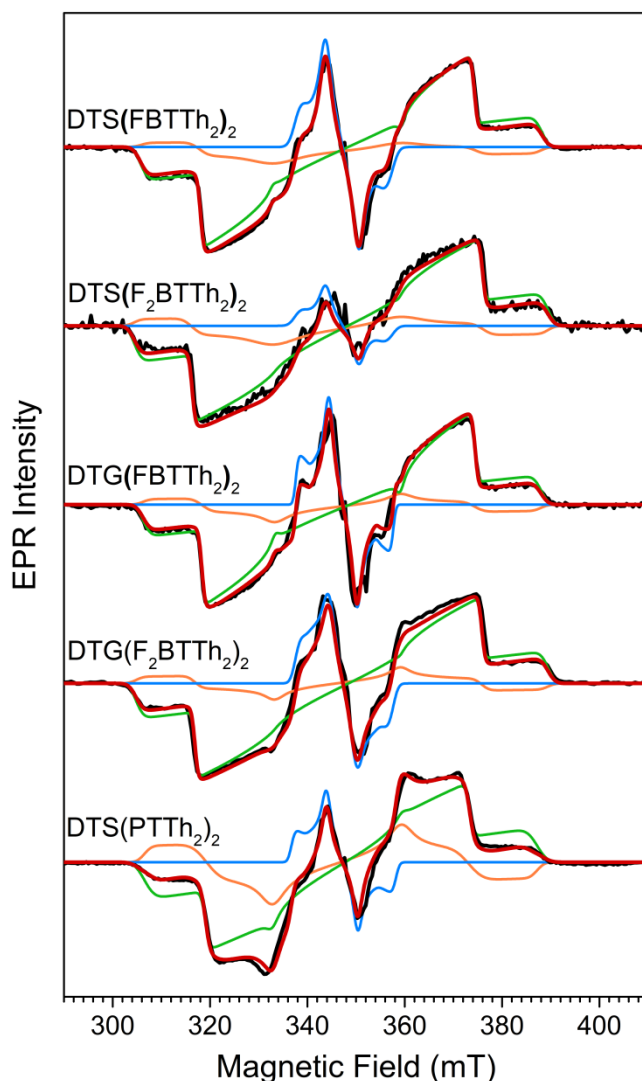


Figure 6.20 Continuous wave direct detection TR-EPR spectra of triplet excitons in dithienosilole and dithienogermole based donors blended with PC₆₁BM in frozen chlorobenzene solution at T = 50 K. The spectra were captured 500 ns after the laser flash and integrated over a 100 ns time period in order to improve the signal to noise. Positive going peaks correspond to microwave absorption (A) and negative to emission (E). The experimental spectrum is shown in black, the total simulation in red, the ISC triplet on PC₆₁BM in blue, the ISC triplet on the donor in green and the BET triplet on the donor in orange.

corresponding to excitons on the PC₆₁BM and a broad component resulting from the excitons on the donor. All spectra could be accurately simulated using an ISC mechanism for the PC₆₁BM triplets and a combination of ISC and BET for the triplets on the donors. The ZFS parameters and weight of the BET component used in the five simulations are listed in Table 6.4.

The magnitude of the D ZFS parameter is a measure of the strength of the dipolar interaction between the spins in the exciton. The more delocalised the exciton the weaker the dipolar interaction and the lower the magnitude of D. Looking at Table 6.4 the magnitude of D only varies slightly across the five donor molecules indicating that the extent of the triplet delocalisation is approximately equal on all the donors. The magnitude of D for triplets on PC₆₁BM is significantly smaller than the donors suggesting that the triplet exciton is heavily delocalised over the fullerene cage. The weight of the PC₆₁BM component was approximately equal across four of the blends with the exception of DTS(F₂BTTh₂)₂ which has a significantly smaller PC₆₁BM contribution, the reason for this outlier is not known. The lineshape of the triplet excitons on the four fluorobenzothiadiazole donors is approximately equivalent and the simulations required similar weights of BET component ranging from 11 to 15 %. This suggests that BET occurs to the same extent in these four blends. In contrast it can be seen from Figure 6.20 that the lineshape of the DTS(PTTh₂)₂ triplet is subtly different and required a much larger BET component of 28 % indicating that BET occurs more readily in the DTS(PTTh₂)₂:PC₆₁BM blend.

Table 6.4 Zero field splitting parameters and BET weights used for the simulation of the TR-EPR spectra in Figure 6.20. The error in the ZFS is approximately 5 % and the weight of the BET component is the ratio of the ISC and BET integrated intensities.

Molecule	 D (MHz)	 E (MHz)	BET Weight (%)
DTS(FBTTh ₂) ₂	1150	143	13
DTS(F ₂ BTTh ₂) ₂	1190	160	15
DTG(FBTTh ₂) ₂	1145	142	11
DTG(F ₂ BTTh ₂) ₂	1185	155	14
DTS(PTTh ₂) ₂	1130	130	28
PC ₆₁ BM	280	30	N/A

The TR-EPR triplet measurements were repeated on film samples to check whether the trend in the BET weight carried over to the films. The triplet TR-EPR spectrum of DTS(FBTTh₂)₂:PC₆₁BM film is shown in Figure 6.21. It can be seen that the broad triplet

corresponding to excitons on the donor retains its overall AAEAE polarisation pattern indicating that ISC of singlet excitons is still occurring on the donor. In contrast the narrow triplet corresponding to ISC triplet excitons on the PC₆₁BM triplet is greatly reduced and within the noise baseline of the measurement. ISC triplets are essentially a measure of poor morphology. In an optimised blend morphology singlet excitons generated on either the donor or acceptor phase should reach the interface before ISC occurs. In frozen solution the distance between the donor and acceptor molecules is greater than in the film and there will be a substantial fraction of molecules which are too far apart for electron transfer to occur and consequently ISC triplet excitons are expected to form. The absence of the PC₆₁BM ISC triplet in the film indicates that all singlet excitons on PC₆₁BM undergo electron transfer and that the fullerene domains in film are therefore small enough that all singlet excitons can reach the donor acceptor interface. Conversely the presence of ISC excitons on the DTS(FBTTh₂)₂ suggests that the domains of DTS(FBTTh₂)₂ are too large and not all singlet excitons are able to reach the interface.

The simulation of triplet exciton on the DTS(FBTTh₂)₂ using the ISC mechanism is shown by the red line in Figure 6.21a. It can be seen that once again the relative height of transitions is not reproduced by the ISC simulation. However the situation is different from Figure 6.19a, as the height of outer transitions are now under estimated by the

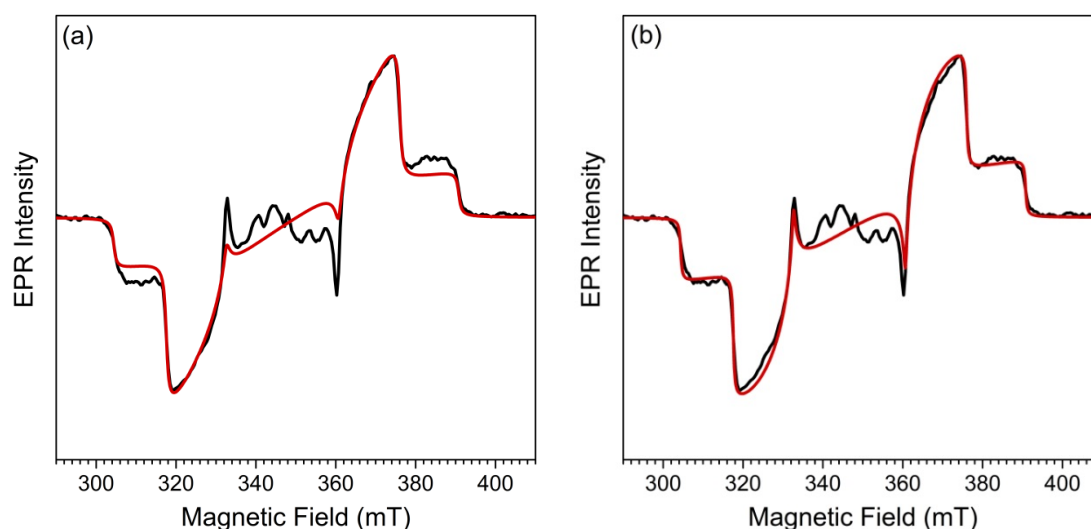


Figure 6.21 Continuous wave direct detection TR-EPR spectra of triplet excitons in DTS(FBTTh₂)₂:PC₆₁BM films at T = 50 K. The spectra were captured 500 ns after the laser flash and integrated over a 100 ns time period in order to improve the signal to noise. Positive going peaks correspond to microwave absorption (A) and negative to emission (E). The experimental spectrum is shown in black and the simulation in red. (a) The spectrum is fit using the ISC mechanisms with a full powder average. (b) The spectrum is fit using the ISC mechanism with partial orientation selection.

simulation rather than over estimated. The addition of a BET triplet in the simulation therefore exacerbates the fit rather than improving it. Instead the discrepancy between the simulation and the experiment is likely due to partial orientation selection. The simulation in Figure 6.21a uses a full power average but the dithienosilole and dithienogermole family of donors are known to exhibit crystalline phases.^[9, 33] A full powder average, as used for the frozen solution simulations, is therefore not suitable and the orientations of the molecules with respect to the magnetic field axis were instead weighted using the distribution shown in Figure 6.22. It is a simple inverse Gaussian centred on the azimuthal angle $\phi = 0$. This distribution preferentially aligns the molecules so that the y-axis of the dipolar principal axis reference frame is parallel with magnetic field. The ISC simulation using this orientation distribution is shown in Figure 6.21b and reproduces the experimental lineshape with good accuracy. This orientation distribution should be considered an experimental tuning parameter rather than a physical reality as the chosen distribution is not unique and the orientation of the molecules in sample tube cannot be inferred from it.

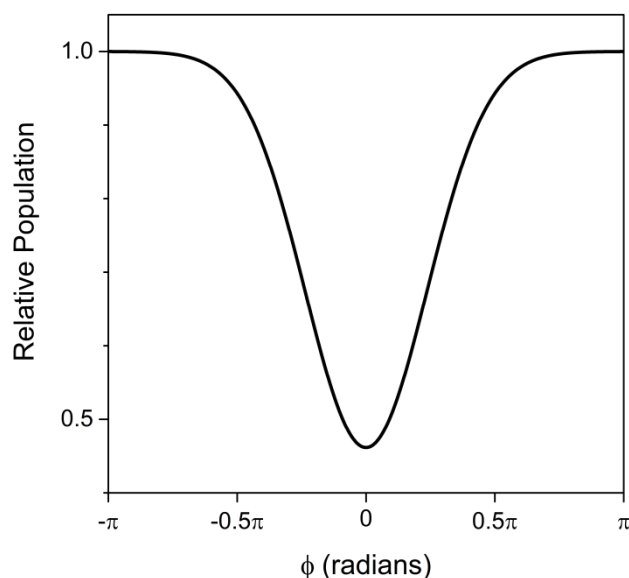


Figure 6.22 Orientation distribution used to weight the azimuthal angle ϕ .

The experimental and simulated spectra of all five blends are shown in Figure 6.23. The four fluorobenzothiadiazole blends have nearly identical polarisation patterns and all were simulated accurately using the orientation distribution in Figure 6.22. The spectrum of DTS(PTTTh₂)₂:PC₆₁BM exhibits a notably different polarisation pattern from the others. To simulate the DTS(PTTTh₂)₂:PC₆₁BM using only the ISC mechanism requires

an orientation distribution that is orthogonal to that used for the fluorobenzothiadiazole donors. DTS(PTTTh₂)₂ is structurally very similar to the four fluorobenzothiadiazole donors and would therefore be expected to orientate in a similar manner. The use of an orthogonal orientation distribution in the simulation is therefore unphysical. Instead the orientation distribution in Figure 6.22 can be treated as a global fitting parameter, and applied to the DTS(PTTTh₂)₂ molecules. To accurately reproduce the experimental lineshape of DTS(PTTTh₂)₂ both ISC and BET triplet excitons have to be included in the simulation and are shown in green and orange in Figure 6.23 respectively. The weight of

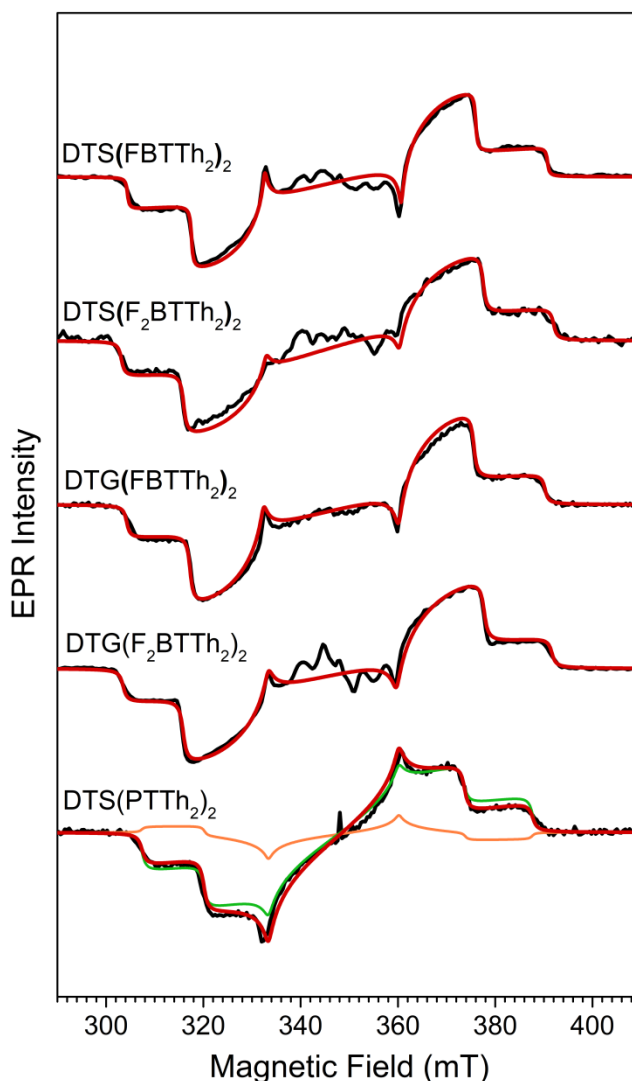


Figure 6.23 Continuous wave direct detection TR-EPR spectra of triplet excitons in dithienosilole and dithienogermole based donors blended with PC₆₁BM in solution cast films T = 50 K. The spectra were captured 500 ns after the laser flash and integrated over a 100 ns time period in order to improve the signal to noise. Positive going peaks correspond to microwave absorption (A) and negative to emission (E). The experimental spectrum is shown in black, the total simulation in red. For DTS(PTTTh₂)₂:PC₆₁BM the two components of the simulation, BET and ISC triplets are shown in orange and green respectively.

the BET component required to accurately reproduce the experimental lineshape was 13 %. It should be noted that the fluorobenzothiadiazole donors are also likely to have some BET component present, but there are too many free parameters in the simulation when both variable partial orientation and variable BET weight are included to accurately determine the BET weight. It is therefore more reasonable to use the approach described here where no BET component is included in the fluorobenzothiadiazole simulations and use them to accurately obtain the orientation distribution. The BET component that is required in the DTS(PTTTh₂)₂ simulation then shows that more BET must be occurring DTS(PTTTh₂)₂:PC₆₁BM blend than in the fluorobenzothiadiazole blends, in agreement to what was observed in the frozen solution.

As BET excitons are caused by S-T₀ mixing in the polaron pair, more BET excitons are expected when the polaron pairs separate slowly. The presence of greater BET exciton population on DTS(PTTTh₂)₂ therefore indicates that the charge separation occurs more slowly in this blend. This is in agreement with the slower charge separation dynamics of the DTS(PTTTh₂)₂ blend inferred from the polarisation patterns of the polaron pairs in Section 6.5.7.

6.6 Conclusion

The photogenerated excited states in a family of five small molecule donors blended with PC₆₁BM were investigated using LEPR, ENDOR and TR-EPR spectroscopy. Using LEPR the g-tensors of the light induced polarons on the donor molecules were determined. Comparison of these values to those obtained from DFT calculations indicated that the positive polaron is delocalised over a dimer or trimer, and this was confirmed by the reduced hyperfine coupling constants measured using ENDOR spectroscopy. The delocalisation of the positive polaron across several molecules will aid charge separation in these systems and may be a contributing factor in their high efficiency. Using TR-EPR spectroscopy the charge separation dynamics and triplet exciton formation pathways were also investigated. From the polarisation patterns of the polaron pair spectra it can be inferred that charge separation is slowest in the DTS(PTTTh₂)₂ blend and involves a longer lived primary or intermediate polaron pair. By simulating the polarisation patterns of the triplet spectra the presence of BET triplet excitons in all five blends was identified, and there are a higher population of them in the

DTS(PTTh₂)₂ blend. The higher population of BET triplet excitons is in agreement with the slower charge separation in the DTS(PTTh₂)₂ blend inferred from the polaron pair spectra, since slower charge separation results in greater S-T₀ mixing and increased BET formation. This finding demonstrates that back electron transfer to the triplet of the donor is a loss mechanism in these molecular systems when charge separation is slow, and could be partly responsible for the lower device efficiencies obtained in the DTS(PTTh₂)₂ blend compared with those of DTS(FBTTh₂)₂ and DTG(FBTTh₂)₂.^[9, 10, 13]

6.7 References

1. S. A. J. Thomson, J. Niklas, C. Mallares, K. L. Mardis, I. D. W. Samuel and O. Poluektov, Charge Separation and Triplet Exciton Formation Pathways in Small Molecule Solar Cells as Studied by Time-resolved EPR Spectroscopy. *J. Phys. Chem. C* **121** (41), 22707–22719.
2. G. Yu, J. Gao, J. C. Hummelen, F. Wudl and A. J. Heeger, Polymer Photovoltaic Cells - Enhanced Efficiencies Via A Network Of Internal Donor-acceptor Heterojunctions. *Science* **270** (5243), 1789-1791 (1995).
3. S. D. Collins, N. A. Ran, M. C. Heiber and T.-Q. Nguyen, Small Is Powerful: Recent Progress in Solution-Processed Small Molecule Solar Cells. *Adv. Energy Mater.*, 1602242 (2017).
4. T. P. Osedach, T. L. Andrew and V. Bulovic, Effect of synthetic accessibility on the commercial viability of organic photovoltaics. *Energy Environ. Sci.* **6** (3), 711-718 (2013).
5. B. Kan, M. M. Li, Q. Zhang, F. Liu, X. J. Wan, Y. C. Wang, W. Ni, G. K. Long, X. Yang, H. R. Feng, Y. Zuo, M. T. Zhang, F. Huang, Y. Cao, T. P. Russell and Y. S. Chen, A Series of Simple Oligomer-like Small Molecules Based on Oligothiophenes for Solution-Processed Solar Cells With High Efficiency. *J. Am. Chem. Soc.* **137** (11), 3886-3893 (2015).
6. S. Q. Zhang, L. Ye and J. H. Hou, Breaking the 10% Efficiency Barrier in Organic Photovoltaics: Morphology and Device Optimization of Well-Known PBDTTT Polymers. *Adv. Energy Mater.* **6** (11), 20 (2016).
7. B. Kan, Q. Zhang, M. M. Li, X. J. Wan, W. Ni, G. K. Long, Y. C. Wang, X. Yang, H. R. Feng and Y. S. Chen, Solution-Processed Organic Solar Cells Based on Dialkylthiol-Substituted Benzodithiophene Unit With Efficiency Near 10%. *J. Am. Chem. Soc.* **136** (44), 15529-15532 (2014).
8. Q. Zhang, B. Kan, F. Liu, G. K. Long, X. J. Wan, X. Q. Chen, Y. Zuo, W. Ni, H. J. Zhang, M. M. Li, Z. C. Hu, F. Huang, Y. Cao, Z. Q. Liang, M. T. Zhang, T. P. Russell

- and Y. S. Chen, Small-molecule solar cells with efficiency over 9%. *Nature Photon.* **9** (1), 35-41 (2015).
9. Y. M. Sun, G. C. Welch, W. L. Leong, C. J. Takacs, G. C. Bazan and A. J. Heeger, Solution-Processed Small-molecule Solar Cells With 6.7% Efficiency. *Nat. Mater.* **11** (1), 44-48 (2012).
 10. J. S. Miao, H. Chen, F. Liu, B. F. Zhao, L. Y. Hu, Z. C. He and H. B. Wu, Efficiency Enhancement in Solution-Processed Organic Small Molecule: Fullerene Solar Cells via Solvent Vapor Annealing. *Appl. Phys. Lett.* **106** (18), 5 (2015).
 11. T. S. van der Poll, J. A. Love, T. Q. Nguyen and G. C. Bazan, Non-Basic High-Performance Molecules for Solution-Processed Organic Solar Cells. *Adv. Mater.* **24** (27), 3646-3649 (2012).
 12. Y. M. Sun, J. Seifert, L. J. Huo, Y. L. Yang, B. B. Y. Hsu, H. Q. Zhou, X. B. Sun, S. Xiao, L. Jiang and A. J. Heeger, High-Performance Solution-Processed Small-Molecule Solar Cells Based on a Dithienogermole-Containing Molecular Donor. *Adv. Energy Mater.* **5** (3), 7 (2015).
 13. M. M. Tanya Kumari, So-Huei Kang, Changduk Yang, Improved Efficiency of DTGe(FBTTh2)2-Based Solar Cells by Using Macromolecular Additives: How Macromolecular Additives Versus Small Additives Influence Nanoscale Morphology and Photovoltaic Performance. *Nano Energy* **24**, 56-62 (2016).
 14. O. G. Poluektov, S. Filippone, N. Martin, A. Sperlich, C. Deibel and V. Dyakonov, Spin Signatures of Photogenerated Radical Anions in Polymer- 70 Fullerene Bulk Heterojunctions High Frequency Pulsed EPR Spectroscopy. *J. Phys. Chem. B* **114** (45), 14426-14429 (2010).
 15. K. L. Mardis, J. N. Webb, T. Holloway, J. Niklas and O. G. Poluektov, Electronic Structure of Fullerene Acceptors in Organic Bulk-Heterojunctions: A Combined EPR and DFT Study. *Journal of Physical Chemistry Letters* **6** (23), 4730-4735 (2015).
 16. V. Dyakonov, G. Zorinians, M. Scharber, C. J. Brabec, R. A. J. Janssen, J. C. Hummelen and N. S. Sariciftci, Photoinduced Charge Carriers in Conjugated Polymer-Fullerene Composites Studied With Light-induced Electron-Spin Resonance. *Physical Review B* **59** (12), 8019-8025 (1999).
 17. J. De Ceuster, E. Goovaerts, A. Bouwen, J. C. Hummelen and V. Dyakonov, High-Frequency (95 GHz) Electron Paramagnetic Resonance Study of the Photoinduced Charge Transfer in Conjugated Polymer-Fullerene Composites. *Physical Review B* **64** (19), 6 (2001).
 18. A. Aguirre, P. Gast, S. Orlinskii, I. Akimoto, E. J. J. Groenen, H. El Mkami, E. Goovaerts and S. Van Doorslaer, Multifrequency EPR Analysis of the Positive Polaron in I-2-doped Poly(3-hexylthiophene) and in Poly 2-methoxy-5-(3,7-dimethyloctyloxy)-1,4-phenylenevinylene. *Phys. Chem. Chem. Phys.* **10** (47), 7129-7138 (2008).

19. N. S. Sariciftci, L. Smilowitz, A. J. Heeger and F. Wudl, Photoinduced Electron-Transfer From a Conducting Polymer to Buckminsterfullerene. *Science* **258** (5087), 1474-1476 (1992).
20. O. G. Poluektov, J. Niklas, K. L. Mardis, S. Beaupre, M. Leclerc, C. Villegas, S. Erten-Ela, J. L. Delgado, N. Martin, A. Sperlich and V. Dyakonov, Electronic Structure of Fullerene Heterodimer in Bulk-Heterojunction Blends. *Adv. Energy Mater.* **4** (7), 7 (2014).
21. K. Marumoto, N. Takeuchi, T. Ozaki and S. Kuroda, ESR Studies of Photogenerated Polarons in Regioregular poly(3-alkylthiophene) Fullerene composite. *Synth. Met.* **129** (3), 239-247 (2002).
22. K. Marumoto, M. Kato, H. Kondo, S. Kuroda, N. C. Greenham, R. H. Friend, Y. Shimoi and S. Abe, Electron spin resonance and electron nuclear double resonance of photogenerated polarons in polyfluorene and its fullerene composite. *Physical Review B* **79** (24), 11 (2009).
23. N. A. Schultz, M. C. Scharber, C. J. Brabec and N. S. Sariciftci, Low-temperature recombination kinetics of photoexcited persistent charge carriers in conjugated polymer/fullerene composite films. *Physical Review B* **64** (24), 7 (2001).
24. J. Niklas, K. L. Mardis, B. P. Banks, G. M. Grooms, A. Sperlich, V. Dyakonov, S. Beaupre, M. Leclerc, T. Xu, L. P. Yu and O. G. Poluektov, Highly-Efficient Charge Separation and Polaron Delocalization in Polymer-Fullerene Bulk-Heterojunctions: A Comparative Multi-frequency EPR and DFT Study. *Phys. Chem. Chem. Phys.* **15** (24), 9562-9574 (2013).
25. M. Reichenberger, J. A. Love, A. Rudnick, S. Bagnich, F. Panzer, A. Stradomska, G. C. Bazan, T. Q. Nguyen and A. Kohler, The Effect of Intermolecular Interaction on Excited States in p-DTS(FBTTH2)(2). *J. Chem. Phys.* **144** (7), 10 (2016).
26. C. Gemperle and A. Schweiger, Pulsed Electron Nuclear Double-resonance Methodology. *Chem. Rev.* **91** (7), 1481-1505 (1991).
27. P. E. Doan, N. S. Lees, M. Shanmugam and B. M. Hoffman, Simulating Suppression Effects in Pulsed ENDOR, and the 'Hole in the Middle' of Mims and Davies ENDOR Spectra. *Appl. Magn. Reson.* **37** (1-4), 763-779 (2010).
28. J. Niklas and O. Poluektov, Charge Transfer Processes in OPV Materials as Revealed by EPR Spectroscopy. *Adv. Energy Mater.* **7** (10), 1602226 (2017).
29. A. Rao, P. C. Y. Chow, S. Gelinas, C. W. Schlenker, C. Z. Li, H. L. Yip, A. K. Y. Jen, D. S. Ginger and R. H. Friend, The role of spin in the kinetic control of recombination in organic photovoltaics. *Nature* **500** (7463), 435-+ (2013).
30. M. Liedtke, A. Sperlich, H. Kraus, A. Baumann, C. Deibel, M. J. M. Wirix, J. Loos, C. M. Cardona and V. Dyakonov, Triplet Exciton Generation in Bulk-Heterojunction Solar Cells Based on Endohedral Fullerenes. *J. Am. Chem. Soc.* **133** (23), 9088-9094 (2011).

31. H. Kraus, M. C. Heiber, S. Vath, J. Kern, C. Deibel, A. Sperlich and V. Dyakonov, Analysis of Triplet Exciton Loss Pathways in PTB7: PC71BM Bulk Heterojunction Solar Cells. *Scientific Reports* **6**, 8 (2016).
32. L. Franco, A. Toffoletti, M. Ruzzi, L. Montanari, C. Carati, L. Bonoldi and R. Po, Time-Resolved EPR of Photoinduced Excited States in a Semiconducting Polymer/PCBM Blend. *J. Phys. Chem. C* **117** (4), 1554-1560 (2013).
33. A. K. K. Kyaw, D. Gehrig, J. Zhang, Y. Huang, G. C. Bazan, F. Laquai and T. Q. Nguyen, High Open-Circuit Voltage Small-molecule p-DTS(FBTTh2)(2):ICBA Bulk Heterojunction Solar Cells - Morphology, Excited-State Dynamics, and Photovoltaic Performance. *J. Mater. Chem. A* **3** (4), 1530-1539 (2015).

7 EPR Spectroscopic Signatures of Negative Polarons on the Non-Fullerene Acceptors ITIC and IDTBR

7.1 Introduction

In this chapter the spectroscopic signatures of negative polarons on two high efficiency non-fullerene acceptors, ITIC and IDTBR, are identified. The acceptors were blended with the donor polymer P3HT and 9.8 GHz, 34 GHz and 94 GHz light induced EPR spectra obtained. The signatures of the negative polaron on ITIC and IDTBR were found to heavily overlap with the positive polaron on P3HT at all three microwave frequencies. By applying a global fit across the three frequencies the negative polaron signatures and principal values of the g-tensors could be accurately determined. In addition the hyperfine coupling of the polarons to the surrounding nuclei was measured using 9.8 GHz and 34 GHz ENDOR spectroscopy. These results provide information on the electronic excited state of these important non-fullerene acceptor molecules and help guide the direction of DFT calculations.

7.2 Background

In 1993 Sariciftci et al. demonstrated the first polymer:fullerene planar heterojunction solar cell.^[1, 2] Only three years later the first bulk heterojunction polymer:fullerene cell was reported,^[3] using the newly synthesised methanofullerene derivative PC₆₁BM.^[4] Since their inception fullerene derivatives have dominated the role of electron acceptors in OPV cells. The development of new donor polymers and small molecules has proceeded rapidly and has driven the impressive efficiency enhancement achieved by OPV over the last 15 years. In contrast progress on non-fullerene acceptors has been far more sluggish with few materials able to match the excellent electron transporting properties of fullerene derivatives. While fullerene derivatives are capable of achieving high efficiency cells they suffer from several intrinsic deficiencies. They have poor absorption characteristics, non-scalable synthesis with associated high production costs and are difficult to functionalise resulting in limited tunability of the absorption and energy levels.^[5, 6] In addition they are known to be sensitive to air degradation and some polymer fullerene blends have been shown to be inherently thermodynamically

unstable.^[7] In recent years progress in non-fullerene acceptors has picked up pace and they are now achieving efficiencies comparable to fullerene derivatives.^[5, 6] Having achieved comparable efficiency to their fullerene counterparts and with their greater scope for further improvement, non-fullerene acceptors look poised to become the new standard in OPV cells. Very little is known about non-fullerene acceptors from an EPR perspective. The vast majority of OPV LEPR and TR-EPR studies to date have used PC₆₁BM or PC₇₁BM as the electron acceptor and focused on the change of the positive polaron signature with different donors. We therefore investigated two high performance fullerene acceptors ITIC and IDTBR using EPR in order to identify the spectroscopic signatures of the negative polarons on these materials and how they differ from PC₆₁BM. The experimental EPR results can then be used to guide DFT calculations to obtain an accurate picture of the electronic structure of the excited states.

7.3 Materials

7.3.1 ITIC

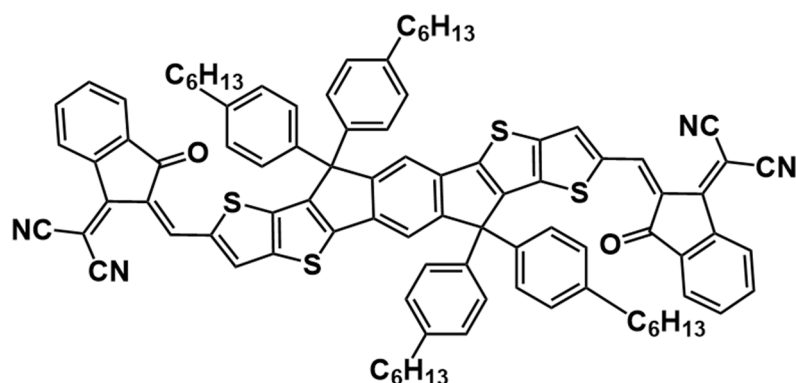


Figure 7.1 Chemical structure of ITIC.

ITIC was developed by the Zhan group and achieved efficiencies of up to 6.8 % when blended with PTB7-Th. This is higher than control cells using PC₆₁BM (6.1 %) and approaching that obtained by using PC₇₁BM (7.5 %).^[8] When blended with the polymer donor PBDB-T, PCEs of over 11 % were achieved.^[9] The chemical structure is shown in Figure 7.1 and consists of central donor core of indacenodithieno[3,2-b]thiophene with two flanking 2-(3-oxo-2,3-dihydroinden-1-ylidene)malononitrile acceptor units. This A-D-A structure promotes intermolecular charge transfer and extends the absorption range. ITIC was purchased from 1-Material (NFA005) and used without further purification.

7.3.2 IDTBR

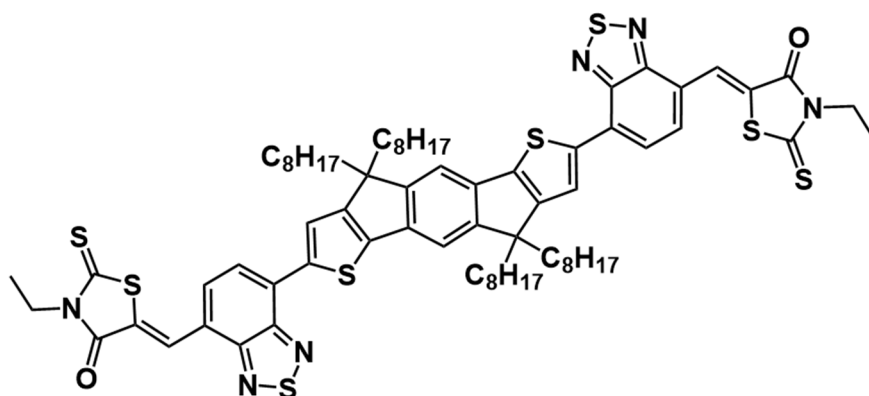


Figure 7.2 Chemical structure of IDTBR.

IDTBR was developed by the McCulloch group,^[10] and is shown in Figure 7.2. Like ITIC, IDTBR utilises an A-D-A structure. When blended with the polymer P3HT it achieved efficiencies of 6.4 % which was the highest reported efficiency for a non-fullerene P3HT solar cell.^[10] In addition the cells were shown to be much more air stable compared to other high performance polymer:fullerene systems.^[10] More recently IDTBR was blended with the new donor polymer PvBDTTAZ to create cells with PCEs of up to 11.6 % which is one of the highest efficiency non-fullerene cells reported to date.^[11] IDTBR exists in two isomers O-IDTBR and EH-IDTBR which have linear and branched alkyl solubilising groups respectively. In this work the EH-IDTBR isomer was used. IDTBR (NFA004) was purchased from 1-Material and used without further purification.

7.3.3 PC₆₁BM

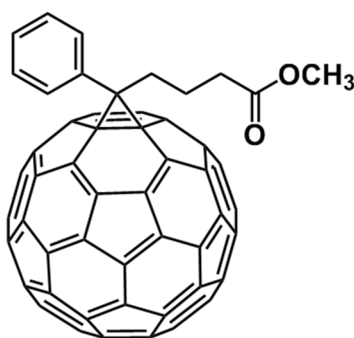


Figure 7.3 PC₆₁BM

As discussed in the previous chapter, [6,6]-Phenyl-C₆₁-butyric acid methyl ester (PC₆₁BM) is a soluble fullerene derivative that has been extensively used as the electron

acceptor in OPV cells and is the archetypical acceptor molecule. The PC₆₁BM was in this study was purchased from American Dye Source (ADS61BFA) had a purity of > 99.5 % and was used without further purification.

7.3.4 P3HT

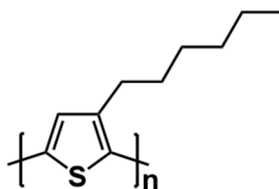


Figure 7.4 Chemical structure of P3HT

Poly-3-hexyl thiophene is one of the most widely studied electron donors in OPV. As shown in Figure 7.4 it consists of a simple thiophene repeat unit with a solubilising alkyl chain. Due to its simple structure, good film formation properties and wealth of previous literature it is used as a benchmark material in many OPV studies. P3HT was purchased from Rieke Metals (4002-EE) and had a molecular weight of 50 – 70 kDa and was 91 – 94 % regioregular. It was used without further purification.

7.4 Experimental

P3HT and the acceptor (PC₆₁BM, ITIC or IDTBR) were dissolved in anhydrous chlorobenzene in a 1:1 weight ratio to give a total concentration of 35 mg cm⁻³ inside a nitrogen glovebox and stirred at 50 °C overnight. The solution was pipetted into quartz EPR tubes and sealed under nitrogen atmosphere using paraffin film. To minimise the chance of sample degradation the tubes were then quickly transferred to the spectrometer lab where they were flash frozen in liquid nitrogen and stored at 77 K in the dark until required.

7.5 Results

7.5.1 LEPR Spectra of P3HT:Acceptor Blends

The LEPR spectra of the two new non-fullerene blended with P3HT were measured in frozen solution at 9.8 GHz, 34 GHz and 94 GHz. The LEPR spectra of the well-studied P3HT:PC₆₁BM blend was also measured to serve as a reference. Measuring frozen solutions prevents partial orientation effects from complicating the interpretation and simulation of the spectra. LEPR spectra at the three microwave frequencies are shown in Figure 7.5. The dark spectrum of the three blends was very weak and after illumination the EPR intensity grew by over an order of magnitude indicating that the species displayed in Figure 7.5 correspond to light induced charge separated states.

In the P3HT:PC₆₁BM blend, the EPR signatures of the positive and negative polarons can clearly be discriminated and spectrally separate as the frequency is increased. From previous EPR studies the broad low field signature can be assigned to positive polarons (P⁺) on the P3HT and the sharp high field signal to negative polarons (P⁻) on the PC₆₁BM.^[12-14] In contrast the EPR signatures of the P⁺ and P⁻ in the blends with ITIC and IDTBR cannot be clearly differentiated. At 9.8 GHz the P⁻ on ITIC is almost completely obscured by the P⁺. Moving to 34 GHz allows the peak of the P⁻ to be resolved and shows that it lies of the low field side of the spectrum. Even at 94 GHz there is substantial overlap of the P⁺ and P⁻ signatures which indicates that their principal values are intermixed and the signatures therefore cannot be separated by moving to higher frequencies. The situation is similar in the IDTBR blend, with strong overlap of the P⁺ and P⁻ at 94 GHz. However the IDTBR P⁻ signature extends to much lower fields which causes a distinctive bump on the low field side of the spectrum that can be seen at all three frequencies. The strong overlap of the P⁻ signature with P⁺ makes determination of its lineshape and principal values difficult. The aim of the first half of this chapter is to accurately determine the principal values of P⁻ on ITIC and IDTBR through multifrequency simulations and comparisons with the P3HT:PC₆₁BM spectra.

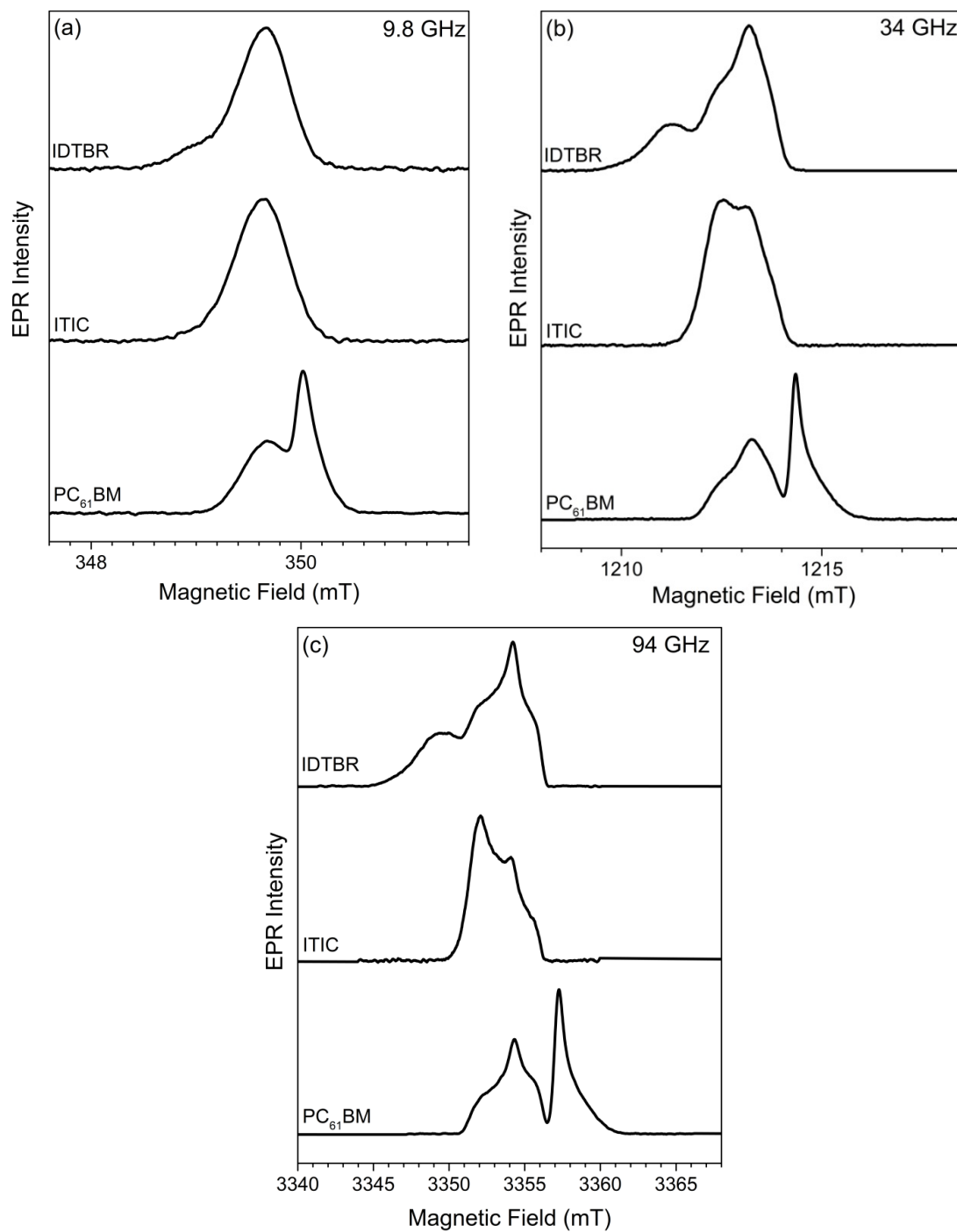


Figure 7.5 LEPR spectra of ITIC, IDTBR and PC₆₁BM blended with P3HT in frozen chlorobenzene solution at T = 50 K. The spectra were recorded at (a) 9.8 GHz, (b) 34 GHz and (c) 94 GHz using a Hahn echo pulse sequence. The dark spectrum has been subtracted from each.

7.5.2 Simulation of P3HT:PC₆₁BM LEPR Spectra

In order to determine the spectral signatures and principal values of P[•] on IDTBR and ITIC, the signature of P[•] on P3HT must be accurately known at each frequency. The P[•] signature can then be held constant during the simulations of the P3HT:ITIC and P3HT:IDTBR spectra, greatly reducing the number of free parameters. The spectra of the P3HT:PC₆₁BM blend is ideally suited to characterise the P[•] signature as the P[•] and P[•] are well separated at all three frequencies.

The simulations of the P3HT:PC₆₁BM LEPR spectra are shown in Figure 7.6. The principal values of the P[•] and P[•] g-tensors were determined from the 94 GHz spectra and used to constrain the 9.8 GHz and 34 GHz simulations. It can be seen that the simulation captures the experimental lineshape accurately across the three frequencies. The principal values used to simulate the spectra are given in Table 7.1 and are in agreement with previous reports.^[12, 14-17]

Table 7.1 Principal values of the P[•] and P[•] g-tensors. The relative error in the principal values is ±0.0002. The error in the g_z component of P[•] is larger, ±0.0004, due to the high g-strain.

Polaron	g_x	g_y	g_z
P [•] on P3HT	2.0039	2.0022	2.0011
P [•] on PC ₆₁ BM	2.0005	2.0005	1.9992

One curiosity is that the weights of the positive and negative polaron components required in the simulation are not equal and vary across the three frequencies. The relative weight of the P[•] component required in the simulations was 1.19, 1.21 and 1.28 for the 9.8 GHz, 34 GHz and 94 GHz spectra respectively. If the P[•] and P[•] are generated from electron transfer between the polymer and fullerene there will be equal numbers of P[•] on P3HT as there is P[•] on PC₆₁BM due to charge neutrality. One would therefore expect the intensity of the P[•] and P[•] signatures to be equal and require equal weights in the simulation. The greater intensity of the P[•] component at all three frequencies cannot be due to spin lattice relaxation effects as the T₁ of P[•] on P3HT is substantially longer than P[•] on PC₆₁BM (see Figure 7.7). Therefore if the intensities of P[•] and P[•] were spin lattice relaxation limited the P[•] would have less intensity than P[•]. Different weights of the P[•] and P[•] components have been observed in polymer fullerene systems previously.^[14, 18, 19] One proposed explanation is that a fraction of the excitons directly dissociate on the polymer, rather

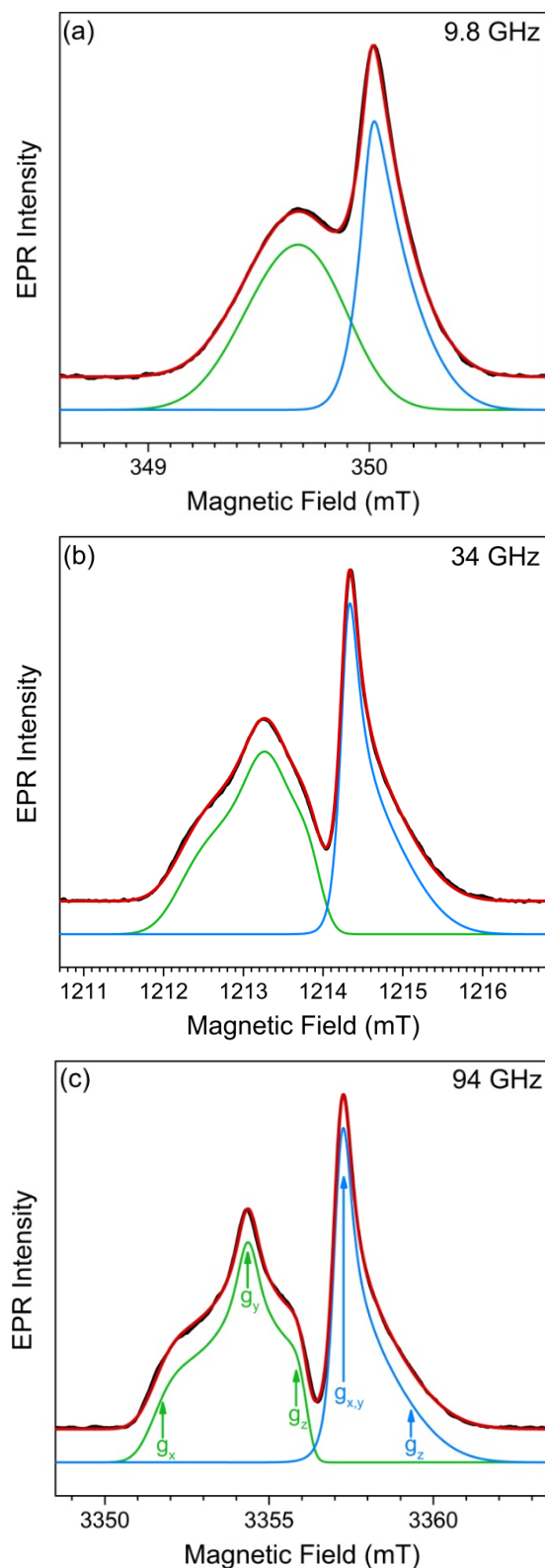


Figure 7.6 LEPR spectra of P3HT:PC₆₁BM in frozen chlorobenzene solution at T = 50 K. The experimental spectra (black) are shown alongside theoretical simulations of the P⁺ residing on the donor (green), P⁺ on the PC₆₁BM (blue) and the superposition of both (red).

than through electron transfer to the fullerene which leaves both P^+ and P^- on P3HT and both contribute to the intensity of the ‘positive’ polaron signature in the spectra.^[18] The variation in P^+ weight across the three frequencies likely arises from differences in light intensity in each measurement rather than an EPR effect. Due to the differing optical access of the resonators the light intensity is greatest in the 9.8 GHz and weakest at 94 GHz. Previous studies have shown that the weight of P^- component increases with increasing light intensity, in agreement with the trend observed here.^[14, 19]

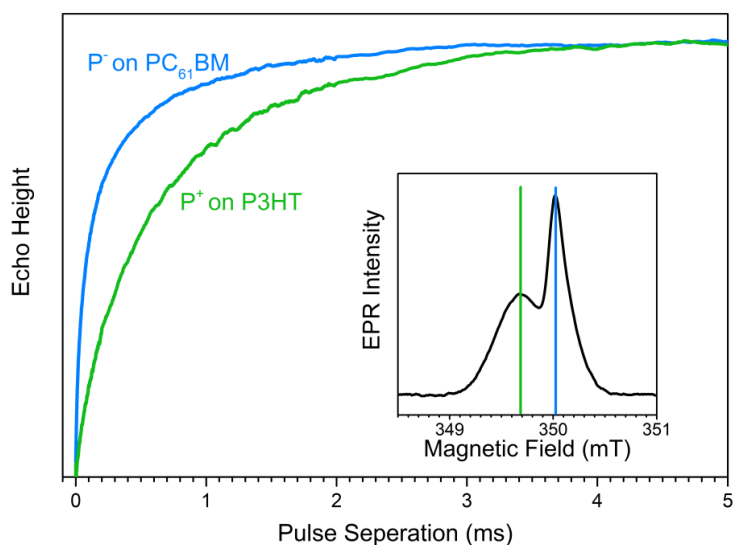


Figure 7.7 Inversion recovery of P^+ and P^- in P3HT:PC₆₁BM frozen chlorobenzene solution at $T = 50$ K. The spectra were recorded at 9.8 GHz using the inversion recovery pulse sequence. The recovery of the P^+ echo height is shown in green and the P^- in blue. The magnetic field positions of the recovery experiments are shown in the inset.

A potential method to help deconvolute the overlapping signatures of the P^+ and P^- in the non-fullerene blends is to take advantage of the different spin lattice relaxation times of each polaron. By decreasing the shot repetition time (time between each Hahn echo pulse sequence) the intensity of the component with longer T_1 can be suppressed which provides an extra constraint during deconvolution. Before applying this technique it is important to characterise any variations that occur in the P^+ when the shot repetition time is varied. The effect of changing the shot repetition time on the P3HT:PC₆₁BM spectra was therefore investigated. The inversion recovery measurement of the P3HT:PC₆₁BM blend is shown in Figure 7.7. It can be seen that if the shot repetition time is decreased below ~ 3 ms the P^+ will not have had time to fully recover and will be suppressed. The decrease of the P^+ intensity with decreasing shot repetition time is shown in Figure 7.8a. The same

spectra but now normalised to the height of the P^+ peak is shown in Figure 7.8b where it can be seen that the use of short repetition times also distorts the lineshape of the P^+ , which indicates that the spin lattice relaxation is anisotropic.

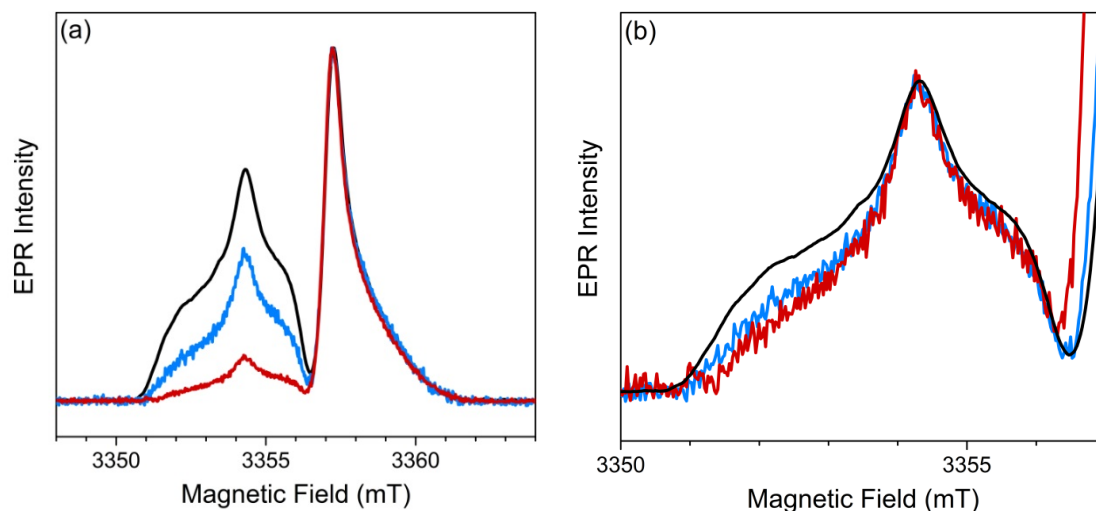


Figure 7.8 Influence of the shot repetition time on the LEPR spectrum of P3HT:PC₆₁BM in frozen chlorobenzene solution at T= 50 K. The spectra were recorded at 94 GHz using shot repetition times of 10 ms (black), 1 ms (blue) and 0.1 ms (red). In (a) the spectra are normalised to the height of the P^- and in (b) normalised to the height of the P^+ .

In order to accurately simulate the P^+ this spin lattice relaxation distortion has to be taken into account. The distortion appears to behave like orientation selection where the intensity of the g_x , g_y and g_z components is no longer equal and the spectrum can't be treated as a powder average. However the EasySpin toolbox,^[20] that was used to simulate the spectra is not capable of incorporating orientation selection and anisotropic broadening simultaneously. Instead the distortion was simulated by convoluting the P^+ lineshape with a Gaussian distribution centred on 3355 mT which suppresses the outer shoulders of the P^+ . The lineshape of the P^+ can be accurately simulated through this method using Gaussians with FWHM of 9 mT and 6 mT for the 1 ms and 0.1 ms spectra respectively as shown in Figure 7.9. The characterisation of the P^+ presented in this section can now be used to help uncover the signatures of the P^- on ITIC and IDTBR.

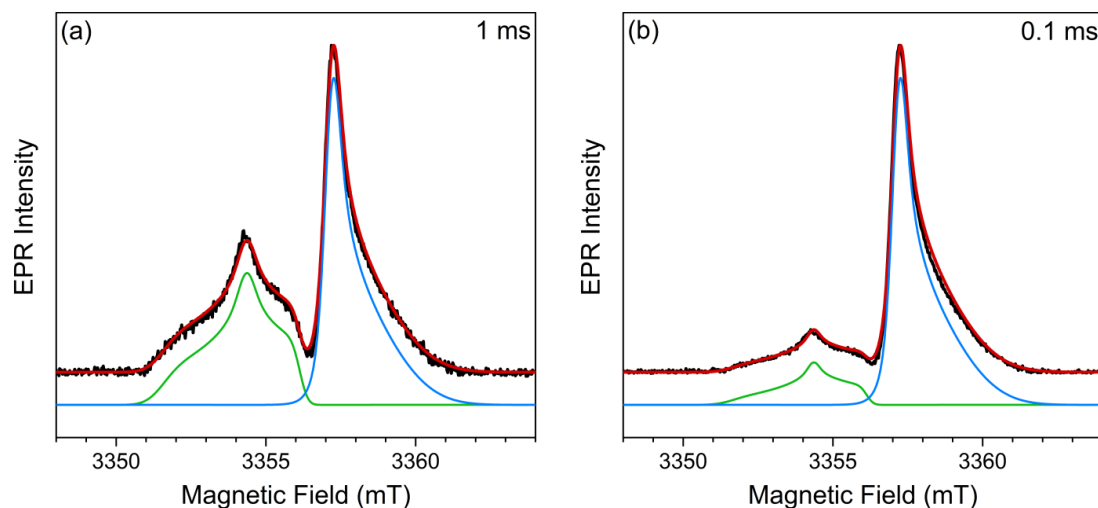


Figure 7.9 LEPR spectra of P3HT:PC₆₁BM in frozen chlorobenzene solution at T= 50 K recorded using short shot repetition times. The experimental spectra (black) are shown alongside theoretical simulations of the P⁺ residing on the donor (green), P⁺ on the PC₆₁BM (blue) and the superposition of both (red). (a) Experimental spectrum was recorded using a shot repetition time of 1 ms and the distorted P⁺ lineshape simulated by convoluting the P⁺ lineshape with a Gaussian distribution centred on 3355 mT and a FWHM of 9 mT. (b) Experimental spectrum was recorded using a shot repetition time of 0.1 ms and the distorted P⁺ lineshape simulated by convoluting the P⁺ lineshape with a Gaussian distribution centred on 3355 mT and FWHM of 6 mT.

7.5.3 Simulation of P3HT:ITIC LEPR Spectra

To determine the lineshape and principal values of P[•] on ITIC, the P3HT:ITIC spectra were simulated using EasySpin across the three frequencies. The lineshape of the P⁺ was assumed to be identical to that in the P3HT:PC₆₁BM blends, and the principal values and anisotropic broadening parameters used to simulate the P⁺ in Figure 7.6 were therefore used without change in the P3HT:ITIC simulations. This is a reasonable assumption as in frozen solution the local environment of each polymer is dominated by solvent molecules rather than interactions with the acceptor molecules and therefore switching acceptors should not significantly alter the P⁺ lineshape. Furthermore previous studies have shown that the principal values of P⁺ on P3HT are insensitive to changing PC₆₁BM with PC₇₁BM.^[12] The weight of the P⁺ component was left as a freely varying parameter in the simulation. The 94 GHz spectrum was simulated first using a least squares regression. The principal values obtained from the 94 GHz simulation were then used to constrain the 34 GHz and 9.8 GHz simulations. The principal values of P[•] that gave the best fit across the three frequencies are given in Table 7.2. The g-tensor exhibits approximately axial symmetry in agreement with the square like nature of its chemical structure

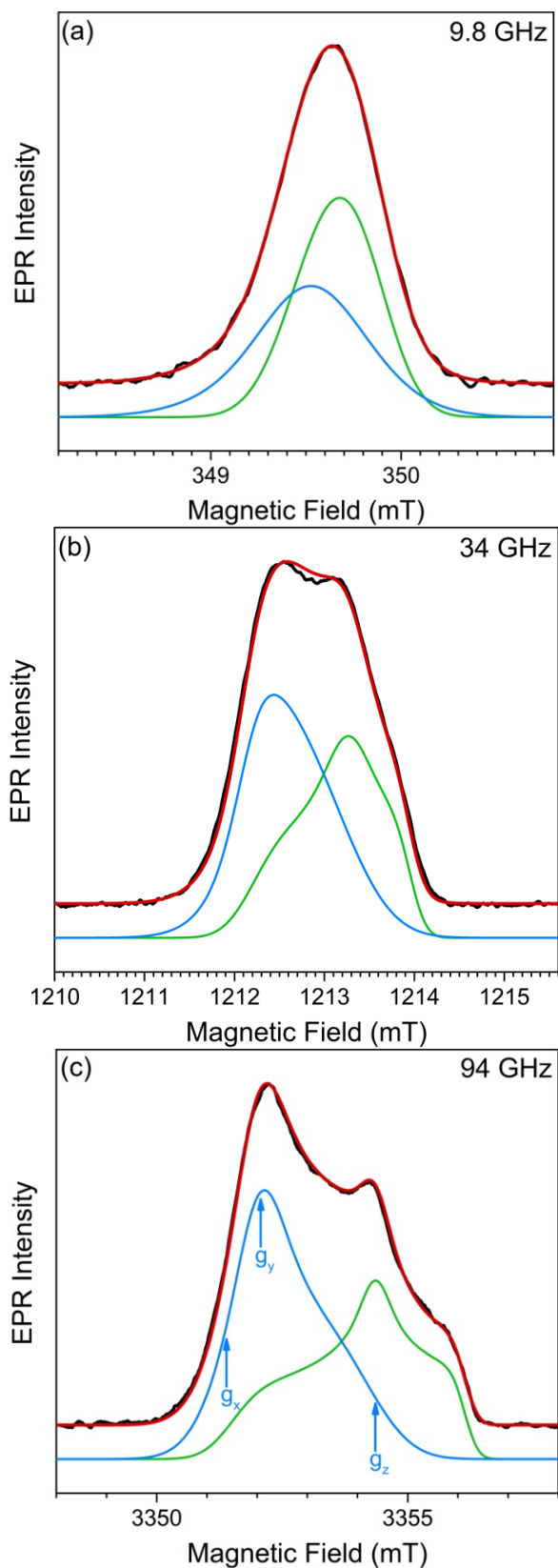


Figure 7.10 LEPR spectra of P3HT:ITIC in frozen chlorobenzene solution at T = 50 K. The experimental spectra (black) are shown alongside theoretical simulations of the P⁺ residing on the donor (green), P⁺ on the ITIC (blue) and the superposition of both (red).

(see Figure 7.1). The simulations using the principal values in Table 7.2, are shown in Figure 7.10. It can be seen that the simulation captures the experimental lineshape with good accuracy at all frequencies which supports the validity of the determined principal values. In order to estimate the error in the simulations, particularly the completely obscured g_z value, the simulations were repeated while holding one of principal values fixed. For example, to determine the range of possible g_z values the simulation was run 8 times and during each run a different value of g_z was used. The chosen g_z value was held constant and the g_x and g_y values allowed to vary freely. The range of g_z values where the simulation was able to accurately converge on the experimental lineshape then defines the error in g_z value. The range of g_z values which achieved successful convergence was 2.0019 to 2.0024 giving an error of approximately ± 0.0003 . An analogous procedure was used for the g_x and g_y values which gave approximate errors of ± 0.0002 .

Table 7.2 Principal values of the P^- g-tensor on ITIC.

Principal Values	
g_x	2.0040 ± 0.0002
g_y	2.0036 ± 0.0002
g_z	2.0022 ± 0.0003

In order to try and observe the lineshape of the P^- directly and confirm chosen principal values, the shot repetition time was varied in an effort to suppress the P^+ . The lineshape at different shot repetition times is shown in Figure 7.11. Overall the change in relative intensity of the P^+ and P^- is minimal indicating that the T_1 of the P^+ and P^- is similar in value. More interestingly is that as the shot repetition time is decreased from 10 ms to 1 ms the relative intensity of the P^+ component increases, however when the shot repetition time is decreased further to 0.1 ms the relative intensity of the P^+ then decreases. This again indicates that the inversion recovery of both species is highly similar and that the recovery curves are multi-exponential which results in a crossing point.

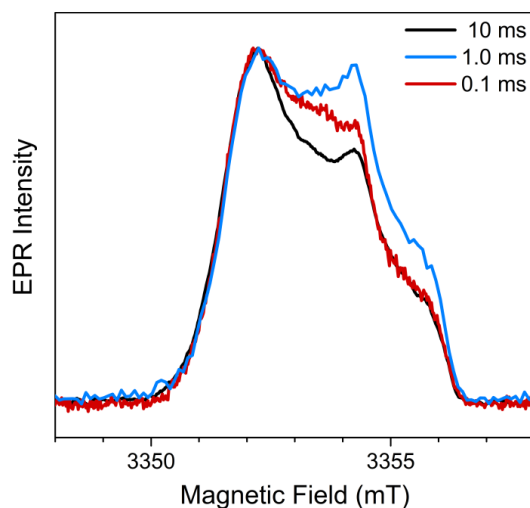


Figure 7.11 Influence of the shot repetition time on the LEPR spectrum of P3HT:ITIC in frozen chlorobenzene solution at $T= 50$ K. The spectra were recorded at 94 GHz using shot repetition times of 10 ms (black), 1 ms (blue) and 0.1 ms (red). The spectra have been normalised.

The spectra recorded at the 1 ms and 0.1 ms shot repetition times were simulated using the suppressed P^+ lineshapes from Figure 7.9 and are shown in Figure 7.12. The relative weight of the P^+ was 1.20, 1.25 and 0.72 in the 10 ms, 1ms and 0.1 ms simulations respectively. The principal values required to simulate the 1 ms and 0.1 ms were slightly different from those in Table 7.2 with g_x and g_z values of 2.0038 and 2.0023, but are in overall good agreement. This reduced anisotropy is likely due to distortion of the P^+ lineshape, in a similar manner to that observed in the P^+ in P3HT in the previous section.

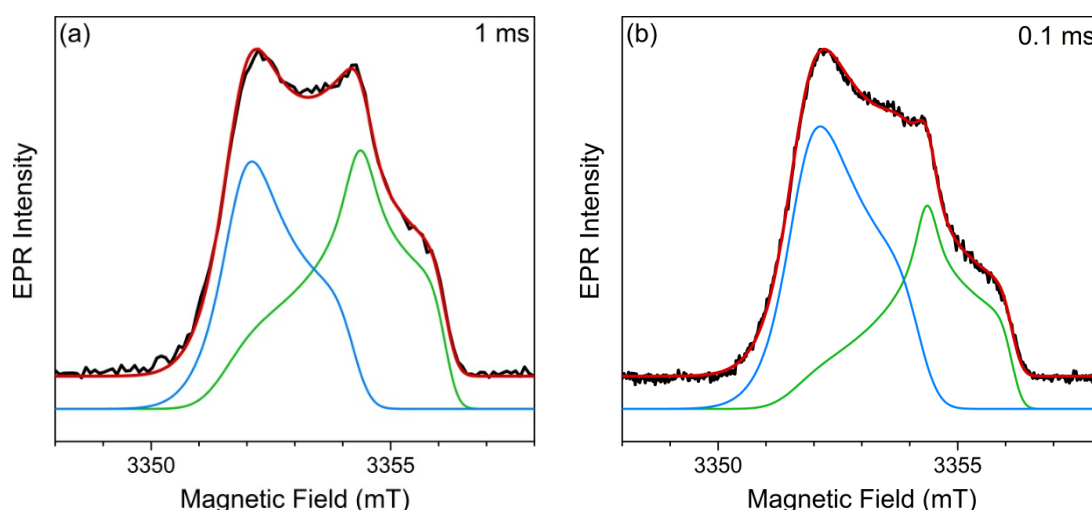


Figure 7.12 LEPR spectra of P3HT:ITIC in frozen chlorobenzene solution at $T= 50$ K recorded at low shot repetition times. The experimental spectra (black) are shown alongside theoretical simulations of the P^+ residing on the donor (green), P^+ on the ITIC (blue) and the superposition of both (red). (a) Experimental spectrum was recorded using a shot repetition time of 1 ms and the distorted P^+ lineshape simulated by convoluting the P^+ lineshape with a Gaussian distribution centred on 3355 mT and a FWHM of 9 mT. (b) Experimental spectrum was recorded using a shot repetition time of 0.1 ms and the distorted P^+ lineshape simulated by convoluting the P^+ lineshape with a Gaussian distribution centred on 3355 mT and FWHM of 6 mT.

7.5.4 Simulation of P3HT:IDTBR LEPR Spectra

A similar approach was adopted to determine the spectral lineshape and principal values of P^+ on IDTBR. Least squares simulations were first run on the 94 GHz spectra in order to determine the range of possible principal values. Similarly to P3HT:ITIC, the simulations were ran where one principal value was locked in position and the other two allowed to vary freely in order to determine the extrema of each principal value beyond which the simulated spectra no longer converge. Despite being completely obscured the g_z value has the smallest range and can only take values between 2.0020 to 2.0024 before the simulations fail to adequately converge. In contrast the g_x and g_y values are rather ill defined and the experimental spectra can be accurately simulated with values ranging from 2.0058 to 2.0066 and 2.0050 to 2.0057 for g_x and g_y respectively. This process was repeated for the 34 GHz spectra where the range of possible g_z values was similar to the 94 GHz and varied from 2.0020 to 2.0025. The g_x value is more defined than in the 94 GHz spectra with extrema of 2.0060 to 2.0064 while the g_y values vary from 2.0052 to 2.0060. There is noticeable skew in the g_y range obtained from the 34 GHz simulations to higher g-factors than the range obtained from the 94 GHz simulations. The reason for this discrepancy is unclear but there is still substantial overlap of the two ranges. The overlap region of the two ranges is 2.0052 to 2.0057 and the mean value of this overlap region is therefore taken the principal value of g_y . The principal values of the g_x and g_z were determined in the same manner. The principal values and uncertainties are listed in Table 7.3.

Table 7.3 Principal values of the P^+ g-tensor on IDTBR.

Principal Values	
g_x	2.0062 ± 0.0003
g_y	2.0055 ± 0.0004
g_z	2.0022 ± 0.0002

The simulations using the principal values in Table 7.3 at the three microwave frequencies are shown Figure 7.13. The 9.8 and 94 GHz simulations reproduce the experimental lineshape with good accuracy. The 34 GHz simulation is less accurate, as the simulation is unable to reproduce the sharpness of the P^+ peak on the low field side. This discrepancy may be due to assumption that the P^+ lineshape is unchanged between P3HT:PC₆₁BM and

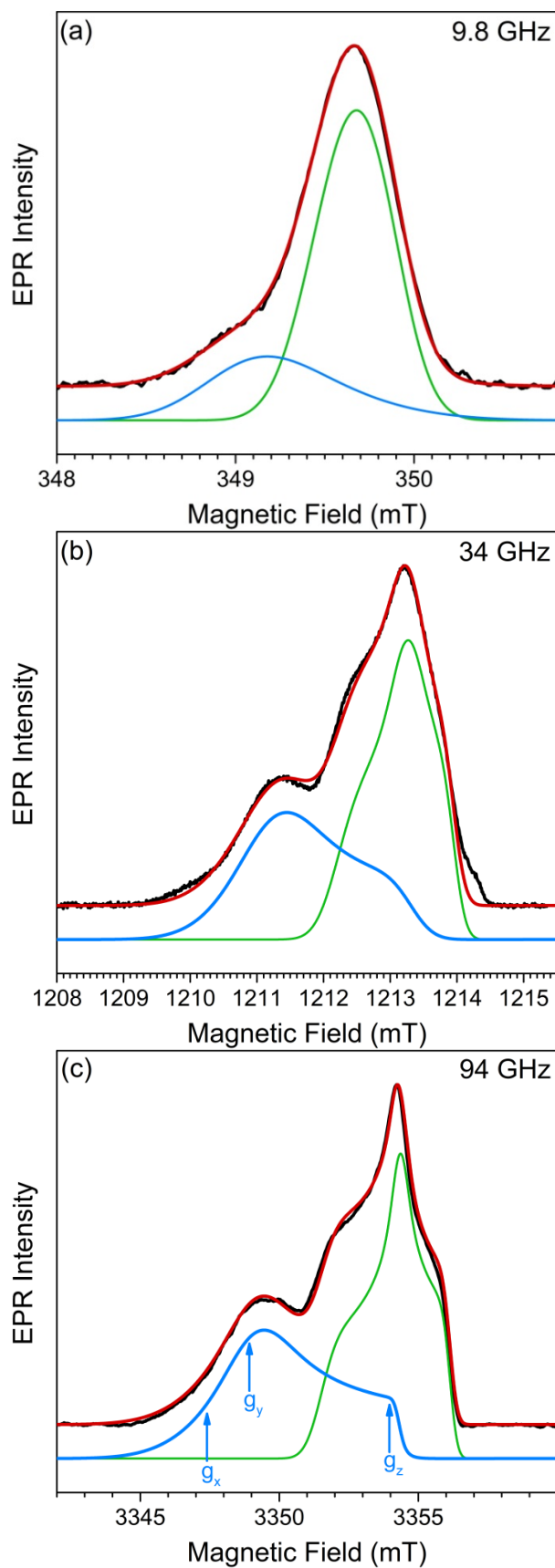


Figure 7.13 LEPR spectra of P3HT:IDTBR in frozen chlorobenzene solution at T = 50 K. The experimental spectra (black) are shown alongside theoretical simulations of the P⁺ residing on the donor (green), P⁺ on the IDTBR (blue) and the superposition of both (red).

P3HT:IDTBR. A slight reduction in the g_x value of P^+ or its broadening would allow greater reproduction of the experimental spectrum. The bump on the high field side of the 34 GHz simulation that is not captured by the simulation is due to a background signal in the resonator and not the P3HT:IDTBR sample under study.

In order to confirm the principal values in Table 7.3, spin relaxation suppression of the P^+ using variable shot repetition times was once again explored. The P^+ on P3HT and P^- IDTBR are sufficiently spectrally separated to measure the inversion recovery of the two polarons. The inversion recovery of the P^+ and P^- at 50 K using 34 GHz microwave pulses is shown in Figure 7.14, where it can be seen that the recovery of the P^- is substantially faster than the P^+ which allows spin relaxation suppression to be effectively used. The P3HT:IDTBR sample was measured at 94 GHz at 50 K using shot repetition times of 1 ms and 0.1 ms giving the spectra shown in Figure 7.15. The least squares simulations of the 1 ms and 0.1 ms returned principal values of (2.0060, 2.0055, 2.0023) and (2.0057, 2.0055, 2.0023) respectively. Comparing these values to those in Table 7.3 it can be seen that the anisotropy of the g-tensor is reduced as the shot repetition time is decreased, with a pronounced shift in g_x towards lower values. This is likely a similar mechanism to the anisotropy reduction observed for the P^- on ITIC and P^+ on P3TH where the weights are

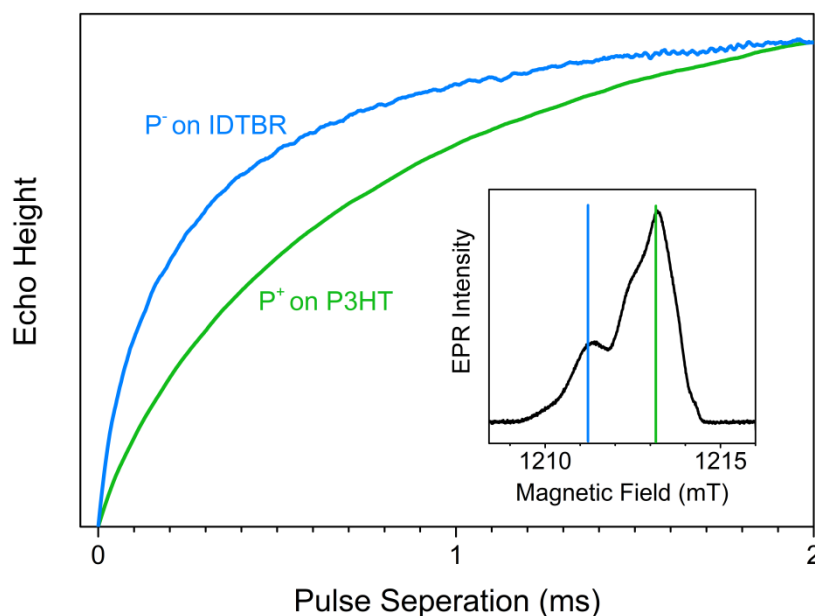


Figure 7.14 Inversion recovery of P^+ and P^- in P3HT:IDTBR frozen chlorobenzene solution at $T = 50\text{K}$. The spectra were recorded at 34 GHz using the inversion recovery pulse sequence. The recovery of the P^+ echo height is shown in green and the P^- in blue. The magnetic field positions of the recovery experiments are shown in the inset.

of the three principal values are no longer equivalent. Overall the g-tensors at short shot repetition times support the principal value assignment in Table 7.3

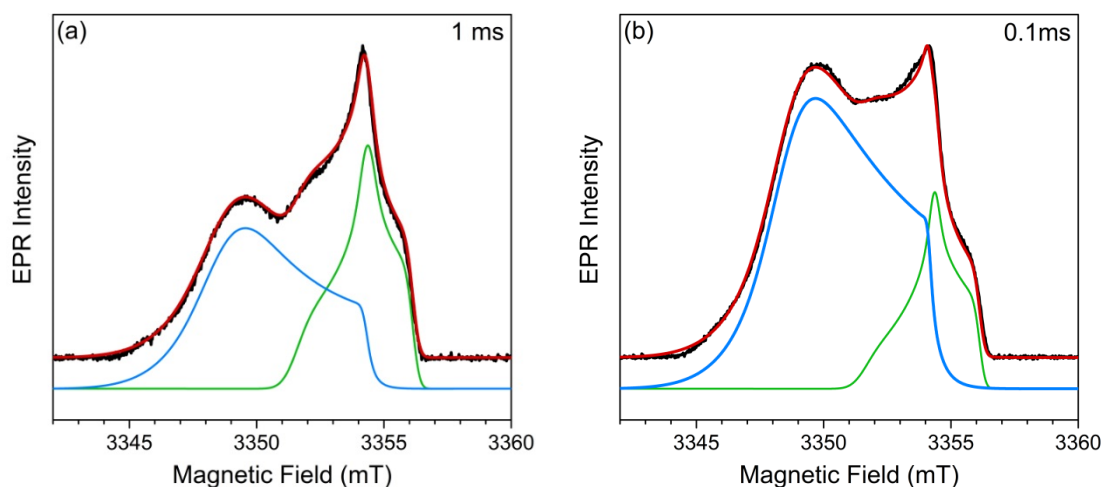


Figure 7.15 LEPR spectra of P3HT:IDTBR in frozen chlorobenzene solution at $T=50$ K recorded at low shot repetition times. The experimental spectra (black) are shown alongside theoretical simulations of the P^+ residing on the donor (green), P^- on the IDTBR (blue) and the superposition of both (red). (a) Experimental spectrum was recorded using a shot repetition time of 1 ms and the distorted P^+ lineshape simulated by convoluting the P^+ lineshape with a Gaussian distribution centred on 3355 mT and a FWHM of 9 mT. (b) Experimental spectrum was recorded using a shot repetition time of 0.1 ms and the distorted P^+ lineshape simulated by convoluting the P^+ lineshape with a Gaussian distribution centred on 3355 mT and FWHM of 6 mT.

Even at the shortest shot repetition times at 94 GHz there is still a sizable P^+ component. The shot repetition time measurement was therefore repeated on 34 GHz spectrometer where the shot repetition time can be decreased to 0.02 ms. In addition the sample was cooled down to 10 K to enhance the difference between the P^+ and P^- recovery time. The

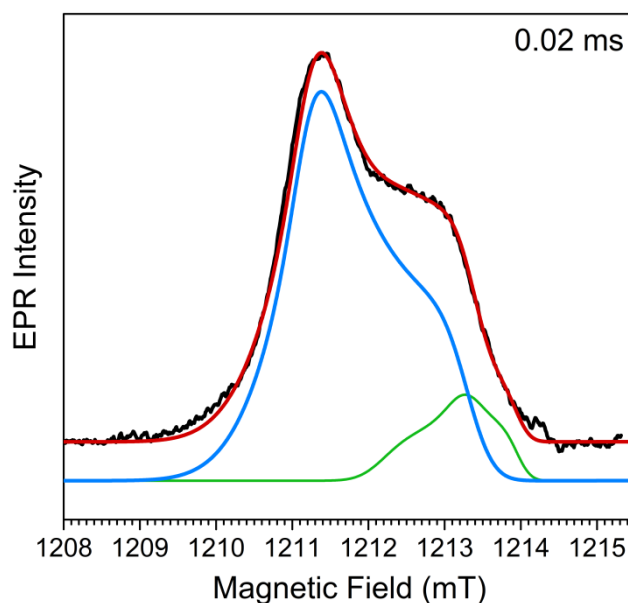


Figure 7.16 LEPR spectra of P3HT:IDTBR in frozen chlorobenzene solution at $T=10$ K recorded using a shot repetition time of 0.02 ms. The experimental spectrum (black) is shown alongside theoretical simulations of the P^+ residing on the donor (green), P^- on the IDTBR (blue) and the superposition of both (red).

0.02 ms shot repetition time measurement is shown in Figure 7.16. At this short a time the P^+ is nearly completely suppressed and Figure 7.16 provides an almost direct visualisation of the P^- lineshape. The least squares simulation of the experimental spectrum returns principal values of (2.0063, 2.0056, 2.0022) which is in good agreement to those reported in Table 7.3.

7.5.5 ENDOR

In order to get more information on the environment of the negative polarons, ENDOR spectroscopy was used to measure the strength of the hyperfine coupling. Due to the strong overlap of the P^+ and P^- selective pulse sequences are required which makes Davies ENDOR the natural choice as it requires a selective first pulse (Section 4.3.3). The ENDOR spectra of the P3HT:PC₆₁BM blend was first measured in order to isolate the signature of P^+ on P3HT and investigate whether there is any variation in the P^+ ENDOR spectrum with field position.

9.8 GHz ENDOR spectra of P3HT:PC₆₁BM are shown in Figure 7.17. A 256-128-256 Davies pulse sequence was used to record the spectra which has an excitation width of approximately 0.1 mT and therefore only probes a small region of the P^+ . ENDOR spectra were recorded at three field positions on the P^+ as shown in the top panel. The P^+ ENDOR spectra are centred on the proton Larmor frequency and have a FWHM of 2.4 MHz at the low field positions which decreases slightly to 2.1 MHz at the peak of the P^+ LEPR signature. This measurement was repeated at 34 GHz using the same Davies pulse sequence. The 34 GHz spectra are shown in Figure 7.18 and exhibit a FWHM of 2.4 GHz at both field positions. In summary the FWHM of the P^+ ENDOR spectrum is approximately 2.4 GHz and is relatively invariant with field position. Using this information the ENDOR spectra of the P^- on ITIC and IDTBR can now be identified.

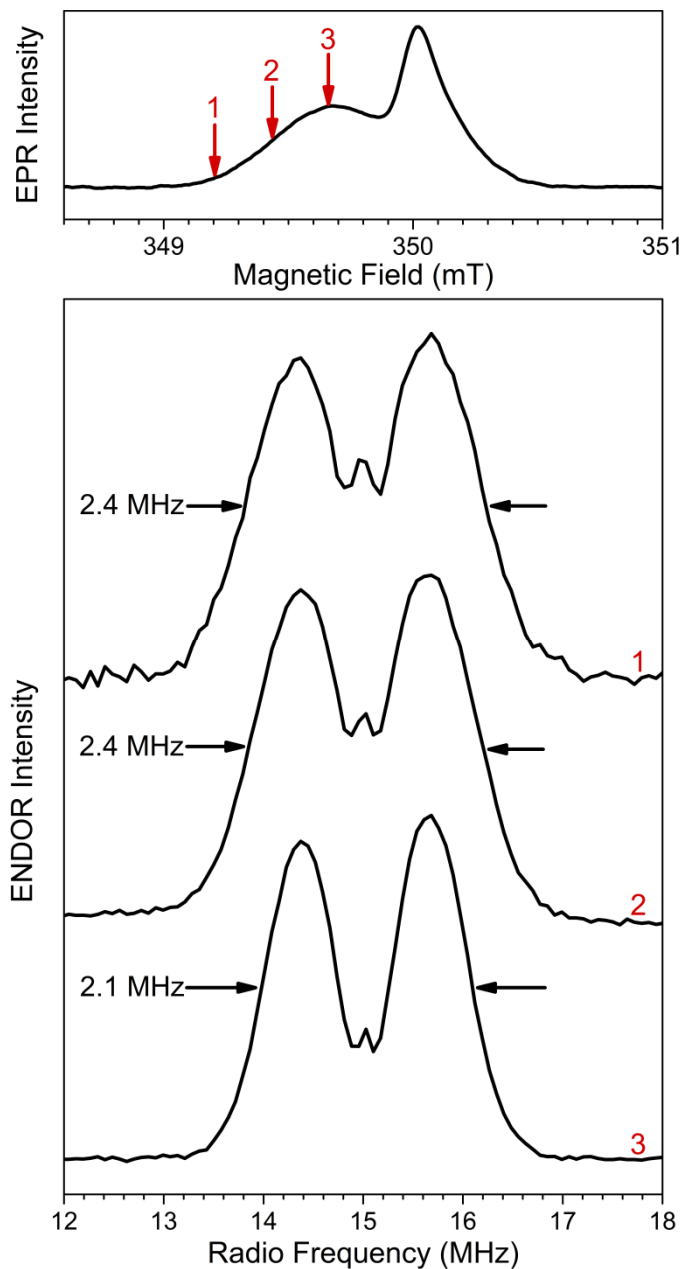


Figure 7.17 ENDOR spectra of P3HT:PC₆₁BM in frozen chlorobenzene solution at T = 50 K. The spectra were recorded at 9.8 GHz using a selective Davies pulse sequence. The spectra were recorded at three locations on the P⁺, shown by the red arrows in the top figure. The spectra are centred on the Larmor frequency of ¹H and the black arrows denote the FWHM.

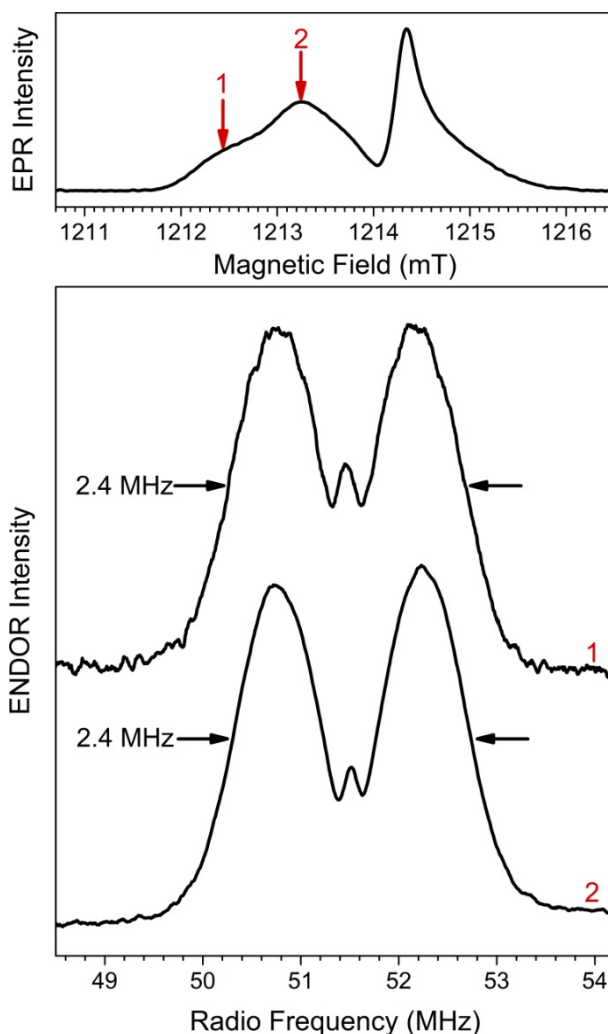


Figure 7.18 ENDOR spectra of P3HT:PC₆₁BM in frozen chlorobenzene solution at T = 50 K. The spectra were recorded at 34 GHz using a selective Davies pulse sequence. The spectra were recorded at two locations on the P⁺, shown by the red arrows in the top figure. The spectra are centred on the Larmor frequency of ^1H and the black arrows denote the FWHM.

The 34 GHz ENDOR spectra of P3HT:ITIC at five field positions are shown in Figure 7.19. At position 1 the ENDOR spectrum arises solely from P⁻ and consists of a central component with a spread of 3.5 MHz and a much broader component which can be seen from the distortion in the baseline. At higher field positions the FWHM of the central component narrows. This is primarily due to an increasing contribution from P⁺ since the central component becomes a superposition of the 3.5 MHz coupling distribution from P⁻ and the 2.4 MHz distribution from P⁺. At position 3 the central feature is dominated by the contribution from P⁺ and the only indication of P⁻ coupling is a small baseline distortion. By positions 4 and 5 the spectrum is wholly comprised of the coupling from the P⁺. Due to the contribution from P⁺ it is difficult to discern whether the linewidth of the P⁻ coupling also changes with field position.

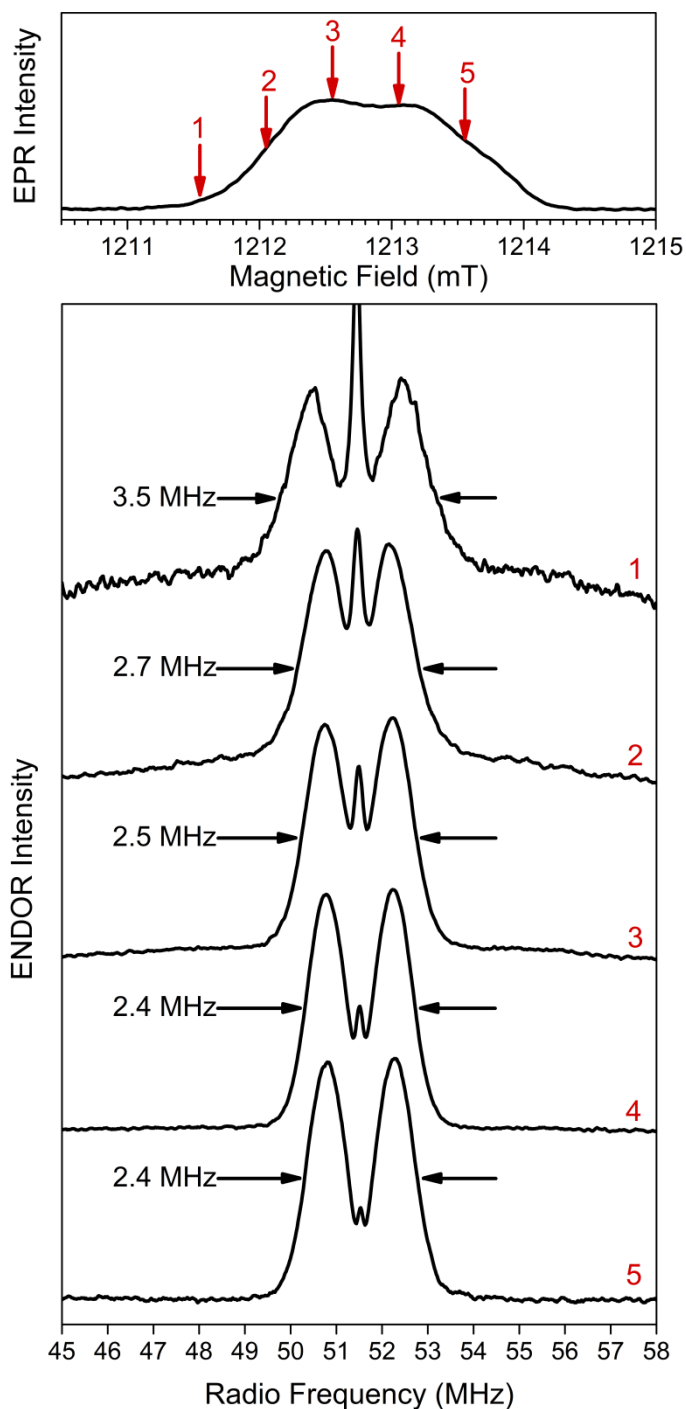


Figure 7.19 ENDOR spectra of P3HT:ITIC in frozen chlorobenzene solution at $T = 50$ K. The spectra were recorded at 34 GHz using a selective Davies pulse sequence. The spectra were recorded at five locations, shown by the red arrows in the top figure. The spectra are centred on the Larmor frequency of ^1H and the black arrows denote the FWHM.

In order to observe the broad component, the spectrum at position 2 was captured over a wider field range as shown in Figure 7.20. The spectrum consists of a narrow component with a FWHM of 2.7 MHz which is a combination of the 3.5 MHz P^- and the 2.4 MHz P^+ coupling distributions in addition to a much broader component with a FWHM of 11.6

MHz which indicates the $P^{\cdot-}$ is very strongly coupled to a subset of the protons in the molecule.

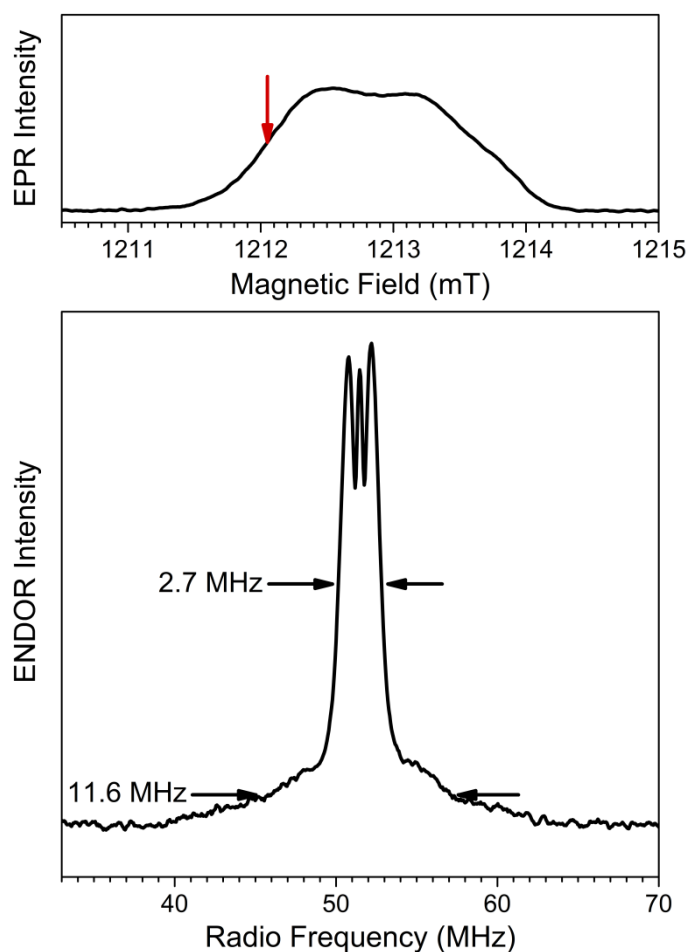


Figure 7.20 Wide frequency range ENDOR spectrum of P3HT:ITIC in frozen chlorobenzene solution at $T = 50$ K. The spectrum was recorded at 34 GHz using a selective Davies pulse sequence. The spectrum was recorded at the location shown by the red arrow in the top figure. The spectrum is centred on the Larmor frequency of ^1H and the black arrows denote the FWHM of the two components.

The ENDOR spectra of P3HT:IDTBR are shown in Figure 7.21. At positions 1 and 2 the ENDOR spectra are comprised solely from coupling in $P^{\cdot-}$ and the FWHM is around 4.5 MHz. Upon closer inspection it can be seen that characterising the ENDOR spectra with a single FWHM is misleading. The spectra at positions 1 and 2 appear to be comprised of a superposition of two coupling distributions which gives rise to broad wings in the spectra and indicates that the $P^{\cdot-}$ is coupled more strongly to a subset of the protons in the molecule. As the magnetic field is increased the spectra again narrow due to increasing contribution from the P^+ coupling and by positions 4 and 5 and ENDOR spectra wholly arise from the P^+ .

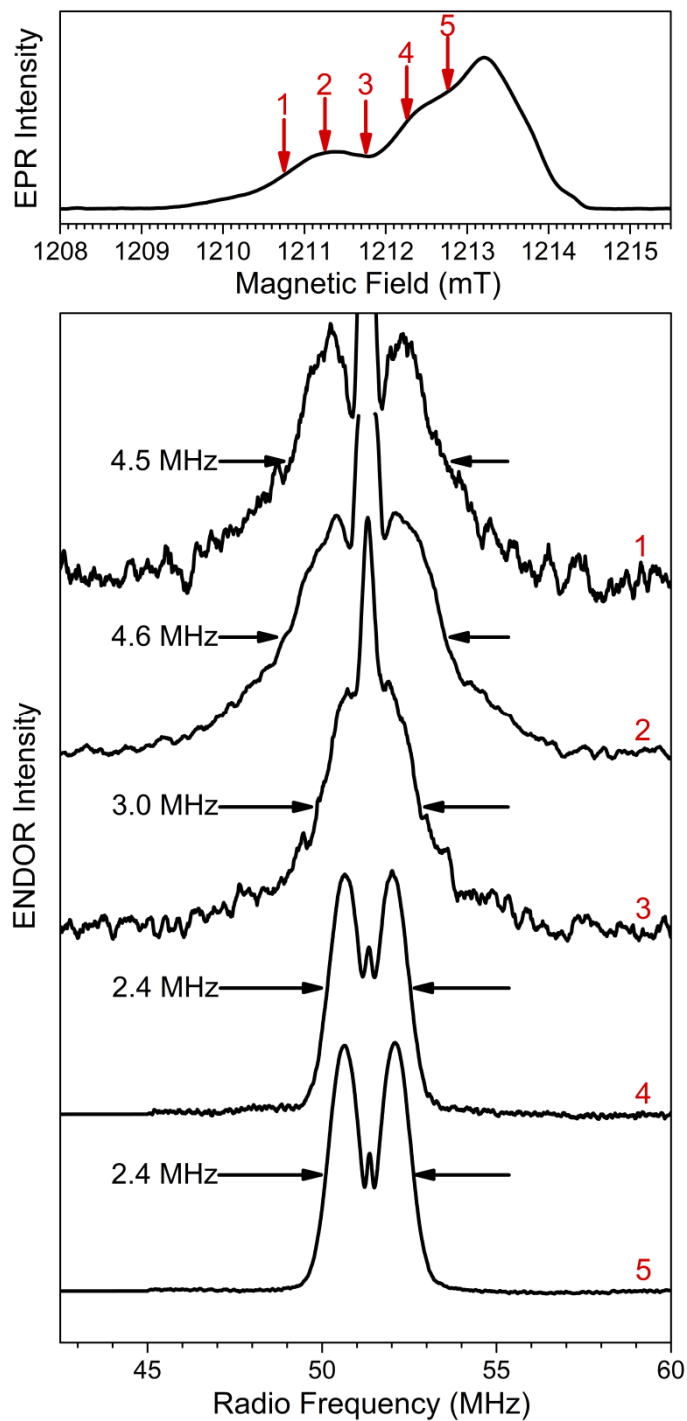


Figure 7.21 ENDOR spectra of P3HT:IDTBR in frozen chlorobenzene solution at $T = 50$ K. The spectra were recorded at 34 GHz using a selective Davies pulse sequence. The spectra were recorded at five locations, shown by the red arrows in the top figure. The spectra are centred on the Larmor frequency of ^1H and the black arrows denote the FWHM.

7.5.6 DFT and Future Work

DFT electronic structure calculations of ITIC and IDTBR to support this work are currently being undertaken by Dr. Trevor Dines at the University of Dundee. These calculations are ongoing but the preliminary results shall be briefly discussed here. A comparison of the principal values from the experimental simulations and DFT calculations is shown in Table 7.4. The DFT calculations reproduce the experimental g_y and g_z principal values with good accuracy but overestimate the g_x value severely in all instances. The reason for this discrepancy is currently being investigated. A possible cause is solvation effects, which were neglected in the DFT calculations, and have been shown in the past to lower the g_x value.^[12] The values in Table 7.4 are also only for the lowest energy conformation of the molecular structure and calculations on other energetically accessible conformations have still to be undertaken.

Table 7.4 Comparison of experimental principal values with those from DFT calculations.

Species	g_x	g_y	g_z
ITIC Experimental	2.0040(2)	2.0036(2)	2.0022(2)
ITIC DFT 6-31G	2.0054	2.0040	2.0026
ITIC DFT EPRII	2.0055	2.0037	2.0026
IDTBR Experimental	2.0062(3)	2.0055(4)	2.0022(2)
IDTBR DFT 6-31G	2.0067	2.0051	2.0023
IDTBR DFT EPRII	2.0074	2.0061	2.0024

Using DFT the proton hyperfine coupling constants were also calculated and ENDOR simulations using these calculated values run as shown in Figure 7.22. The simulation of the P3HT:ITIC ENDOR spectrum uses the ten largest hyperfine couplings from the DFT calculations of ITIC to simulate the P^- component (blue) and an isotropic $A = 2.3$ MHz coupling to simulate the P^+ component (green). It can be seen the simulation using the DFT coupling values is in reasonable agreement to the experimental spectrum in that it reproduces the superposition of a narrow and vary broad component for P^- , signifying that there is a broad range of coupling strengths. However the width of the broad component is underestimated by the simulation indicating that the DFT calculations are therefore underestimating the strength of hyperfine coupling. The inclusion of solvation effects may somewhat improve the accuracy of the simulation due to the additional coupling to ^1H on the solvent molecules. The situation is similar for P3HT:IDTBR where the

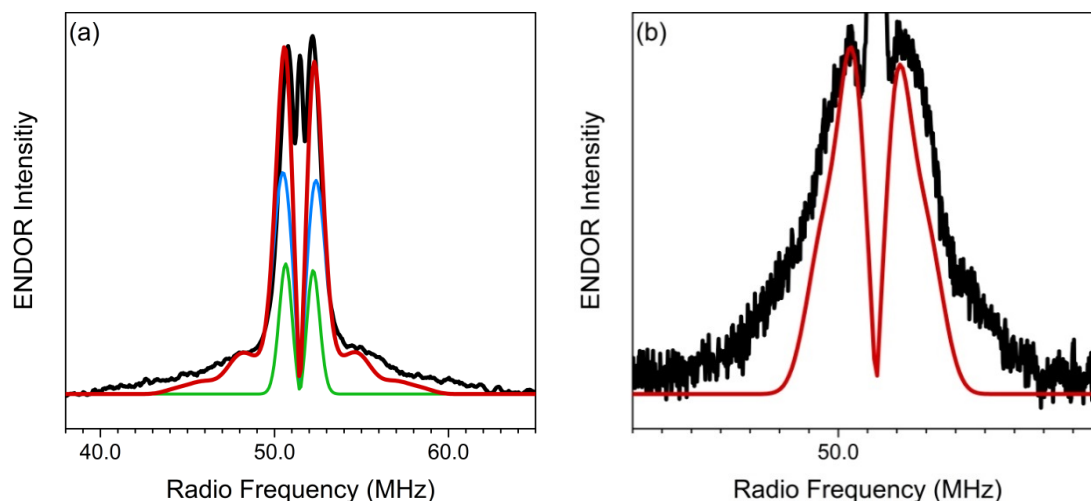


Figure 7.22 Comparison of experimental and simulated ^1H ENDOR spectra of (a) P3HT:ITIC and (b) P3HT:IDTBR. The simulation of the coupling to the P^+ is shown in green, the P^- in blue and the total simulation in red. The simulated spectra were corrected to include suppression effects.

simulation reproduces the general lineshape of the ENDOR spectrum but greatly underestimates its width. One takeaway from the comparison of the simulated and experimental ENDOR spectra is that since the simulated spectra are underestimating the width, the polaron cannot be delocalised over an aggregate. Delocalising the spin density over two or more molecules in the DFT calculation would reduce the hyperfine coupling constants even further and worsen the agreement with the experimental data. The discrepancy between the DFT and experimental results therefore cannot be due to aggregation effects as it was in Chapter 6.

7.6 Conclusion

The first experimental identification of the negative polaron on the non-fullerene acceptors ITIC and IDTBR was achieved using LEPR. The negative polaron of both acceptors overlaps with the positive polaron of P3HT which prevents direct identification. However, by simulating the spectra across three microwave frequencies the negative polaron lineshapes and principal values of the g -tensors could be accurately determined. In addition the coupling of the polaron to ^1H was investigated using ENDOR spectroscopy which reveals remarkably large ^1H coupling in ITIC. These results provide information on the electronic excited states of these important molecules and will direct and validate the spin density distributions and molecular conformations obtained from DFT calculations.

7.7 References

1. N. S. Sariciftci, D. Braun, C. Zhang, V. I. Srdanov, A. J. Heeger, G. Stucky and F. Wudl, Semiconducting Polymer-buckminsterfullerene Heterojunctions - Diodes, Photodiodes, and Photovoltaic Cells. *Appl. Phys. Lett.* **62** (6), 585-587 (1993).
2. N. S. Sariciftci, L. Smilowitz, A. J. Heeger and F. Wudl, Semiconducting Polymers (as Donors) and Buckminsterfullerene (as Acceptor) - Photoinduced Electron Transfer and Heterojunction Devices. *Synth. Met.* **59** (3), 333-352 (1993).
3. G. Yu, J. Gao, J. C. Hummelen, F. Wudl and A. J. Heeger, Polymer Photovoltaic Cells - Enhanced Efficiencies Via A Network Of Internal Donor-acceptor Heterojunctions. *Science* **270** (5243), 1789-1791 (1995).
4. J. C. Hummelen, B. W. Knight, F. Lepeq, F. Wudl, J. Yao and C. L. Wilkins, Preparation and Characterization of Fulleroid and Methanofullerene Derivatives. *J. Org. Chem.* **60** (3), 532-538 (1995).
5. W. Q. Chen and Q. C. Zhang, Recent progress in non-fullerene small molecule acceptors in organic solar cells (OSCs). *J. Mater. Chem. C* **5** (6), 1275-1302 (2017).
6. N. Liang, W. Jiang, J. Hou and Z. Wang, New developments in non-fullerene small molecule acceptors for polymer solar cells. *Materials Chemistry Frontiers* **1** (7), 1291-1303 (2017).
7. D. Bartsaghi, G. Ye, R. C. Chiechi and L. J. A. Koster, Compatibility of PTB7 and 70 PCBM as a Key Factor for the Stability of PTB7: 70 PCBM Solar Cells. *Adv. Energy Mater.* **6** (13), 9 (2016).
8. Y. Z. Lin, J. Y. Wang, Z. G. Zhang, H. T. Bai, Y. F. Li, D. B. Zhu and X. W. Zhan, An Electron Acceptor Challenging Fullerenes for Efficient Polymer Solar Cells. *Adv. Mater.* **27** (7), 1170-1174 (2015).
9. W. C. Zhao, D. P. Qian, S. Q. Zhang, S. S. Li, O. Inganäs, F. Gao and J. H. Hou, Fullerene-Free Polymer Solar Cells with over 11% Efficiency and Excellent Thermal Stability. *Adv. Mater.* **28** (23), 4734-4739 (2016).
10. S. Holliday, R. S. Ashraf, A. Wadsworth, D. Baran, S. A. Yousaf, C. B. Nielsen, C. H. Tan, S. D. Dimitrov, Z. R. Shang, N. Gasparini, M. Alamoudi, F. Laquai, C. J. Brabec, A. Salleo, J. R. Durrant and I. McCulloch, High-efficiency and air-stable P3HT-based polymer solar cells with a new non-fullerene acceptor. *Nat. Commun.* **7**, 11 (2016).
11. S. S. Chen, Y. H. Liu, L. Zhang, P. C. Y. Chow, Z. Wang, G. Y. Zhang, W. Ma and H. Yan, A Wide-Bandgap Donor Polymer for Highly Efficient Non-fullerene Organic Solar Cells with a Small Voltage Loss. *J. Am. Chem. Soc.* **139** (18), 6298-6301 (2017).

12. J. Niklas, K. L. Mardis, B. P. Banks, G. M. Grooms, A. Sperlich, V. Dyakonov, S. Beaupre, M. Leclerc, T. Xu, L. P. Yu and O. G. Poluektov, Highly-Efficient Charge Separation and Polaron Delocalization in Polymer-Fullerene Bulk-Heterojunctions: A Comparative Multi-frequency EPR and DFT Study. *Phys. Chem. Chem. Phys.* **15** (24), 9562-9574 (2013).
13. A. Aguirre, P. Gast, S. Orlinskii, I. Akimoto, E. J. J. Groenen, H. El Mkami, E. Goovaerts and S. Van Doorslaer, Multifrequency EPR Analysis of the Positive Polaron in I-2-doped Poly(3-hexylthiophene) and in Poly 2-methoxy-5-(3,7-dimethyloctyloxy)-1,4-phenylenevinylene. *Phys. Chem. Chem. Phys.* **10** (47), 7129-7138 (2008).
14. O. G. Poluektov, S. Filippone, N. Martin, A. Sperlich, C. Deibel and V. Dyakonov, Spin Signatures of Photogenerated Radical Anions in Polymer- 70 Fullerene Bulk Heterojunctions High Frequency Pulsed EPR Spectroscopy. *J. Phys. Chem. B* **114** (45), 14426-14429 (2010).
15. J. De Ceuster, E. Goovaerts, A. Bouwen, J. C. Hummelen and V. Dyakonov, High-Frequency (95 GHz) Electron Paramagnetic Resonance Study of the Photoinduced Charge Transfer in Conjugated Polymer-Fullerene Composites. *Physical Review B* **64** (19), 6 (2001).
16. K. L. Mardis, J. N. Webb, T. Holloway, J. Niklas and O. G. Poluektov, Electronic Structure of Fullerene Acceptors in Organic Bulk-Heterojunctions: A Combined EPR and DFT Study. *Journal of Physical Chemistry Letters* **6** (23), 4730-4735 (2015).
17. O. G. Poluektov, J. Niklas, K. L. Mardis, S. Beaupre, M. Leclerc, C. Villegas, S. Erten-Ela, J. L. Delgado, N. Martin, A. Sperlich and V. Dyakonov, Electronic Structure of Fullerene Heterodimer in Bulk-Heterojunction Blends. *Adv. Energy Mater.* **4** (7), 7 (2014).
18. V. Dyakonov, G. Zorinians, M. Scharber, C. J. Brabec, R. A. J. Janssen, J. C. Hummelen and N. S. Sariciftci, Photoinduced Charge Carriers in Conjugated Polymer-Fullerene Composites Studied With Light-induced Electron-Spin Resonance. *Physical Review B* **59** (12), 8019-8025 (1999).
19. K. Marumoto, N. Takeuchi, T. Ozaki and S. Kuroda, ESR Studies of Photogenerated Polarons in Regioregular poly(3-alkylthiophene) Fullerene composite. *Synth. Met.* **129** (3), 239-247 (2002).
20. S. Stoll and A. Schweiger, EasySpin, A Comprehensive Software Package for Spectral Simulation and Analysis in EPR. *J. Magn. Reson.* **178** (1), 42-55 (2006).

8 Charge Carrier Mobility of Non-Fullerene Acceptors

8.1 Introduction

An important property of any acceptor is its electron mobility. In order to study the materials of the previous chapter further, the electron mobility was measured using Time of Flight (ToF). The electron mobility of neat ITIC was found to increase from $6 \times 10^{-5} \text{ cm}^2 \text{ V}^{-1} \text{ s}^{-1}$ to $1 \times 10^{-4} \text{ cm}^2 \text{ V}^{-1} \text{ s}^{-1}$ over the measured field range of $1.1 \times 10^5 \text{ V cm}^{-1}$ to $2.2 \times 10^5 \text{ V cm}^{-1}$. When blended with the donor PTB7-Th the electron mobility is unchanged, with the neat and blend both having an electron mobility of $8(2) \times 10^{-5} \text{ cm}^2 \text{ V}^{-1} \text{ s}^{-1}$ at $1.5 \times 10^5 \text{ V cm}^{-1}$ which indicates that the microstructure of the blend does not limit the electron mobility. In addition the hole mobility of the blend was also measured and found to be approximately a factor of two to three higher than electron mobility at similar electric fields, which indicates that the mobility in PTB7-Th:ITIC is reasonably well balanced. This chapter lays the groundwork for a larger study into the mobility of non-fullerene acceptors.

8.2 Background

As discussed in Chapter 7, the field of OPV has been dominated by blends of conjugated polymer donors and fullerene based acceptors. This is now changing, with several novel non-fullerene acceptors recently reported that have achieved efficiencies approaching those of fullerene based cells.^[1, 2] In the previous chapters of this thesis the influence that processes such as charge separation, triplet exciton formation and charge recombination have on the operation and performance of OPV cells has been investigated. Another key parameter which determines the efficiency of OPV cells is the mobility of the charge carriers. After charge separation there is competition between charge extraction and recombination; the longer it takes for the charge carriers to be extracted, the more are lost to recombination processes. The extraction time is determined by the morphology of the cell and the mobility of charge carriers, and low charge carrier mobility will therefore result in loss of J_{sc} and fill factor. In addition the electron and hole mobility should be approximately balanced to prevent charge build up and loss of fill factor. One of the key properties that has made fullerenes so successful is their high electron mobility which few other acceptors are able to achieve.^[2] For non-fullerene cells to become the new standard

in OPV, mobilities comparable to those of fullerene need to be achieved. One of the most promising new acceptors is ITIC which achieved an efficiency of 6.8 % when blended with PTB7-Th.^[3] Accurately determining the charge carrier mobility in this material is important to understand the sources of the performance loss and to influence the development of new acceptors. The mobility of neat ITIC and the blend with PTB7-Th was therefore investigated using ToF.

8.3 Materials

8.3.1 ITIC

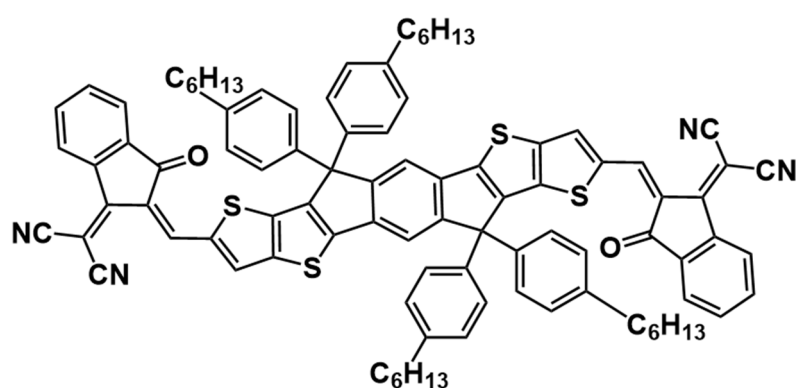


Figure 8.1 Chemical structure of ITIC.

As explained in Chapter 7, ITIC has achieved efficiencies of up to 6.8 % when blended with PTB7-Th and over 11 % with PBDB-T.^[3,4] The structure is shown in Figure 8.1 and consists of central donor core of indacenodithieno[3,2-b]thiophene with two flanking 2-(3-oxo-2,3-dihydroinden-1-ylidene)malononitrile acceptor units. ITIC was purchased from 1-Material (NFA005) and used without further purification.

8.3.2 PTB7-Th

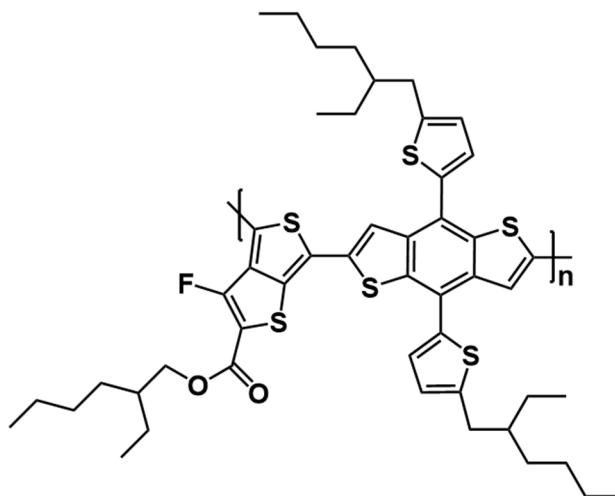


Figure 8.2 PTB7-Th chemical structure.

PTB7-Th (also known as PCE10 and PBDTTT-EFT) is an iteration of the PTB7 design with two additional conjugated thiophene side groups. These side groups extend the absorption further into the red and therefore enable greater photon harvesting compared with PTB7.^[5] As a result of this improved harvesting, PTB7-Th based cells have reached efficiencies of nearly 11%.^[6] PTB7-Th was purchased from 1-Material (OS0100) and used without further purification.

8.4 Experimental

8.4.1 Sample Preparation

An anode of PEDOT:PSS (Heraeus Clevious P VP AI 4083) was deposited onto cleaned ITO substrates by spin-coating at 4000 rpm. The substrates were then annealed on a hotplate at 120 °C for 20 minutes to remove residual water. The active layer for the TOF measurements was deposited using the drop casting method (see Section 4.5.2). It proved to be highly challenging to obtain good quality films of neat ITIC due to its tendency to aggregate and form islands during drop casting. Chlorobenzene, dichlorobenzene, trichlorobenzene and tetrachloroethane were tested as drop casting solvents. Using chlorobenzene and dichlorobenzene no continuous film was formed upon drop casting. Trichlorobenzene solutions were marginally more successful and formed a semi-continuous film; however the patchy nature prohibited cell fabrication as it would result in short circuit. Tetrachloroethane proved to be most successful solvent and formed a continuous film with acceptable roughness. For ToF measurements ITIC was dissolved

in tetrachloroethane at a concentration of 40 mg cm^{-3} and left stirring at $50 \text{ }^\circ\text{C}$ overnight inside a nitrogen glovebox. The solution was then passed through a $0.45 \text{ }\mu\text{m}$ filter to remove undissolved particles, pipetted onto the substrates and left to dry overnight inside the glovebox. A top contact of 10 nm calcium followed by 20 nm aluminium was deposited using thermal evaporation. Cells using the PTB7-Th:ITIC blend were prepared in analogous manner, where ITIC and PTB7-Th were dissolved in tetrachloroethane in a 1.0:1.3 ratio with a total concentration of 30 mg cm^{-3} .

8.4.2 ToF Measurement

The ToF mobility was measured using the detection circuit and dye laser described in Section 4.5.3. The cell was excited with a short 715 nm laser pulse through the Ca/Al electrode for hole mobility and through the PEDOT:PSS/ITO for electron mobility. The laser pulse energies used were such that the extracted charge was around $\sim 10 \%$ of the total capacitor charge of the cell in most measurements.

8.5 Results

8.5.1 Electron Mobility of Neat ITIC

The electron mobility of neat ITIC was measured using the ToF method. The drop cast ITIC films had thickness between 1.4 and $1.6 \text{ }\mu\text{m}$. The peak absorption wavelength of ITIC is around 700 nm .^[3] In order to minimise the absorption depth of the excitation pulse into the sample it is important to excite the sample where it absorbs strongest. A pyridine 1 dye laser was therefore constructed (see Section 4.5.3) and used as the pump source which has a lasing wavelength of 715 nm . The cell was placed under reverse bias and excited through the PEDOT:PSS electrode and electrons collected at Ca/Al electrode. The electron photocurrent transients of neat ITIC cells after photoexcitation are shown in Figure 8.3 at two different electric fields. The transients are shown in a linear scale in panels (a) and (c) and are featureless with no sign of a plateau, which indicates that the electron transport is highly dispersive. Dispersive transients are a common occurrence in organic semiconductors and the transients are therefore plotted on a double log scale, as shown in panels (c) and (d), which enhances the clarity of the transition from the plateau to tail region. However it can be seen that even in the double log scale the change in gradient between the plateau and tail regions is minimal which makes determination of

transit time difficult. Linear fits were applied to these two linear regions and the intersection of the fits used to determine the transit time. As the electric field is increased the transit time decreases as would be expected and indicates that the chosen transit time is physically real and not an experimental artefact. The transit time could only be determined over a narrow field range of $1.1 \times 10^5 \text{ V cm}^{-1}$ to $2.2 \times 10^5 \text{ V cm}^{-1}$. At fields below $1.1 \times 10^5 \text{ V cm}^{-1}$ the signal to noise is too poor to determine the transit time. As the cell is composed solely of ITIC there is no electron transfer to break apart the exciton. Instead the exciton is broken apart by the applied electric field and the magnitude of the photocurrent transient is therefore strongly field dependent and weak at low fields. The upper limit of the electric field is due to the transient becoming increasingly dispersive as the electric field is increased. This can be seen by comparing the linear fits in panel (c) with those in (d). At the higher electric field in panel (d) the difference in gradient between the two linear regions is less pronounced than in (c). This trend continues as the electric

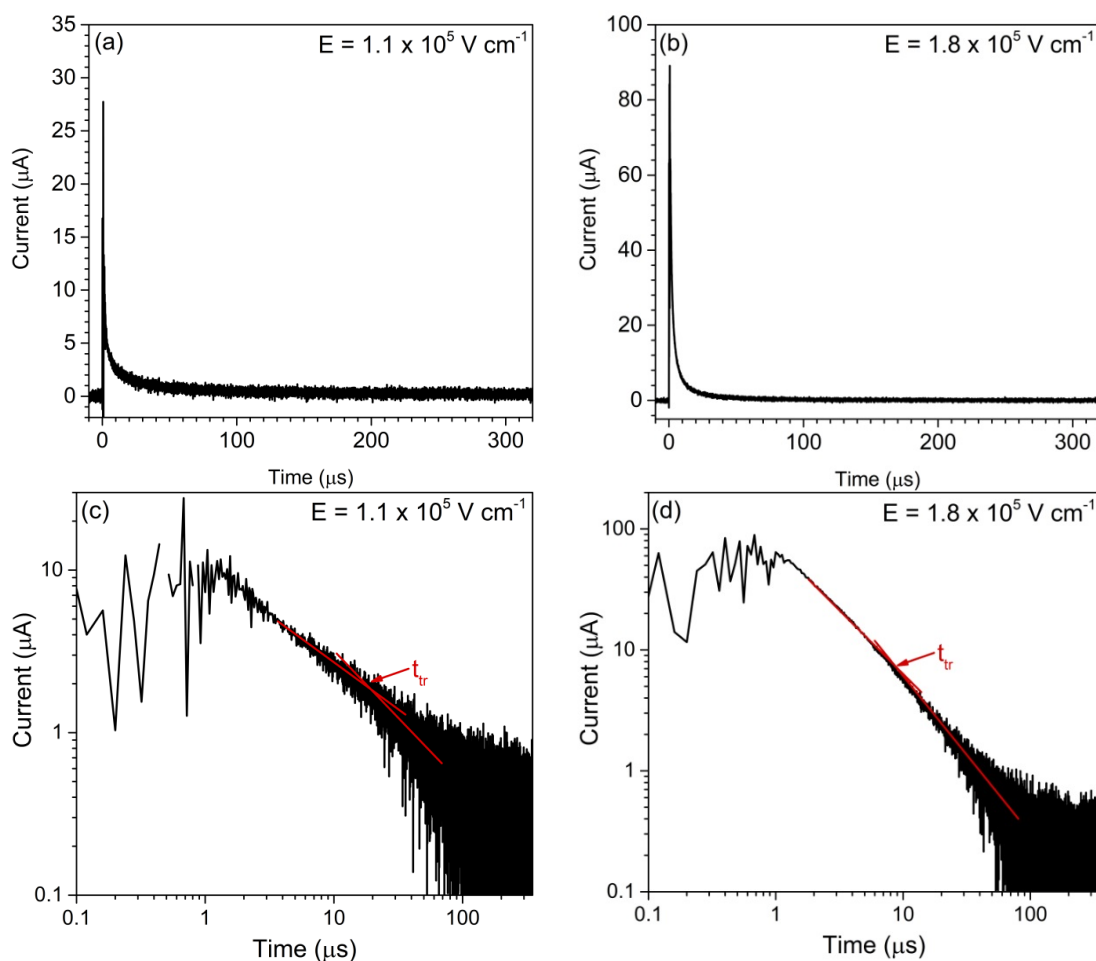


Figure 8.3 Electron photocurrent transient of ITIC. The transient at $E = 1.1 \times 10^5 \text{ V cm}^{-1}$ is shown in (a) linear and (c) double scales. The transient at $E = 1.8 \times 10^5 \text{ V cm}^{-1}$ is shown in (b) linear and (d) double scale.

field is increased until the two gradients are equal and the kink vanishes, which defines the maximum electric field of the measurement. Increasing dispersion with electric field has been shown to occur in heterogeneous systems using Monte Carlo simulations and is due to spatial disorder in the system.^[7] A similar mechanism may be responsible here. If there is large distribution of hopping distances (high spatial disorder) then there will be ‘dead ends’ in the transport pathway and the carriers may need to hop against the field to progress. The time the carriers spend stuck at these dead ends gets longer as the field strength is increased and the dispersion of the charge carrier packet therefore increases as the electric field is increased, causing the kink to disappear.

The variation of the transit time across the utilisable electric field range was measured on two cells, and the mobility calculated using Eq 4.18. The electric field dependence of the mobility is shown in a Poole-Frenkel plot,^[8] in Figure 8.4. It can be seen that the mobility increases with applied field which is the expected behaviour for field assisted hopping transport according to the Gaussian disorder model of charge transport as long as spatial and energetic disorder are not too large (See Section 2.2.5).^[9] Over the field range measured the mobility varies from about $6 \times 10^{-5} \text{ cm}^2 \text{ V}^{-1} \text{ s}^{-1}$ to $1 \times 10^{-4} \text{ cm}^2 \text{ V}^{-1} \text{ s}^{-1}$. For comparison the electron mobility of PC₇₁BM measured at an electric field of

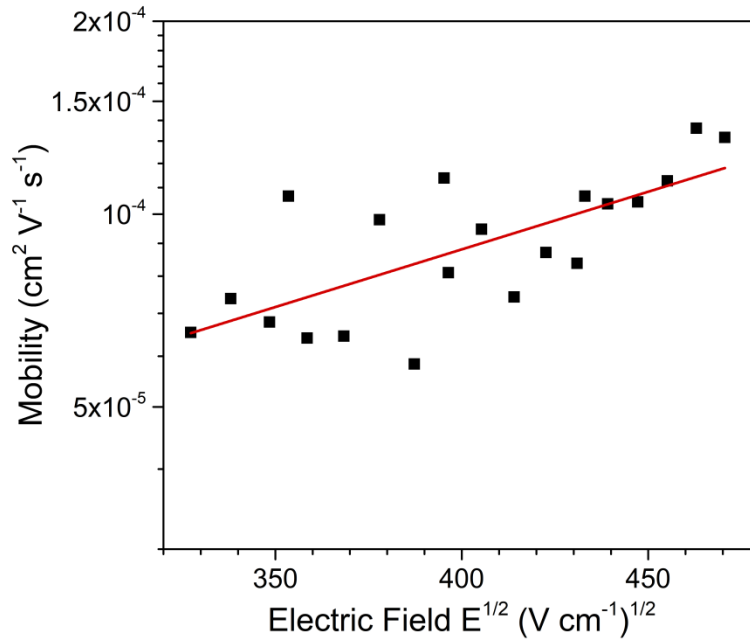


Figure 8.4 Poole Frenkel plot of electron mobility in neat ITIC films.

$0.9 \times 10^5 \text{ V cm}^{-1}$ using the ToF method is $1.0(2) \times 10^{-3} \text{ cm}^2 \text{ V}^{-1} \text{ s}^{-1}$,^[10] while the electron mobility in ITIC at a similar field of $1.2 \times 10^5 \text{ V cm}^{-1}$ is over an order of magnitude lower at $7(2) \times 10^{-5} \text{ cm}^2 \text{ V}^{-1} \text{ s}^{-1}$. This shows that while electron mobilities in non-fullerene acceptors are improving they have not yet reached the level achievable using fullerenes. The mobility of ITIC has been previously measured by using the Space Charge Limited Current (SCLC) method. SCLC is a good method to measure the mobility during rapid material screening. However the success of a SCLC measurement depends crucially on the formation of an ohmic injection electrode which can be difficult to achieve in many materials.^[11] In addition it is difficult to determine the field dependence of the mobility using SCLC and the SCLC mobility is therefore frequently quoted as a single field independent number. The reported SCLC electron mobility of ITIC is $2.6 \times 10^{-4} \text{ cm}^2 \text{ V}^{-1} \text{ s}^{-1}$,^[3] which is around a factor of two higher than the highest mobilities observed here. Directly comparing SCLC and ToF mobility values is difficult as the single mobility value obtained using SCLC is an oversimplification, though it appears to be reasonable agreement to the electron mobility measured here.

8.5.2 Electron and Hole Mobility of PTB7-Th:ITIC

The mobility can vary strongly on the morphology of the film and is therefore expected to differ when the acceptor is blended with a donor to form a bulk heterojunction. Since ITIC is blended with the donor PTB7-Th in high performance cells,^[3] the electron and hole mobilities of PTB7-Th:ITIC films were therefore measured. Drop casting was used to deposit PTB7-Th:ITIC films $4 \mu\text{m}$ to $10 \mu\text{m}$ in thickness. Electron photocurrent transients of PTB7-Th:ITIC are shown in Figure 8.5. Similarly to the neat ITIC, the transients on a linear scale are featureless and a kink is only visible on the double log scale. At low electric fields the kink is far more pronounced than in neat ITIC. This is likely due to greater confinement of the initial photogenerated charge carrier sheet in the blend. Neat ITIC films were a little over $1 \mu\text{m}$ thick while the blend varies from $4\text{-}10 \mu\text{m}$. This increased thickness coupled with the higher absorption coefficient of PTB7-Th reduces the absorption depth of the laser pulse, resulting in greater spatial confinement of the photogenerated carriers and lower dispersion in the transient. As the electric field is increased the kink becomes less pronounced and eventually vanishes; the same behaviour that was observed for neat ITIC.

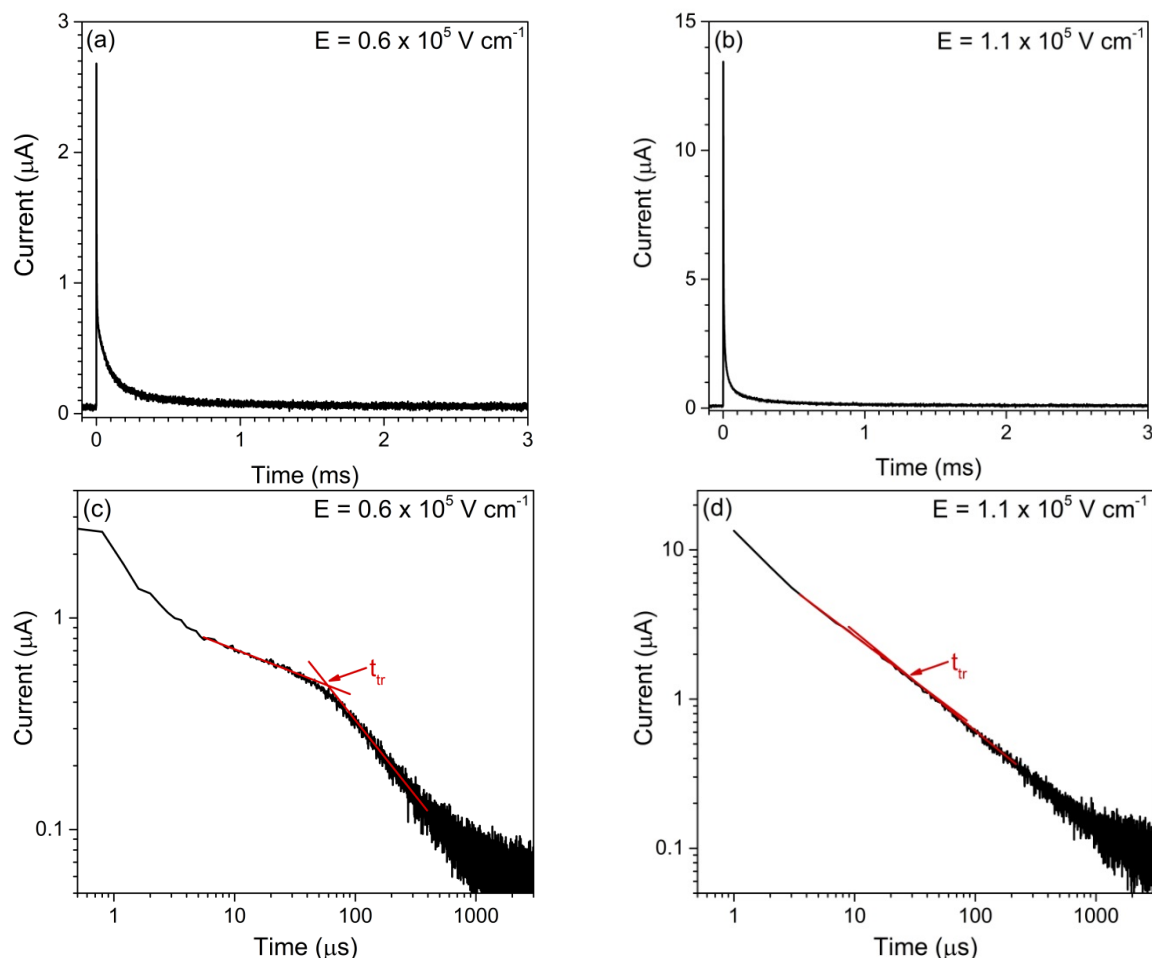


Figure 8.5 Electron photocurrent transient of PTB7-Th:ITIC. The transient at $E = 0.6 \times 10^5 \text{ V cm}^{-1}$ is shown in (a) linear and (c) double log scale. The transient at $E = 1.1 \times 10^5 \text{ V cm}^{-1}$ is shown in (b) linear and (d) double log scale.

In some of the measured cells the photocurrent transients exhibited two kinks which are shown in Figure 8.6. Double transients have been observed previously in ToF studies of P3HT:PC₆₁BM and PTB7:PC₇₁BM and were attributed to a high degree of phase separation in the blend.^[10, 12] The transit time from the first kink, t_{fast} , decreases as the electric field is increased and has similar value to the transit times in Figure 8.5. In contrast the transit time from the second kink, t_{slow} , gets longer as the electric field is increased, reaching times of 4 ms at the highest electric field. While this second kink could in principle be due to deep trapping or dead ends in the transport network; the exceptionally long transit time and increasing extraction time with field suggests that that the second kink may be an experimental artefact or due recombination of trapped charges, and these delayed transit times were therefore disregarded.

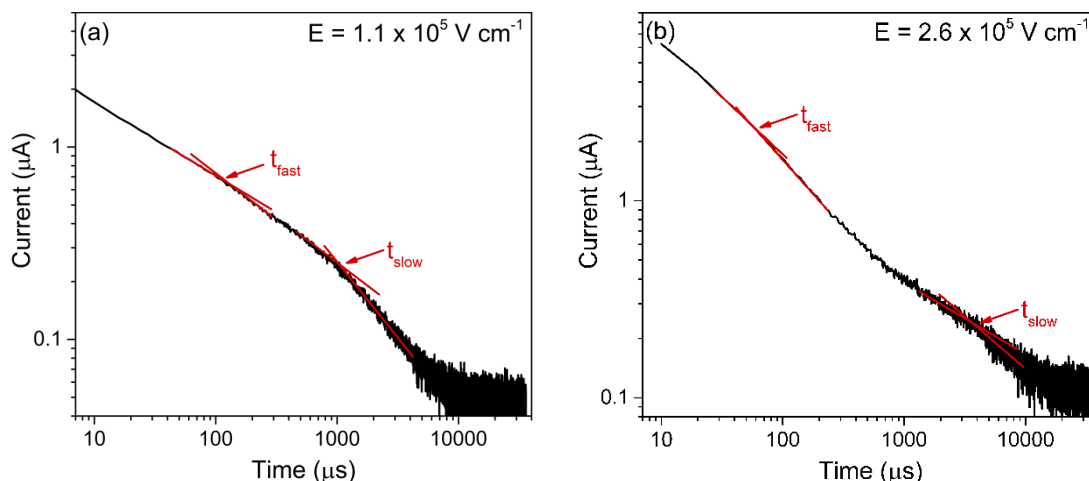


Figure 8.6 Electron photocurrent transient of ITIC:PTB7-Th exhibiting double kinks. The transient is shown at (a) $E = 1.1 \times 10^5 \text{ V cm}^{-1}$ and (b) $E = 2.6 \times 10^5 \text{ V cm}^{-1}$.

The electron mobility was calculated using Eq. 4.18 and its variation with electric field shown in Figure 8.7. It can be seen that, in contrast to neat ITIC, the electron mobility in the blend exhibits a negative field dependence. This behaviour has been observed previously in ToF studies of similar blends,^[7, 10, 13] and arises from high spatial disorder in the bulk heterojunction.^[9, 14] The electron mobility varies from $1.4\text{--}0.5 \times 10^{-4} \text{ cm}^2 \text{ V}^{-1} \text{ s}^{-1}$ over the measured field range which is in agreement to value obtained from SCLC of $1.1 \times 10^{-4} \text{ cm}^2 \text{ V}^{-1} \text{ s}^{-1}$. At an electric field of $1.5 \times 10^5 \text{ V cm}^{-1}$ the electron mobility in the blend is $8(2) \times 10^5 \text{ cm}^2 \text{ V}^{-1} \text{ s}^{-1}$ compared with $8(2) \times 10^5 \text{ cm}^2 \text{ V}^{-1} \text{ s}^{-1}$ in the neat ITIC

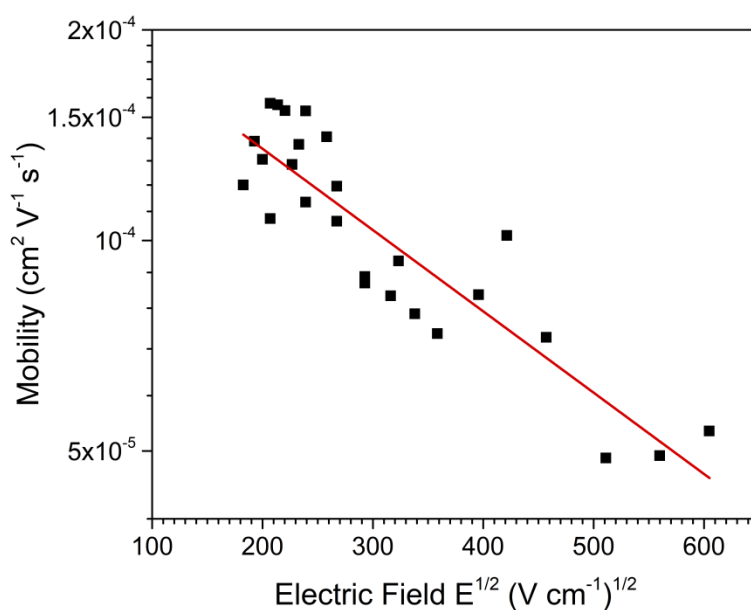


Figure 8.7 Poole Frenkel plot of electron mobility in PTB7-Th:ITIC.

film, demonstrating that blending the acceptor with PTB7-Th does not significantly alter the electron mobility.

For comparison the hole mobility of the ITIC:PTB7-Th cells was also measured. The hole photocurrent transients are shown in Figure 8.8 and exhibit similar behaviour to the electron transient, with the dispersion increasing with electric field. This increasing dispersion severely limited the measurable field range.

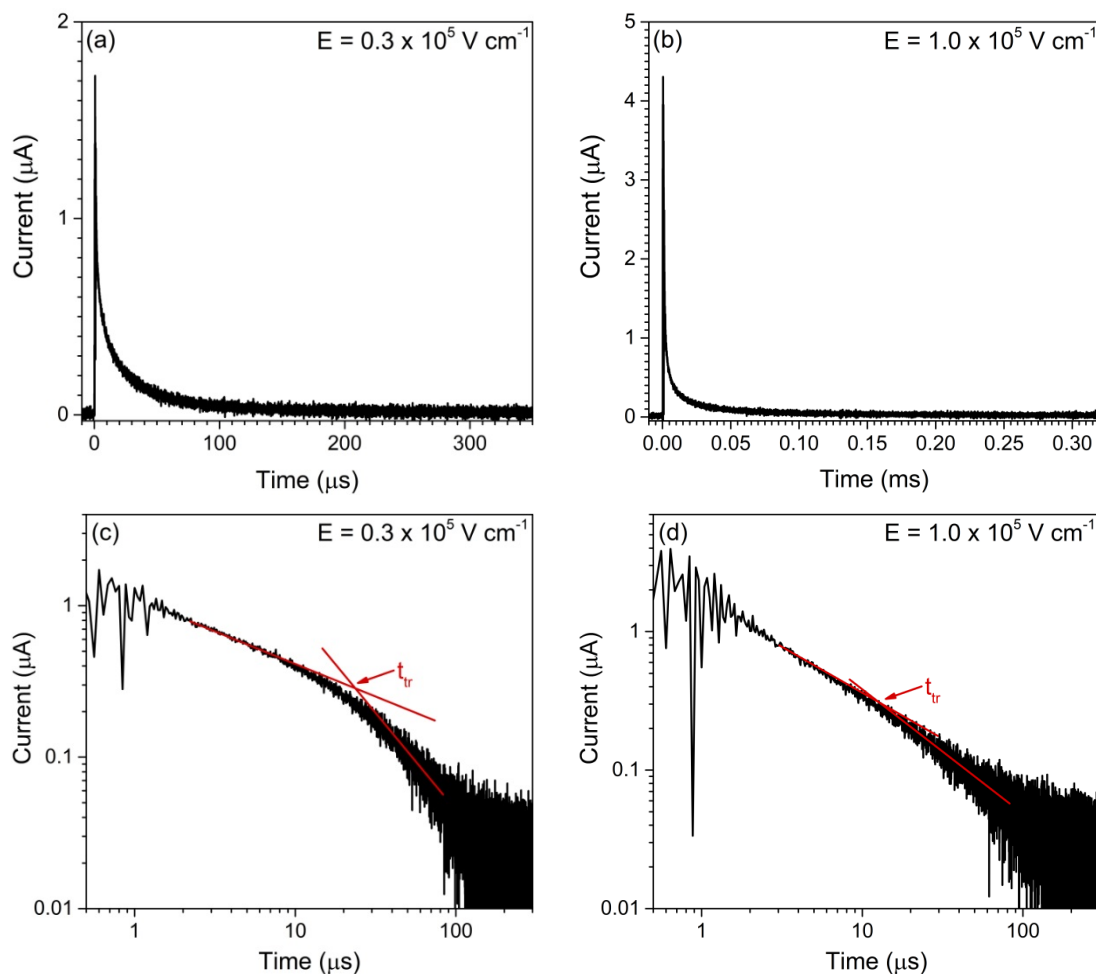


Figure 8.8 Hole photocurrent transient of ITIC:PTB7-Th. The transient at $E = 0.3 \times 10^5 \text{ V cm}^{-1}$ is shown in (a) linear and (c) double scales. The transient at $E = 1.0 \times 10^5 \text{ V cm}^{-1}$ is shown in (b) linear and (d) double scale.

A Poole-Frenkel plot of the hole mobility is shown in Figure 8.9. At a field of $E = 0.9 \times 10^5 \text{ V cm}^{-1}$ the hole mobility is $2.2(6) \times 10^{-4} \text{ cm}^2 \text{ V}^{-1} \text{ s}^{-1}$ compared with $1.0(2) \times 10^{-4} \text{ cm}^2 \text{ V}^{-1} \text{ s}^{-1}$ for the electron, indicating that the electron and hole mobilities are reasonably well balanced in this blend. The measured hole mobility is similar to that previously reported for PTB7:PC₇₁BM blends,^[10] but is significantly higher than the value of $4.3 \times 10^{-5} \text{ cm}^2 \text{ V}^{-1} \text{ s}^{-1}$ measured using SCLC.^[3] This discrepancy may be due to the fact

that charge carriers in ToF are photogenerated high in their density of states and then relax during the measurement which leads to a higher effective mobility or due to morphological differences in the films.^[7, 15] The gradient of the negative field dependence of the hole mobility in Figure 8.9 is approximately a factor of three greater than exhibited by the electron mobility in Figure 8.7. While this increased negative field dependence could in principle arise from a larger spatial disorder in the hole transport network, this should be interpreted with caution as the field range that the hole mobility was measured over is rather limited. It has been shown that ToF may overestimate the mobility when the electric field is low which gives rise to an artificially strong negative field dependence that levels out at higher electric fields.^[16] This effect may also be partly responsible for higher mobility measured by ToF compared to SCLC.

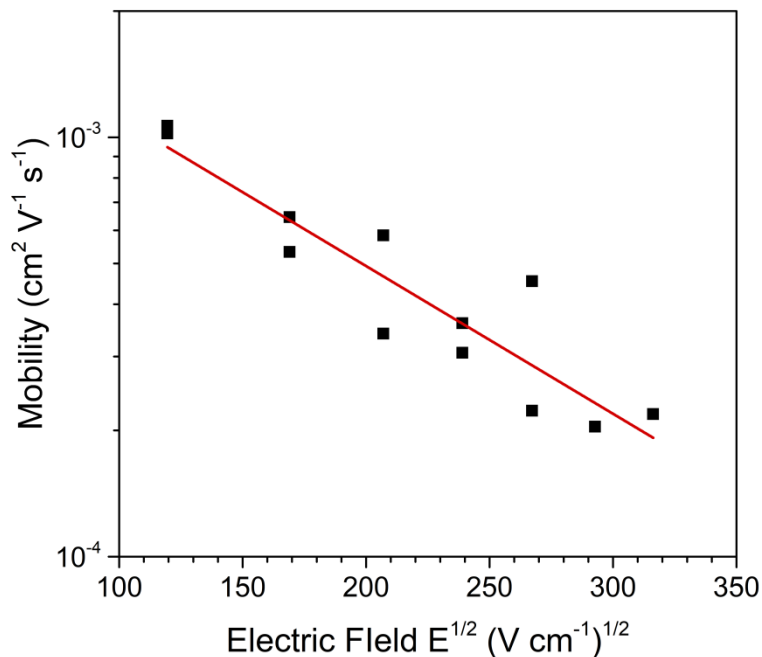


Figure 8.9 Poole Frenkel plot of hole mobility in ITIC:PTB7-Th.

Finally, a comparison of the field dependence of the three measured mobilities is shown in Figure 8.10 which highlights the similarity between the electron mobility in neat ITIC and the blend and the higher mobility exhibited by the holes. Work is currently underway to expand the number datasets in this plot, with measurements being undertaken on blends with different polymers, weight ratios and other new acceptors such as IDTBR.

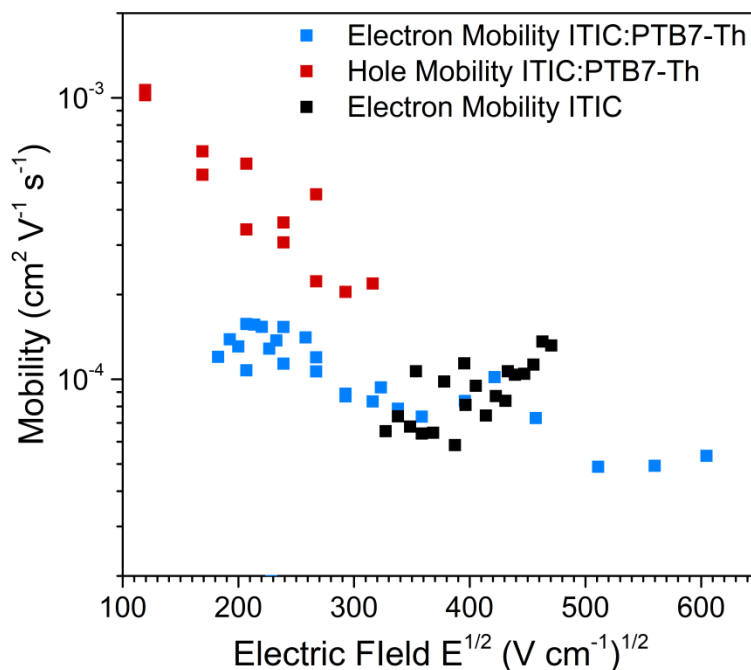


Figure 8.10 Comparison of electron and hole mobility of the blend and neat ITIC.

8.6 Conclusion

The electron and hole mobilities of ITIC and ITIC:PTB7-Th blends were measured using the ToF technique. The electron mobility of ITIC exhibits a positive field dependence and varies from $6 \times 10^{-5} \text{ cm}^2 \text{ V}^{-1} \text{ s}^{-1}$ to $1 \times 10^{-4} \text{ cm}^2 \text{ V}^{-1} \text{ s}^{-1}$ over the measured field range of $1.1 \times 10^5 \text{ V cm}^{-1}$ to $2.2 \times 10^5 \text{ V cm}^{-1}$. When ITIC is blended with PTB7-Th the field dependence of the electron mobility becomes negative due to increased spatial disorder in the bulk heterojunction. However the magnitude is approximately unchanged with both neat ITIC and the blend having a mobility of $8(2) \times 10^{-5} \text{ cm}^2 \text{ V}^{-1} \text{ s}^{-1}$ at $1.5 \times 10^5 \text{ V cm}^{-1}$ which shows that the electron transport is not hindered by the inclusion of the polymer. For comparison the hole mobility in the blend was also measured and found to be approximately a factor of two higher than electron mobility, which shows that the mobility in this blend is reasonably well balanced.

8.7 References

1. W. Q. Chen and Q. C. Zhang, Recent progress in non-fullerene small molecule acceptors in organic solar cells (OSCs). *J. Mater. Chem. C* **5** (6), 1275-1302 (2017).
2. N. Liang, W. Jiang, J. Hou and Z. Wang, New developments in non-fullerene small molecule acceptors for polymer solar cells. *Materials Chemistry Frontiers* **1** (7), 1291-1303 (2017).
3. Y. Z. Lin, J. Y. Wang, Z. G. Zhang, H. T. Bai, Y. F. Li, D. B. Zhu and X. W. Zhan, An Electron Acceptor Challenging Fullerenes for Efficient Polymer Solar Cells. *Adv. Mater.* **27** (7), 1170-1174 (2015).
4. W. C. Zhao, D. P. Qian, S. Q. Zhang, S. S. Li, O. Inganäs, F. Gao and J. H. Hou, Fullerene-Free Polymer Solar Cells with over 11% Efficiency and Excellent Thermal Stability. *Adv. Mater.* **28** (23), 4734-4739 (2016).
5. S. H. Liao, H. J. Jhuo, Y. S. Cheng and S. A. Chen, Fullerene Derivative-Doped Zinc Oxide Nanofilm as the Cathode of Inverted Polymer Solar Cells with Low-Bandgap Polymer (PTB7-Th) for High Performance. *Adv. Mater.* **25** (34), 4766-4771 (2013).
6. Q. Wan, X. Guo, Z. Y. Wang, W. B. Li, B. Guo, W. Ma, M. J. Zhang and Y. F. Li, 10.8% Efficiency Polymer Solar Cells Based on PTB7-Th and PC71BM via Binary Solvent Additives Treatment. *Adv. Funct. Mater.* **26** (36), 6635-6640 (2016).
7. J. M. Frost, F. Cheynis, S. M. Tuladhar and J. Nelson, Influence of polymer-blend morphology on charge transport and photocurrent generation in donor-acceptor polymer blends. *Nano Lett.* **6** (8), 1674-1681 (2006).
8. J. G. Simmons, Poole-Frenkel Effect and Schottky Effect in Metal-Insulator-Metal Systems. *Phys. Rev.* **155** (3), 657-& (1967).
9. H. Bassler, Charge Transport In Disordered Organic Photoconductors - A Monte-carlo Simulation Study. *Physica Status Solidi B-Basic Research* **175** (1), 15-56 (1993).
10. B. Ebenhoch, S. A. J. Thomson, K. Genevicius, G. Juska and I. D. W. Samuel, Charge carrier mobility of the organic photovoltaic materials PTB7 and PC71BM and its influence on device performance. *Org. Electron.* **22**, 62-68 (2015).
11. A. Kokil, K. Yang and J. Kumar, Techniques for characterization of charge carrier mobility in organic semiconductors. *J. Polym. Sci. Pt. B-Polym. Phys.* **50** (15), 1130-1144 (2012).
12. A. Baumann, J. Lorrmann, C. Deibel and V. Dyakonov, Bipolar charge transport in poly(3-hexyl thiophene)/methanofullerene blends: A ratio dependent study. *Appl. Phys. Lett.* **93** (25), 3 (2008).

13. A. M. Ballantyne, L. Chen, J. Dane, T. Hammant, F. M. Braun, M. Heeney, W. Duffy, I. McCulloch, D. D. C. Bradley and J. Nelson, The effect of poly(3-hexylthiophene) molecular weight on charge transport and the performance of polymer : fullerene solar cells. *Adv. Funct. Mater.* **18** (16), 2373-2380 (2008).
14. A. J. Mozer and N. S. Sariciftci, Negative Electric Field Dependence of Charge Carrier Drift Mobility in Conjugated, Semiconducting Polymers. *Chem. Phys. Lett.* **389** (4-6), 438-442 (2004).
15. J. C. Blakesley, F. A. Castro, W. Kylberg, G. F. A. Dibb, C. Arantes, R. Valaski, M. Cremona and J. S. Kim, Towards reliable charge-mobility benchmark measurements for organic semiconductors. *Org. Electron.* **15** (6), 1263-1272 (2014).
16. G. Juska, K. Genevicius, K. Arlauskas, R. Osterbacka and H. Stubb, Charge Transport at Low Electric Fields in Pi-conjugated Polymers. *Physical Review B* **65** (23), 4 (2002).

9 Conclusions

This thesis explored how EPR and EDMR spectroscopy can help further the understanding of OPV. OPV is a fascinating technology in terms of both the underlying physics and its potential role as a low carbon energy source. While cell efficiencies have improved threefold over the past 15 years they are still lower than other competing thin film PV technologies.^[1] Innovative materials design, improved device engineering and a greater understanding of the loss pathways will be required to further improve efficiencies and open the door to commercialisation. Short cell lifetimes also remain an issue that must be overcome. Intrinsic degradation processes such as phase instability and extrinsic mechanisms due to water, oxygen and light exposure therefore need to be understood and eliminated in order to improve cell stability and extend operational lifetimes. As EPR spectroscopy is exclusively sensitive to species with spin it is a particularly well suited to study the operation of OPV cells, in which the desired process is the dissociation of an initial singlet exciton into free electrons and holes. In addition, loss mechanisms such as charge carrier recombination and triplet exciton formation involve states with net spin which makes EPR a powerful method for their study. The goal of this thesis was to use EPR and EDMR spectroscopy to investigate charge separation and competing loss pathways in OPV cells and to gain a greater understanding of some of the potential degradation mechanisms so that they can be mitigated in future cell designs.

Many of the highest performing OPV blends are also those most susceptible to degradation. An example of such a blend is PTB7:PC₇₁BM which boasts impressive efficiencies of over 9 %, ^[2] but suffers from severely reduced performance when processed under ambient atmosphere.^[3-5] Good ambient processability is important for OPV materials as one of their main advantages over other thin film PV technologies is their ability to be solution processed using large area and high throughput roll-to-roll techniques.^[6] Since it is likely that such large area processing will be carried out under ambient atmosphere rather than the controlled inert environment of a glovebox used in research cells, it is important that OPV blends retain their high efficiency when processed under ambient atmosphere.^[3] A study of the ambient processing performance loss in PTB7:PC₇₁BM was undertaken and presented in **Chapter 5**. It was shown that the efficiency drop when cells are processed under ambient atmosphere is substantially worse

when the cells contain the solvent additive 1,8-diiodooctane (DIO) with a relative PCE drop of 73 % for DIO containing cells compared with 31 % for non-DIO cells, in agreement with previous observations.^[5] Using variable light intensity J-V analysis the origin of the performance loss was determined to arise from a substantial increase in trap assisted recombination. To gain insight into the underlying cause of the recombination, the cells were analysed using EDMR spectroscopy. The EDMR response was found to be a factor of 50 greater in those cells which had been exposed to both ambient atmosphere and DIO. This shows that a strong spin-dependent transition forms when DIO containing cells are exposed to ambient atmosphere and likely corresponds to the trap assisted recombination process identified by the variable light intensity J-V analysis. Using pulsed EDMR and selective carrier injection the spin dependent mechanism was confirmed to consist of a weakly coupled electron and hole undergoing spin-dependent recombination. By comparing the EDMR spectra of the neat components PC₇₁BM and PTB7 to the blend, the recombination mechanism was assigned to mobile holes on the PTB7 recombining with electrons localised to oxidised PC₇₁BM traps. This study shows that exposure of DIO containing PTB7:PC₇₁BM films to ambient atmosphere leads to oxidation of the PC₇₁BM which acts as a recombination centre in the cell, resulting in increased trap assisted recombination and loss of efficiency. The solvent additive DIO is a key agent in this trap formation process. The OPV field should therefore move away from DIO towards more inert solvent additives in order to improve the ambient processability of OPV cells. In the broader picture it is hoped that this study also demonstrates that EDMR can be a powerful technique for studying recombination and degradation mechanisms in OPV cells.

There are several directions to expand upon the study presented in Chapter 5. One possibility is the investigation of other materials systems such as those containing non-fullerene acceptors to determine if the oxidation reported here is unique to fullerenes. It would also be interesting to explore whether the degradation arising from dark exposure to oxygen, photo oxidation and DIO induced oxidation results in the same degraded species and investigate the ability of EDMR to distinguish between them. Given its high sensitivity it would be beneficial to investigate the applicability of EDMR spectroscopy to study other loss processes in OPV cells, such as the rapid ‘burn-in’ performance loss

when PTB7:PC₇₁BM cells are exposed to UV light which appears to be due to an intrinsic instability of the material system that is not yet fully understood.^[7]

The main avenue for further improving OPV efficiency is continued materials development. Replacement of the conjugated polymer electron donor with a small molecule is a possible approach as small molecules have reduced batch to batch variation which enables the fabrication of OPV cells with more reproducible performance,^[8] and their well-defined molecular structures allow greater energy level control.^[9, 10] Furthermore small molecules often have a simpler synthetic work-up than polymers and are easier to purify which could lower cell costs.^[8, 11] The operation of small molecule cells has received much less attention than their polymeric counterparts, particularly from an EPR perspective. In **Chapter 6** an EPR study of the DTS family of small molecule donors was presented. Blends of the five donors with PC₆₁BM were studied using LEPR spectroscopy and the spectral signatures and g-tensors of the positive polarons on the donor molecules determined for the first time. The study was supported by DFT calculations and comparison of the experimental and DFT g-tensors indicated that the positive polaron is delocalised over 2-3 molecular units of the donor. To confirm this, ENDOR spectroscopy was used to measure the hyperfine coupling constants of positive polarons. The measured coupling constants were consistent with those obtained from DFT calculations for a polaron delocalisation over 2-3 donor molecules. This study therefore demonstrates that the positive polarons in the DTS family of donors are intermolecularly delocalised which will aid charge separation in these systems and may be a contributing factor in their high efficiency. A valuable future study would be to expand upon this work by systematically investigating how the extent of the intermolecular delocalisation influences charge separation in these systems.

The second half of **Chapter 6** presents a time-resolved EPR study of the charge separation dynamics and triplet exciton formation pathways across the DTS family. The polarisation patterns of the polaron pair spectra showed that charge separation in the blend with the DTS(PTTh₂)₂ donor is slower than in the four fluorobenzothiadiazole donor blends and involves a longer lived primary or intermediate polaron pair. Triplet exciton formation was detected in all blends studied. Simulations of the triplet exciton spectra show that there is a higher population of triplet excitons generated through back electron

transfer from the triplet polaron pair in the DTS(PTTh₂)₂ blend. The higher population of back electron transfer excitons supports the assignment of slower charge separation in the DTS(PTTh₂)₂ blend since slower charge separation results in a longer S-T₀ mixing time and an increased likelihood for back electron transfer to occur. This result shows that back electron transfer to the triplet of the donor is a loss mechanism in these molecular systems when charge separation is slow.

A future direction of this work is to investigate the role that film morphology plays. In the presented study the charge separation and triplet exciton formation were measured in frozen solutions and thick solution cast films. The charge separation and exciton formation behaviour was found to be broadly similar in both cases despite the difference in morphology. A future study should move towards samples that are closer in morphology to those used in high efficiency thin film cells and investigate whether there is any change in behaviour when thin film morphologies are used. The move towards thin films will prove a challenge due to signal to noise limitations of TR-EPR spectroscopy. Combining the TR-EPR spectroscopy with other more sensitive techniques such as the recently reported transient EDMR spectroscopy setup would likely prove crucial.^[12]

A major shift in the OPV field during the time frame of this thesis has been the recent rapid development of high efficiency non-fullerene acceptors. The majority of the efficiency enhancement enjoyed by OPV cells over the past 15 years has been due to the design of new electron donors with improved absorption, optimised energy levels and higher charge mobilities. In contrast there was very little development of new acceptors as none were able to match the efficiency of the well-established methanofullerene derivatives. While efficient, fullerene derivatives suffer from high production costs and poor absorption characteristics,^[13, 14] and are also particularly sensitive to degradation as shown by the results of Chapter 5. Recent progress in non-fullerene acceptors has been highly promising as they are now achieving efficiencies comparable to fullerene derivatives.^[13, 14] Due to their simpler synthesis, improved stability and their greater scope for further improvement, non-fullerene acceptors will likely become the new standard in OPV cells. Very little was known about non-fullerene acceptors from an EPR perspective and two high performance non-fullerene acceptors ITIC and IDTBR were therefore investigated in **Chapter 7**.

In this study light induced EPR was used to characterise the negative polarons on ITIC and IDTBR. The negative polaron on both acceptors was found to severely overlap with the positive polaron on P3HT which made identification difficult. To determine the signatures of the negative polarons, the spectra were measured and simulated across three microwave frequencies which enabled the g-tensors to be accurately determined. Knowledge of the g-tensor is important as it characterises the structure and symmetry of the photoinduced excited state of these molecules. It is hoped that results can direct and validate the geometries and spin density distributions predicted from DFT calculations which are currently ongoing. It would be beneficial to repeat the measurements presented here using blends with a different donor polymer. As the g-tensors of the negative polarons are now known, the donor polymer can be chosen such that the positive and negative polarons have minimum overlap which would enable the negative polaron to be more directly observed and increase the accuracy of the reported g-tensor.

Due to the importance of non-fullerene acceptors their charge carrier mobility was also studied and was presented in **Chapter 8**. The electron and hole mobility of ITIC and ITIC:PTB7-Th were measured using the time of flight technique. The electron mobility of ITIC and ITIC:PTB7-Th was found to be similar with a value of $8(2) \times 10^{-5} \text{ cm}^2 \text{ V}^{-1} \text{ s}^{-1}$ at $1.5 \times 10^5 \text{ V cm}^{-1}$ which shows that the electron transport is not hindered by the microstructure of the blend. For comparison the hole mobility of the blend was also measured and found to be only a factor of 2-3 higher than the electron mobility, which indicates that the mobility is reasonably well balanced in this blend and is therefore likely not a limiting factor in cell performance. This chapter lays the groundwork for a larger study on the charge carrier mobility of non-fullerene acceptors and the influence that it has on cell performance, which is currently being undertaken.

Overall the thesis has shown that EPR and EDMR spectroscopy can help further the understanding of the operation of OPV cells and complement the more common optoelectronic characterisation techniques.

1. <http://nrel.gov/pv/assets/images/efficiency-chart.png>, Accessed 04/06/17.
2. Y. C. Cheng Gu , Zhongbo Zhang , Shanfeng Xue , Shuheng Sun , Chengmei Zhong , Huanhuan Zhang , Ying Lv , Fenghong Li , Fei Huang , and Yuguang Ma, Achieving High Efficiency of PTB7-Based Polymer Solar Cells via Integrated Optimization of Both Anode and Cathode Interlayers. *Adv. Energy Mater.* (2014).
3. N. Li and C. J. Brabec, Air-processed polymer tandem solar cells with power conversion efficiency exceeding 10%. *Energy Environ. Sci.* **8** (10), 2902-2909 (2015).
4. J. Noh, S. Jeong and J. Y. Lee, Ultrafast formation of air-processable and high-quality polymer films on an aqueous substrate. *Nat. Commun.* **7**, 9 (2016).
5. S. Lee, J. Kong and K. Lee, Air-Stable Organic Solar Cells Using an Iodine-Free Solvent Additive. *Adv. Energy Mater.* **6** (21), 9 (2016).
6. M. J. Griffith, N. A. Cooling, B. Vaughan, D. C. Elkington, A. S. Hart, A. G. Lyons, S. Quereshi, W. J. Belcher and P. C. Dastoor, Combining Printing, Coating, and Vacuum Deposition on the Roll-to-Roll Scale: A Hybrid Organic Photovoltaics Fabrication. *IEEE J. Sel. Top. Quantum Electron.* **22** (1), 14 (2016).
7. D. Bartesaghi, G. Ye, R. C. Chiechi and L. J. A. Koster, Compatibility of PTB7 and 70 PCBM as a Key Factor for the Stability of PTB7: 70 PCBM Solar Cells. *Adv. Energy Mater.* **6** (13), 9 (2016).
8. S. D. Collins, N. A. Ran, M. C. Heiber and T.-Q. Nguyen, Small Is Powerful: Recent Progress in Solution-Processed Small Molecule Solar Cells. *Adv. Energy Mater.*, 1602242 (2017).
9. B. Kan, M. M. Li, Q. Zhang, F. Liu, X. J. Wan, Y. C. Wang, W. Ni, G. K. Long, X. Yang, H. R. Feng, Y. Zuo, M. T. Zhang, F. Huang, Y. Cao, T. P. Russell and Y. S. Chen, A Series of Simple Oligomer-like Small Molecules Based on Oligothiophenes for Solution-Processed Solar Cells With High Efficiency. *J. Am. Chem. Soc.* **137** (11), 3886-3893 (2015).
10. S. Q. Zhang, L. Ye and J. H. Hou, Breaking the 10% Efficiency Barrier in Organic Photovoltaics: Morphology and Device Optimization of Well-Known PBDTTT Polymers. *Adv. Energy Mater.* **6** (11), 20 (2016).
11. T. P. Osedach, T. L. Andrew and V. Bulovic, Effect of synthetic accessibility on the commercial viability of organic photovoltaics. *Energy Environ. Sci.* **6** (3), 711-718 (2013).
12. F. Kraffert, R. Steyrlleuthner, C. Meier, R. Bittl and J. Behrends, Transient electrically detected magnetic resonance spectroscopy applied to organic solar cells. *Appl. Phys. Lett.* **107** (4), 5 (2015).
13. W. Q. Chen and Q. C. Zhang, Recent progress in non-fullerene small molecule acceptors in organic solar cells (OSCs). *J. Mater. Chem. C* **5** (6), 1275-1302 (2017).

14. N. Liang, W. Jiang, J. Hou and Z. Wang, New developments in non-fullerene small molecule acceptors for polymer solar cells. *Materials Chemistry Frontiers* **1** (7), 1291-1303 (2017).